Investigations of the Properties of Materials for the Optics and Suspensions of Future Gravitational Wave Detectors

Eleanor C. Chalkley MSci.

Submitted in fulfilment of the requirements for the Degree of Ph. D.

in the University of Glasgow

Department of Physics and Astronomy

University of Glasgow, University Avenue, Glasgow, G12 8QQ

Contents

List of Figures

List of Tables

Acknowledgements

The years I spent in Glasgow doing the work that became this thesis were extraordinary and life-changing. I'd like to offer my most sincere gratitude to my academic supervisors Sheila Rowan and Jim Hough, for teaching me about how problems are solved and how research is done and their extreme patience as I wrote up my thesis. My friends and colleagues in the lab were constantly helpful and fantastic to work with: especially Iain, Stuart, Ronny, Alan, Mariëlle, Peter, Karen, Riccardo, Matt and Nicola. I also had great support from our technicians, Colin and Stevie, and the assistance of Alastair Grant as I learned some of the finer points of analogue electronics. The IGR was a lively and stimulating place to work, and it was a great privilege to be able to be a part of it; thank you all. I'd also like to thank PPARC/STFC, the LIGO Scientific Collaboration and the University of Glasgow for supporting my studies.

I also made some very good friends in the Kelvin Building at Glasgow: Bob, Hazel, Matt, James, Jen, Jennifer, Bryan, Dave, Siong, Fiona, Iain, Chris and everyone else who came to lunch, drank tea, attended parties, came to Mr India's for curry and were generally all round good sports. My friends outside of physics helped me keep perspective, in particular Karina, Elaine, Lilith, Paula and the rest of my knitting group who provided evenings of amazing, diverse conversation and helped me appreciate the finer fibres. My new colleagues and friends at Birmingham have also been very understanding in the final weeks of thesis writing and helped cheer me to the finish line.

My family have been brilliantly supportive and encouraging all the way through my education, and they were especially helpful during the time I was writing up. John has been a great friend and totally brilliant all the time I've known him, and now this thesis isn't taking all my time, we can have lots of adventures together. This is for everyone who knew I could achieve it.

Preface

This thesis contains descriptions of my studies at the University of Glasgow between October 2005 and October 2009, where I investigated the mechanical properties of materials for use in future gravitational wave detectors.

Chapter One describes the phenomenon of gravitational radiation, how it is produced and how it may be detected using long-baseline laser interferometry. The network of gravitational wave detectors currently in operation is described and the routes for upgrades and future detectors are explained.

Chapter Two contains theoretical background on the sources of noise in gravitational wave detectors which are related to and caused by the thermal motions of the constituent molecules. The connection between thermal noise and mechanical loss is made and used to motivate the measurement of mechanical loss as a probe for assessing optical materials for use in future gravitational wave detectors.

In Chapter Three the current status of mechanical loss measurements on materials used in the optics of gravitational wave detectors is assessed. High-reflective dielectric multilayer coatings are described. The motivation for measuring the mechanical loss of a dielectric coating material as a function of temperature is given.

The apparatus used to produce the cryogenic mechanical loss measurements that form the basis for Chapters Four, Five and Six is described and explained. The apparatus was constructed by the author, S. Reid and R. Nawrodt. The semi-automated measurement software was written by R. Nawrodt. Measurements were carried out by the author in order to characterise the performance of the cryostat. The measurements which form the explanation for the low temperature and thermal cycling anomalies were performed by M. Abernathy using the apparatus constructed by the author.

Chapter Four focuses on cryogenic mechanical loss measurements of silica coatings. Ellipsometric measurements of the thicknesses of the silica coatings and thermal oxide layers upon the cantilevers were conducted using an ellipsometer by S. Lewis, P. Murray and S. Reid. All measurements of the silica coated sample heat-treated at 300^{o}C were carried out by the author. The measurements of the control sample heat-treated at 300^{o}C were carried out by M. Abernathy. All measurements of the silica coated samples heat-treated at 600^{o}C and 800^{o}C and their respective control samples were carried out by the author. The analysis of the measurements was performed by the author.

Chapter Five concerns cryogenic mechanical loss measurements of hafnia coatings. The measurements of the hafnia coated sample heat-treated at 300^{o}C were carried out by the author and the control data used to calculate the coating losses were taken by I. Martin. The electron micrograph and electron diffraction images were produced by R. Bassiri. The hafnia sample which remained un-heat-treated was measured by the author and M. Abernathy, and the control data used to cal-

culate the coating losses were taken by S. Reid.

Chapter Six describes a study of the cryogenic mechanical loss of a hydroxy-catalysis bond between two silicon components. The silicon cantilevers were oxidised by S. Reid. Cryogenic mechanical loss measurements on the component cantilevers were carried out by the author. The hydroxy-catalysis bonding process and the infra-red photography was performed by S. Reid. The measurements of the bonded cantilever structure and the calculations to extract the upper limit for the mechanical loss of the bond material were performed by the author, using a method developed during discussions with S. Reid, J. Hough and S. Rowan.

Chapter Seven contains an account of room temperature measurements on materials considered as mirror substrates for future gravitational wave detectors. The finite element calculations were carried out in ANSYS by the author. The initial nodal support was designed and constructed by the author and A. Cumming and the measurements were carried out in a system refitted by the author, A. Cumming, P. Murray and I. Martin. The mechanical loss measurements of sapphire and silicon samples on thread suspensions were carried out by P. Murray and all nodal support measurements were made by the author. Suggestions and assistance in improving the nodal support were given by J. Faller, M. Perreur-Lloyd and R. Jones. The profiles of the damaged samples were carried out by the author and L. Cunningham. The cryostat system used in this chapter was refitted by the author with the assistance of I. Martin, P. Murray and S. Reid. The mechanical loss measurements were carried out by the author.

Appendix One describes work towards developing a system for measuring the coefficient of thermal expansion and biaxial modulus of coating materials using the existing coated silicon cantilever samples. The measurement system was developed by the author and M. Abernathy with the assistance of L. Cunningham. Ellipsometric measurements and investigations into measurements of the radius of curvature were carried out by Z. Pierpoint. The analysis of the data was performed by the author.

Summary

Gravitational waves are a consequence of General Relativity and while indirect measurements strongly imply their existence, they have not yet been directly detected. Gravitational waves are manifest as extremely weak quadrupolar strains in spacetime itself. The effects of these cosmically weak strains upon the travel of a laser between test particles may be detectable using sophisticated variations of a Michelson interferometer. Chapter One describes the theoretical basis for the construction of large ground-based interferometric gravitational wave detectors.

The scientific effort to detect gravitational waves has grown continually since the inception of the field in the 1960s, and has led to the construction and commissioning of a world-wide network of sophisticated and sensitive instruments for the detection of gravitational waves. The construction of these detectors has involved the development of many new technologies for precision measurement, but as sensitive as the detectors are, we have not yet reached the level where a detection is certain to be made. Chapter One also contains descriptions of the current detectors and outlines of the plans for their future upgrades.

Future generations of gravitational wave detectors will require significant progress

in the reduction of all forms of noise affecting the system. One form of noise it is critical to reduce is thermal noise, which can be described as the consequence of the atoms which make up the measurement optics experiencing vibrations because of their non-zero temperature. The dielectric multilayer coatings of the mirror in an interferometric gravitational wave detector are known to contribute significantly to the overall levels of thermal noise. The next generation of gravitational wave detectors may need to use exotic coatings, cryogenic operating temperatures and silicon mirror substrates in an effort to mitigate the effects of thermal noise. Chapter Two describes thermal noise in detail, and introduces the concepts of substrate noise, coating noise, thermoelastic dissipation, mechanical loss and the formulae used to calculate them.

Chapter Three describes the current state of research on the factors affecting mechanical loss in dielectric coatings. The technique of probing the structure and dissipation characteristics of materials by assessing the shape and position of the low temperature excess loss feature known as a Debye peak is introduced. The cryogenic mechanical loss measurement apparatus used in Chapters Four, Five and Six is described and characterised.

Chapter Four concerns the variation of mechanical loss of ion-beam sputtered silica coatings with temperature and investigates the effects of heat-treatment upon them. The low-temperature Debye peak was found in some modes of a sample heat treated at 300^{o}C and an Arrhenius analysis provided a characteristic energy for the dissipation process of (17.3 ± 2.3)meV. Further heat treatment of silica at 600^{o}C and 800^{o}C appears to narrow the Debye peak, which is thought to be indicative

of the narrowing of the distribution of bond angles in the amorphous silica network.

Hafnia is investigated as an alternative coating material in Chapter Five. The mechanical loss of hafnia heat-treated at 300^{o}C was measured and two excess loss features were discovered, one below 100K and one above 200K. Electron scattering measurements indicate that this sample may already have developed polycrystalline regions which are known to be connected to high levels of mechanical loss. The mechanical loss of an un-heat-treated hafnia coating is also measured and an extremely low coating loss of 1.87×10^{-5} is found at 20K.

Chapter Six describes an experiment to find the mechanical loss of a hydroxy-catalysis bond between silicon cantilevers at temperatures between 10K and 300K. This new technique for the measurement of the mechanical loss of bond material produced a minimum upper limit of the bond loss of (0.13 ± 0.03) occurring in the fundamental mode at 80K and upper limit of the bond loss of (0.19 ± 0.07) occurring in the third mode at 15K.

Chapter Seven describes the development and testing of a nodal support system to enable cryogenic measurements of cylindrical bulk mirror substrates to be made. The efficacy of the support varied significantly with the frequency of the mode and the cryogenic measurements were partially successful.

Appendix One contains a description of the development of an experimental system to simultaneously measure the coefficient of thermal expansion, α and biaxial modulus, B, of coating materials. The first set of measurements of tantala coat-

ings on silicon cantilevers produced measurements which excluded the literature values of α and B.

The major results in this work are the successful measurements of the mechanical loss of amorphous hafnia coatings at low temperatures and the use of a structure made from hydroxy-catalysis bonded silicon cantilevers to obtain an upper limit for the mechanical loss of the bond material. These results may inform technological advances that reduce the level of thermal noise experienced in future gravitational wave detectors.

Chapter 1

The Origin and Detection of Gravitational Waves

1.1 Introduction

Advances in our knowledge of the Universe have gone hand-in-hand with advances in the technologies we use to quantify, measure and observe it. In astronomy, observations are critical. In pre-history, watching the sky provided information on the changing seasons and gave humanity a sense of place in the Universe. By the Renaissance, naked eye observations were enhanced by the use of marked quadrants to enable the location of bodies to be more precisely measured, and the use of lenses to create astronomical telescopes provided evidence that the Universe was a very different place to the one suggested by the prevailing thought of the time. Over the centuries, the design of astronomical instruments expanded and improved to provide science with ground-breaking observations of objects over the whole electromagnetic spectrum, with each new method of observing the sky pro-

viding views of the previously unexpected, such as other galaxies, pulsars, quasars and vast clouds of interstellar dust.

As a consequence of Einstein's 1916 General Theory of Relativity, an opportunity to supplement the information provided by the electromagnetic observations arises that has the potential to begin a new area of exploration in astronomy. General relativity is the interpretation of gravitational forces as resulting from curvature of spacetime, which reciprocally acts on and reacts to the motion of masses. When bodies accelerate under certain conditions, they create fluctuations in spacetime which travel outwards at the speed of light. If these fluctuations - which have become known as gravitational waves - can be observed when they reach Earth, they could provide a new observation method for astronomy. Gravitational wave astronomy could open a window onto the strange world of extreme astrophysical phenomena, moving beyond the information provided by radiation in the electromagnetic spectrum.

1.2 Gravitational Wave Generation and Sources

In order to consider the generation and detection of gravitational waves, it is first necessary to qualitatively examine General Relativity through the application of Einstein's field equations,

$$G_{\mu\nu} = 8\pi T_{\mu\nu} \tag{1.1}$$

which are the set of tensor equations that show the curvature of spacetime, $G_{\mu\nu}$, in terms of the density of energy and matter as described by the stress-energy tensor, $T_{\mu\nu}$ and with units defined so that $G = c = 1$. Because the perceived gravitational field acting on a body is contributed to by the gravitational field generated by the body itself, the general form of Einstein's field equations is non-linear. The curvature of spacetime is fully described by the Einstein tensor, $G_{\mu\nu}$, which may be expanded as [1],

$$G_{\mu\nu} = R_{\mu\nu} - \frac{1}{2} g_{\mu\nu} R. \tag{1.2}$$

The metric tensor, $g_{\mu\nu}$, defines the distance between points in spacetime and the symbols $R_{\mu\nu}$ and R represent the Ricci curvature tensor and scalar curvature of the space-time manifold respectively. These quantities taken together with the metric tensor, $g_{\mu\nu}$, describe the deviation of the curvature of real spacetime from the flat, isotropic model spacetime postulated by Minkowski. The flat Minkowski spacetime metric is called $\eta_{\mu\nu}$ and is defined as [1],

$$\eta_{\mu\nu} = \begin{pmatrix} -1 & 0 & 0 & 0 \\ 0 & 1 & 0 & 0 \\ 0 & 0 & 1 & 0 \\ 0 & 0 & 0 & 1 \end{pmatrix}$$

In situations where bodies are not very massive and speeds are only a small fraction of c, calculations using the full set of Einstein's field equations give results which only have small deviations from Newtonian calculations - this gives rise to the *slow speed approximation* and the *weak field approximation*.

In the region of Earth, there are no local bodies of relativistic masses or velocities, so a weak field may be assumed and these approximations may be used in calculations. In this approximation, the local spacetime curvature only deviates from a flat spacetime, $\eta_{\mu\nu}$, by a very small perturbation, $h_{\mu\nu}$, and the metric, $g_{\mu\nu}$ is given by,

$$g_{\mu\nu} = \eta_{\mu\nu} + h_{\mu\nu}. \tag{1.3}$$

If $h_{\mu\nu}$ is the perturbation in spacetime curvature due to the behaviour of a distant mass, then when this perturbation reaches a set of points, the metric underlying the local co-ordinate system is changed. Far from the source the perturbation can be represented as a plane wave of form

$$h_{\mu\nu} = \Re[A_{\mu\nu}e^{-ikx}], \tag{1.4}$$

with amplitude, $A_{\mu\nu}$, and wave vector, k [1]. The wave travels in the direction of k at the speed of light, where the amplitude of the wave is related to the amplitude of the perturbation.

By switching to a particular co-ordinate system, the components of $A_{\mu\nu}$ may be simplified. The most useful of these systems is the transverse-traceless gauge, which behaves as if all objects were in free-fall along geodesics in spacetime [2]. In the transverse-traceless gauge tensors such as the amplitude of the gravitational perturbation discussed above are constrained to have non-zero components only in those elements which are transverse to the direction of the tensor. If $A_{\mu\nu}$ is orientated to travel along the z direction, only the transverse elements A_{yy}, A_{yx}, A_{xy}

and A_{xx} may have a non-zero value. The 'traceless' part of the name 'transverse-traceless' refers to the sum of the diagonal components of the tensor being equal to zero. In the case of $A_{\mu\nu}$, this means that $A_{yy} = -A_{xx}$.

This leaves the amplitude of the perturbation of spacetime with only two independent components. As the average magnitude of the perturbation, $h_{\mu\nu}$, is proportional to the amplitude, $A_{\mu\nu}$, the same constraints also carry through to the perturbation tensor, $h_{\mu\nu}$. This means that the components of the perturbation can be written as,

$$h_{\mu\nu} = \begin{pmatrix} 0 & 0 & 0 & 0 \\ 0 & a & b & 0 \\ 0 & b & -a & 0 \\ 0 & 0 & 0 & 0 \end{pmatrix} \tag{1.5}$$

A perturbation like this can be thought of as the sum of two independent polarizations of the gravitational radiation, $h_{\mu\nu} = ah_+ + bh_\times$. This produces a model of the gravitational wave as the linear sum of two basic orthogonal wave polarisations, h_+ and $h_\times$, as written here [2]:

$$h_+ = \begin{pmatrix} 0 & 0 & 0 & 0 \\ 0 & 1 & 0 & 0 \\ 0 & 0 & -1 & 0 \\ 0 & 0 & 0 & 0 \end{pmatrix} \tag{1.6}$$

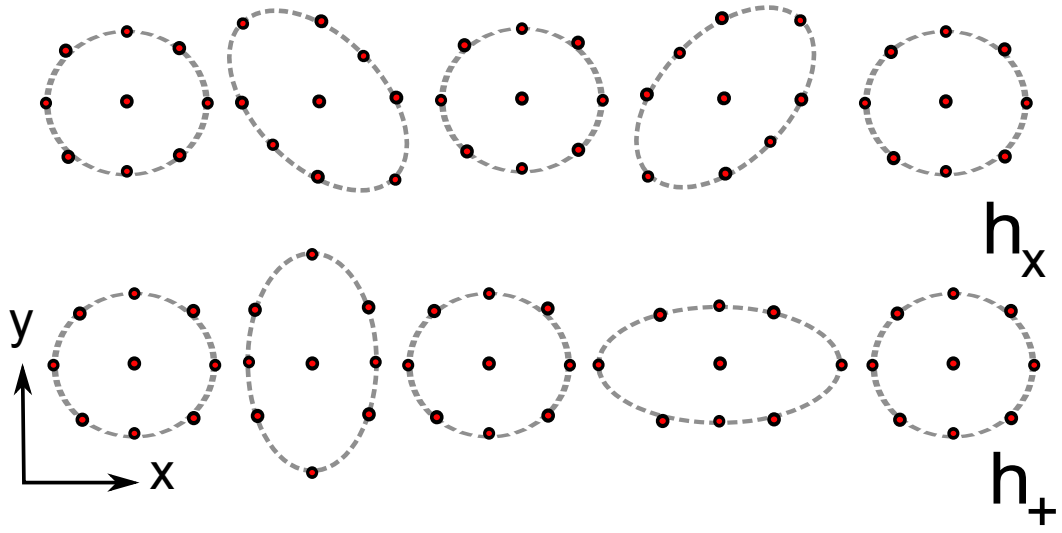

Figure 1.1: The motion of a ring of test particles for incident gravitational waves of polarisation h_+ and h_x.

$$h_\times = \begin{pmatrix} 0 & 0 & 0 & 0 \\ 0 & 0 & 1 & 0 \\ 0 & 1 & 0 & 0 \\ 0 & 0 & 0 & 0 \end{pmatrix}. \tag{1.7}$$

The h_+ polarisation of a gravitational wave only has non-zero components at h_{xx} and h_{yy}. The effect of this polarisation is to stretch spacetime in the x-direction whilst shrinking it in the y-direction, then shrink it in the x-direction while stretching it in the y-direction, as illustrated in Figure 1.1.

The $h_\times$ polarisation has non-zero components at h_{xy} and h_{yx}, and causes the same alternating stretching-shrinking behaviour as the h_+ polarisation, but with principal directions based on rotating the x and y axes by 45° [2].

This stretching and shrinking of distances due to a gravitational wave leads to the interpretation of gravitational waves as strains in spacetime. By definition, a strain is the ratio of a length change, δl to the original length, l. Referring back to the ring of test particles shown in Figure 1.1 , the distance between the central particle and the particles on the principle axes changes over the course of one oscillation. The size of this length change is proportional to the size of the perturbation due to the gravitational wave, and it can be shown that [1],

$$h = \frac{2\delta l}{l}, \tag{1.8}$$

where l is the separation of two test particles in the path of the gravitational wave and δl is the change in separation due to the passing gravitational wave and h is the metric perturbation due to the gravitational wave.

These gravitational waves are emitted by the acceleration of masses in a manner analogous to the emission of electromagnetic waves by accelerated charges. The analogy with the generation of electromagnetic radiation falters somewhat, as there can be no dipole gravitational radiation. Gravitational dipole radiation is prohibited by the single sign of gravitational 'charge' and the conservation of linear momentum. The lowest multipole moment of a mass distribution which can produce gravitational radiation is the quadrupole [3].

1.2.1 Sources of Gravitational Waves

The most readily observable gravitational waves will be those associated with large spatially non-axisymmetric accelerations of large masses. The lower frequency limit for ground-based observations is around 1Hz below which fluctuations in the gravitational field of the Earth will obscure the radiation from distant sources, although gravitational radiation of a lower frequency is expected to exist. It is expected that some extragalactic sources emit gravitational waves with frequencies of up to a few kilohertz, and some cosmological sources could emit gravitational waves of higher frequency still.

The following section contains examples of potential gravitational wave sources. This list is not intended to be exhaustive but provides some limits on the source frequencies and amplitudes which are of relevance to the attempt to detect them.

Compact Binaries

Astrophysical systems composed of two compact stellar objects are expected sources of gravitational waves. As the bodies orbit each other, part of the energy of the system is radiated as low frequency gravitational waves. This results in the orbital decay of the system and the increase in amplitude and frequency of the gravitational waves until the two bodies coalesce, resulting in an audio frequency chirp. The 'chirp' is one of the most likely gravitational waveforms to be detected in ground-based detectors, due to the distinctive shape of the waveform and the frequency of compact binaries in the Universe.

In general, the gravitational wave amplitude for a binary star system consist-

ing of objects with masses M_1 and M_2, with an orbital frequency, f at a distance, r, from the observer can be estimated as [4],

$$h_{binaries} \sim 10^{-23} \left(\frac{100Mpc}{r}\right) \left(\frac{M_b}{1.2M_\odot}\right)^{\frac{5}{3}} \left(\frac{f}{200Hz}\right)^{\frac{2}{3}}, \tag{1.9}$$

where M_b is the mass parameter, given by

$$M_b = \frac{(M_1 M_2)^{\frac{3}{5}}}{(M_1 + M_2)^{\frac{1}{5}}}.$$

As the objects in these systems orbit each other, energy is lost by electromagnetic and gravitational radiation and the two compact objects form a tighter and faster orbit, which corresponds to a gravitational wave signal of increasing frequency and amplitude. After the last stable orbit, which for a binary system is not rigidly defined but corresponds to the point at which the rate of increase in gravitational wave frequency becomes very large, the two objects move closer and coalesce to form a larger compact object.

Applying equation 1.9 for a neutron star/neutron star binary within the Galaxy at a distance of 15kPc from Earth with $M_1 = M_2 = 1.4M_\odot$ orbiting around the common centre of mass with a frequency, $f = 1Hz$, gives a gravitational wave amplitude of $h \sim 2 \times 10^{-21}$.

The form of compact binary source thought to be most prevalent in the Universe are black hole/black hole binaries formed in globular clusters, where the level of gravitational interaction with other systems forces the black holes into closer orbits which lose most of their energy through gravitational radiation. Ap-

plying equation 1.9 for a black hole/black hole binary with $M_1 = M_2 = 10M_\odot$ orbiting around the common centre of mass with a frequency, $f = 10Hz$, at a distance of 20MPc from Earth, gives a gravitational wave amplitude of $h \sim 2 \times 10^{-22}$.

In the case of a black hole/black hole coalescence this is also thought to produce a strong burst of gravitational waves with complex signal forms, the study and prediction of which has been a topic for numerical relativistic modelling and some results of which can be found in [5].

Other sources of gravitational waves associated with compact objects include the tidal disruption of a neutron star by a black hole companion, and sources known as low mass X-ray binaries [6] [7].

Pulsars and Periodic Emitters

Neutron stars may form an important source of gravitational waves - the enormous density of the nuclear material that constitutes the post-supernova remnant of a large star combined with the conserved angular momentum provides several possibilities for gravitational wave emission. If a neutron star which spins with a frequency, f, develops a mountain which gives the star an ellipticity, ϵ, then the asymmetry caused by the 'mountain' will act in the same manner as a an astrophysical scale mass on a centrifuge. The gravitational wave amplitude can be estimated as follows [8]:

$$h_{pulsar} \sim 6 \times 10^{-25} \left(\frac{f}{500Hz}\right)^2 \left(\frac{1kpc}{r}\right) \left(\frac{\epsilon}{10^{-6}}\right). \tag{1.10}$$

The luminosity of the gravitational waves emitted in this way is limited by the maximum potential size of the mountain on the neutron star, which is limited by the strength of the surface material. Recent work by Owen suggests that the maximum ellipticity that can be supported by a neutron star is of the order of $\sim 10^{-4}$ [9]. If such a pulsar is within our Galaxy, at $r = 15$kPc, and rotating at a frequency of $100Hz$ then the value of $h_{pulsar} \sim 1 \times 10^{-25}$. These signals from pulsars are likely to be detected by coherently averaging data over a long observation period.

The use of gravitational wave data to provide upper limits to the decay in the spin rate of known pulsars such as the Crab and Vela is already providing upper limits on the amount of energy lost through gravitational radiation. Whether we have already observed the optical counterpart or not, the gravitational wave emission from relatively nearby pulsars and neutron stars is a potentially important source of information about their structure.

Gravitational Waves From Supernovae

As the explosive dènouement to the life of a large star in an iron core collapse in a Type II supernova is one of the most energetic processes in the known universe, the emission of a proportion of that energy as gravitational radiation would provide an excellent candidate source. Around 99% of the energy of the core collapse is thought to be dissipated as neutrinos, with most of the remaining $\sim$ 1% being emitted as electromagnetic radiation, leaving only a very small portion to be emitted as gravitational radiation. The emission of gravitational waves requires non-axisymmetric acceleration, which could be linked to the rotation of the core

of the star, asymmetries in the distribution of matter in the core and surrounding shells of the star or magnetic phenomena [10].

The rate of these cataclysms in the local group of galaxies is less than one event per decade, which would make detections of these events during the running of a detection experiment unlikely, but at distances of $3 \sim 5$MPc, core collapse events are estimated to occur at a rate of 1 per $\sim$2 years [10]. The proportion of energy from a core collapse that is emitted as gravitational radiation is a current topic in numerical modelling, and would allow the calculation of a value for the resultant h for an observer on Earth.

If the amount of energy emitted from the supernova as gravitational waves, ΔE is known, then an estimate of the amplitude of a gravitational wave can be made using the following formula [11],

$$h_{supernova} \sim 10^{-20} \left(\frac{\Delta E}{M_{\odot}c^2}\right) \left(\frac{15Mpc}{r}\right) \left(\frac{1kHz}{f}\right) \left(\frac{1ms}{\Delta t}\right)^{\frac{1}{2}}, \tag{1.11}$$

where Δt is the time it takes for the supernova to collapse and r is the distance from the collapsing supernova to the observer and ΔE is the fraction of the core collapse energy dispersed as gravitational waves.

Stochastic Sources

It is also possible to imagine the detection of gravitational wave emissions which can only be described in terms of their statistical properties. These emissions would form a background in the gravitational wave spectrum and could be caused by two broad ranges of phenomena. A stochastic background of gravitational

waves could be caused by large populations of astrophysical gravitational wave sources such as compact binaries or neutron stars.

Alternatively, most cosmological descriptions of the birth and development of the Universe contain some predictions for gravitational wave emissions. As the interaction of gravitational radiation with matter is exceedingly weak, it is likely that these relic gravitational waves will still exist in a detectable form. Relic gravitational waves are proposed to be amplified remnants of vacuum fluctuations in the inflationary era of the Universe. Observation of the level of cosmic gravitational wave background would allow constraints to be placed upon cosmological models and provide a picture of the Universe 300,000 years before the surface of last scattering seen in the cosmic microwave background and only a very short time after $t = 0$. Even the definite non-observation of a gravitational wave background at a certain level can be used to place bounds and upper limits on Ω_{gw}, the energy density of gravitational waves in the Universe [12].

1.3 Gravitational Wave Detection: Are Gravitational Waves Detectable?

The analogy between electromagnetic waves and gravitational waves breaks down when considering their interactions with matter. Because the gravitational force is around 38 orders of magnitude smaller than the other forces of nature, a gravitational wave hardly interacts with matter as it passes through it. This means that when it reaches Earth, a gravitational wave from a distant astrophysical source

will retain the characteristics of the emitted wave to a much greater extent than an electromagnetic wave emitted from the object would, but the effects of the interaction of the wave with a detector will be extremely small, making the wave difficult to detect.

Gravitational waves have already been seen indirectly through the rate of orbital decay of the binary pulsar PSR 1913+16 [13] [14], resulting in Hulse and Taylor receiving the 1993 Nobel Prize for Physics. The rate of orbital decay measured over thirty years of observations agrees with the General Relativistic predictions of energy loss by gravitational waves to better than 0.2% [15]. No other forms of energy loss can fully account for the sign and magnitude of the decay rate, so the observed energy loss must be due to the emission of gravitational radiation.

A direct observation of gravitational waves requires an entirely new form of astronomical instrument - one that can sense the minute interactions of gravitational waves with matter.

1.4 Principles of Gravitational Wave Detection Using A Michelson Type Interferometer

As described in Section 1.2, the incident gravitational wave acts like a propagating strain that compresses space in one transverse direction while simultaneously stretching it in the orthogonal transverse direction.

Information about the acceleration of the quadrupolar moment of the gravitational wave source is contained in the perturbation of the metric, $h_{\mu\nu}$. The perturbation can in principle be measured by considering a distribution of unconstrained point masses placed upon geodesics in spacetime. In general relativity, the distance between these masses is determined by the curvature of the spacetime between the masses.

When using the transverse-traceless gauge described in section 1.2, the effect of a passing gravitational wave is to perturb the metric, altering the distances between the masses without changing their positions relative to their geodesics. By using the travel time of a light beam to measure the distances between the masses, the presence of a gravitational wave can be inferred from the variations in the measured distance.

There is a simple arrangement of masses that allows the measurement of the changes in spacetime caused by an incident gravitational wave. This consists of a mass representing the co-ordinate system origin, and two masses with mirrored faces placed at a distance, L, from the origin mass so that the paths between the origin mass and the mirror masses are orthogonal - see Figure 1.2 for a diagram. If the origin mass is taken to be a beam splitter, then this arrangement is recognisable as the Michelson interferometer.

When no gravitational wave is incident upon this instrument, the light takes a time $\tau = 2\frac{L}{c}$ to travel from the beam splitter to the mirror at the end of the interferometer arm, be reflected and return to the beam splitter. As the distance

L is the same for both arms of the interferometer, beams of light which enter the interferometer coherently will leave in phase.

However, if a suitably polarized gravitational wave passes through the detector in the z-direction (out of the page, according to the convention used in Figure 1.2) the differential strain will effectively result in the change of the arm lengths. If the gravitational wave produces a change in arm length of δl, the light travel time is now:

$$\tau = 2\frac{(L \pm \delta l)}{c} = L\frac{(2+h)}{c} \tag{1.12}$$

For one arm of the interferometer, the light will take $^{2\delta l}/_{c}$ longer to return to the beam splitter, and for the other arm, the light will take $^{2\delta l}/_{c}$ less time to return. It is more useful to think of these changes in travel time for light as relative changes of the phase of the light at the output port of the beamsplitter. If the wavelength of the coherent light used is λ, then the phase change due to a gravitational wave of amplitude, h, is given by:

$$\delta\phi = h\frac{4\pi L}{\lambda}. \tag{1.13}$$

These changes in phase will be detectable at the output of the beamsplitter, which implies that a Michelson interferometer can in principle be satisfactorily used to detect the changes in spacetime caused by an incident gravitational wave [16][2], subject to obtaining a high enough sensitivity.

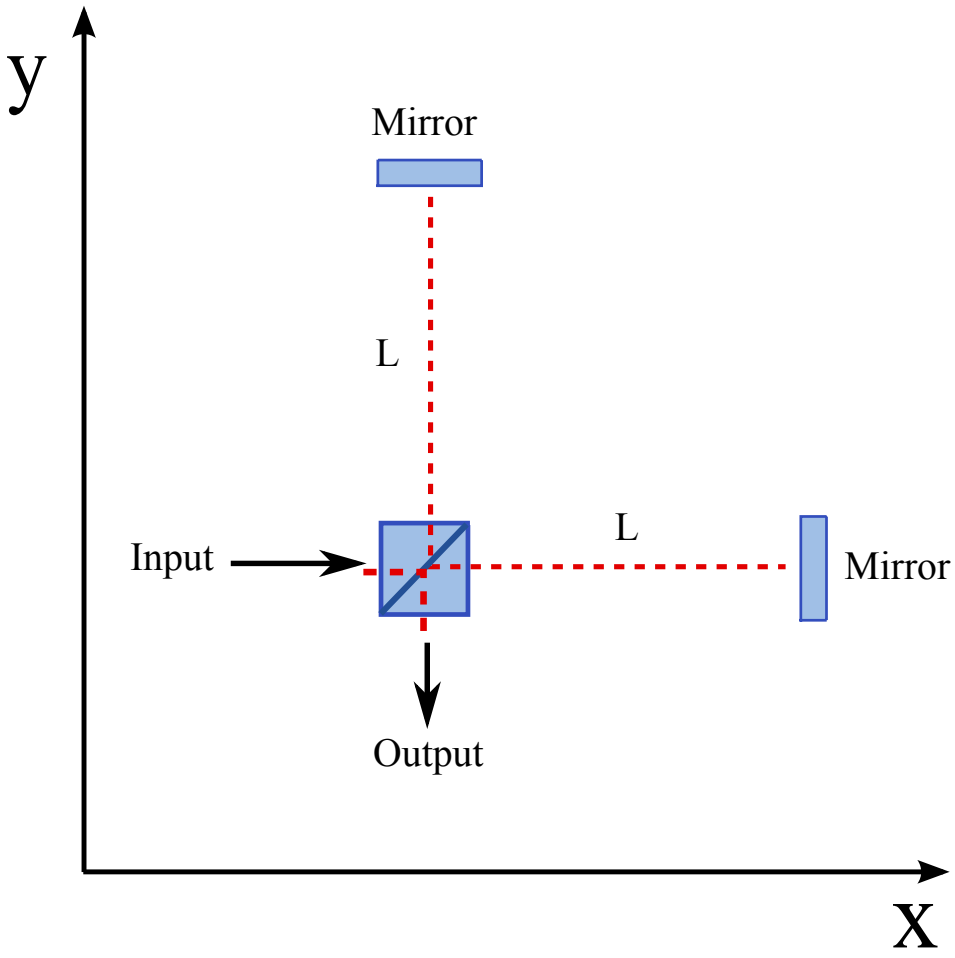

Figure 1.2: Two mirror masses and a beam-splitter, arranged to form a Michelson interferometer.

This technique is still a technical and scientific challenge, as the stiffness of spacetime, the weakness of the gravitational interaction and the enormous distances between the sources and the Earthbound observers results in the motions due to an incident gravitational wave from even the most dramatic of astronomical events being several orders of magnitude smaller than the radius of an atomic nucleus. Using the value for the amplitude of a gravitational wave from an inspiralling neutron star binary calculated in Section 1.2.1, $h = 2 \times 10^{-21}$, the change in the arm length of a 4km interferometer is 1.6×10^{-17}m and the resultant phase change for an interferometer employing a 1064nm laser is 9×10^{-11} radians.

1.5 Early Detection Attempts

In order to appreciate the technological advances made in the effort to detect gravitational waves, it is useful to briefly recount the history of gravitational wave experimentation. In the late 1950s, Joseph Weber of the University of Maryland made the first attempt at construction of a serious gravitational wave detector. These first detectors consisted of one ton aluminium bars, at room temperature, the resonant modes of which would be excited if a gravitational wave of the appropriate frequency passed through it, with piezoelectric transducers monitoring for any motion of the mass. Weber claimed to have detected gravitational waves, but his results could not be reproduced and it was later estimated that the room temperature bar detectors lacked the sensitivity to detect gravitational waves from any plausible sources.

The invention of lasers meant that the sensitivity of Michelson type interferometers

could be improved greatly. Robert Forward's team at the Hughes Research laboratory developed the first Michelson type laser interferometer with suspended optics that was intended for use as a gravitational wave antenna. The 2m long arms and low laser power meant that the strain sensitivity was limited to $1 - 5 \times 10^{-16}\sqrt{Hz}$, but this prototype has provided the basic template for all current ground-based laser interferometer detectors to date [17]. Further small prototypes followed at MIT, Glasgow, MPI Garching, Caltech, where many of the techniques used in the current generation of gravitational wave detectors were developed.

1.6 Laser Interferometric Gravitational Wave Detectors

In order for a Michelson interferometer to be operated as a useful instrument for the detection of gravitational waves, the instrument must be operated under a certain control scheme. If the interferometer is held in a condition where the light from both arms produces maximum constructive interference, in the terminology of interferometry, this is known as the 'bright fringe'. While this is simple to arrange, the amplitude change resulting from the altered travel time of the light from each arm due to a gravitational wave is extremely small in comparison to the base amplitude of the bright fringe. This arrangement therefore provides poor signal to noise performance, as the useful signal will only be manifest as a very small magnitude change against the background of the carrier signal of large magnitude.

A useful alternative would be to set the arm lengths so that the two light beams

destructively interfere, resulting in an output signal with amplitude close to zero when no gravitational wave is present and with a small but measurable amplitude when a differential arm length change occurs. The minimum amplitude observed at the output of the interferometer is known as the 'dark fringe' - operating the gravitational wave detector in this condition or close to it will result in a better signal to noise ratio than bright fringe operation.

To make real measurements possible, the interferometer is operated in a 'locked' condition. In a locked interferometer, a feedback control system uses the output signal of the interferometer to control the motion of a part of the interferometer to bring the output signal close to zero. In this scheme, the actual signal representing the effects of the gravitational wave is part of the signal used to control the system. This interferometer operating scheme lies at the heart of all the advanced optical techniques used in modern gravitational wave detectors.

1.7 Sources of Noise in Long Baseline Interferometric Gravitational Wave Detectors

As the change in interferometer arm length resulting from a gravitational wave is extremely small and easily swamped by differential mode signals not caused by gravitational waves, all possible noise sources must be reduced or compensated for in order to obtain a satisfactory signal to noise ratio. The following sections outline the major noise components present in interferometric gravitational wave detectors and the steps taken to reduce them.

1.7.1 Laser-related Noise and the Standard Quantum Limit

The use of a real laser in a real interferometric system brings the limitations of instrumentation into focus when considering the measurement of extremely small displacements. The light from a real laser contains frequency fluctuations, which contribute unpredictably to the phase difference at the output port of the interferometer. The size of this phase difference is equivalent to a gravitational wave strain proportional to the ratio of the size of the fluctuations to the mean frequency of the laser. The amplitude of the laser light is also subject to fluctuations, and these also contribute to non-gravitational wave signals at the output of the interferometer [2][18]. Other aspects of the laser light can couple into the interferometer and lead to noise, such as imperfections in the alignment of the laser beam, beam jitter, optical scattering and the effect of higher order spatial modes of the laser beam passing into the interferometer. Many technological achievements have been made in order to suppress and mitigate these sources of noise.

These technical laser-related noise sources may be challenging, but they do not fundamentally limit the performance of this form of instrument. The fundamental limit to the precision of interferometry is related to the quantum interpretation of what occurs when the gravitational wave detector interacts with the laser beam. This may be considered as a combination of two complementary effects: the fluctuating radiation pressure on the gravitational wave detector optics and the unavoidable phenomenon of shot noise in the electronics detecting photons at the output port of the interferometer.

Radiation Pressure Noise

Radiation pressure noise is caused by fluctuations in the number of photons colliding with the reflecting surfaces of the test masses of the interferometer. The photons exchange momentum with the test masses, resulting in slight random motions of the test mass and causing an intensity change at the output of the interferometer. The equivalent gravitational wave amplitude due to this form of noise is given by,

$$h_{r.p.}(f) = \frac{1}{mf^2L}\sqrt{\frac{\hbar P_{in}}{8\pi^3 c\lambda}}, \tag{1.14}$$

where L is the arm length of the interferometer, m is the mass of the test mass mirrors, P_{in} is the laser input power, λ is the wavelength of the laser light and f is the signal frequency [2].

As can be seen in Equation 1.14, the effects of radiation pressure noise can be reduced by increasing the mass of the test masses, m and length of the arms, L, and reducing the laser power, P_{in}.

Photon Shot Noise

Part of the operation of the interferometer readout involves measuring the intensity of the light at the output port of the interferometer using a photodetector. Real-world photodetectors have an efficiency, η, which represents the probability that an incident photon will induce a photoelectron in the detector. In this way, photon shot noise can be thought of as the statistical uncertainty in the number

of photo-electrons detected at the output of the interferometer. This process can be modelled using Poisson statistics, so for every N photo-electrons detected at the photodiode, there will be an uncertainty of $\sqrt{N}$ in the output signal.

An estimate of h, the equivalent strain caused by shot noise in a Michelson interferometer can be written as,

$$h_{shot}(f) = \frac{1}{\eta L}\sqrt{\frac{\hbar c\lambda}{2\pi P_{in}}}. \tag{1.15}$$

Where L is the arm length of the interferometer, P_{in} is the laser input power, η is the efficiency of the photodiode and λ is the wavelength of the laser light. As can be seen from the equation above, the effect of this form of noise can be reduced by increasing the laser power or the length of the interferometer arms [2].

For a simple, ideal Michelson interferometer, the shot noise does not vary with frequency. When the additional characteristics of the interferometers in gravitational wave detectors are taken into account, extra frequency dependent terms are required to describe the shot noise spectrum, resulting in higher shot noise for high frequencies. For a Michelson interferometer in which the arms are Fabry-Perot cavities, the shot noise is given by [2],

$$h_{shot}(f) = \frac{1}{8FL}\sqrt{\frac{\hbar\lambda c}{\pi\eta C P_{in}}}\sqrt{1+\left(\frac{f}{f_{FP}}^2\right)} \tag{1.16}$$

where F is the finesse of the Fabry-Perot arm cavities, and f_{FP} is the Fabry-Perot cut-off frequency, given by,

$$f_{FP} = \frac{c}{4L_{arm}F}. \tag{1.17}$$

The Quantum Limit for Interferometric Precision

As the effects of radiation pressure noise can be decreased by reducing the laser power, and photon shot noise can be decreased by increasing the laser power, there is a tradeoff for the optimum value of input laser power that results in the lowest level of noise for the two effects combined. For each value of P_{in} the best sensitivity to a gravitational wave signal occurs for a different gravitational wave signal frequency. It is sensible to set P_{in} to a value that places the frequency of peak sensitivity at a region of interest on the gravitational wave spectrum.

Taken together, the radiation pressure noise and the photon shot noise form a lower limit on the sensitivity of this form of detector. The radiation pressure noise results in a fluctuation of the momentum being imparted to the test mass, Δp, and the photon shot noise results in an uncertainty in the position of the mass, Δx. Provided these two quantities represent uncorrelated noise sources it can be shown that they can be related by a form of the Heisenberg Uncertainty Principle,

$$\Delta x \Delta p \geqslant \hbar \tag{1.18}$$

Radiation pressure and shot noise can also be thought of as the effect of zero-point fluctuations in the vacuum entering the interferometer by coupling with the unused port of the beam splitter. Upon leaving the laser, the light entering the input port of the interferometer is in a coherent state, which becomes mixed with the

random vacuum fluctuations upon passing through the beam splitter, resulting in a random variability in the amount of light impinging upon the arm mirrors and the photodetector.

The lower limit of the sensitivity of an interferometer is known as the standard quantum limit or SQL, and is given by [2][19],

$$h_{SQL} = \sqrt{\frac{8\hbar}{m\omega^2 L^2}}, \tag{1.19}$$

where $\hbar$ is the reduced Plank constant, m is the mass of the test mass mirrors, ω is the angular frequency and L is the length of the interferometer arms.

1.7.2 Seismic and Gravity Gradient noise

The experimental environment for a gravitational wave detector must be highly controlled if the interferometer is to detect the motion of the arm end mirrors due to a passing gravitational wave. Motions of anthropological, geological, meteorological and oceanic origin form a background level of vibrations at a wide range of frequencies. As a certain proportion of the vibrations which couple into the experimental system are of human origin, regions with less intense human activity have a more favourable seismic noise profile, but even at remote locations there is an ambient seismic noise spectrum which would cause motions of the mass on a scale of $10^{-9}m\left(\frac{10Hz}{f^2}\right)\sqrt{Hz}$ above 10Hz and $10^{-9}m\sqrt{Hz}^{-1}$ below 10Hz [2]. Mirror motions of this size would cause significant difficulty for experimenters wishing to detect gravitational waves, so attenuation of external vibrations is necessary.

As the principle of detection requires that the mirrors be free to move, one obvious solution is that they be suspended as pendulums. A simple pendulum has the useful function of attenuating the transfer of external vibrations above its own natural frequency, which can be determined from the length of pendulum suspension. The transfer function of a single pendulum is similar to that of a 2-pole low pass filter with the poles at the natural frequency and is shown in a form which takes into account the resonances of the pendulum suspension [2]. By suspending one pendulum from another pendulum, greater vibrational attenuation can be achieved.

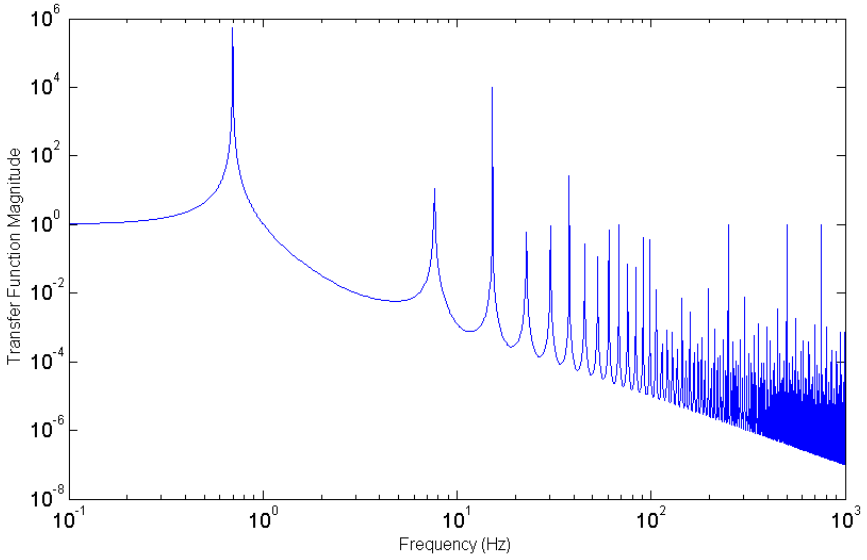

Figure 1.3: The response function for a single pendulum of length 33cm, showing the high frequency structure due to the resonances of the suspension wires [2].

There are also vibrational noise sources that cannot be reduced by use of attenuators. Because the detector is placed in Earth's gravitational field, which also contains a time-dependent matter distribution, the detector will experience fluc-

tuating gravitational fields that result in low frequency displacement noise in the mirror positions. This displacement has become known as gravity gradient noise, and provides the limit for groundbased gravitational wave detection at around 1Hz, where the gravity gradient noise becomes the dominant source of noise [20].

1.7.3 Thermal noise

This topic will be discussed in more detail in Chapter 2 and encompasses the effects of non-zero temperature upon the optical and mechanical elements of the interferometer. The level of thermal noise in an interferometer may be calculated from the thermomechanical properties of the optical and mechanical components of the interferometer, with the an important variable being the intrinsic mechanical loss angle, $\phi(\omega)$ of the component materials.

1.8 Current Interferometric Gravitational Wave Detectors

This section contains descriptions of the current generation of interferometric gravitational wave detectors. Six detectors based on variations upon the Michelson interferometer are currently in operation as the beginning of a global network. They all rely upon the principle of using long interferometer arms to increase the amount of length change observed for a given gravitational wave strain and use positional feedback control signals to obtain values for h. As yet, none of these detectors has identified a definite gravitational wave signal, but ongoing improvements in sensitivity increase the likelihood of detection.

A network of spatially separated multiple detectors is required because the transmission of gravitational waves through spacetime can be seen as analogous to the transmission of sound through air, and gravitational wave detectors can be seen as analogous to an ear or microphone. Unlike an optical telescope, ears and gravitational wave detectors have a very wide antenna pattern that is able to receive signals from the whole sky, although not with uniform strength. By correlating the signals detected by multiple detectors at different locations, it is possible to obtain higher sensitivity over a larger proportion of the sky and also provide information on the position of the sources in the sky. Also, because of the difficulty in ensuring that a given signal is caused by a gravitational wave, quasi-co-incident events in non-co-located detectors will be required to discount false positives.

The following sections describe the four large-scale interferometric gravitational wave detector projects currently in operation.

1.8.1 LIGO

LIGO consists of three interferometers, H1 and H2, with armlengths of 4km and 2km respectively, located in Hanford, Washington State and L1, a 4km arm length interferometer located at a facility in Livingston, Louisiana [21].

The standard LIGO optical layout consists of a Michelson type interferometer with additional Fabry-Perot cavities in the 4km arms. The Fabry-Perot cavities allows light to make multiple trips along the arms before returning to the beam splitter, which increases the interaction of light with incoming gravitational wave

signals, therefore increasing the change in phase that occurs for a given gravitational wave amplitude. The level of laser power in the system is increased, leading to a corresponding decrease in the level of shot noise.

The LIGO detectors also employ power recycling. This technique develops from the operation of gravitational wave detector interferometers operating on the dark fringe, as described in Section 1.6, above. If the detector is locked to the dark fringe, and the optical elements absorb very little power, then almost all the laser power that has been sent into the interferometer must be exiting the interferometer through the input port. Power recycling uses an extra controlled mirror at the input port to send the wasted light back into the interferometer coherently with the input light from the laser. In this case, the parts of the interferometer after the beam splitter are effectively acting as a single mirror with extra parameters, which forms a resonant cavity with the power recycling mirror [18].

The laser in each LIGO detector is a 10W Nd:YAG operating at 1064nm and undergoes frequency and amplitude stabilisation and is passed through an optical mode cleaner in order to ensure that only the lowest order spatial mode of the laser beam enters the interferometer [22]. The interferometer optics are suspended on steel wire slings which form pendulums with a frequency of 0.76Hz, which provides seismic isolation of the form $1/f^2$. The suspended optics are in turn suspended from 4-stage spring/mass stacks which provide $1/f^8$ attenuation of seismic noise above 1Hz [23].

Since LIGO began running in 2001, there have been five science data taking periods. The most recent data taking period, S5, began in November 2005 and

ended in October 2007 and collected data throughout. For a total of 365 days over the period of S5, science quality data at design sensitivity was taken from all three detectors simultaneously, otherwise known as 'triple co-incident' data. Each individual interferometer had a duty cycle of around 75% and the overall duty cycle for triple co-incident data was 53%. Using the data taken in S5, the signal due to the inspiralling of a $1.4M_{\odot}/1.4M_{\odot}$ neutron star binary up to 14Mpc away would be visible, enabling gravitational astronomy to reach to the Virgo cluster. The strain sensitivities of the three interferometers are shown in Figure 1.4 [22]. Initial LIGO expects to see neutron star binary coalescences to a radius of 33Mpc at a rate of one every fifty years, and one black hole binary coalescence every 140 years to a horizon distance of 161Mpc. Advanced LIGO expects to see neutron star binary coalescences to a radius of 445Mpc at a rate of 40 per year. In Advanced LIGO the expected detection rate of black hole binaries will increase to 20 per year to a horizon distance of 2.2Gpc [24].

1.8.2 Virgo

VIRGO is a French-Italian collaboration, based around a 3km arm interferometer outside Pisa, Italy [25]. The interferometer topology is similar to the LIGO detectors, employing Fabry-Perot cavities in the arms of the detector to increase the resultant phase shift due to the interaction of a gravitational wave and a power recycling cavity as described above. The laser system comprises of a 20W Nd:YVO_4 laser, injection seeded by a $1W$ Nd:YAG master laser operating at 1064nm [26].

Isolation from seismic disturbances is achieved by an innovative seven stage pendulum suspension, the superattenuator, which is designed to suppress seismic

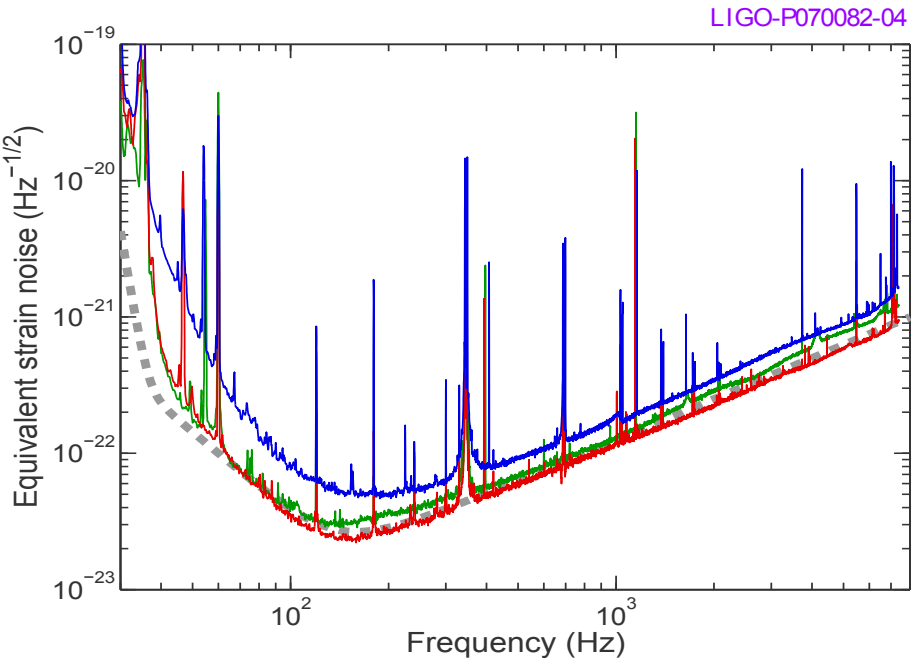

Figure 1.4: The strain sensitivities of the three LIGO detectors (red line: H1, blue line: H2, green line:L1) and in grey, the design sensitivity [22].

disturbances by ten orders of magnitude for frequencies above 4Hz and allows the Virgo detector to surpass the LIGO detectors in sensitivity at the lowest part of the frequency range. The superattenuator consists of a cascade of pendulum isolation stages, suspended from a tower which acts as an inverted pendulum, providing additional isolation. The final 'marionetta' suspension stage consists of four tungsten wires from which the test mass mirror is suspended [27][28]. The optical elements, as in the LIGO and GEO600 detectors, consist of fused silica substrates with silica/tantala multilayer reflective coatings. In its most recent science run, VSR1, the instrument achieved a duty cycle of 84.2% and a horizon distance for neutron star binaries of 4.5Mpc.

1.8.3 GEO600

The GEO600 gravitational wave detector is located in Ruthe, near Hannover in Germany. The detector consists of a 600m singly folded arm Michelson interferometer, with signal and power recycling, as shown in Figure 1.6. It has been operational since 2002 and has participated in four of the five science data gathering runs as part of the LIGO Scientific Collaboration, averaging a strain sensitivity of $3 \times 10^{-22}\sqrt{Hz}$ in the most recent, S5 [29].

Unlike LIGO and Virgo, the arms of GEO600 do not contain Fabry-Perot cavities. However, GEO600 is the first detector to make use of the dual recycling technique, which builds upon the power recycling technique described and also uses signal recycling.

The signal recycling technique aims to increase the power of the output light 'signal' at the output port of the detector. As the interferometer is operated at the dark fringe in order to maximise the signal-to-noise ratio, the signal due to an incoming gravitational wave is rather small. In order to best utilise this light, a partially transmissive mirror is placed in front of the output port to produce another cavity that is controlled to resonance in order to produce constructive interference and improve the size of a gravitational wave signal by a factor related to the finesse of the new resonant cavity [30].

The optical elements are suspended from triple stage pendulums to provide seismic attenuation. The final stage is a quasi-monolithic suspension consisting of fused silica fibres welded onto fused silica ears which are bonded using the

hydroxy-catalysis technique onto the barrel of the test mass [31].

As will be explained in more detail in Chapter 2, the level of thermal noise in a system can be calculated from the mechanical loss of the constituent materials. Fused silica has a lower level of mechanical loss than the steel or tungsten wire used in the other detectors and can be formed into strong and reliable fibres by heating and pulling high quality silica rods [31]. The fused silica fibres are attached to the fused silica optic by the hydroxy-catalysis bonding process rather than by welding as the bond produces a quasi-monolithic end result. This mitigates some of the stress in the join that other bonding methods may cause and also eliminates the dissipation of energy which results from friction between a wire suspension loop and the mass.

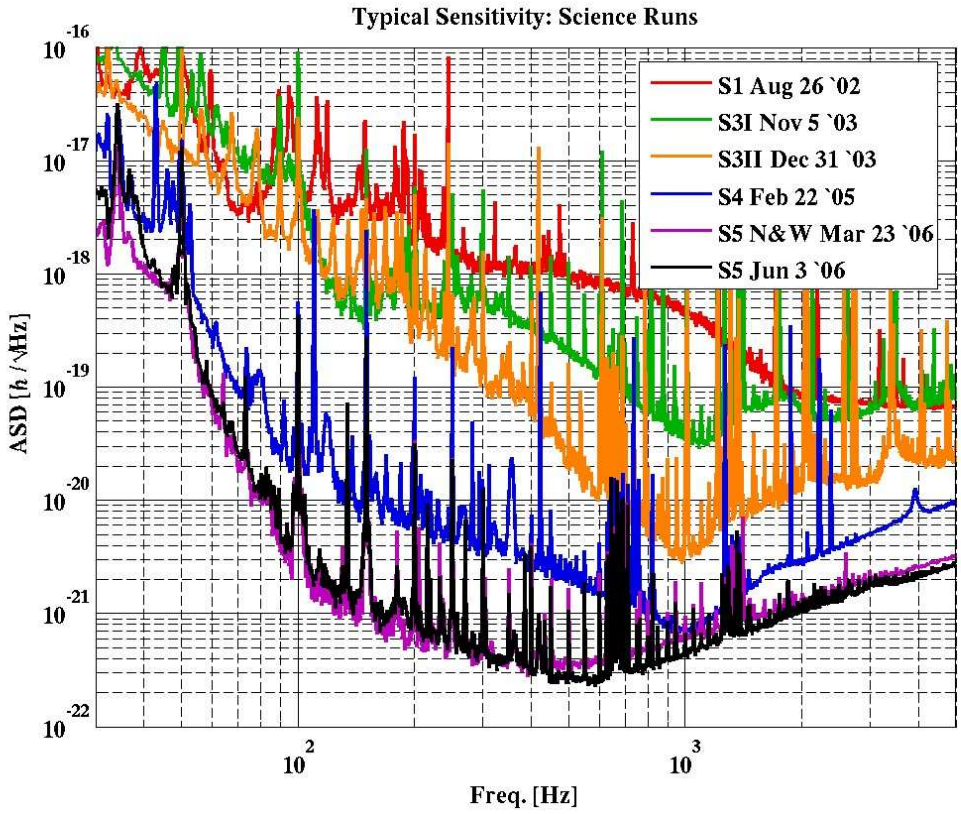

Figure 1.5: A series of noise curves for GEO600 from the beginning of operation to Summer 2008.

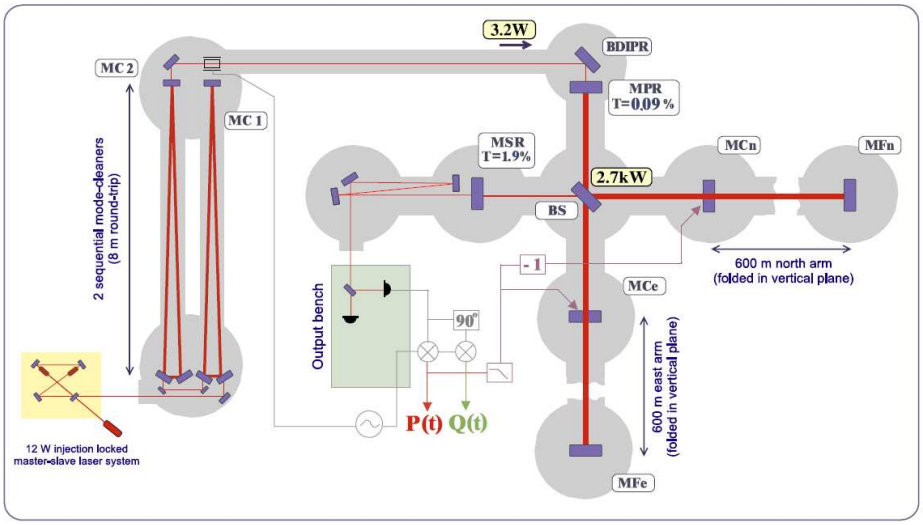

Figure 1.6: Optical layout of the GEO600 detector. H. Grote for the Ligo Scientific Collaboration [29].

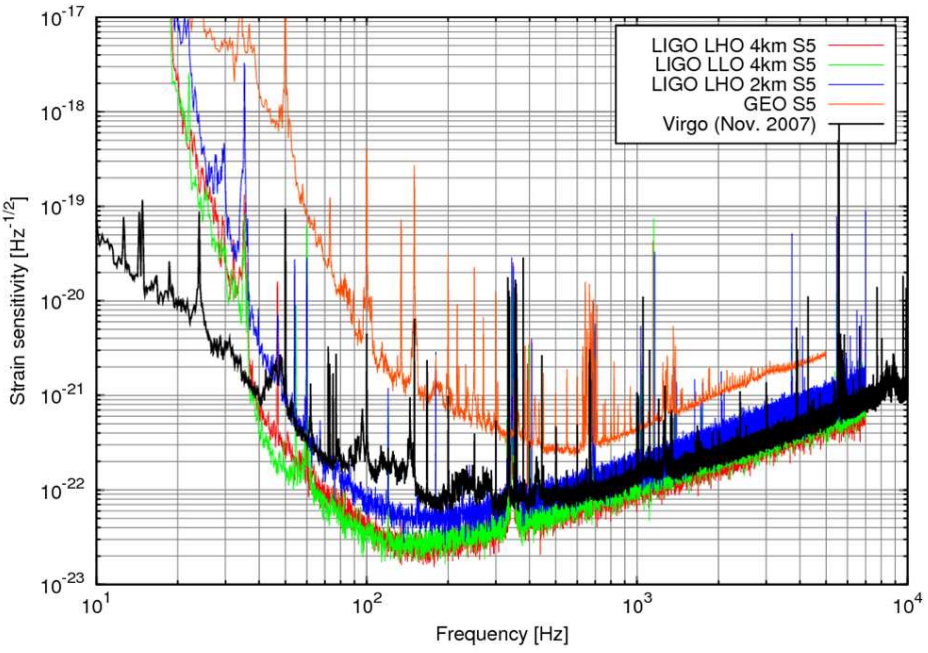

Figure 1.7: Summary of the comparative sensitivities of the large scale detectors in operation.

1.8.4 TAMA

The TAMA 300 interferometer project has been active since 1999 and has been taking science data intermittently since 2004. The interferometer is a power-recycled Fabry-Perot Michelson interferometer with a 300m arm length which has recently been upgraded to utilise a similar superattenuating suspension technology to that used in the Virgo detector [32]. The detector optics are composed of superpolished fused silica, with a diameter of 100mm and a thickness of 60mm and the high reflection coatings are composed of a multilayer stack of ion beam sputtered tantala and silica. The main laser is a pre-stabilised 10W Nd:YAG and the most recent science data run could observe neutron star binaries to a horizon of 73kpc.

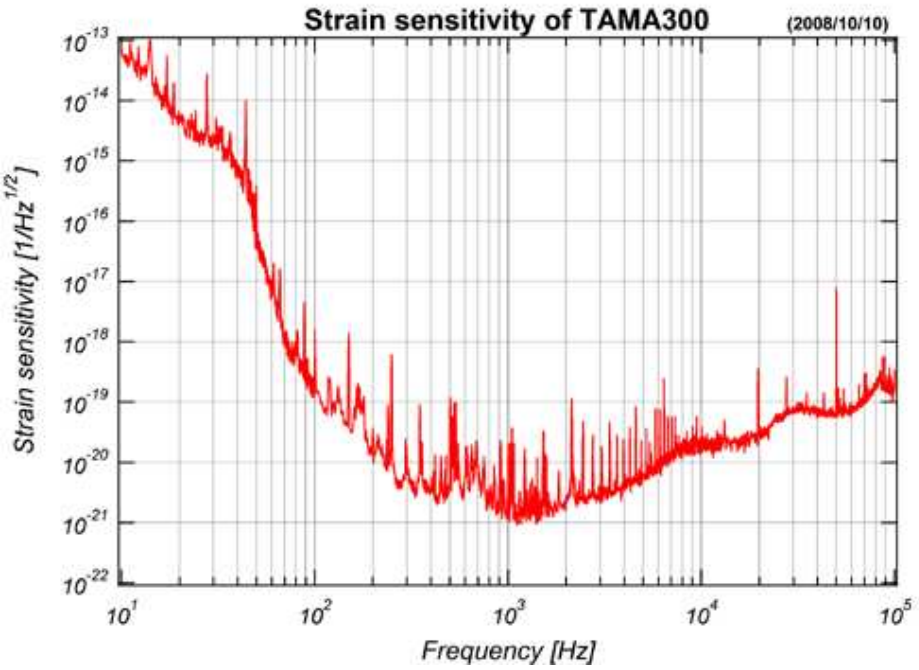

Figure 1.8: The strain sensitivity of the TAMA300 detector as of October 10th, 2008.

1.9 Future Gravitational Wave Detectors

1.9.1 Enhanced and Advanced LIGO

At the time of writing, the initial improvements to the LIGO detectors to form Enhanced LIGO are currently underway and aim to forms a bridge between the current technologies and those to be used in the future Advanced LIGO upgrade.

A major change to the optical system is that the 10W main laser is to be replaced with a 35W laser to obtain higher levels of optical power within the interferometer, which brings requirements for additional changes to the optical setup to allow for accurate operation with higher power levels. The sensing optics at the dark port of the interferometer are to be placed in vacuum, along with an output mode cleaner to remove 'waste' light outside the lowest energy spatial mode [33].

The tripling of the power entering into circulation in the interferometer brings with it the prospect of disadvantageous thermal lensing effects and so a thermal compensation system is to be installed on each of the key optics. The incident laser spot produces a warm area on the face of each test mass, which the thermal compensation system mitigates by using a ring heater to heat the outer edge and reduce the thermal gradient between the centre and edge of the test mass. The Enhanced LIGO additions to the detectors are expected to produce an increase in sensitivity by a factor of ~ 2, which translates into an eightfold increase in observable volume, extending the observation horizon for a $1.4M_{\odot}/1.4M_{\odot}$ neutron star binary from 15Mpc to 30Mpc [34].

Advanced LIGO represents the application of second generation detector technologies to the largest instruments in the global network to move gravitational wave astronomy from initial detections to full observations of multiple sources. The baseline design aims to decrease the noise floor by an order of magnitude and will hopefully produce multiple observations of gravitational waves per year. The extra sensitivity will allow observation of as many as 40 $1.4M_{\odot}/1.4M_{\odot}$ neutron star binary coalescences per year at distances of up to 200Mpc and 20 black hole binary coalescences per year to a horizon distance of 1Gpc [24].

Laser input power for Advanced LIGO will be increased to 180W, resulting in 800kW of laser power in the resonant cavities. The upgraded detector will increase the size of the test mass optics from the 25cm diameter, 11kg masses used in the initial detector to 34cm diameter, 40kg masses [35]. Heavier masses reduce the displacement caused by radiation pressure and the larger diameter will enable the optics to support the large increase in laser power.

The optics will be isolated from outside disturbances by a seven stage pendulum system, consisting of three active stages of horizontal and vertical attenuation and four passive stages of attenuation. The final attenuating stage will follow the technology developed in GEO600 and suspend the test mass with four silica fibres, which are welded to silica 'ears' that are silicate bonded to the barrel of the test mass.

The fruits of decades of research and development in optical coatings is also expected to be evident in Advanced LIGO and enable the sensitivity of the detector to reach levels limited by quantum noise sources (as described in Section 1.7.1) in

the middle of its detection band. The experimental work reported in this thesis is part of this research and development effort.

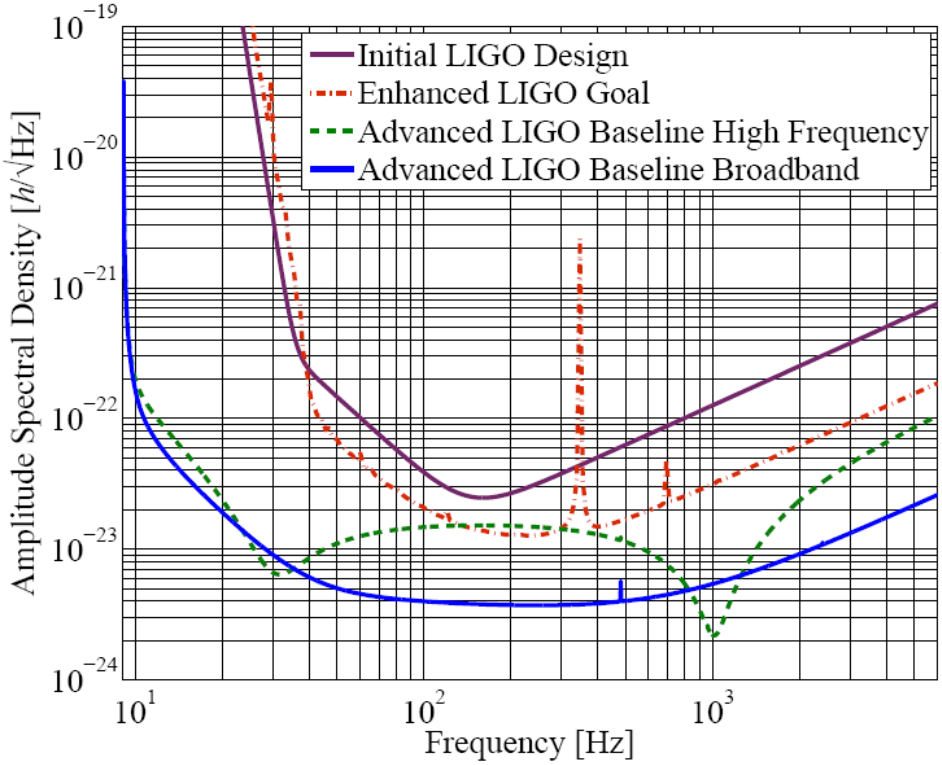

Figure 1.9: The strain sensitivity curves showing the design sensitivities of the current LIGO detectors alongside the design sensitivity for Enhanced LIGO and Advanced LIGO in both broadband and high frequency operational modes.

1.9.2 Virgo+ and Advanced Virgo

The Virgo+ upgrade project is an analogue to Enhanced LIGO, consisting of upgrades to first generation technologies in preparation for second generation interferometry. The main upgrades are to the laser system and suspension, where the wire sling final stage is to be replaced with a quasi-monolithic all-silica sus-

pension and the original 20W laser is to be increased to 50W by the addition of an amplifier and replacement of the original laser with a fibre laser. The higher laser power will induce thermal lensing effects on the detector optics, so a thermal compensation system is to be installed. Some detector optics are also to be replaced [36].

The Advanced Virgo technology upgrade will provide more than a factor of ten increase in detection horizon distance for BH-NS and BH-BH binaries.

The interferometer configuration is to be upgraded to a dual-recycled Fabry-Perot Michelson, similar to the Advanced LIGO configuration, with a tunable signal recycling cavity to secure extra sensitivity in the 10kHz range and the input laser power is to be increased to around 200W. The end test mass mirrors will be doubled in mass in order to support the increase in laser power and a wider beam diameter. The new mirrors are likely to be suspended using a quasi-monolithic silicate bonded final stage as in GEO600 and Advanced LIGO. An improved thermal compensation system will also be installed to minimise thermo-optic disturbances [36] and as in the LIGO detector upgrades. Improved dielectric coatings are expected to deliver reduced thermal noise.

1.9.3 The Large Cryogenic Gravitational Telescope (LCGT)

The team who built the Japanese TAMA300 detector intend to construct a gravitational wave detector that is capable of detecting at least one neutron star coalescence per year of operation. This detector is to consist of a 3km arm-length

power recycled Fabry-Perot Michelson interferometer operated at 20K, using single crystal sapphire mirrors with a diameter of 25cm and a mass of 30kg [37]. It is to be located in the seismically quiet Kamioka mine facility, where the CLIO interferometer is currently being used in research to establish the technologies required to support the LCGT [38].

1.9.4 GEOHF

The enhancements to the GEO600 detector, which already uses some advanced techniques to attain sensitivities on the same order as those in much longer baseline interferometers, are limited at low frequencies by the shorter arm length. Therefore, future improvements are aimed at increasing the sensitivity of the detector at high frequencies and to allow for narrowband observations at enhanced sensitivities [39].

The two limiting noise sources at high frequencies are coating thermal noise and photon shot noise. It is anticipated that advances in coating research, some of which are within the scope of the work described here, will provide a level of reduction in coating thermal noise. Two techniques that are anticipated to provide significant noise reductions are doping the coating material, and varying the thickness of the component layers in coatings. Further discussion of thermal noise in coating materials and how it may be reduced can be found in later chapters.

The shot noise in GEOHF is to be reduced by increasing the power in the interferometer to the highest sustainable by the optics (approximately 200W) and to introduce so-called 'squeezed light' into the interferometer. This technique uses

deliberately induced correlations in the vacuum fluctuations at the ports of the interferometer and therefore reduce the shot noise at the expense of increased radiation pressure fluctuations [40].

1.9.5 The Einstein Telescope

The Einstein Telescope is the first third generation gravitational wave detector to be planned, and aims for an order of magnitude increase in sensitivity over the second generation detectors. A two-year design study to gather together the knowledge at the forefront of gravitational wave detector technologies and develop a baseline design and noise budget began in 2008 [41].

It is currently planned that the detector will consist of two or three coincident interferometers in an underground, seismically quiet location. Current plans are for the interferometers to consist of very low temperature silicon optics with exotic coatings and use extremely high powered lasers.

It is also likely that the instrument will utilize measurement techniques that will allow the Einstein Telescope to surpass the quantum noise limit set by radiation pressure and photon shot noise described in Section 1.7.1 [40].

1.9.6 LISA

Many interesting gravitational wave sources are predicted to have frequencies below the 1Hz gravity gradient 'wall' that limits all earthbound measurements. A project to build a spacebound instrument to detect gravitational waves between 100μHz and 1 Hz is currently in development [42]. LISA will consist of three iden-

tical spacecraft travelling in triangular formation around the Sun in the quiet zone, 20° behind the Earth. LISA will have an arm length of 5 million km, a peak design sensitivity of around $10^{-20}m\sqrt{Hz}$ and is predicted to make detections from the first minutes of operation. This project presents interesting technical challenges such as low-intensity, high-loss interferometry, precision metrology and actuation to maintain the 'free-falling' proof masses, the locking of an interferometer with a 33.3s round-trip time for light and the application of all these techniques in the hostile environment of space [43].

Chapter 2

Thermal Noise

2.1 The Origins of Thermal Noise

Thermal noise in an interferometric gravitational wave detector is the result of the thermal motions of the atoms within the optical and suspension elements. The suspended optics form a system of classical oscillators where thermal excitation contributes mechanical energy equivalent to $\frac{1}{2}k_BT$ to each degree of freedom, according to the Equipartition Theorem. This energy is manifest as thermally induced rotation, translation and vibration of the overall system. While these motions will be on the molecular scale, in a gravitational wave detector this may be of the same magnitude as the arm length change induced by a passing gravitational wave. Therefore, thermally induced vibrations can become a critical source of noise in gravitational wave detectors.

Einstein's re-examination of the work of Robert Brown on the random motions of particles [44] provides a starting point for an understanding of the connection

between microscopic and macroscopic thermal processes relevant to thermal noise. Brown deduced from his observations of the random motions of pollen grains suspended in water that the bombardment of the grains by thermally excited water molecules caused fluctuating random forces to be applied to the pollen grains. Einstein further observed that the kinetic energy of initially excited pollen grains decreased over time, and hypothesized that the observed energy dissipation was due to the viscosity of the water. This provides a connection between fluctuations and a form of dissipation.

This idea was further explored by Callen, Welton and Greene and formulated as the Fluctuation-Dissipation theorem as described in the papers [45][46][47]. This states that for any linear system in equilibrium which is capable of undergoing a dissipative process, there will be fluctuations in a measurable parameter. For the case of Brownian thermal noise, the driving force is provided by random thermal excitations of molecular degrees of freedom, which result in fluctuations of the velocities of the molecules.

This section aims to introduce the calculations which predict the magnitude at a given frequency of the motion of a gravitational wave detector optic that is due to thermal excitations of the test mass. If the power spectral density of the fluctuating force due to $\frac{1}{2}k_BT$ thermal effects is $S_F(f)$, and the mechanical impedance of the optic is given by $Z(f)$, then according to the Fluctuation-Dissipation theorem, the relationship between these two quantities is given by,

$$\langle S_F(f)\rangle^2 = 4k_BT\Re[Z(f)], \tag{2.1}$$

where $\Re[Z(f)]$ is the real, or dissipative, part of the mechanical impedance [46]. In order to assess the level of noise by finding the power spectral density of the displacement of the optic, we make use of the relation $v = {}^{F}/_{Z}$, which states that a force is the product of a characteristic impedance and velocity, and the relation between the mechanical impedance and the mechanical admittance, $Y(f) = Z^{-1}(f)$. Substituting these relations into Equation 2.1 produces the relationship, [48]

$$\langle x(f) \rangle^2 = \frac{4k_B T}{f^2} \Re[Y(f)]. \tag{2.2}$$

This formula describes the magnitude of the displacement of the optic in terms of the admittance of the system, which can be used to calculate the level of positional noise in the detector optics.

2.2 Anelasticity, Internal Friction and Mechanical Loss

The dissipation mechanisms present in the suspended optics in a gravitational wave detector can be divided into two groups - those sources of dissipation external to the test mass, and those caused by internal phenomena relating to the test mass itself. The main external sources of dissipation in gravitational wave detector optics are viscous damping due to residual gas particles, friction, hysteresis and electrostatic test mass damping due to excess charge buildup.

The internal dissipation mechanisms which are related to intrinsic properties of the test mass are less easily mitigated than the external dissipation mechanisms. An examination of internal dissipation mechanisms as they relate to thermal noise in materials requires that the solid be modelled as an arrangement of oscillators.

When considering a perfectly elastic ideal linear oscillator, the relationship between an applied stress, σ, and the resultant strain, ϵ, is $\sigma = E\epsilon$, where E is the Young's Modulus of the material. For this situation, the appropriate form of Hooke's Law is $F = -kx$, and the strain occurs instantaneously upon the application of the stress.

In real materials, however the stress-strain response is not instantaneous, and the resultant strain lags behind the applied stress by a loss angle, ϕ. In this case, the stress and resultant strain can be represented as follows, [49]

$$\sigma = \sigma_0 e^{i\omega t}, \tag{2.3}$$

$$\epsilon = \epsilon_0 e^{i(\omega t - \phi)}. \tag{2.4}$$

This phase-lag between the action and response can be interpreted as the material moving through a series of intermediate structural, thermal or vibrational states until it reaches equilibrium, a process known as relaxation. The relaxation process dissipates energy into the oscillating system which may be interpreted as a complex and frequency dependent value for the elastic modulus E or spring constant, k.

Whichever physical process is involved in the anelastic relaxation, it can be char-

acterised by three parameters: E, the elastic modulus of the material in a fully relaxed state, $E + \delta E$, the elastic modulus of the material at the instant the external stress is applied and before relaxation has begun, and τ, the characteristic time taken for the relaxation process to complete.

These parameters can be used to calculate the frequency dependent loss angle, $\phi(\omega)$ using the formula, [49]

$$\phi(\omega) = \frac{\delta E}{E} \frac{\omega\tau}{(1 + \omega^2\tau^2)}, \tag{2.5}$$

with an equivalent hyperbolic form,

$$\phi(\omega) = \frac{\delta E}{2E} sech(\ln(\omega\tau)). \tag{2.6}$$

The curve $\phi(\omega)$ describes a function known as a Debye peak. The loss angle due to a particular process is greatest at the frequency which corresponds to the relaxation time, τ^{-1}, and has a value determined by the changes to the elastic modulus caused by the process under consideration, represented here as $\frac{\delta E}{E}$.

Some of the processes which lead to anelastic dissipation are thermally activated. If the relaxation process which is responsible for the dissipation of energy is thermally activated, the process has an activation energy H_b and a characteristic rate parameter, τ_0^{-1}. The characteristic rate, τ^{-1}, of a thermally activated process as a function of temperature, T, is given by the Arrhenius formula, [50][49]

$$\tau^{-1} = \tau_0^{-1} e^{-\frac{H_b}{k_B T}}. \tag{2.7}$$

The relaxation time of the process will be extremely large if the energy provided by the temperature of the system, $k_B T$, is much less than the barrier height energy, and the relaxation time becomes very small when $k_B T > H_b$ and the thermal energy of the system is enough to overcome the potential barrier. This formula for the relaxation time allows the effect of temperature on the dissipative system to be taken into consideration. Multiplying Equation 2.7 by ω and taking the natural logarithm of both sides shows that a linear relationship exists between $\ln(\omega\tau)$ and T^{-1}.

$$\ln(\omega\tau) = \ln(\omega\tau_0) + \frac{H_b}{k_B T} \tag{2.8}$$

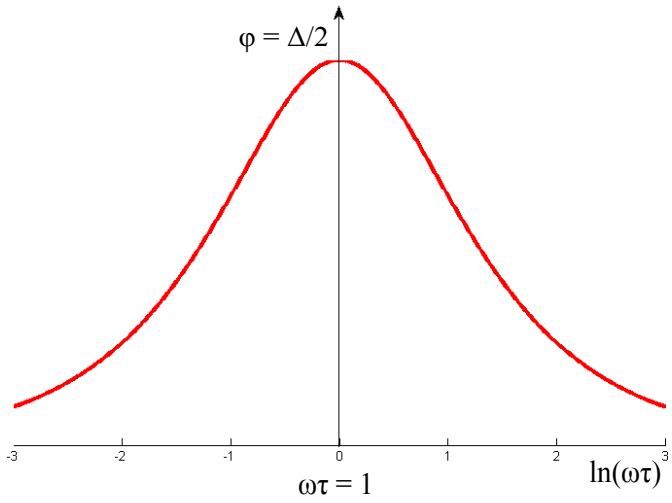

Figure 2.1: Illustration showing a Debye peak of mechanical loss as a function of $\ln(\omega\tau)$, as given in Equations 2.5 and 2.6.

This can be substituted into Equation 2.6 to give,

$$\phi = \frac{\delta E}{2E} sech \left[\ln(\omega\tau_0) + \frac{H_b}{k_B T} \right] \tag{2.9}$$

Plotting the ϕ values calculated using Equation 2.9 as a function of reciprocal temperature produces a curve with the same Lorentzian shape as the $\phi(\omega)$ curve as shown in Figure 2.2. The peak of this curve occurs at $T^{-1} = -\frac{k_B}{H_B} ln(\omega\tau_0)$.

The linear relationship between $ln(\omega\tau)$ and T^{-1} can be used to determine the characteristic energy and relaxation times of a particular dissipative process. If the loss angle of a body is measured at several frequencies over an appropriate range of temperatures, then the loss measurements will exhibit Debye peaks at discernable temperatures. Plotting the inverse of each peak temperature against the natural logarithm of the frequency at which it was measured will produce a line of gradient k_B/H_b, allowing the height of the energy barrier that characterises the dissipation process to be found [51].

The model of a thermally activated dissipative process with a unique energy barrier height and relaxation time only represents situations occurring for perfectly crystalline materials. However, the amorphous forms of materials are used in current gravitational wave detector optics. It is postulated that the disordered structure of the amorphous materials will introduce a distribution of barrier heights, resulting in the broadening of the Debye peak.

The concepts of dissipation-related Debye peaks and the Arrhenius relationships concerning thermally activated dissipation mechanisms are used in Chapter 4, in the analysis of the mechanical loss of optical coating materials.

2.2.1 Calculating Thermal Noise Due To Brownian Motion

In the case of real anelastic materials such as the fused silica used in gravitational wave detector optics, the power spectral density of the displacement of the optic due to Brownian thermal noise may be calculated by modelling each resonant mode of the system as a harmonic oscillator using the anelastic form of Hooke's Law incorporating the complex spring constant [49][2],

$$F(\omega) = -kx(1 + i\phi(\omega)). \tag{2.10}$$

Here, $F(\omega)$ is the applied force, x is the displacement and the imaginary term $\phi(\omega)$ is the phase angle by which x lags $F(\omega)$. Using the conventional symbols, we use Equation 2.10 to describe a damped harmonic oscillator where the force on the oscillator is given as follows,

$$F(\omega) = i\omega m\frac{\delta x}{\delta t} + \frac{k}{i\omega}\frac{\delta x}{\delta t}(1 + i\phi(\omega)) \tag{2.11}$$

By applying the Fluctuation-Dissipation theorem as described in the first section of this of this chapter, it can be shown that there is a relationship between the thermal noise spectral density due to each mode, $S_x(\omega)$, and $\phi(\omega)$ or the loss angle of the mode.

This relationship may be derived by first finding the impedance of the oscillator system, $\boldsymbol{Z}$. By definition,

$$\boldsymbol{Z} = \frac{F}{\delta x / \delta t}. \tag{2.12}$$

Applying this to equation 2.11 gives,

$$\boldsymbol{Z} = \frac{F(\omega)}{\delta x / \delta t} = i\omega m + \frac{k}{i\omega}(1 + i\phi(\omega)) \tag{2.13}$$

which simplifies to:

$$\boldsymbol{Z} = \frac{-\omega^2 m + k + ik\phi(\omega)}{i\omega} \tag{2.14}$$

The admittance of the system, $\boldsymbol{Y}$, is the reciprocal of the impedance, $\boldsymbol{Y} = \boldsymbol{Z}^{-1}$. Rationalising and inverting Equation 2.14 gives,

$$\boldsymbol{Y} = \frac{i\omega k - i\omega^3 m + \omega k\phi(\omega)}{(k - \omega^2 m)^2 + (k^2\phi^2(\omega))} \tag{2.15}$$

The final step is to substitute the real part of equation 2.15 into equation 2.2, giving the power spectral density of the displacement,

$$S_x(\omega) = \frac{4k_B T}{\omega^2} \frac{\omega k\phi(\omega)}{(k - \omega^2 m)^2 - (k^2\phi^2(\omega))}. \tag{2.16}$$

As $k = \omega_0^2 m$ and for materials used in gravitational wave detectors $\phi(\omega)$ is very small, Equation 2.16 can rewritten in terms of the mass and resonant mode frequency of the system,

$$S_x(\omega) = \frac{4k_B T}{\omega} \frac{\omega_0^2 \phi(\omega)}{m(\omega_0^4 \phi^2(\omega) + (\omega_0^2 - \omega^2)^2)}. \tag{2.17}$$

This equation can be used to calculate the thermal displacement of an anelastic oscillator at temperature, T, from its mass, m, resonant frequency, ω_0 and mechanical loss, $\phi(\omega_0)$. Further information and detail on this subject can be found in Chapter 7 of [2].

Equation 2.17 may be used in an approximate form for cases where $\omega \ll \omega_0$,

$$S_x(\omega_0) \approx \frac{4k_B T \phi(\omega_0)}{m\omega_0^2 \omega}. \tag{2.18}$$

2.2.2 Mechanical Loss and The Quality Factor

Alternatively, the dissipation present in a material can be described in terms of the quality factor of a resonance, Q. This is a common physical descriptor of a resonance, which allows a connection between the width of the resonance and its rate of energy loss to be made. In general, the quality factor of a resonance is given by,

$$Q(\omega_0) = \frac{\omega_0}{\Delta\omega} \tag{2.19}$$

where $\Delta\omega$ is the full-width half-maximum of the peak of the resonance in the frequency domain. Alternatively, the quality factor of a resonance may be defined as,

$$Q(\omega_0) = \frac{2\pi E_{stored}}{E_{diss}}, \tag{2.20}$$

where E_{stored} is the total energy stored in the resonating system and E_{diss} is the energy dissipated per cycle of the resonance.

Examining the definitions of the loss angle ϕ shows a connection with Q. The loss angle is the angle by which strain lags stress in an anelastic material and represents the proportion of total energy dissipated per oscillatory cycle,

$$\phi(\omega) = \frac{E_{diss}}{2\pi E_{stored}}. \tag{2.21}$$

By comparing Equation 2.20 and Equation 2.21 it can be seen that at a resonant frequency $\omega = \omega_0$, the mechanical loss angle $\phi(\omega_0)$ is equivalent to Q^{-1}.

From the definition of Q, it can be seen that a material whose resonances have a high quality factor will dissipate most of the energy of a resonance at frequencies concentrated around ω_0. Therefore it is reasonable to assume that materials whose resonant modes have a high quality factor will have low levels of dissipation away from the resonant frequency and therefore contribute less thermal noise to the

assembly at frequencies far from resonance.

As the resonant frequencies of the mirror substrates in a gravitational wave detector are in the tens of kilohertz, far above the gravitational wave detection band, the concentration of dissipation at the resonances allows a lower noise floor in the detection band. The fibres or wires upon which the mirrors are suspended often have resonant modes in the range of a few 100Hz to several kHz, which lies towards the high end of the detection band. These resonant modes produce sharp peaks in the thermal noise spectrum.

2.3 Calculating Thermal Noise for a System with Multiple Resonances

To calculate the total Brownian thermal noise in a gravitational wave detector mirror using Equation 2.18 requires the summing of the off-resonance thermal noise for each of the resonant modes of the substrate. This formula was adapted to produce the thermal noise spectrum due to n modes of the mirror [52],

$$S_x(\omega) = \sum \frac{4k_B T \phi_n(\omega)}{\alpha_n m \omega_n^2 \omega}, \tag{2.22}$$

where α_n is a coefficient which corrects for the non-point size of the mass by describing energy coupling to the different resonant mode shapes and $\phi_n(\omega)$ is the loss of the resonant mode at ω_n [52].

Equation 2.22 is only valid when the stochastic thermal driving forces for each resonant mode are the same, which is equivalent to assuming a totally homogeneous distribution of mechanical loss throughout the system [53]. This method also has the disadvantage of the computational intensity of the calculation of the α_n coefficients for each element in the summation series.

Another method of calculating the total Brownian thermal noise which may be a more appropriate physical approximation was proposed by Levin [53] and considers the effect of spatially inhomogeneous and correlated losses. The method calculates the effect of an oscillating pressure that simulates the effect of the incident laser beam upon the front face of the test mass, represented by the force F_0. The Fluctuation-Dissipation theorem is then directly applied.

Levin uses the fact that the real part of the admittance, $\Re[Y(f)]$ is a description of the coupling between the energy dissipated in the test mass per cycle, W_{diss}, and the motion of the front face such that,

$$\Re[Y(f)] = \frac{2W_{diss}}{F_0^2}. \tag{2.23}$$

By substituting this into the form of the Fluctuation-Dissipation theorem in Equation 2.2 we find that

$$S_x(f) = \frac{2k_BT}{\pi^2 f^2}\frac{W_{diss}}{F_0^2}, \tag{2.24}$$

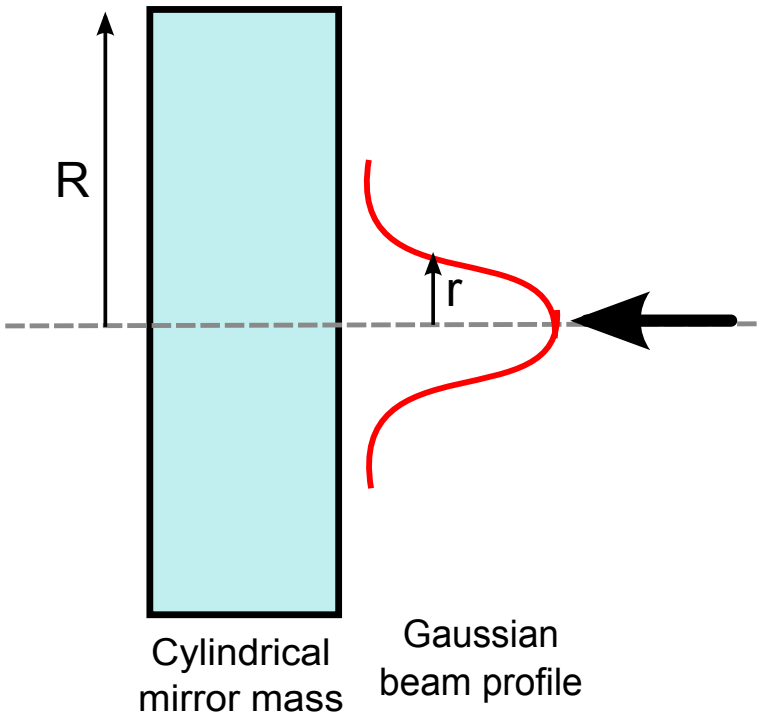

Figure 2.2: Illustration of the assumptions made when applying the F-D theorem directly to a mirror substrate

so the noise spectral density for an arbitrary system can be found if the power dissipated for an applied force can be calculated. For a homogenous distribution of dissipation throughout a cylinder, W_{diss} may be expressed as,

$$W_{diss} = 2\pi f U_{max} \phi(f), \tag{2.25}$$

where $\phi(f)$ is the loss angle for the appropriate frequency and U_{max} is the elastic energy stored at maximum compression or expansion due to the applied force F_0, which may be calculated using elasticity theory [53]. To simulate the contact

of a laser beam with the surface of the optic, the calculation is performed for a Gaussian beam profile whose centre is co-located with the centre of the test mass face. We therefore assume that the pressure applied to the test mass face is given by,

$$P(f) = F_0 f(r) = F_0 \frac{1}{\pi r_0^2} e^{-\frac{r^2}{r_0^2}}, \tag{2.26}$$

where r_0 is the distance from the beam centre at which the intensity is $1/e$ of the maximum. If the size of the test mass, $R \gg r_0$ then the size of the optic can be approximated as infinite when finding U_{max}. In [53] Levin shows analytically that the strain energy in a test mass deformed by a Gaussian beam under the aforementioned assumptions is given by,

$$U_{max} = \frac{F_0^2}{\pi^2 E_0 r_0}(1-\nu^2) I \left(1 + O\left(\frac{r_0}{R}\right)\right), \tag{2.27}$$

where I is a geometrical correction factor of 1.87322, ν and E_0 are Poisson's ratio and the Young's Modulus for the substrate material, and $O(\frac{r_0}{R})$ is a geometrical correction factor for the finite size of the optic. Substituting this expression for U_{max} into Equation 2.24 gives,

$$S_x(f)^2 = \frac{4k_B T}{f} \frac{(1-\nu^2)}{\pi^3 E_0 r_0} I\phi \left(1 + O\left(\frac{r_0}{R}\right)\right). \tag{2.28}$$

$S_x(f)$ gives the spectrum of fluctuations in the measurement variable - the x po-

sition of the surface of the optic - due to the Brownian motion of the molecules in the mirror when a gaussian-profiled force is applied to one face, assuming that dissipation is distributed homogeneously throughout the system [53][54].

The assumption that dissipation is distributed homogeneously throughout the system is unlikely to represent a real mirror well. It is already known that the high-reflectivity mirror coatings on the mirror faces ($\phi \sim 10^{-4}$ at room temperature [51][55][56]) are much lossier than the substrate ($\phi \sim 1 \times 10^{-8}$ at room temperature [57][58]), and that any welds or silicate bonds that link the mass to the suspension fibres represent regions with higher levels of dissipation.

The loss angle of the optic enters the Levin calculation in the description of the equivalent force impinging on the front face, shown in Equation 2.25. In [53], it is shown that a lossy area closer to the point at which the notional force is applied contributes a higher level of noise than an equivalent area further away. As optical coatings are by necessity applied on the surface of the optic and therefore placed extremely close to the exciting force, their contribution to the level of thermal noise will be greater than if the coating could be placed elsewhere. This unequal contribution of noise due to the loss present in the coatings along with their already relatively high loss motivates the research effort to identify and mitigate the dissipative processes in these coatings and therefore reduce the overall levels of resulting thermal noise.

Referring back to the Equipartition theorem, one obvious way of reducing the Brownian thermal noise in a gravitational wave detector is to reduce the tem-

perature of the system thus reducing the thermal energy available per degree of freedom. Initial steps towards the significant technical challenge of cryogenic precision interferometry are underway in the form of the CLIO project [59] which is a stepping stone towards a fully cryogenic gravitational wave detector, LCGT [38][37].

Though the decrease in temperature tends to lower thermal motion, Brownian thermal noise is also affected by any changes in mechanical loss as a function of temperature. Cryogenic measurements of the materials used in gravitational wave detector mirror substrates and coatings show that the mechanical loss may change significantly below room temperature. However, these measurements also show that there are peaks of high dissipation in the curve of mechanical loss as a function of temperature, which are connected to the characteristic energies of the anelastic dissipation processes which occur in the material as discussed in Section 2.2. This topic is one of the core theoretical elements behind the experimental work in this thesis, with special relevance to Chapters 4 and 5.

2.4 Brownian Noise From Optical Coatings

The direct application of the Fluctuation-Dissipation theorem shows that the positional distribution of mechanical loss throughout the mirror system has a significant effect upon the resultant magnitude of the thermal noise. Most importantly, lossy regions contribute more thermal noise when they are close to the surface upon which the pressure due to the impinging laser beam occurs.

When using the direct application of the Fluctuation-Dissipation theorem method to calculate the effect of a layer of lossy material upon the overall level of thermal noise, alteration must be made to the terms $U_{max}\phi(\omega)$ in Equation 2.25. These terms refer to the maximum energy stored in the elastic deformation of the mirror substrate and the mechanical loss of the substrate. For a coated substrate this becomes,

$$U_{max}\phi_{mirror} = U_S\phi_S + U_C\phi_C, \tag{2.29}$$

where the subscripts $_S$ and $_C$ refer to the properties of the substrate and coating respectively. As the thickness of the coating, l, is extremely thin in comparison with the substrate, U_C may be written as $\delta U l$, where δU is the elastic energy stored in an infinitesimal layer of the material. As the vast majority of the energy in the mirror system is contained within the substrate, $U_S = U_{max} = U$. By substituting these expressions into Equation 2.29 we find,

$$\phi_{mirror} = \phi_S + \frac{\delta U l}{U}\phi_C. \tag{2.30}$$

This assumes that the material used in the coating is isotropic and homogeneous. As the coatings for gravitational wave detector mirrors consist of layers of different materials, this assumption cannot be held. By separating the elastic response and mechanical loss of the coating into the components which are parallel to the surface of the substrate and those which are perpendicular, Equation 2.31 becomes, [60]

$$\phi_{mirror} = \phi_S + \frac{\delta U_\parallel l}{U}\phi_\parallel + \frac{\delta U_\perp l}{U}\phi_\perp. \tag{2.31}$$

The strain energy stored in the mirror system, U, may be approximated as,

$$U = \frac{(1-\nu^2)}{2\sqrt{\pi}Er_0} \tag{2.32}$$

where ν is the Poisson's ratio, E is the Young's Modulus and r_0 is the radius of the laser beam. The perpendicular and parallel components of the ratio of elastic strain energy stored in the coating are calculated in Appendix A of [60] and are,

$$\frac{\delta U_\perp}{U} = \frac{1}{\sqrt{\pi}\omega}\frac{E_C(1+\nu_S)(1-2\nu_S)^2 + E_S\nu_C(1+\nu_C)(1-2\nu_S)}{E_S(1+\nu_S)(1-\nu_C)(1-\nu_S)} \tag{2.33}$$

$$\frac{\delta U_\parallel}{U} = \frac{1}{\sqrt{\pi}\omega}\frac{E_S(1+\nu_C)(1-2\nu_C) - E_C\nu_C(1+\nu_S)(1-2\nu_S)}{E_C(1-\nu_C)(1+\nu_S)(1-\nu_S)} \tag{2.34}$$

Substituting these formulae into Equation 2.31 gives the mechanical loss of the whole mirror in terms of the Young's Moduli and Poisson's ratios of the substrate and coating and the component mechanical losses,

$$\phi_{mirror} = \phi_S + \frac{1}{\sqrt{\pi}}\frac{l}{\omega}\left[\frac{E_S(1+\nu_C)(1-2\nu_C) - E_C\nu_C(1+\nu_S)(1-2\nu_S)}{E_C(1-\nu_C)(1+\nu_S)(1-\nu_S)}\phi_{\parallel} + \ldots\right.$$

$$\left.\ldots\frac{E_C(1+\nu_S)(1-2\nu_S)^2 + E_S\nu_C(1+\nu_C)(1-2\nu_S)}{E_S(1+\nu_S)(1-\nu_C)(1-\nu_S)}\phi_{\perp}\right] \tag{2.35}$$

To obtain the power spectral density of the noise for a coated substrate, Equations 2.32 and 2.35 are substituted into Equation 2.24 to give [60],

$$S_x(f) = \frac{2k_BT}{\pi^{3/2}f}\frac{(1-\nu^2)}{\omega E}\left(\phi_S + \frac{l}{\sqrt{\pi}\omega}\frac{1}{E_SE_C(1-\nu_C^2)(1-\nu_S^2)}\ldots\right.$$

$$\ldots\left[E_C^2(1+\nu_S)^2(1-2\nu_S)^2\phi_{\parallel} + \ldots\right.$$

$$\ldots E_CE_S\nu_S(1+\nu_S)(1+\nu_C)(1-2\nu_S)(\phi_{\parallel}-\phi_{\perp}) + \ldots$$

$$\left.\left.\ldots E_S^2(1+\nu_C)^2(1-2\nu_C)\phi_{\perp}\right]\right) \tag{2.36}$$

This equation may be simplified to produce more useful forms in certain situations. For the current generation of gravitational wave detectors, which use a fused silica substrate and a coating consisting of Ta_2O_5 and SiO_2, the Poisson's ratios are all small (< 0.25) and approximately equal. In [60], it is assumed that the Poisson's

ratios of both the substrate and the coating are equal to zero then the power spectral density, accurate to around 30%, so the power spectral density of the coating thermal noise is given by,

$$S_x(f) = \frac{2k_BT}{\pi^{3/2}f}\frac{1}{\omega E_S}\left[\phi_S + \frac{l}{\sqrt{\pi}\omega}\left(\frac{E_S}{E_C}\phi_{\parallel} + \frac{E_C}{E_S}\phi_{\perp}\right)\right]. \tag{2.37}$$

As the methods of measuring mechanical loss in coatings are only sensitive to $\phi_{\parallel}$, it is assumed that $\phi_{\parallel} \approx \phi_{\perp}$. If this is true, then the lowest level of thermal noise for a coated substrate occurs when the Young's Moduli of the substrate and coating are roughly equal.

2.5 Thermoelastic Noise

Another form of dissipation related to thermal effects in the suspended optic is thermoelastic damping. This occurs when stress fluctuations caused by random thermal inhomogeneities occurring in the material are transformed by the thermal expansion of the material into additional motion of the front face of the test mass. The initial theoretical investigation of this phenomenon was by Zener, and considered the effect of a thermal gradient on a thin vibrating body [61][62].

If the motion of the vibrating body is modelled as a pure bending mode as shown in Figure 2.3, then regions where the material of the body is compressed will occur. As the strain experienced by a body is linked to the temperature by the ther-

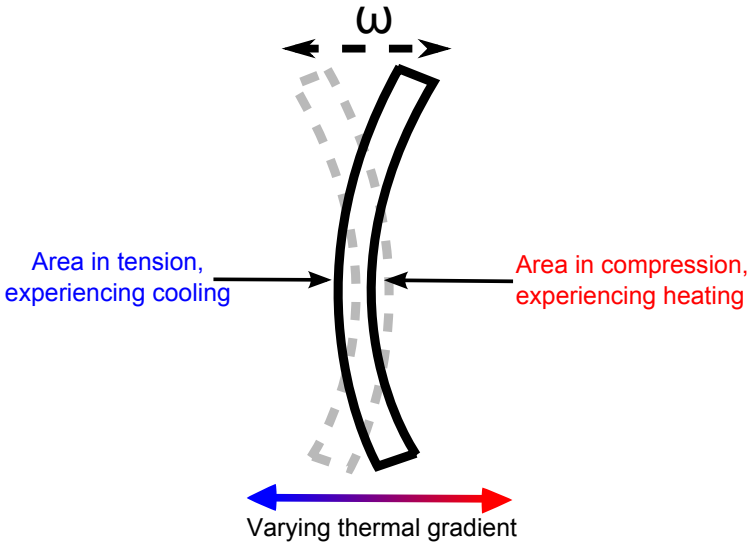

Figure 2.3: Illustration of the connection between the motion of a body and internal thermal gradients

mal expansion coefficent, the compressed area becomes warmer and conversely, the parts of the body experiencing expansion will become cooler. This sets up a thermal gradient across the thickness of the body which the body will attempt to equalise by dissipating heat into the bulk of the material. The characteristic time for the relaxation process to equalise the temperature gradient across a thin vibrating body is given by, [63]

$$\tau_{th} = \left(\frac{a}{\pi}\right)^2 \frac{C_V}{\kappa}, \tag{2.38}$$

where a is the thickness of the body and C_V and κ are the volumetric heat capacity and thermal conductivity of the material, respectively.

At the extremes of each cycle of vibration the thermal gradient changes direc-

tion, as the compressed region becomes the region in tension and vice versa, which introduces a frequency dependence for thermoelastic dissipation. If τ_{th}^{-1} is much smaller than the vibration frequency, then the relaxation process will never have enough time to be complete and the amount of energy dissipated will be small. If τ_{th}^{-1} is much larger than the vibration frequency, then the body does not undergo the process of developing and then relaxing a thermal gradient very often, and the system is effectively static, and so little energy is dissipated. The peak dissipation occurs when τ_{th}^{-1} has the same value as the vibration frequency, as each gradient reversal is perfectly timed to allow each relaxation process to complete before the next reversal occurs.

As the thermoelastic response is an anelastic relaxation process, it may be described in terms of the complex form of Hooke's Law described in Equation 2.10, leading to a formula for the loss of the form,

$$\phi(\omega)_{thermoelastic} = \Delta_E \frac{\omega\tau_{th}}{1 + (\omega\tau_{th})^2} \tag{2.39}$$

Where ω is the frequency of the vibrations of the body, τ is the relaxation time as defined above, and Δ_E is a coefficient which describes the strength of the relaxation process [63].

The peak thermoelastic dissipation occurs where $\omega\tau = 1$, with the value of the peak thermoelastic loss being given by the relaxation strength, $\Delta/2$. For the thermoelastic effect, the relaxation strength is the difference between the Young's

modulus of the material in its relaxed state and the Young's modulus in the thermally excited state before relaxation, which can be calculated from the known thermomechanical properties of the material [63][49]. Substituting the formula for Δ_E into Equation 2.39 gives,

$$\phi(\omega)_{thermoelastic} = \frac{E\alpha^2 T}{\rho C} \frac{\omega\tau_{th}}{1 + (\omega\tau_{th})^2} \tag{2.40}$$

The magnitude of thermoelastic dissipation as a function of temperature exhibits non-trivial behaviour. As well as the explicit temperature dependence built into the formulation, the thermoelastic parameters of the material also vary with temperature. For example, silicon experiences points where, α, the linear thermal expansion passes through zero. This leads to points free of thermoelastic dissipation at around 125K and 18K. A gravitational wave detector that used mainly silicon-based optics and operated at one of these points would be almost free of thermoelastic dissipation.

In Figures 2.4 and 2.5, the thermoelastic loss for a 100μm thick silicon wafer is shown as a function of frequency and temperature respectively. Figure 2.4 shows a steady increase in the frequency at which the loss peaks occur and the decrease in the overall magnitude of thermoelastic loss as the temperature is lowered. Figure 2.5 shows the frequency independent points at 125K and 18K at which the thermoelastic loss in silicon becomes negligibly small. This method of calculating the level of thermoelastic dissipation present in a body is used throughout Chapters 4, 5 and 6 to aid in the extraction of the mechanical loss of a coating from the

measured mechanical loss of a film/substrate system.

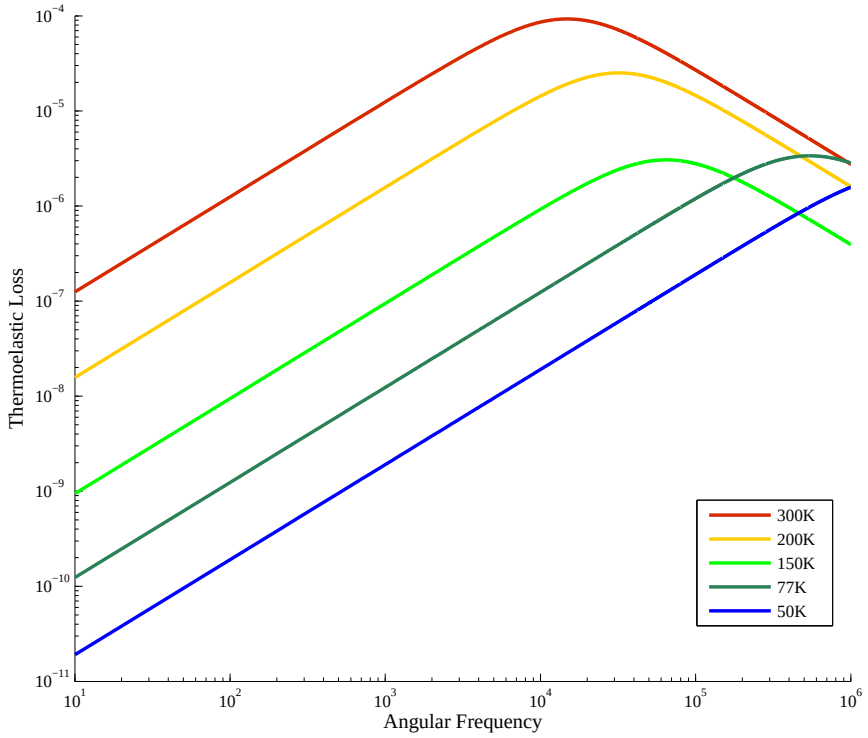

Figure 2.4: Thermoelastic loss for a 100μm thick silicon wafer as a function of frequency, shown for several temperatures.

2.5.1 Thermal noise due to thermoelastic dissipation for a substrate

The formulation discussed above specifically refers to thin flexures, where the characteristic time of the thermoelastic process, τ contains the variables which contribute to the time it takes a thermal change to dissipate across the body, but as the thermoelastic effect occurs universally across vibrating bodies, the implications of thermoelastic dissipation processes in the displacement of test mass

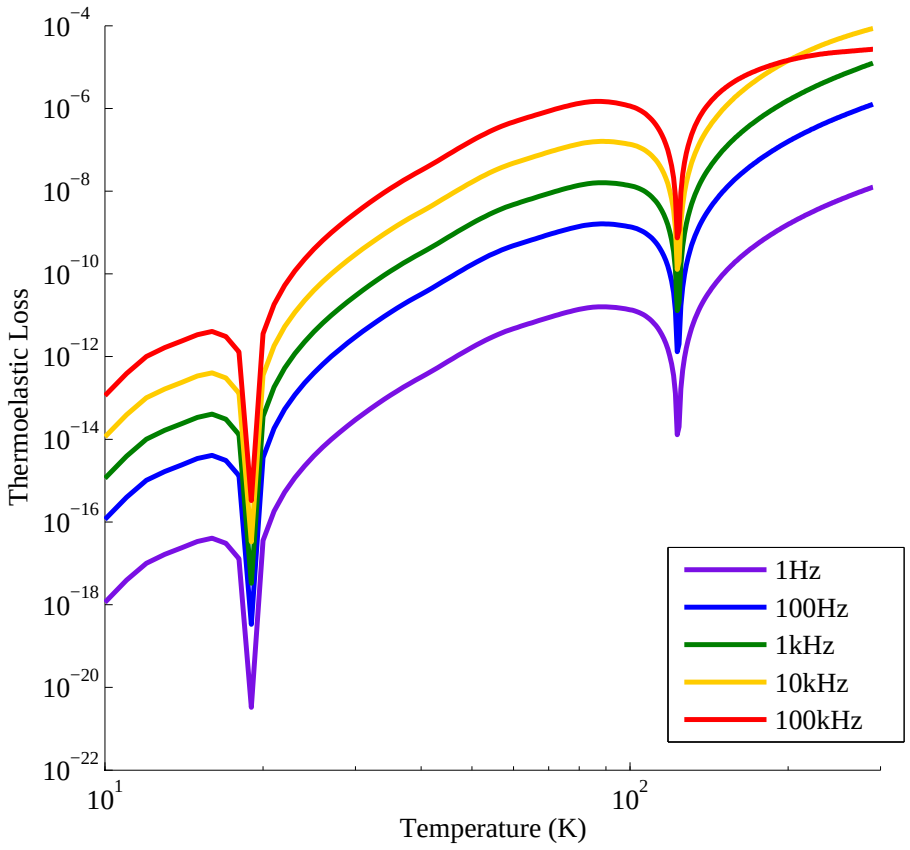

Figure 2.5: Thermoelastic loss for a 100μm thick silicon wafer as a function of temperature, shown for several frequencies.

substrates are also of interest.

In the calculation of the displacement noise due to thermoelastic dissipation the driving variable is the collective effect of the thermal fluctuations throughout the test mass substrate, which couple to displacements of the mirror surface through the coefficient of thermal expansion.The effect may be calculated either by considering of the effect of a field of random, normalised thermal fluctuations or by the direct application of the Fluctuation-Dissipation Theorem to the body, beginning

with the application of a periodic force representing the beam spot. If E, ν, and α are the Young's modulus, Poisson's ratio and coefficient of thermal expansion of a substrate material of density ρ, thermal conductivity κ and specific heat capacity C, and r_0 is the distance from the beam centre at which the intensity is $1/e$ of the maximum then the power spectral density of thermoelastic noise for a mirror which is half-infinite in relation to the width of the Gaussian probe beam will be given by [64][65],

$$S_x^{SubstrateTE} = \frac{8}{\sqrt{2\pi}} \frac{k_B T^2 \alpha^2 (1+\nu)^2 \kappa}{\rho^2 C^2 r_0^3 \omega^2} \tag{2.41}$$

Thermoelastic dissipation for a film/substrate system

For the case of a thin film applied to a substrate, the effect of thermoelastic noise requires the thermomechanical mismatch between the substrate and film to be taken into account. The thermoelastic noise in a substrate comes from random temperature gradients occurring within a homogeneous system, which cause strain gradients that lead to stored energy being dissipated. For a structure that contains materials with different thermomechanical properties, not only does the strain occurring from the body vibrating cause thermal fluctuations, but the thermal fluctuations cause differential expansion or contraction in the body which sets up additional strains, which feeds back into further thermal gradients and further thermoelastic dissipation.

Following the method in Fejer's 2004 paper [66], the mechanical loss due to the thermoelastic dissipation can be calculated, leading to a formula that describes the temperature and frequency variance of the loss for a body undergoing the pure

bending mode motion common in mechanical loss measurement experiments,

$$\phi_{thermoelastic} = \frac{2E_f\alpha_f^2 T}{C_f(1-\nu_f)}\left[1 - \frac{\alpha_s E_s(1-\nu_f)C_f}{\alpha_f E_f(1-\nu_s)C_s}\right]^2 g(\omega). \tag{2.42}$$

This formula assumes that the structure consists of a substrate that is much thicker than the film, and that the thermal diffusion length through the film is smaller than the major transverse dimensions of the structure in order that heat diffuses directly into the substrate. The symbols for Young's modulus, Poisson's ratio, the volumetric heat capacity and the thermal expansion coefficient are E, ν, C and α are as defined before with the subscripts f and s denoting the film and substrate respectively.

The frequency dependent term, $g(\omega)$ represents the reaction of the structure to a sinusoidally varying strain field and is calculated as follows,

$$g(\omega) = Im\left[-\frac{1}{\sqrt{i\omega\tau_f}}\frac{\sinh(\sqrt{i\omega\tau_f})}{\cosh(\sqrt{i\omega\tau_f}) + R\sinh(\sqrt{i\omega\tau_f})}\right]. \tag{2.43}$$

In this equation, τ_f is the thermal diffusion time across the film,

$$\tau_f = \frac{l^2 C_f}{\kappa_f}, \tag{2.44}$$

where l is the thickness of the film, C_f is the volumetric heat capacity of the film material and κ_f is the thermal conductivity of the material. The coefficient R, is the following combination of the constants:

$$R = \sqrt{\frac{\kappa_f C_f}{\kappa_s C_s}}. \tag{2.45}$$

This case is of special interest to the work carried out in chapters 4 and 5, where calculations using this formula are carried out for silica and tantala monolayers on silicon substrates.

To perform this calculation for a gravitational wave detector mirror, the calculation method requires alteration to account for the effect of the multilayer high reflectivity coating. The values $E_F, \nu_F, \alpha_F, C_F, \kappa_F$ and τ_F now represent the averaged value across the layers of silica and tantala. This results in the following changes to Equation 2.42:

$$\phi_{thermoelastic} = \frac{2C_F T}{\frac{E}{(1-\nu_f)}_{av}} \left[\frac{1}{C_F} \Big(\frac{E\alpha}{1-\nu} \Big)_{av} - \frac{1}{C_s} \Big(\frac{E_s \alpha_s}{1-\nu_s} \Big) \right]^2 g(\omega). \tag{2.46}$$

The formula for $g(\omega)$ remains as before, with the exception of the changes from the single film parameters to the averaged multilayer parameters.

For the multilayer coating on a gravitational wave detector mirror the appropriate equation to calculate the level of thermoelastic noise is,

$$S_x(f)^{CoatingTE} = \frac{8k_B T^2}{\pi^2 f} \frac{l}{r_0^2} \frac{\alpha_s^2 C_f}{C_s^2} (1+\nu_s)^2 \bar{\Delta}^2 g(\omega). \tag{2.47}$$

where all previously defined symbols retain their meanings, r_0 is the distance from the beam centre at which the light intensity has reached $1/e$ of its peak value and

Δ^2 is the following combination of material parameters,

$$\Delta^2 = \left\{ \frac{C_s}{2\alpha_s C_f} \left(\frac{\alpha}{1-\nu} \left[\frac{1+\nu}{1+\nu_s} + (1-2\nu_s)\frac{E}{E_s} \right] \right)_{av} - 1 \right\}^2 . \tag{2.48}$$

2.6 Suspension Pendulum Modes

As described in Chapter 1, the optical elements of an interferometric gravitational wave detector are suspended to form long period pendulums in order to attenuate unwanted external vibrations. As with the other elements of the optical suspension, the resonant modes of each pendulum are associated with unwanted thermally excited motion which may be calculated from the mechanical loss of the material used in the suspension fibres.

Part of the energy of the oscillation of a pendulum is stored in the gravitational field of the Earth, which can be regarded as having zero mechanical loss. Only the energy of the oscillation of the pendulum that is stored in the flexing of the suspension fibre is subject to dissipation due to the mechanical loss of the fibre material. The effective reduction of the mechanical loss is known as the 'dilution', and allows extremely low loss pendulums to be constructed from moderately lossy materials.

The mechanical loss of a pendulum is given by,

$$\phi_{pendulum} \approx \phi_{fibre} \frac{E_{flex}}{E_{grav}}. \tag{2.49}$$

The ratio of the energies stored in the flexure and the gravitational field is equivalent to the ratio of the spring constants. By replacing E_{flex} and E_{grav} with the appropriate formulae for the spring constants (E_{grav} = mg/L and $E_{flex} = n\sqrt{TEI}/2L^2$) the mechanical loss of the pendulum is given by,

$$\phi_{pendulum} \approx \phi_{fibre}\frac{n\sqrt{TEI}}{2mgL}, \tag{2.50}$$

where T is the tension in the wire, E is the Young's Modulus of the wire, I is the second moment of area of the cross-section of the wire, m and L are the mass and length of the suspension fibre and n is the number of wires of which the pendulum is composed [48].

The value for $\phi_{pendulum}$ can then be used as ϕ in Equation 2.17. This gives the displacement of the front face of the optic as a result of the thermal excitation of the pendulum modes of the suspension,

$$S_x(\omega) \approx \frac{4k_BT\phi_{fibre}}{m}\frac{\omega_0^2}{\omega^5}. \tag{2.51}$$

2.7 Thermal Noise Contributions

The contributions to the overall thermal noise can be described in terms of the part of the suspension they relate to - the optical substrate, the high reflection coating and the suspensions used to isolate the optics. The following section deals with the procedure for calculating the different thermally induced noise sources in

each part of the optical suspension chain of a gravitational wave detector.

The components of the optical suspension chain can be broken down into three categories: the substrate, the coating and the suspension fibre.

2.7.1 Substrates

In all currently operating long-baseline interferometric gravitational wave detectors, the substrate is a single piece of high grade fused silica, typically one of the Heraeus Suprasil brands [67]. The substrate is machined and polished to exacting optical standards with very low surface roughness and astigmatism, plus a tight tolerance on the radius of curvature and parallelism [68].

The thermal noise associated with the optical substrates and coatings is mainly due to the internal dissipation present. The major noise sources due to the substrate are the Brownian thermal noise and thermoelastic effects that stem from random thermal fluctuations in the optic. The calculation of Brownian thermal noise may be performed using equation 2.17 and performing the sum of the noise levels far from resonance or by the direct application of the fluctuation-dissipation theorem expressed as above by Equation 2.28. The phenomenon of thermoelastic noise is further discussed in section 2.4, where Equation 2.41 is used to calculate the equivalent noise level caused by thermoelastic noise in the substrate.

2.7.2 Coatings

To obtain the high reflectivity surfaces required to operate a gravitational wave detector, a coating is deposited upon the reflective surfaces of the substrate. These coatings are required to have reflectivities in excess of 99% and very low levels of optical absorption and scatter in order to maintain the high power stored in the arms of the interferometer. A coating formed from a stack of alternating layers of a high refractive index dielectric material and a low refractive index dielectric material can have a very high reflectance.

In one of these coatings, the optical thickness (given by $\delta = nt$ where n is the refractive index of the material and t is the physical thickness of the film) of each layer is equal to a quarter of the wavelength of the light used in the interferometer, which is 1064nm in the current generation of gravitational wave detectors. The reflectance of a multilayer dielectric coating where n_H and n_L are the refractive indices of the high and low index materials and m is the number of layers, is given by [69],

$$R = \left(\frac{1 - \left({}^{n_H}/_{n_L}\right)^{(m-1)} \left({}^{n_H^2}/_{n_s}\right)}{1 + \left({}^{n_H}/_{n_L}\right)^{(m-1)} \left({}^{n_H^2}/_{n_s}\right)} \right)^2 \tag{2.52}$$

The gravitational wave detectors currently in operation use tantalum pentoxide (Ta_2O_5 with $n = 2.03$ at 1064nm) as the high refractive index material and silica (SiO_2 with $n = 1.45$ at 1064nm) as the low refractive index material [70]. By applying Equation 2.52 for tantala and silica layers upon a silica substrate, the minimum number of tantala/silica layer pairs to obtain reflectivity greater than

99% is 15. The reflectivity can be increased by adding more layers or increasing the ratio between the refractive indices of the high and low index materials. Coatings for mirrors in gravitational wave detectors are deposited by ion-beam sputtering, which is a technique known to produce low absorption coatings [71].

These high reflection coatings are required to produce the 99.995% reflectivity required to operate the interferometer, but have been shown to be a major component of thermal noise, which is the dominant source of noise in a gravitational wave detector in the main detection band between 4Hz and 400Hz [55][56].

Research has shown that the main source of thermal noise in the multilayer coating is the high refractive index tantala layers [56]. The study of dissipation mechanisms in the ion beam sputtered amorphous materials used in coatings is part of the following work. Current research indicates that the oxygen atoms in amorphous metal oxides are able to flip between two states, and that the energy used in this process is thought to be a source of dissipation.

The effect of thermoelastic noise from a coating applied to a substrate is complicated by the thermomechanical mismatch between the substrate and coating, and requires a different calculation method. The method of calculating the level of this noise for a mirror in a gravitational wave detector is described in Equation 2.47.

2.7.3 Suspensions

The main contributions to thermal noise from the quasimonolithic silica suspension elements of a second generation gravitational wave detector are due to the modes of the silica fibres and in the bonds and welds that fuse the suspension elements to the optic. The thermal noise due to the pendulum modes can be calculated as shown in Section 2.6. Initial measurements of the mechanical loss of a silicate bond between two silicon surfaces are presented in Chapter 4 of this thesis, relating to the potential requirement for bonding composite test masses and quasi-monolithic silicon suspensions in a silicon-based third generation gravitational wave detector.

2.8 Summary

This chapter has defined the concept of thermal noise as it applies to gravitational wave detectors, and describes two methods of calculating the Brownian thermal noise from known parameters of a gravitational wave detector optic. The mechanical loss angle, $\phi(\omega)$ is an important parameter to reduce if the level of thermal noise for a gravitational wave detector is to be reduced. The relationship between peaks in mechanical loss as a function of temperature and the characteristic rate and energy of the two-level system thought to be responsible for dissipation in amorphous materials motivates measurements of $\phi(\omega)$ as a function of temperature. The method for calculating the noise spectrum resulting from a coated optic is also introduced, and motivates low $\phi(\omega)$ for the coating material. These theoretical factors indicate the usefulness of careful measurements of the mechanical loss of all materials used in the optics of gravitational wave detectors and specifically the high-reflectivity coatings.

Thermoelastic dissipation is also introduced, and a method of calculating an equivalent loss angle for thermoelastic dissipation is given in Equation 2.40. This method will be used to calculate the level of thermoelastic loss present in the samples measured in Chapters 4, 5 and 6.

Chapter 3

Motivation And Methods

3.1 Introduction - The Importance of Coatings

As stated in earlier chapters, the test mass mirrors of gravitational wave detectors use coatings of extremely high reflectivity to maintain the circulation of extremely high laser power in the instrument. Currently, the best method for constructing high reflectivity mirror coatings is to build up a stack of quarter-wavelength thickness layers of dielectric material that alternates between high and low indices of refraction, so that the reflections from each layer of the coating constructively interfere to reflect almost all incident light at a selected wavelength.

As described in Chapter 2, the thermal noise contribution of optical coatings may provide a critical limit to the sensitivity of future generations of gravitational wave detectors. In order to allow advanced and future gravitational wave detectors to reach their fullest potential it is necessary to seek a greater understanding of the processes which cause thermal noise and the variables that shape its effects. From

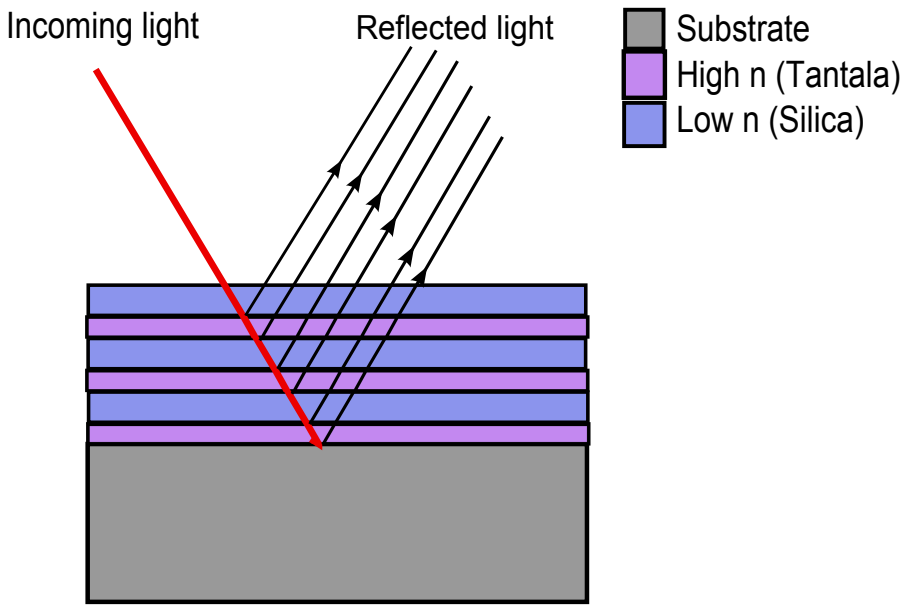

Figure 3.1: The arrangement of dielectric layers in a high reflection multilayer coating.

Equation 2.28 and the discussion of the calculation of thermal noise in Chapter 2, we know that the thermal noise contribution due to an optical coating can be reduced by reducing the temperature of the coating, reducing the mechanical loss of the coating and by altering the beam radius and profile. This work seeks to contribute to the reduction of thermal noise in coatings by investigating the reduction of the mechanical loss of the coating materials [72].

In order to reduce the mechanical loss of a coating material, it is first necessary to identify the relaxation process responsible for the dissipation of energy in the material. At present the material for which we have the best model of dissipation is fused silica. Fused silica is currently used in the mirror substrates and the monolithic suspension elements of gravitational wave detectors and is an amorphous

oxide, consisting of a network of silica molecules arranged so the material has no medium or long range order. Because of the random arrangement of molecules in this form of silica the angle of the bond between the silicon and oxygen atoms forms a wide distribution around a mean value, rather than the discrete value for the bond angle which occurs in crystalline materials.

Experiments examining the variation of mechanical loss with temperature in fused silica have repeatedly found that peaks of maximum dissipation are present in the curve of mechanical loss as a function of temperature [73][74][72][50]. In fused silica, the peaks occur between 40K-60K and are broad and frequency dependent. As discussed in Chapter 2, the temperature at which the peak dissipation occurs for a given frequency is linked to the energy required to activate the dissipation process, and the shape of the peak is thought to be a descriptor of the distribution of bond angles in the material. The width of the distribution of bond angles may be considered as an indirect measure of the short-medium range order.

Early versions of the model for the relaxation process linked to the Debye peak in silica were developed in work by Anderson and Bömmel [75], Strakna [76] and Vukcevich [77], based on the premise that the silica network has two states that occur with roughly equal probabilities and are separated by a potential barrier of height E_B. Further investigations lead to the model proposed by Gilroy and Philips in 1981 [78] which modifies the system of two metastable states by assigning the states different energies, ϵ_1 and ϵ_2. The two states and potential energies represent different configurations of the amorphous silica matrix, such as oxygen atoms performing switches between minimum energy positions in elongated ionic

bonds, the switching of bond angles between two stable values, or the shifting of the short range tetrahedral units of amorphous silica in relation to one another. At higher temperatures, there is enough thermal energy in the silica system to allow the silica to excite and relax between these states freely, but at very low temperatures, excitation and relaxation between the two states can only occur by tunnelling through the potential barrier. The tunnelling process occurs with a rate that varies with the height of the potential barrier and the temperature of the system, with the maximum tunnelling rate occurring when the temperature of the system provides exactly E_B to the relaxing element. The rate of the tunnelling process can be described by a form of the Arrhenius equation,

$$\tau^{-1} = \tau_0^{-1} e^{-\frac{E_B}{k_B T}}. \tag{3.1}$$

The characteristic time for the relaxation of an asymmetric double-well potential system can then be used to calculate the mechanical loss of a dissipation peak caused by this process, using the formula for the shape of Debye peaks discussed in Chapter 2, Section 2.2.

$$\phi(\omega) = \Delta \frac{\omega\tau}{1 + (\omega\tau)^2}. \tag{3.2}$$

If all amorphous materials - a group which includes the materials used as coatings in gravitational wave detector optics - are assumed to possess similar dissipation mechanisms to those postulated for fused silica, then the activation energy of the major dissipation process may be found by measuring the mechanical loss as a

function of temperature for a range of frequencies. Once factors affecting the activation energy and rate of the dissipation process are found, then a method for reducing the loss by changing the activation energy or altering the structure of the coating may be formulated.

Research of this kind is well underway - at Glasgow the mechanical loss of Ta_2O_5 as a function of temperature has been studied by Iain Martin and colleagues [51]. Mechanical loss measurements of a layer of Ta_2O_5 on a silicon substrate, annealed at 600^{o}C exhibited a well defined dissipation peak at around 20K. These measurements were compared with a Ta_2O_5 coating doped with $(14.5 \pm 1)\,\%$ Ta_2O_5, which had been found to exhibit a lower level of loss at room temperature than the undoped coating. A dissipation peak was also present in the doped Ta_2O_5 coating. By assuming that the dissipation process that caused these peaks had the characteristics of a Debye process, the Arrhenius equation can be used to convert the peak temperatures into average activation energies. This experiment indicated that the addition of TiO_2 doping to a Ta_2O_5 coating increases the average activation energy from 24.2 ± 1.7meV to 37.1 ± 3.0meV.

The work on doping in Ta_2O_5 showed that adding TiO_2 increases the average activation energy of a relaxation process in the material. Another process which may affect the activation energy of a relaxation process in the coating material is the annealing which occurs after the coating is deposited. The post-deposition anneal reduces the optical absorption of the coating, but could also make small changes to the amorphous structure which may affect the level of mechanical loss.

Iain Martin investigated the effect of post-deposition annealing on the mechanical loss of Ta_2O_5 coatings by performing mechanical loss measurements on silicon cantilever substrates coated with 500nm of Ta_2O_5 which were annealed at 300^{o}C, 600^{o}C and 800^{o}C. The coating annealed at 300^{o}C did not exhibit the sharp low temperature peak, but instead showed a shallow, broad peak centred around 30K and Arrhenius plot analysis of the frequency dependence of the temperature of peak loss showed this peak represented a process with an activation energy of (138 ± 4) meV and a rate constant of $(3.5 \pm 0.1) \times 10^{-27}$s. The coating annealed at 600^{o}C showed a sharp low temperature peak at around 30K which could possibly be superimposed upon a peak similar to the shallow, broad peak observed in the coating annealed at 300^{o}C. The activation energy calculated from an Arrhenius plot analysis of the sharp low temperature peak was (24.2 ± 1.7) meV and the rate factor was $(7.3 \pm 0.3) \times 10^{-11}$s. As amorphous tantala is known to begin to recrystallise at 650^{o}C the sample annealed at 800^{o}C was expected to exhibit a significant degree of polycrystallisation. The mechanical loss of the coating annealed at 800^{o}C showed two features - a large, sharp peak at around 30K which was partially obscured by a much larger, broader peak at around 90K. The peak at around 20K was thought to be related to the same process that caused the sharp low temperature peak in the coating annealed at 600^{o}C and the 90K peak was thought to be related to the polycrystalline nature of the heat-treated coating material.

Chapters Four and Five of this thesis describe a version of the experiment to assess the effects of post-deposition heat treatment applied to ion-beam sputtered amorphous films of silica and hafnia. Ion-beam sputtered amorphous silica is the low

refractive index material used in the multilayer high reflection coatings, and while the tantala layers are known to contribute the larger proportion of the thermal noise effects from the coating, the silica layers also contribute [79]. It is already known that at room temperature the ion-beam sputtered amorphous form of silica has a higher level of mechanical loss than fused silica (a few 10^{-4} at room temperature [51] compared with $\phi \sim 1 \times 10^{-8}$ [57][58]) and that the Debye peaks derived from measurements of coatings deposited by different methods can show significant differences [73][74]. This points towards the need to examine the specific form of the material as used in the coating, as interpolation from the loss characteristics of amorphous silica deposited by other methods may not be directly relevant.

The samples used in the mechanical loss measurement experiments in Chapters Four and Five were cantilevers etched from silicon wafers, as shown in Figure 3.2. The dimensions of the cantilevers were selected so that the frequencies of the

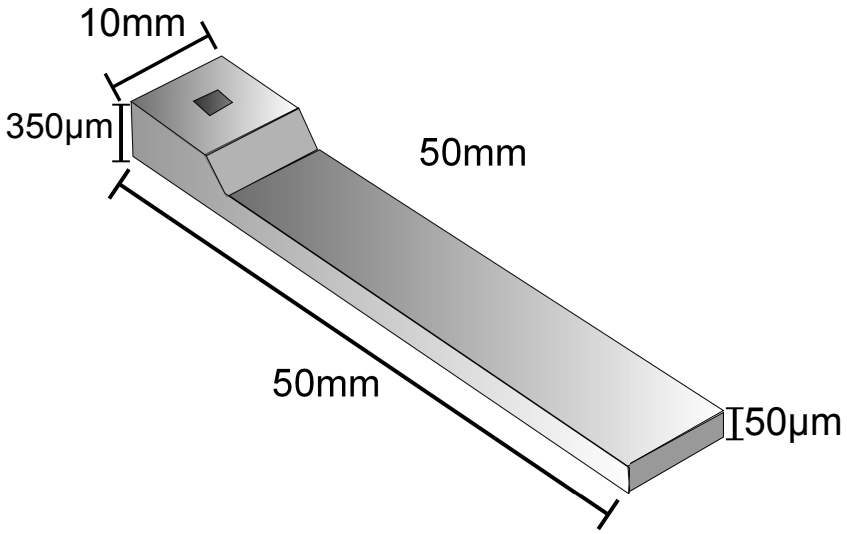

Figure 3.2: Schematic of the silicon cantilevers as used in the mechanical loss measurements in Chapter Four and Five.

bending modes lie within the observational frequency range of a gravitational wave detector. For the experiment on ion-beam sputtered amorphous silica, which is described in Chapter Five, the coatings were applied by the Materials Science and Engineering Division of CSIRO [80] and the samples were subsequently annealed at 300^{o}C, 600^{o}C and 800^{o}C to allow for direct comparison with the measurements of tantala coatings.

While the current formula for creating highly reflective multilayer coatings is highly refined, the study of alternative coating materials may provide pathways to reducing thermal noise in gravitational wave detectors. As research has shown that a large proportion of the coating loss is due to the high index component of the multilayers [56] - the ion beam sputtered tantalum pentoxide - any material that outperforms tantala in terms of thermal noise could, if the optical and thermo-mechanical properties were also favourable, take its place in the high reflective coating. Also, by investigating the dissipation processes that lead to thermal noise in different materials, it may be possible to develop a method of applying and treating a thin film coating to produce the lowest thermal noise possible.

The first alternative coating material to be investigated for future gravitational wave detectors is hafnia, otherwise known as hafnium dioxide. Like tantalum, hafnium is a transition metal which may form an amorphous oxide. While current studies suggest that the level of optical absorption in a typical ion beam sputtered thin film of hafnia is between 60 and 80 parts per million, which lies well above the acceptable band for use in gravitational wave detectors [81], observation of the signature of the dissipation process in this material may provide useful informa-

tion on the correct treatment and doping of other high refractive index coating materials with preferable optical characteristics.

In Chapter 5, the mechanical loss characteristics of hafnia films as a function of temperature are examined. The initial measurements were of an ion-beam sputtered film of hafnia applied to a silicon cantilever with dimensions as shown in Figure 3.2. The sample was annealed at 300^{o}C after the deposition of the coating. As amorphous hafnia coatings are known to recrystallise readily when annealed to around 400^{o}C, this sample may show the initial signs of a transition to polycrystallinity.

Due to the lower crystallisation temperature of hafnia films, applying the same annealing temperatures to the hafnia films as in the post-deposition heat treatment experiments on silica and tantala would have resulted in fully crystallised coatings. The hafnia coatings used in the post-deposition heat treatment tests were deposited on silicon substrates with dimensions as shown in Figure 5.11 by the Materials and Engineering division of CSIRO and annealed for 24 hours at 150^{o}C, 200^{o}C or 400^{o}C. Two final pairs were left unannealed, although the deposition temperature is roughly equivalent to undergoing an annealing process at around 100^{o}C.

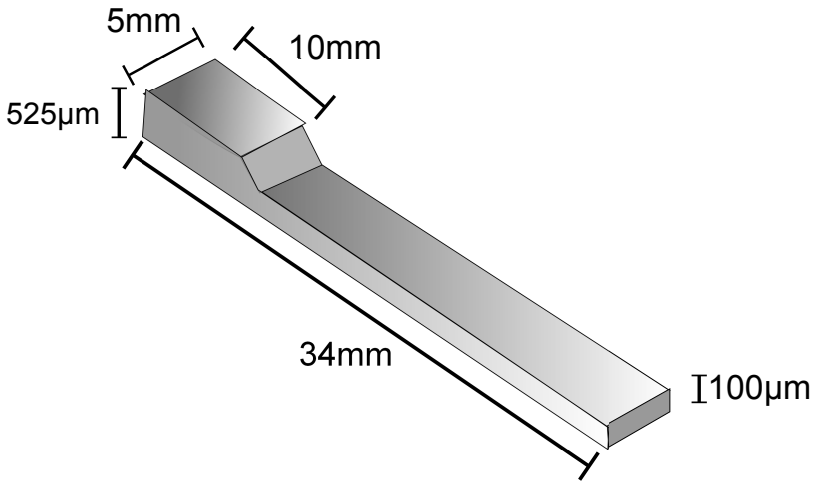

Figure 3.3: The dimensions of the silicon cantilevers manufactured by KNT and used in the measurements of as-deposited amorphous hafnia coatings in Chapter 5.

3.2 Hydroxy-Catalysis Bonding In Gravitational Wave Detectors

Hydroxy-catalysis bonding is a technique for creating strong, permanent adhesion between silica-based optical components. Other technologies for joining optical elements exist, such as optical epoxies and optical contacting, but hydroxy-catalysis bonding has particular advantages such as high shear strength, high visible and infra-red transmission and vacuum compatibility that have led to its application in gravitational wave detectors.

In GEO600, hydroxy-catalysis bonding is used to secure the fused silica suspension 'ear' to the barrel of the fused silica mirror substrate to form a quasi-monolithic

body, onto which silica suspension fibres may be welded. The all-silica final stage suspension technology is to be included in the advanced upgrades to the LIGO and VIRGO detectors, reducing the contribution of suspension thermal noise. The reduction in the level of thermal noise is partly due to the lower level of mechanical loss in fused silica fibres than the steel or tungsten wires used in the previous suspension method and partly due to the removal of an attachment point where one component is free to rub against the other. The silicate bond may however contribute to thermal noise in the optical suspension, and so to fully estimate the effect of more extensive uses of silicate bonding, the mechanical loss of an hydroxy-catalysis bond must be quantified.

The loss of a 33.2cm^2 bond between two similar cylinders of bulk fused silica was found to be $(2.8 \pm 0.4) \times 10^{-1}$ by Sneddon [82]. In this experiment, the bonded region was co-incident with the suspension loop, which may be a cause of excess loss when measuring the bonded sample. The experiment was later repeated using two fused silica cylinders of different lengths, moving the bond region away from the suspension loop. The measured bond loss varied between $(4.8 \pm 0.4) \times 10^{-3}$ and $(2.02 \pm 0.01) \times 10^{-1}$ depending on the frequency of the resonant mode used to make the measurements. Across all the resonant modes measured, the average mechanical loss of the bond at room temperature was 0.1 ± 0.001 [83].

There are two main reasons for extending the study of the mechanical loss of a hydroxy-catalysis bond to low temperatures. Firstly, mechanical loss as a function of temperature is known to provide information on the activation energy of the associated dissipation process, as described in Section 2.2. Identifying the

dissipation process from the characteristic energy may provide information which leads to a method for reducing the loss of the bond. Secondly, if hydroxy-catalysis bonding techniques are to be used in third generation gravitational wave detectors which are required to operate at cryogenic temperatures, the value of the bond loss at the potential operating temperature will be required for thermal noise calculations. Silicon has been suggested as a replacement for silica as the main optical material for a third generation cryogenic interferometer. As the bonding technique requires the presence of oxides, silicon components for hydroxy-catalysis bonding require an interface layer of oxide to be applied.

Chapter 6 of this thesis describes a measurement of the loss of a hydroxy-catalysis bond between two thin silicon cantilevers. At the time of writing, there were no published measurements of the mechanical loss of a hydroxy-catalysis bond between silicon, but if future gravitational wave detectors are to shift to silicon optics and deeper infra-red laser optics, then it is important that the mechanical loss of a representative bond layer is known. The mechanical properties of bonds between silicon components suggest that they are similar to the properties of bonds between silica components [84], but the mechanical loss of the bond material is not known.

Several advantages are obtained by changing the geometry of the bonded samples from large bulk substrates to silicon cantilevers. Firstly, the resonant frequencies of the silicon cantilevers lie within the 1Hz-10kHz range and so the measured losses will be directly applicable to the calculation of thermal noise within the measurement frequencies of a gravitational wave detector. The resonant modes of the large

bulk substrates are typically in the tens of kHz, so values from these experiments may not be directly applicable. Secondly, the cantilever samples are a great deal easier to use in cryogenic measurements - they contain very little thermal mass and so reach equilibrium quickly and as they may be mounted in a simple clamp, are less easily affected by external knocks and vibrations. A bulk sample on a thread suspension would experience sufficient disturbances during the process of cryogen fills to set it swinging and make measurements difficult. Thirdly, the mechanical loss of a bare silicon substrate decreases with temperature and does not contribute its own Debye peak which greatly simplifies the analysis of the measurements.

3.3 The Hydroxy-Catalysis Bonding Process

Hydroxy-catalysis bonding was developed by Dz-Hung Gwo as a method of creating precise, strong, cryogenically-compatible bonds between fused silica optical components in science instruments that flew as part of the Gravity Probe B mission [85]. The technique was adapted to produce the quasi-monolithic fused silica suspensions used in GEO600.

The bonding process requires that the two surfaces to be bonded consist of oxides, are free from all organic contaminants and are flat to $\lambda/10$. After a thorough multi-stage cleaning process in a clean room environment, a very small amount of a high pH solution of sodium or potassium hydroxide in deionized water is applied to the surface to be bonded. The solution flows over the whole of the uncontaminated, hydrophilic surface, and the OH^- groups present in the solution form attachments to the free bonds in the surface of the silica, a process known as hydration.

As the concentration of OH^- groups on the surface of the silica increases, the silica molecules attach to multiple hydroxide groups and leave the bulk silica, becoming solutes in the bonding solution. This process etches away the surface to be bonded, and continues until the concentration of OH^- groups in the bonding solution is lowered enough to reduce the pH of the solution below 11.

Below this pH level, the molecules with multiple hydroxide groups partially dehydrate to form a monomer in the solution. As the concentration of the monomers reaches 1-2%, the monomers form polymeric chains bridging between open bonds in two etched bonding surfaces, chemically linking them. As the remaining water escapes from the bond region, the bond becomes rigid, strong and transparent.

3.4 Apparatus and Method for Measurement of Mechanical Loss

The mechanical losses were measured in a tabletop cryostat as shown in figure 3.5. The cryostat consists of an experimental chamber, one side of which is a cold plate which is in thermal contact with a reservoir filled with liquid helium. The experimental chamber and helium reservoir is surrounded by a heat shield cooled to 77K by connection to a reservoir filled with liquid nitrogen. The experimental chamber and an outer jacket are evacuated to a level of $< 1.0 \times 10^{-6}$ millibar, allowing mechanical loss measurements to be carried out in an environment not

limited by gas damping. The outer vacuum jacket also acts to slow the boiloff rate of the liquid cryogens. The experimental chamber has two optical viewports for contactless laser readout and two electrical feedthroughs, one for low voltages with multiple pins for sensors and monitoring equipment and one for high voltages to power the electrostatic system within the experimental chamber.

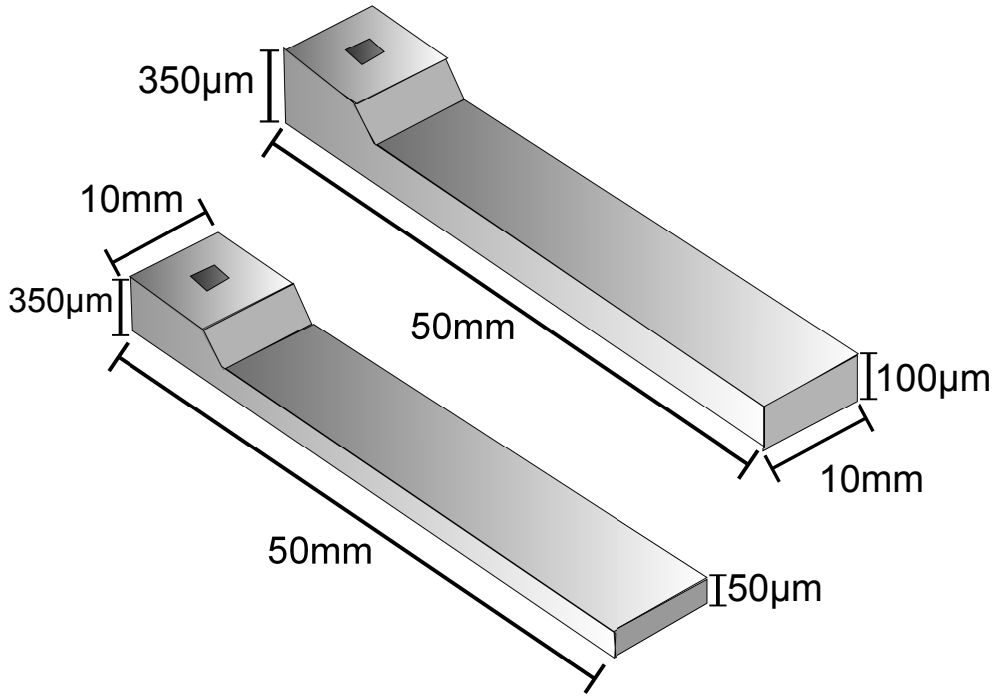

Figure 3.4: A pair of silicon cantilever samples showing major dimensions (not to scale).

The sample space is equipped with two clamps bolted to the cold plate, arranged so that the clamping surfaces are level with the height of the viewport. These clamps cool to near equilibrium with the cold plate, reaching a minimum temperature of 9K.

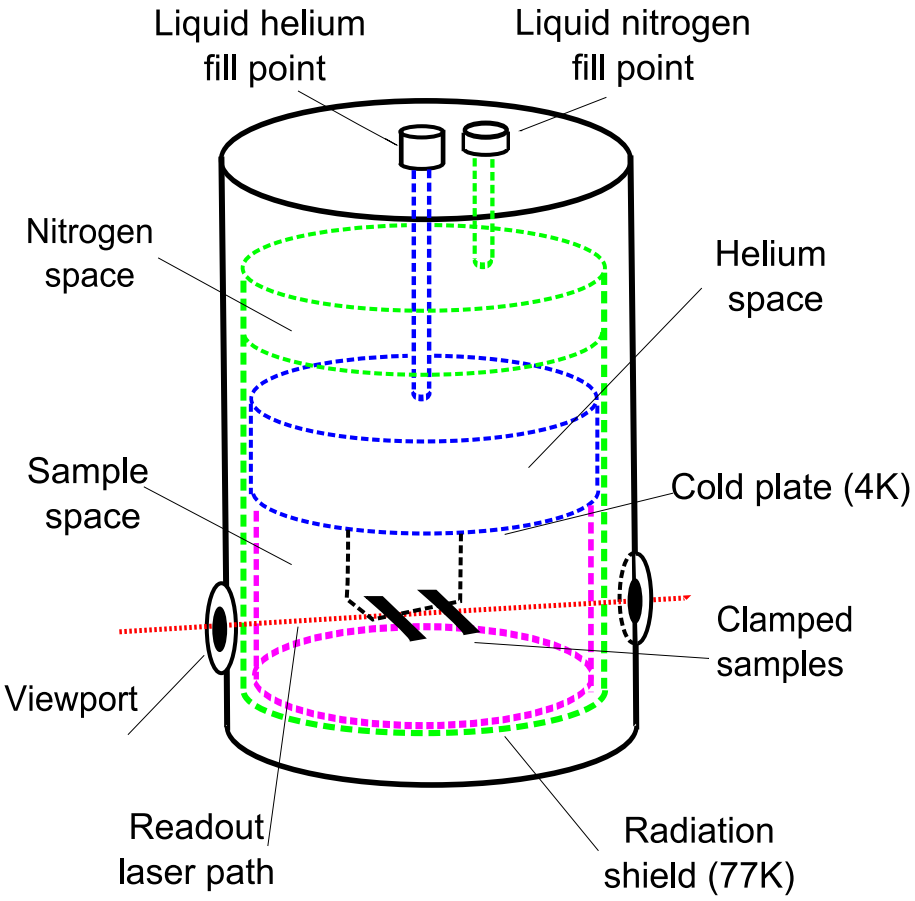

Figure 3.5: The tabletop cryostat, showing placement of helium and nitrogen spaces, evacuated sample space and path of readout laser.

As it is of high importance that the temperature of each the sample is known as accurately as possible, the temperatures of the clamp are monitored using DT-670 silicon diode sensors, which have a very well known and highly calibrated resistive response to temperature change and have an accuracy of ± 0.25K below 100K. The sensors are placed in slots made in the clamp a few millimetres below the position of the sample and are secured using cryogenic and vacuum compatible

varnish. Two further DT-670 sensors are used to monitor the temperature of the cold plate and radiation shield as proxy measurements for the level of cryogen in the helium and nitrogen reservoirs.

In order to ensure a true measurement of the mechanical loss for a particular temperature, the clamp and sample were held at a stable temperature for the duration of the measurement sequence. This was achieved by a feedback loop which used the difference between a measured temperature and the set temperature to alter the power of a heating circuit which acted on the clamp. The four temperature sensors were read by a Lakeshore 340 temperature control unit which monitored one measured temperature and its rate of change and used this to provide the appropriate level of power to the heating circuit in order to maintain a stable temperature. The heating elements consisted of high wattage resistors connected directly to the clamps and operated electrically in parallel. This meant that both clamps may be temperature controlled at once, but that the clamps may not be separately temperature controlled. During cooling, it was observed that the clamps reached equilibrium at slightly different temperatures. Clamp A cooled to around 10K, and Clamp B reached temperatures as low as 9.6K. This temperature gap was likely to be due to differences in the degree of thermal isolation obtained for each clamp component. A duplicate cryostat system which was used to make measurements of this kind also observed a difference in temperature between the two clamps and slightly lower equilibrium temperatures overall.

When loading samples into the cryostat, the clamping block of the sample, the polished surfaces of the top of the clamp and the clamping bar were cleaned us-

ing a clean room wipe dampened with methanol to ensure that no contaminants were present. The sample was placed on centre of the clamping surface so that the edge of the thick part of the sample (the 'clamping block') was aligned with the edge of the clamp. The clamping bar was then placed upon the sample and pressure applied to the centre of the clamping bar to prevent the sample slipping from its original position. The clamping bar was then secured with two M3 bolts, tightened alternately so as to equalise the stress applied across the clamping bar. Once the samples were clamped, the cryostat was then sealed and evacuated. The whole clamping structure around the silicon cantilever is constructed from stainless steel, so the clamp, block and M3 bolts may be modelled together as a 350μm gap in a stainless steel piece in which is placed a 350μm thick silicon cantilever clamping block. The integrated thermal contraction coefficients of stainless steel and silicon between 300K and 10K are 30 parts per 10^4 and 2.2 parts per 10^4 respectively, indicating that at 10K the 350μm gap in the stainless steel would contract by around a micron, but that the silicon would only contract by 77nm. Therefore, the clamping force applied to the cantilever increases as the temperature is lowered. If the cycling of the temperature during the measurements caused a hysteresis effect in the applied clamping force, then excess loss could have been introduced into the measurement system. Clamp hysteresis was counteracted by reclamping the sample between measurement runs.

A collimated laser beam was shone through the optical feedthroughs, producing sharp silhouettes of the samples. The movements of the silhouettes was monitored using a split photodiode, where the shadow is positioned over the split between two photodiodes. When the shadow moves, the difference in potential difference result-

ing from the change in the degree of illumination on the photodiode is proportional to the amount by which the shadow moves. Therefore when the cantilever is at resonance, the circuit outputs a sinusoidally varying voltage signal which may be used as a proxy for the measurement of the extent of vertical motion undergone by the cantilever. This signal was amplified by a simple 2-channel filtering pre-amp circuit set to attenuate unwanted signals below 10Hz and above 5kHz. A separate SR560 amplifier[1] was used to provide on-the-fly control on gain and filtering for each channel.

The filtered and amplified signals were recorded using a PC equipped with a National Instruments data acquisition interface and running a LabVIEW program written by R. Nawrodt and other colleagues at Friedrich-Schiller University in Jena. The LabVIEW program automated many aspects of the mechanical loss measurement process and also communicated with the Lakeshore 340 temperature control unit and the tank pressure gauges. The LabVIEW program requires a list of temperature points and likely mode frequencies to be provided by the user. The program then sets the temperature controller to control the clamp to target temperature according to the list of set points and locates, excites and records the ringdown of the modes covered by the provided modes.

The measurement sequence begins automatically when the measured temperature is within 0.05K of the target temperature and the rate of change of temperature is less than 0.5K/hr. The frequencies of the resonant modes of each cantilever, which

[1]SR560 is a low-noise preamplifier produced by Stanford Research Systems which can be used as a 6dB/octave band pass filter with a frequency range and gain set by the user [86].

were roughly calculated from the known dimensions and properties of the sample, were found by sweeping the frequency of a sinusoidally varying electrostatic field through a range around the roughly calculated value. The electrostatic field was generated by a high voltage amplifier set to a bias of 800-1000V powering the live electrode of an electrostatic exciter plate consisting of two interlocking comb electrodes printed upon a circuit board. A spectrum analyser was used to locate the frequency of the resonant mode more accurately.

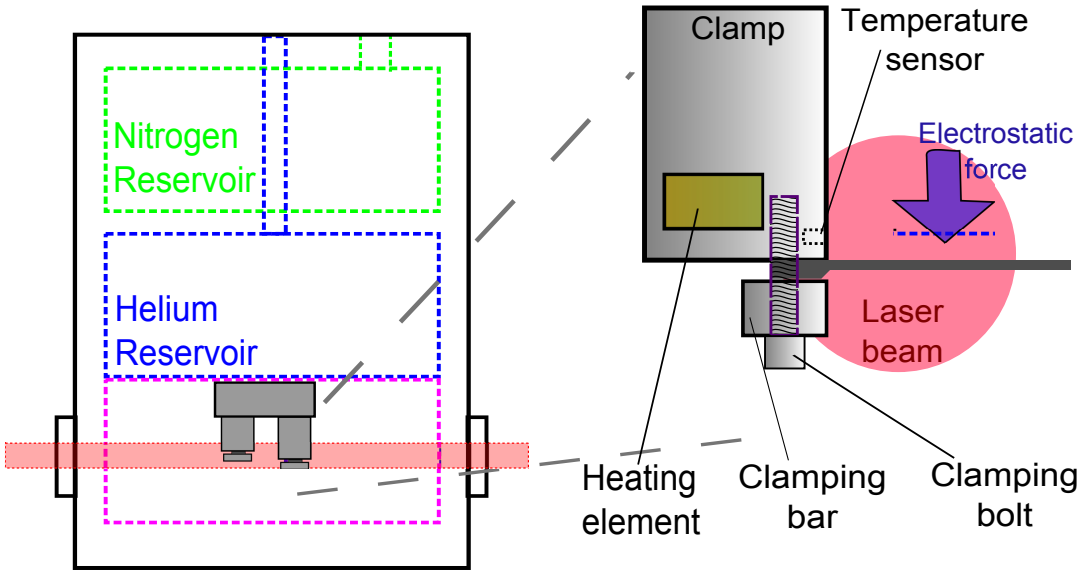

Figure 3.6: Cross-section of tabletop cryostat, showing the major components and the arrangement of the dual clamp, temperature sensors and heating elements.

A single mechanical loss measurement consisted of the following steps:

- The mode was electrostatically excited.
- The automated measurement software began to record the amplitude of the signal from the shadow sensor as the excitation was stopped.

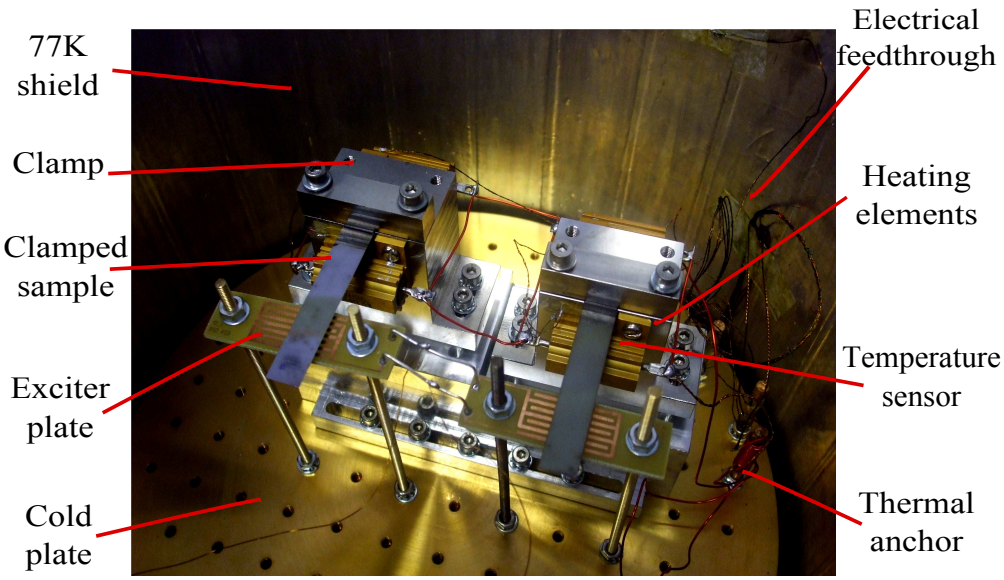

Figure 3.7: Photograph of experimental space of tabletop cryostat, showing cold plate, clamped samples, electrostatic exciter plates, heating elements and the positions of the temperature sensors.

- The automated measurement software recorded the exponentially decaying amplitude of the signal from the shadow sensor until it reached 10% of the starting amplitude.

- The exponentially decaying amplitude was fitted to a curve. From this curve and given the frequency of the mode, a value for the mechanical loss was calculated.

This single measurement was repeated for each resonant mode that it was possible to excite in order of ascending frequency, while the temperature feedback controller held the temperature of the clamp steady. After all the resonant modes were measured at the starting temperature, the set temperature was increased and upon reaching the temperature stability level quoted in Section 3.4 the measurement

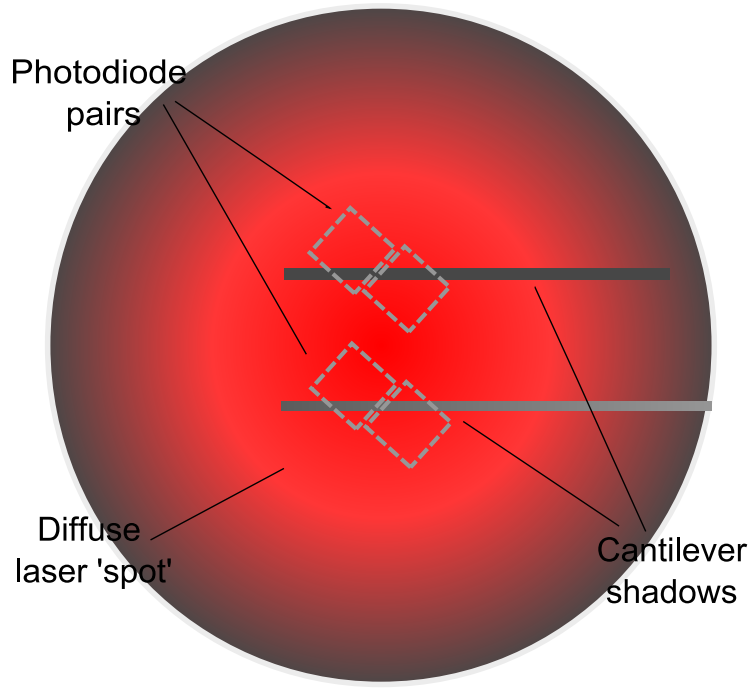

Figure 3.8: Diagrammatic layout of dual cantilever shadow sensor readout system showing beam radius, cantilever shadows and photodiode pair outlines.

step began again. The data acquisition hardware reads in the decaying sinusoid signal from the split photodiode at a very high rate - if the raw measurements were used to calculate ringdowns then the complete dataset would require large amounts of hard disk storage and processing power to manipulate. The LabVIEW automation program reduces the size of the data set by outputting a file that contains the modulus of the photodiode signal taken at intervals, with each point marked with the time at which it occurred. The data in this file can be fit to an exponential curve as shown in Figure 3.9, the decay rate of which can be used to calculate the mechanical loss present in the sample.

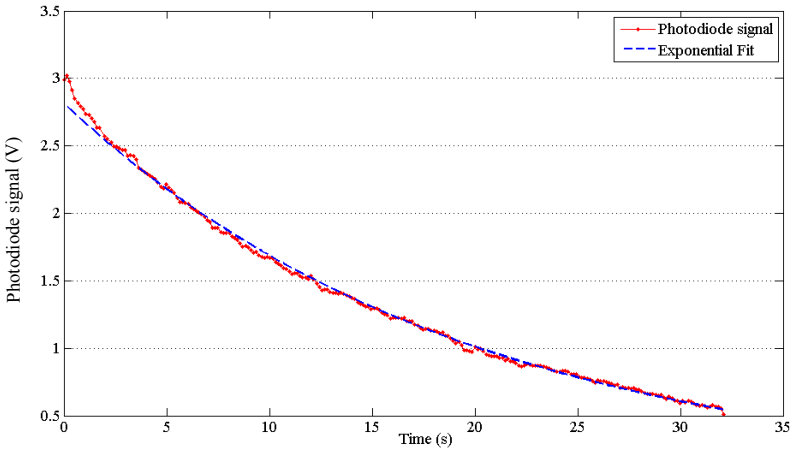

Figure 3.9: A typical ringdown dataset showing exponential decay and the exponential fitting curve.

This method and the use of the automated measurement software allowed continuous measurements with only the occasional intervention of the experimenter. The measurements made using this apparatus are used in Chapters 4, 5 and 6.

3.5 Measurement System Characterisation

As part of the calibration of this system, mechanical loss measurements were made between 10K and 300K using a cantilever coated with 500nm of Ta_2O_5 . The cantilever had previously been characterised in an alternate cryogenic loss measurement system which used an interferometer to read the amplitude of the oscillations of the cantilever, and formed part of a study into the effects of Ti doping on Ta_2O_5 films. The interferometric sensor of the previous cryostat was not stable enough to reliably measure the decaying amplitude of the fundamental modes of cantilever samples. At frequencies of around 25Hz, a single 'ringdown' measurement of a very low loss fundamental mode can take up to an hour, and it is vital that the readout system is continuously stable throughout. The shadow sensor was thought to be a more intrinsically stable sensor for measuring the amplitude of low frequency cantilever oscillations.

The measured modes of the Ta_2O_5 coated silicon cantilever were the fundamental mode at 56.5Hz, and the third and fourth bending modes at 994Hz and 1948Hz respectively. The measured values for the modes at 994Hz and 1948Hz are shown in Figures 3.10 and 3.11 alongside the previous measurements, and the measurements of the 56.5Hz are shown alone in Figure 3.12.

Below 200K in the 994Hz mode data and below 77K in the 1948Hz mode data, there is a strong agreement between two datasets, allowing direct comparisons to be made between samples measured in the different apparatus. An unexpected feature in the data from the new cryostat was the apparent feature at very low

temperatures in the fundamental mode, which is further addressed in Section 3.5.1.

The peak of the low temperature feature in the 994Hz and 1948Hz modes was fitted to a 5th degree polynomial function in order to locate the temperature of highest loss. The fitting curves can be seen in Figure 3.13. For the 994Hz mode, the new cryostat data has a temperature of highest loss of 19.6K, and the previous dataset placed the peak at 19.5K. For the 1948Hz, where the quality of the data measured in the new cryostat system was lower, the temperature of peak loss was 19.4K and the previous dataset produced a peak value at 20.2K. If the assumption that the temperature of highest loss in the feature is an intrinsic property of the material measured, then there is a discrepancy of 0.1K to 0.8K between the two

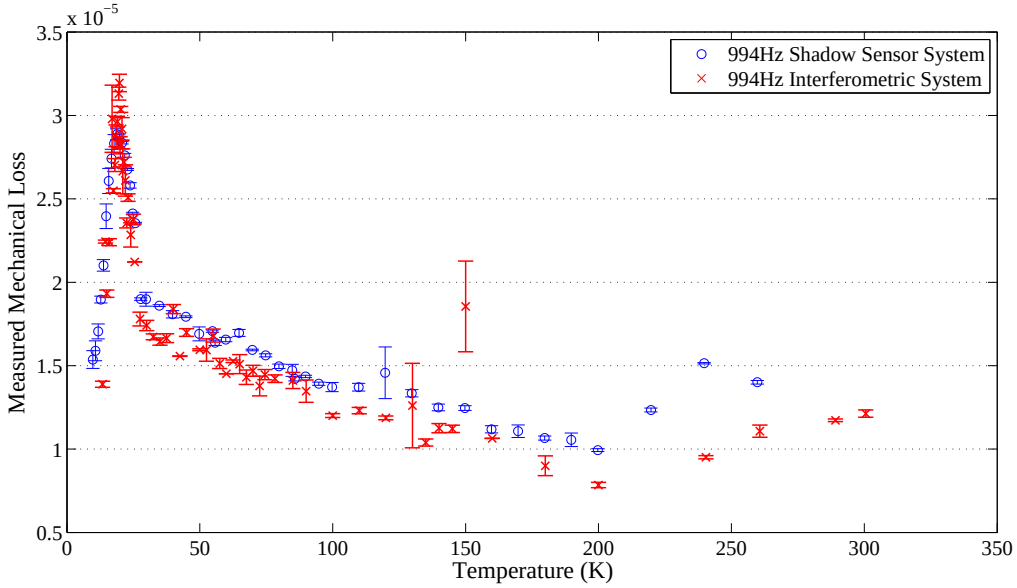

Figure 3.10: Calibration data showing mechanical loss of the 994Hz bending mode of a tantala coated silicon cantilever. Data measured in the cryostat with a shadow sensor readout is shown in blue and the measurements made in the previous interferometric readout cryostat system is shown in red.

measurement setups.

3.5.1 A Low Temperature Anomaly in Fundamental Modes

In the mechanical loss measurements of the fundamental mode of a Ta_2O_5 coated silicon cantilever, shown in Figure 3.12, anomalously high levels of mechanical loss were observed at temperatures below 15K. This feature only manifests itself in the measurements of the fundamental mode made using the new shadow sensor cryostat, and was present across all the samples measured in the work described in Chapters 4, 5 and 6. These samples were of varying sizes, with different sets of resonant mode frequencies, and yet the anomalously high losses were only present in the fundamental mode, seemingly without a dependence on the frequency.

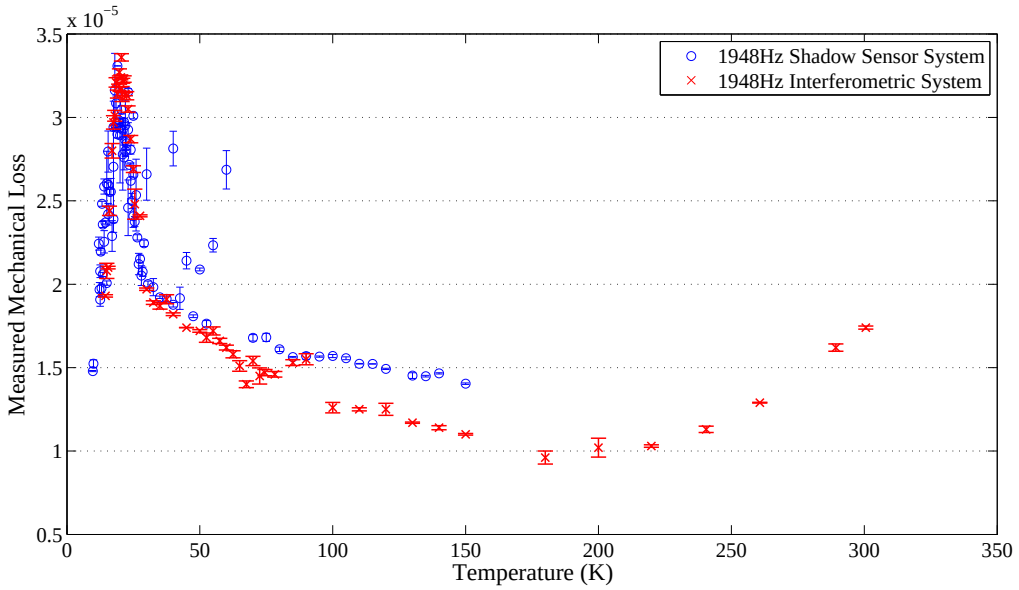

Figure 3.11: Calibration data showing mechanical loss of the 1948Hz bending mode of a tantala coated silicon cantilever. Data measured in the cryostat with a shadow sensor readout is shown in blue and the measurements made in the previous interferometric readout cryostat system is shown in red.

After the measurements used in Chapters 4, 5 and 6 of this thesis were made, it was observed that the anomalous losses of the fundamental mode at low temperature were not observed if the measurement was made whilst the high voltage amplifier driving the electrostatic excitation plate was switched off.

Figure 3.14 shows measurements made using the fundamental mode of a hafnia coated silicon cantilever, made on the same day during the same cooling period. The points with higher loss were measured with the high voltage amplifier delivering a large offset voltage to the excitation plate and the lower losses were measured with the high voltage amplifier set to zero during the 'ringdown' period.

This would seem to indicate that the electric field is able by some mechanism

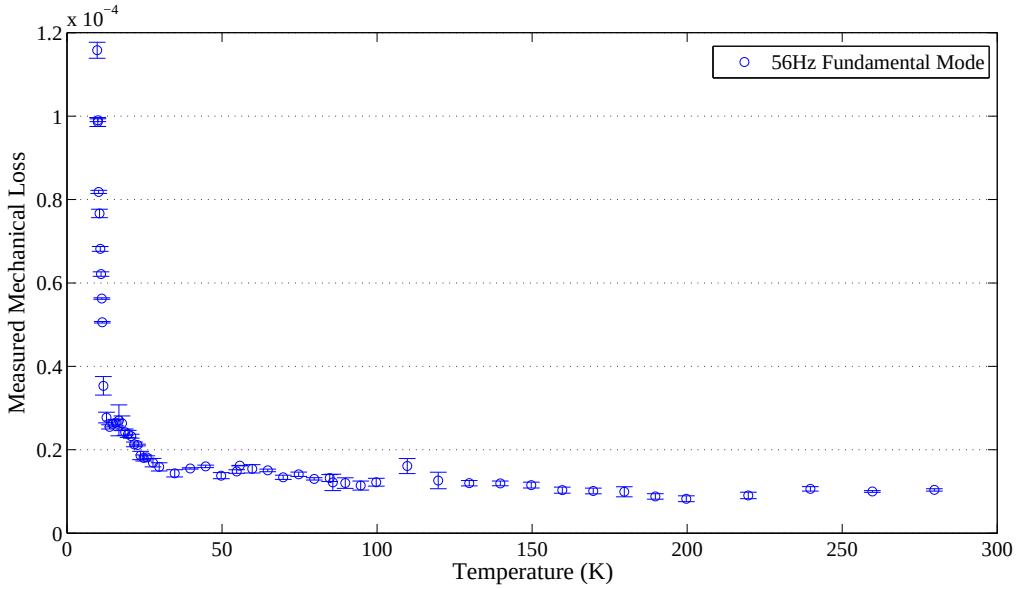

Figure 3.12: The mechanical loss measured in the new cryostat with shadow sensor readout on the 56Hz fundamental bending mode of a tantala coated silicon cantilever, showing the low temperature anomaly.

to couple to the resonances of the cantilevers, but only at an extremely low temperature. The dissipation mechanism is detectable only in fundamental modes, regardless of frequency, which could indicate that the process couples more strongly to a particular modeshape, and much more weakly to higher order modes.

The positioning of the excitation plate could be behind the anomaly and the strong modeshape dependence. The excitation plate is held parallel to, and a few millimetres apart from the cantilever on threaded rods. As shown in Figure 3.7, the excitation plates cover more than a third of the length of a cantilever sample and are placed close to but not at the end of the cantilever. If the damping effect of the gradient of electric field couples only with the part of the cantilever covered by the excitation plate, then the fundamental mode will only experience the

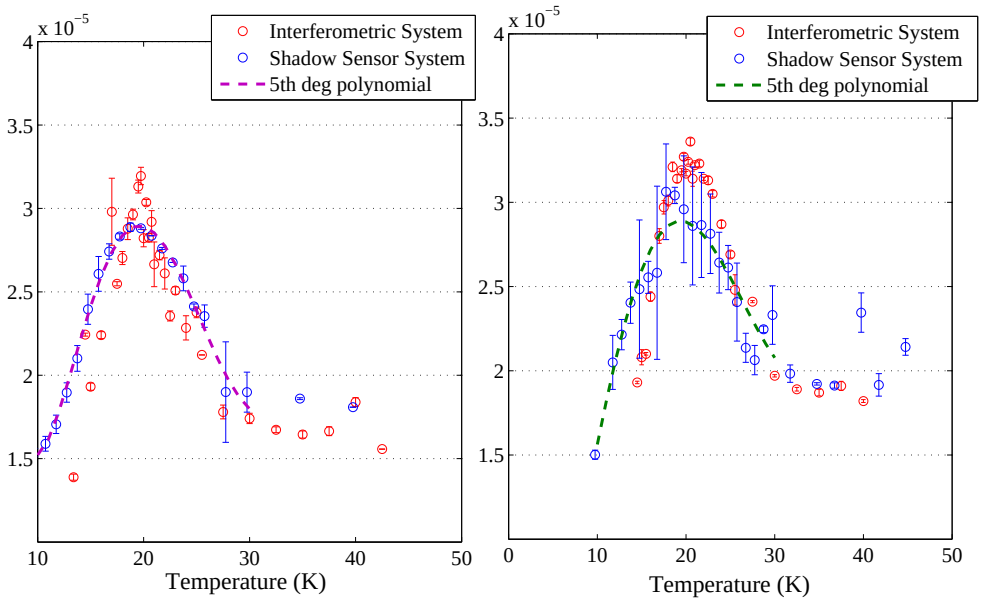

Figure 3.13: The polynomial curves fitted to the low temperature mechanical loss peaks for the 994Hz and 1948Hz modes of the Ta_2O_5 coated silicon cantilever.

damping force along parts of the modeshape which are always moving in the same direction. The higher order modes will experience the damping force over regions which are moving in opposite directions, which could allow the damping effect to be partially cancelled.

Another possibility is that the electrostatic damping effect could increase as the cantilever moves closer to the excitation plate. The excited oscillations of the fun-

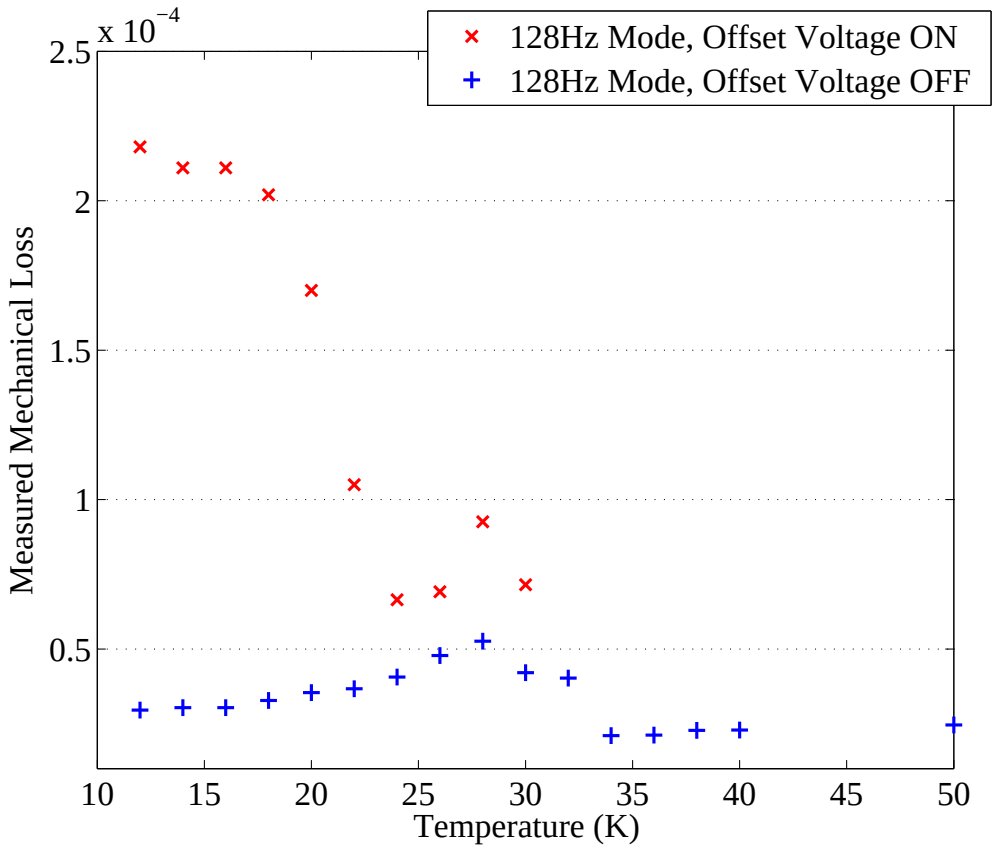

Figure 3.14: The mechanical loss measured on the 127Hz fundamental mode of a hafnia coated silicon cantilever, showing the presence and absence of a low temperature anomaly.

damental mode have the largest initial amplitude and so the fundamental mode would experience the most damping and higher modes would experience much less.

However, neither of the excitation plate mechanisms would directly explain the strong temperature dependence of the anomaly. The majority of shifting of internal resonances of the cryostat, clamps and fittings caused by thermal contraction occurs at higher temperatures than 15K, and this makes it unlikely that cooling brought a resonance of the cryostat system into a range that could couple with the frequency. Regardless of the mechanism by which this anomaly occurred, a simple solution was found and this issue can be taken into account in future measurements using the mechanical loss measurement system and other systems of the type.

Data containing the low temperature fundamental anomaly occurs throughout Chapters 4, 5 and 6. In situations where polynomial curves were fit, the anomalous points below 15K were not used. As it is clear that the anomaly is not a 'real' peak or intrinsic feature of the mechanical loss of the measured materials, low temperature data for the fundamental mode which may be contaminated is not used in any analysis.

3.5.2 Anomalies Due To Thermal Cycling

A feature was also observed at temperatures between 200K-250K in several of the datasets discussed in Chapters 4, 5 and 6. The peak height and width of the feature increase with each cooling and heating cycle, as shown in Figure 3.15. The feature was observed to reduce in size for the first measurement run after replacing

the sample and re-tightening in the clamp. In Figure 3.15, the datasets from the 6th to 21st October represent data taken before the sample was reclamped, and the 27th October and 11th November datasets which show marked reduction in the size of the feature were taken after the sample was reclamped.

This behaviour led to the conclusion that this anomaly was related to a new resonance caused by the bolts which secured the clamp bar working loose after cycles of differential thermal contraction and expansions. On several occasions, the clamp bar bolts, which are tightened to hand tightness and then further tightened using a hex key in the sample loading procedure, were found to be loose when opening the cryostat after a measurement run.

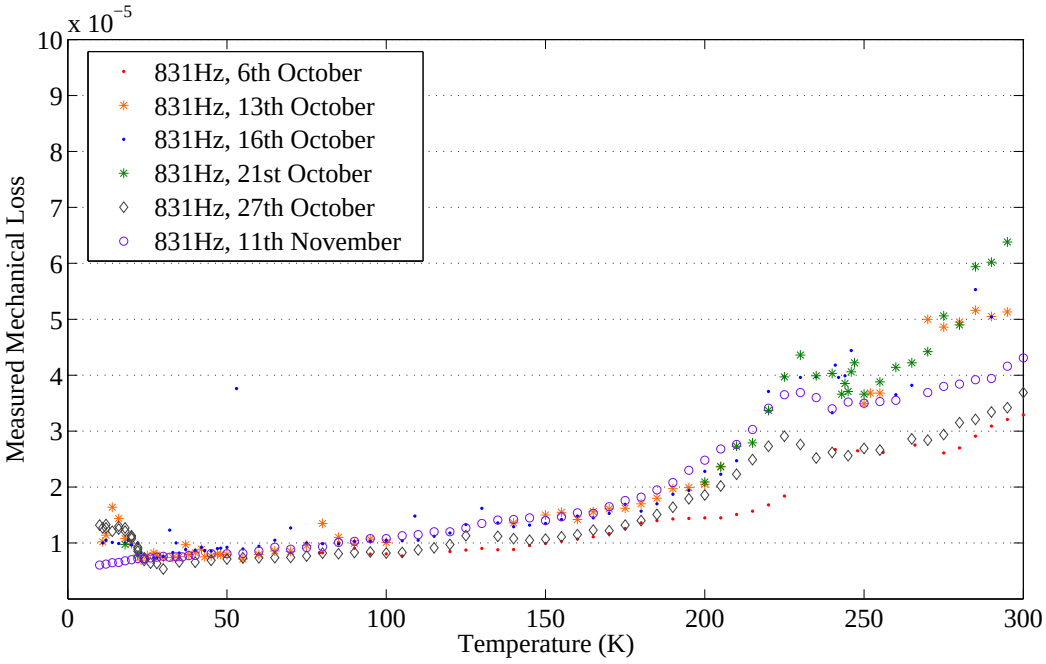

Figure 3.15: The mechanical loss measured on the 127Hz fundamental mode of a hafnia coated silicon cantilever, showing the development of the thermal cycling anomaly over several measurement runs.

3.6 Summary

The small scale cryostat setup for measuring mechanical losses was built, commissioned and characterised and produces mechanical loss measurements which broadly agree with the previous cryostat system and found temperatures of highest loss for the Debye peak of tantala which agreed to better than 1K. Two systematic features of the cryostat were identified, an anomalous level of loss at the lowest temperatures in the fundamental mode and a feature at around 200-250K which increases in loss with repeated thermal cycling.

Chapter 4

The Effect of Post-deposition Heat Treatment On The Mechanical Loss of An Ion-Beam Sputtered Silica Film

The optical coatings used in gravitational wave detectors are annealed to reduce the film stress and reduce overdense regions and it is already known that post-deposition heat treatment of thin ion-beam sputtered films can significantly alter their properties [87]. The work described in this chapter was carried out to ascertain the effect of the annealing process undergone by optical coating films on the level of mechanical loss of the films and to let us develop an optimum set of annealing parameters that will produce a film that fulfills the low-stress criteria and also has a low mechanical loss.

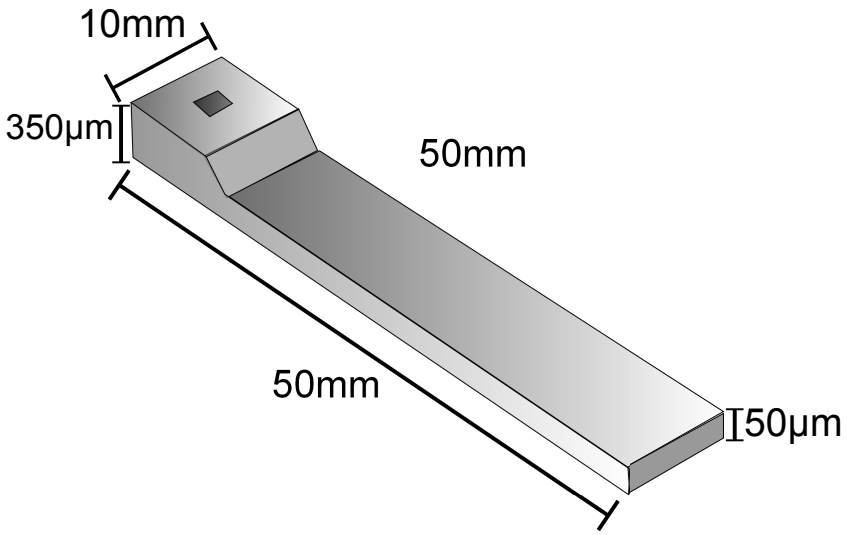

Figure 4.1: Schematic of silicon cantilevers as used in the mechanical loss measurements in Chapter Four and Five.

Three pairs of silicon cantilevers of dimensions shown in Figure 4.1 were etched from a 500μm thick silicon wafer by colleagues at Stanford University. All cantilevers were oxidised at 900^{o}C to grow a layer of silicon dioxide upon which the ion-beam sputtered coating could adhere. An amorphous film of 0.5μm of silica was deposited on one cantilever from each pair using ion-beam assisted sputtering performed by the Materials Science and Engineering Division of CSIRO [80]. The remaining cantilever in each pair was not coated. The post deposition annealing temperatures of 300°C, 600^{o}C and 800^{o}C were chosen to co-incide with the temperatures used in the parallel experiment on tantala coatings. Each set of cantilevers remained at the heat treatment temperature for twenty-four hours before being allowed to cool naturally.

The thicknesses of the ion-beam sputtered silica coatings and the thermally grown silicon oxide layers for the samples annealed at 300°C, 600^{o}C and 800^{o}C were mea-

Sample	Oxide Film Thickness	Sputtered Film Thickness
300C° coated	-	587 ± 3nm
600C° control (top)	6.37 ± 0.79nm	
600C° control (bottom)	9.31 ± 0.85nm	
600C° coated (top)	7.71 ± 0.90nm	575.22 ± 3.40nm
600C° coated (bottom)	7.75 ± 0.93 nm	
800C° control (top)	58.95 ± 1.78 nm	
800C° control (bottom)	62.40 ± 1.67nm	
800C° coated (top)	51.56 ± 1.20nm	558.31 ± 3.08nm
800C° coated (bottom)	51.56 ± 1.20 nm	

Table 4.1: Ellipsometric measurements of the thicknesses of the films on the surface of the cantilever samples.

sured using an ellipsometer by Stephanie Lewis. The results of the measurements are summarised in Table 4.1 and suggest that the silica coatings are slightly thicker than the specified 500nm and also show a marked increase in the thickness of the oxide layer between the samples annealed at 600^{o}C and 800°C. The thickness of the oxide layer on the cantilevers heat treated at 300^{o}C could not be measured using the ellipsometric technique.

The measurements of mechanical loss as a function of temperature were carried out in the temperature controlled tabletop cryostat using the LabVIEW program for automating mechanical loss measurements previously described in Chapter 3, Section 3.4. In parts of this work the uncoated control sample was measured at the same time as the coated sample. As the resonant mode frequencies of the coated samples were very close to those of the control, it was important to ensure that the motion of each cantilever was visible on only the appropriate channel of the dual channel readout system. Ringdown signal crossover confusion could occur for several reasons:

- the divergence of the laser beam is such that the cantilever shadows merge.
- reflections from the faces of the cantilever may enter the output beam if the input beam is not angled correctly.
- the automated LabVIEW software may record a signal from the wrong mode if a mode has a similar frequency across two samples.

To avoid crossover confusion, the divergence of the laser beam was adjusted by changing the position of the lenses controlling the beam width until two distinct, sharp shadows were seen at the photodiode monitoring point. A spectrum analyser was used to monitor the level at which the signal from one cantilever was picked up by the photodiode aligned to the other. When the swept sine signal which was used to excite two modes which were very close in frequency, the excited modes were visible in both channels but a cross-coupling amplitude of less than 5%. Reflections from the cantilever faces could be avoided by ensuring the laser was held parallel to the optical bench. As far as was possible, the automated swept sine was set to sweep through a frequency range that avoided the mode on the opposite channel. Opposite channel excitation was only unavoidable for modes which were within 1-2Hz of each other.

The automated software was set to stop the swept sine mode locating process and begin the ringdown measurement only once the cantilever oscillation signal reaches a preset voltage level. By setting this voltage level at the height to which the intended mode becomes excited, which is more than an order of magnitude above the signal level from the opposite channel, accidental measurement of the wrong mode is prevented.

4.1 Samples annealed at 300^{o}C post deposition

The first five bending modes of the silica coated sample heat-treated at 300^{o}C were measured in the apparatus described in Chapter 3. The control sample heat-treated at 300^{o}C was measured separately, in apparatus of very similar construction. The data shown in Figures 4.2 to 4.6 is the mean mechanical loss calculated from the lowest three values measured at each temperature step.

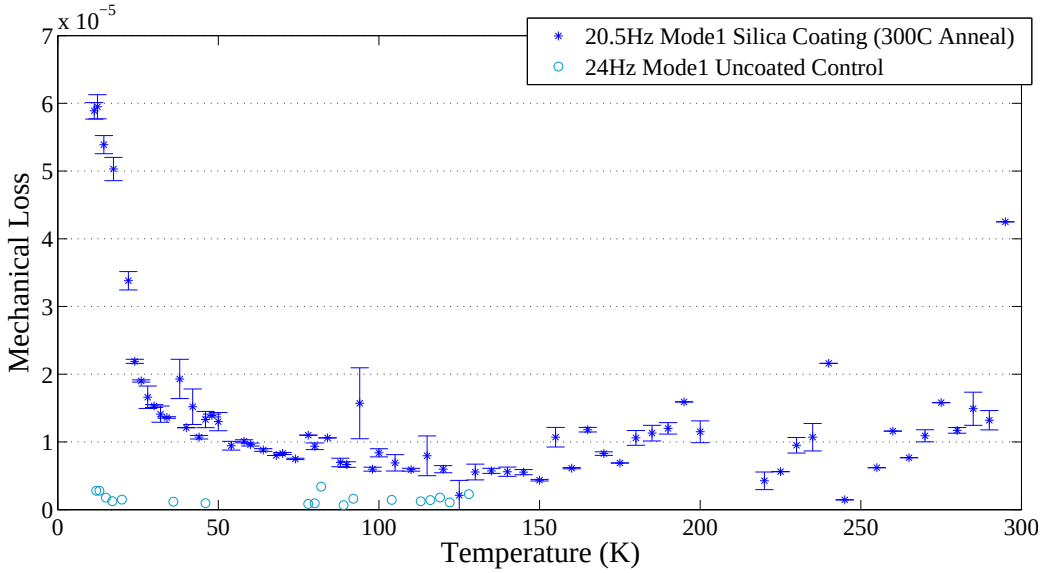

Figure 4.2: The mechanical loss of a silicon cantilever coated with 550nm of ion-beam sputtered silica at 20.5Hz and an uncoated silicon cantilever at 24Hz.

The low temperature excess loss anomaly is present below 20K in the 20.5Hz fundamental mode. The second (125Hz) and third (653Hz) modes showed some scatter at low temperatures, and produced low temperature loss peaks with peak loss values of 2×10^{-5} and 4×10^{-5} respectively. The mechanical loss of the third mode showed the same shape as the fourth and fifth modes although the

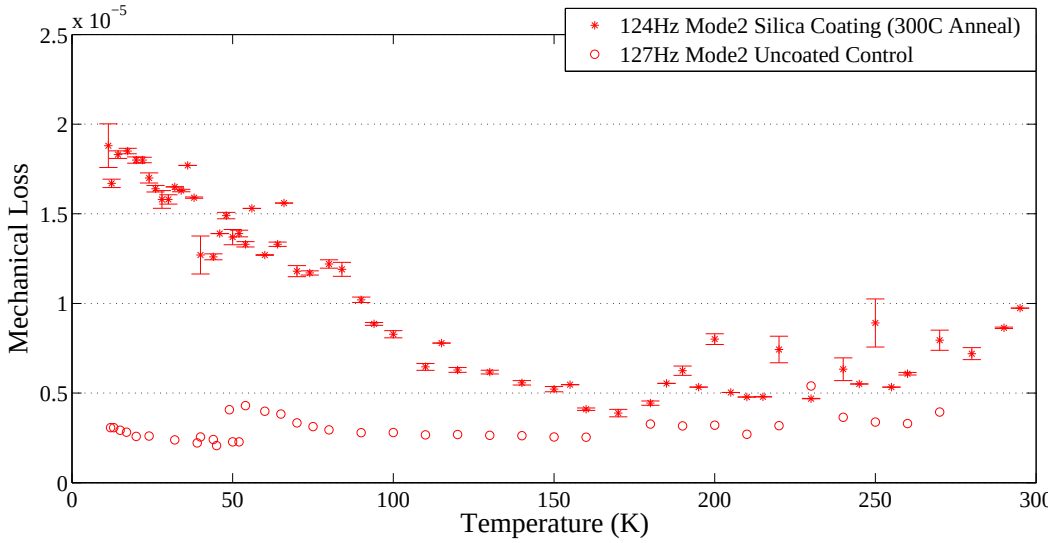

Figure 4.3: The mechanical loss of a silicon cantilever coated with 550nm of ion-beam sputtered silica at 124Hz and an uncoated silicon cantilever at 127Hz.

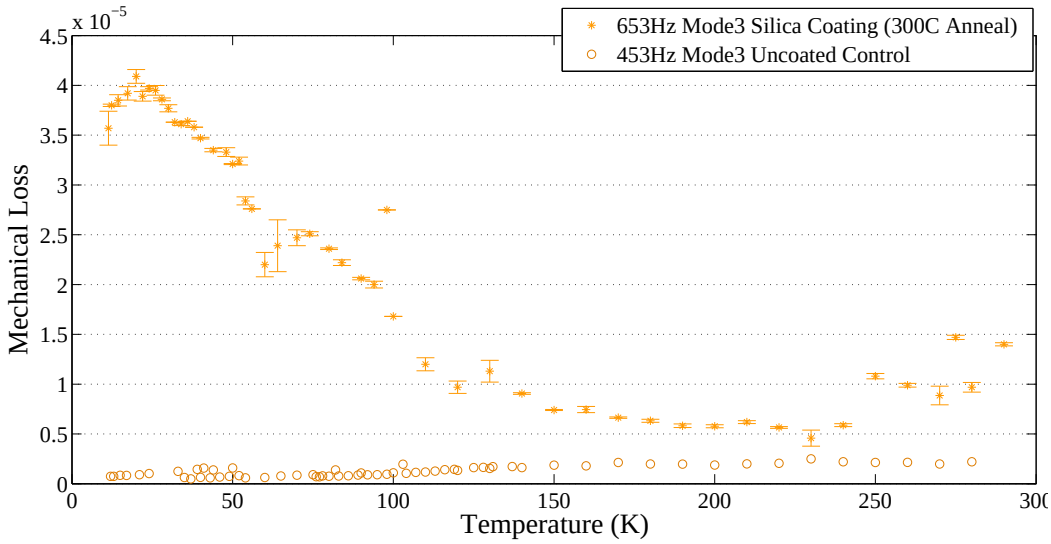

Figure 4.4: The mechanical loss of a silicon cantilever coated with 550nm of ion-beam sputtered silica at 653Hz and an uncoated silicon cantilever at 453Hz.

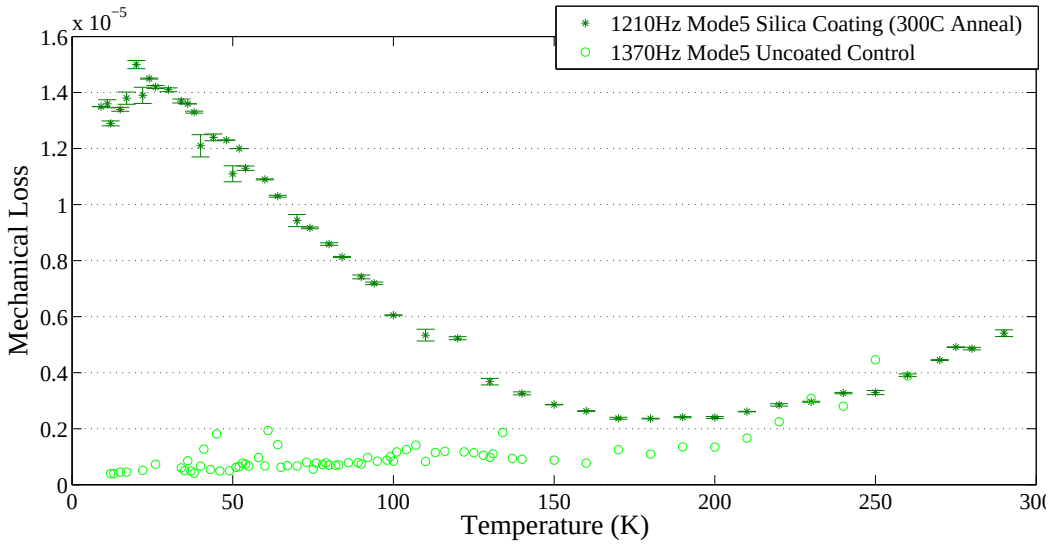

Figure 4.5: The mechanical loss of a silicon cantilever coated with 550nm of ion-beam sputtered silica at 1210Hz and an uncoated silicon cantilever at 1370Hz.

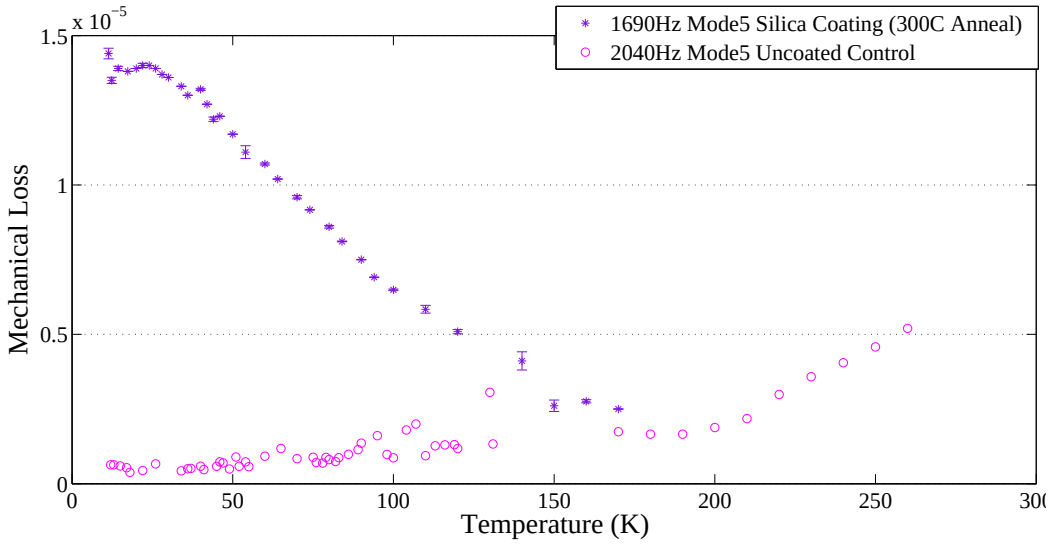

Figure 4.6: The mechanical loss of a silicon cantilever coated with 550nm of ion-beam sputtered silica at 1690Hz and an uncoated silicon cantilever at 2040Hz.

magnitude of the loss was a factor of four higher throughout. The fourth and fifth modes produced data with less scatter and produced low temperature loss peaks with peak loss values of 1.41×10^{-5} and 1.48×10^{-5} respectively. For all mode frequencies, the measured mechanical loss values were several orders of magnitude above substrate thermoelastic noise except at the higher temperatures.

4.1.1 Coating Losses

The mechanical loss in one part of a structure made of several parts contributes to the overall loss of the structure proportionally to the amount of strain energy which is stored in the flexing of that part of the structure. To find the mechanical loss in the coating, the difference between the measured loss and the interpolated control loss was scaled by the energy ratio [88],

$$\frac{E_{coating}}{E_{total}} = \frac{3Y_{silica}t_{silica}}{Y_{silicon}t_{silicon}} \tag{4.1}$$

An equivalent substrate loss for each temperature step in the data for the coated cantilever was estimated from the control cantilever data using a MATLAB spline interpolation routine. This routine produces a smoothed curve following the shape of the original control data, from which the value for the appropriate temperature were selected. It was not necessary to treat the loss of the thermal oxide layer as a separate coating in these calculations. The control samples bore the same thickness of thermal oxide as the coated samples so subtracting the oxidised control measurements subtracts the contribution that the thermal oxide makes to the mechanical loss measured on the coated sample, leaving only the loss of the ion-beam

	Silicon	Silica
Property	Value	Value
Young's Modulus	164 ± 3GPa [89]	72GPa [66]
Thickness	$50 \pm 5\mu$m	587 ± 3nm

Table 4.2: Values used to calculate the ratio of strain energy stored in the silica coating to the total strain energy in the cantilever heat-treated at 300^{o}C .

sputtered coating.

The values in Table 4.2 were used to calculate the energy ratio, $\frac{E_{coating}}{E_{total}}$. The small temperature dependence of Young's Modulus was not taken into account, and the large uncertainty on the thickness is due to the lack of a ellipsometric thickness measurement. The values calculated for the mechanical loss of the 300^{o}C annealed silica coating are shown in Figures 4.7 to 4.11. The main contributions towards the magnitude of the error on each value was the process of averaging several measurements.

4.1.2 Features and Peaks

All modes show an increase in coating loss at temperatures below 50K, in keeping with previous measurements of the temperature variance of mechanical loss in silica. The coating loss increases 1.0×10^{-3} at 10K for the 125Hz mode and 2.1×10^{-3} at 10K for the 653Hz mode. The apparent higher level of coating loss at low temperature in the fundamental mode is unlikely to be an intrinsic feature

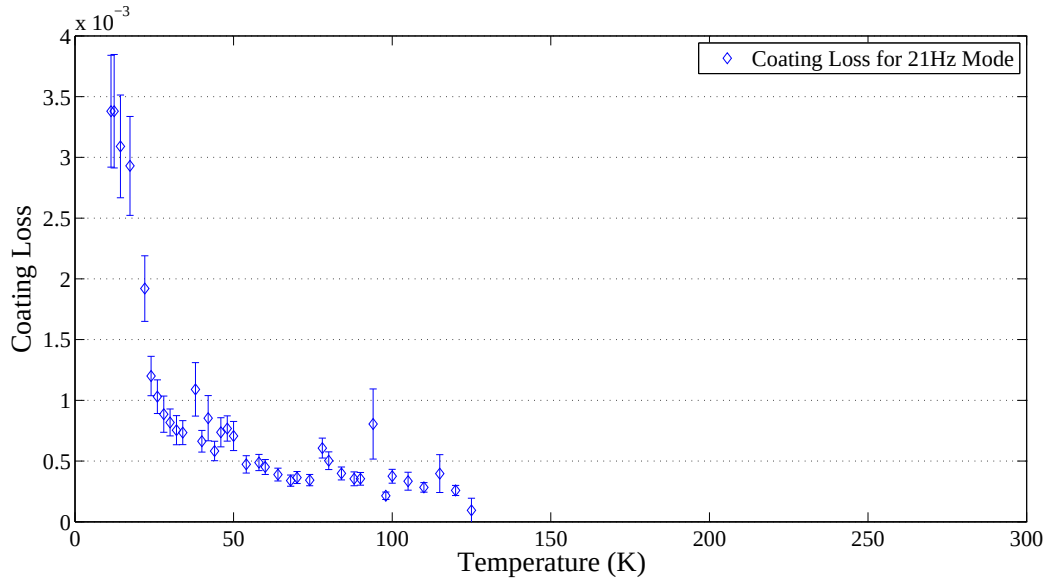

Figure 4.7: The calculated coating loss at 20.5Hz for the ion-beam sputtered silica coating heat-treated at 300^{o}C .

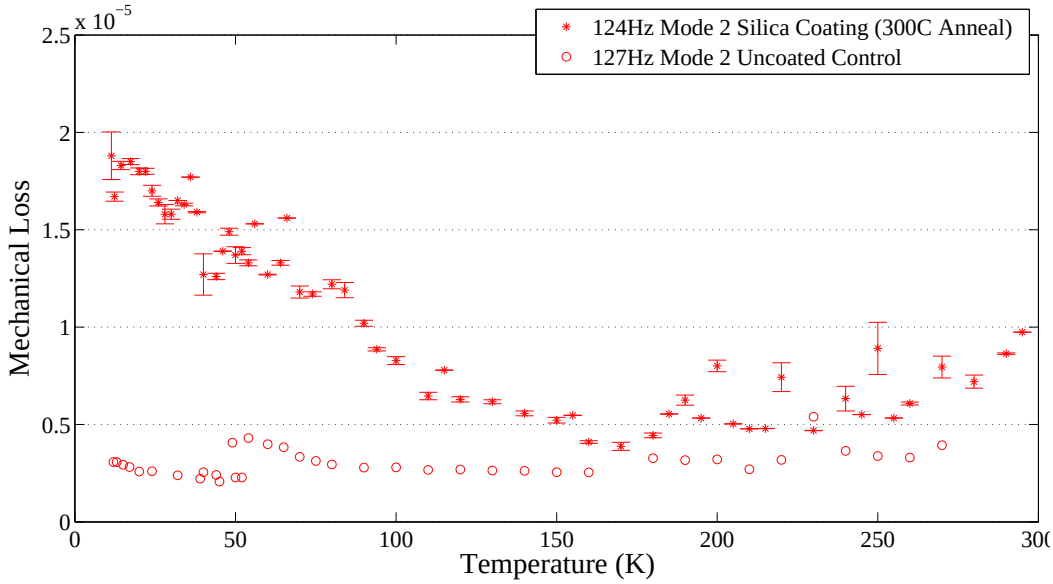

Figure 4.8: The calculated coating loss at 125Hz for the ion-beam sputtered silica coating heat-treated at 300^{o}C .

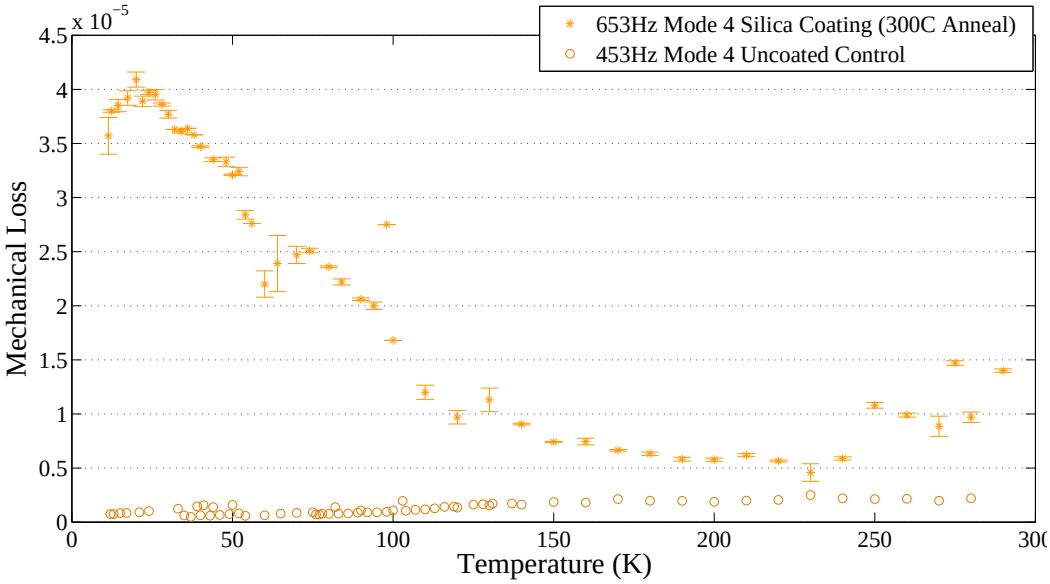

Figure 4.9: The calculated coating loss at 653Hz for the ion-beam sputtered silica coating heat-treated at 300^{o}C .

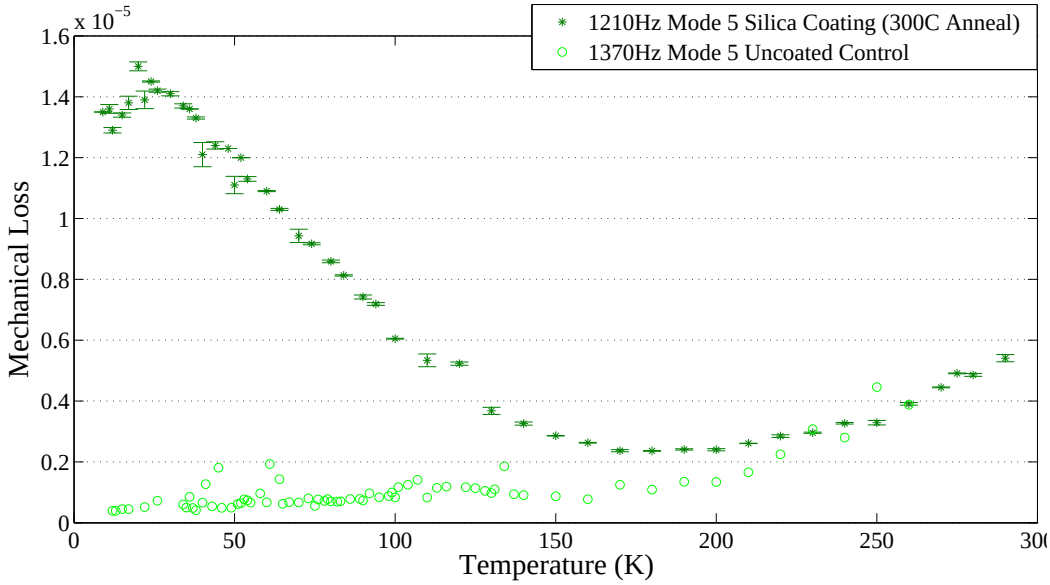

Figure 4.10: The calculated coating loss at 1210Hz for the ion-beam sputtered silica coating heat-treated at 300^{o}C .

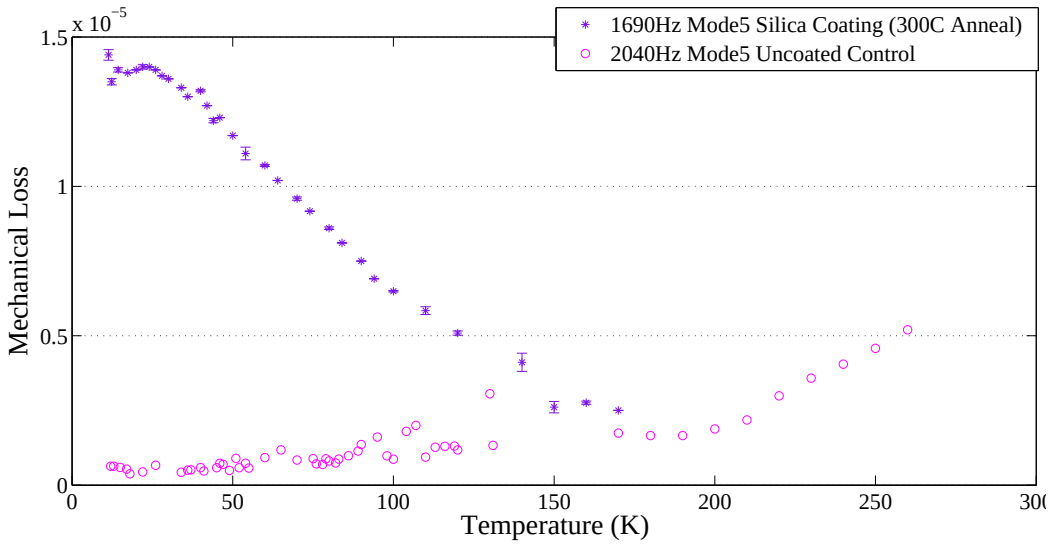

Figure 4.11: The calculated coating loss at 1690Hz for the ion-beam sputtered silica coating heat-treated at 300^{o}C .

of the material, but is likely to be linked to the low temperature anomaly as previously observed in calibration measurements.

The loss of the second mode increased at low temperature but due to scatter in the measurements it was impossible to determine if the measurements show a Debye peak in the highest losses between 10-35K. The third, fourth and fifth modes contained well defined loss peaks. Polynomial curves of the fourth and fifth degree were fitted to the datapoints to locate the local maximum and calculate the temperature of peak loss,as shown in Figure 4.12. The error values on the temperatures of peak loss for each mode were obtained by calculating the standard error from the two fitted curves.

If the low temperature feature in these measurements was caused by a relaxation

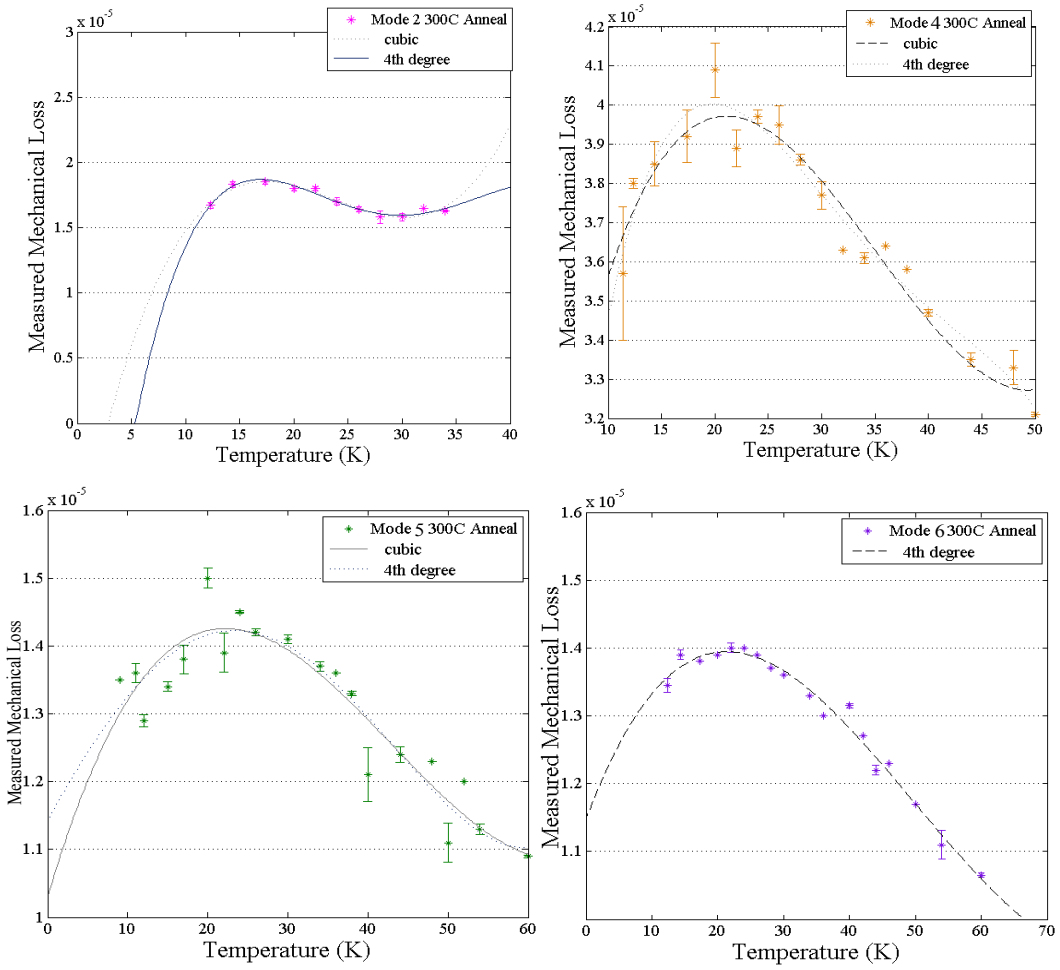

Figure 4.12: The fitting curves used to determine the temperature of peak loss for the four viable modes of the silica coated silicon cantilever heat-treated at 300°C.

Mode	Frequency	Peak Loss Temperature
1	20.5Hz	no fit
2	124Hz	$(17.18 \pm 0.34)K$
4	653Hz	$(20.44 \pm 0.91)K$
5	1205Hz	$(22.74 \pm 0.80)K$
6	1690Hz	$(21.38 \pm 0.71)K$

Table 4.3: The resonant frequency and the temperatures of peak loss for the measured modes of the 300^{o}C heat-treated silica coating.

process in a two-level system that may be described by the Arrhenius equation as introduced in Chapter 2, Section 2.2, then the relationship between the logarithm of the angular frequency of a resonant mode and the temperature at which the loss feature peaks is given by,

$$\ln(\omega_0) = \ln(\tau_0^{-1}) + \frac{H_b}{k_B T_{pk}}, \tag{4.2}$$

where τ_0^{-1} is the rate constant of the process and H_b is the average height of the potential barrier between states in the proposed two level system.

The reciprocal temperature of peak loss for each mode, $1/T$, was plotted against the logarithm of the angular frequency of the resonant mode, $\ln(\omega)$. Two-dimensional least squares regression was used to obtain a best fit line for these data. Using the data from all four modes for which a peak fit could be found, a line of gradient -201 ± 27.4 and intercept 18.3 ± 1.3 was fitted. Comparing the gradient and intercept values with Equation 4.2 gave a value of (17.3 ± 2.3)meV for H_b, the activation or barrier energy, and a value of $(8.86 \pm 0.43) \times 10^7 s^{-1}$ for the relaxation rate, τ.

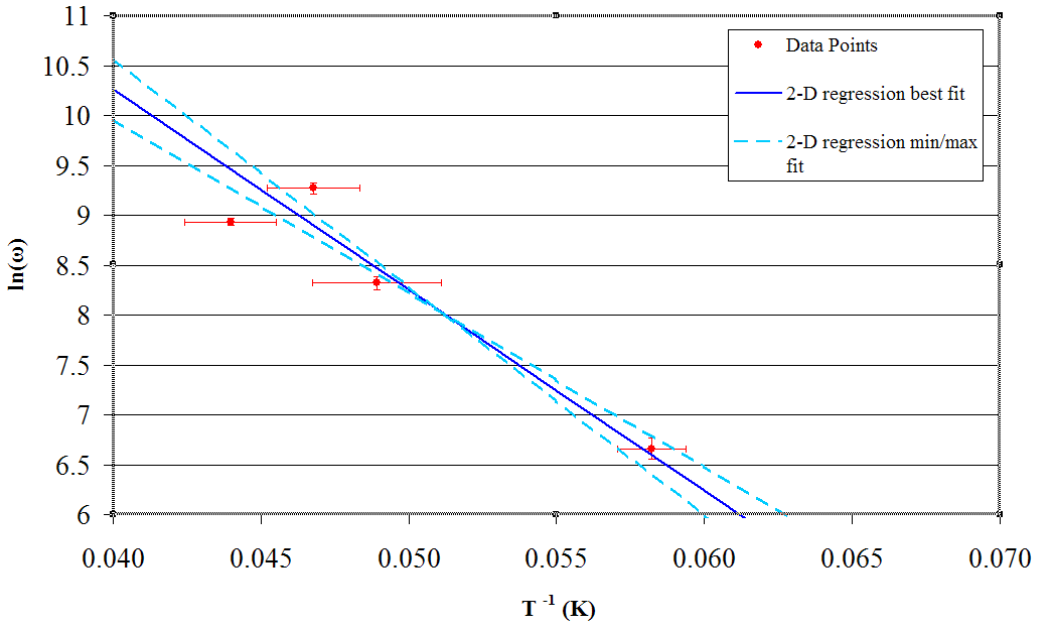

Figure 4.13: Arrhenius plot showing the line of best fit for the four modes for which a peak could be fitted and the minimum and maximum gradients from the fitted gradient of -201 ± 27.4.

At Glasgow, Iain Martin carried out a similar analysis on measurements of a 492nm thick ion-beam sputtered silica layer deposited on a silicon cantilever by LMA and annealed at 600^{o}C [51]. This analysis calculated an activation energy of 54.4 ± 5.5meV which is significantly greater than the activation energy calculated from the measurements described in this work. Another measurement of the activation energy of this process in silica was performed by Anderson and Bommel, resulting in a value of 44meV [75]. The value of (17.3 ± 2.3)meV is significantly lower than the values from the 600^{o}C heat treated silica.

4.2 Samples heat-treated at 600^{o}C post deposition.

The coated sample heat-treated 600^{o}C was initially measured with no other sample in the two-channel loss measurement apparatus. After the first reclamp, the control sample was added and measured. It was difficult to obtain useful ringdowns for the fundamental modes of both the coated and control sample. Across all modes the measured ringdowns from the control sample at high temperatures were largely unusable. The first six bending modes of the cantilevers were measured along with one other mode of the coated sample which did not fit in with the progression of bending modes, which was likely to be a torsional mode.

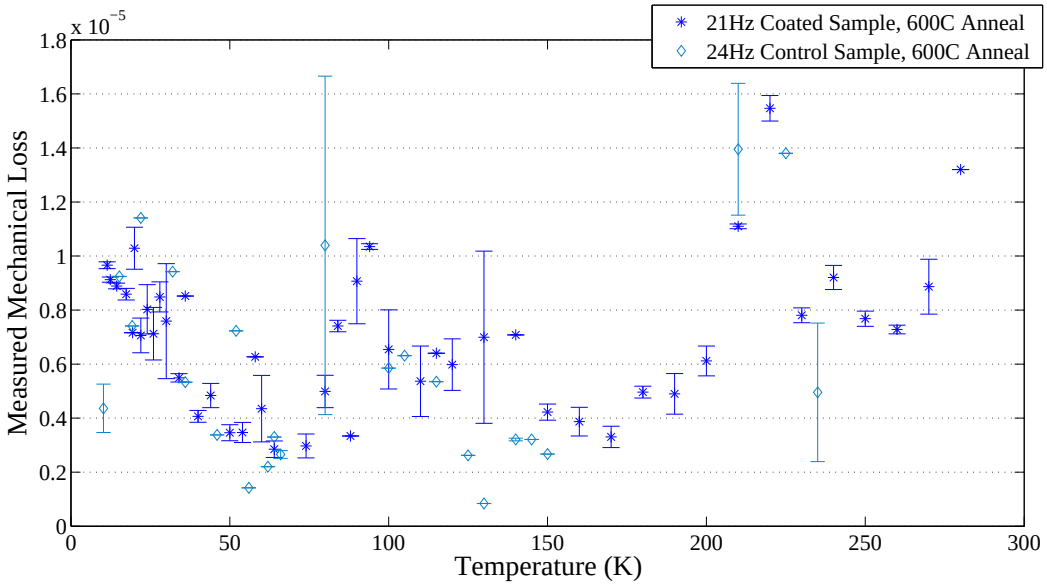

Figure 4.14: The mechanical loss of a silicon cantilever coated with 557.0 ± 3.4nm of ion-beam sputtered silica at 21Hz and heat-treated at 600^{o}C and an uncoated silicon cantilever at 24Hz.

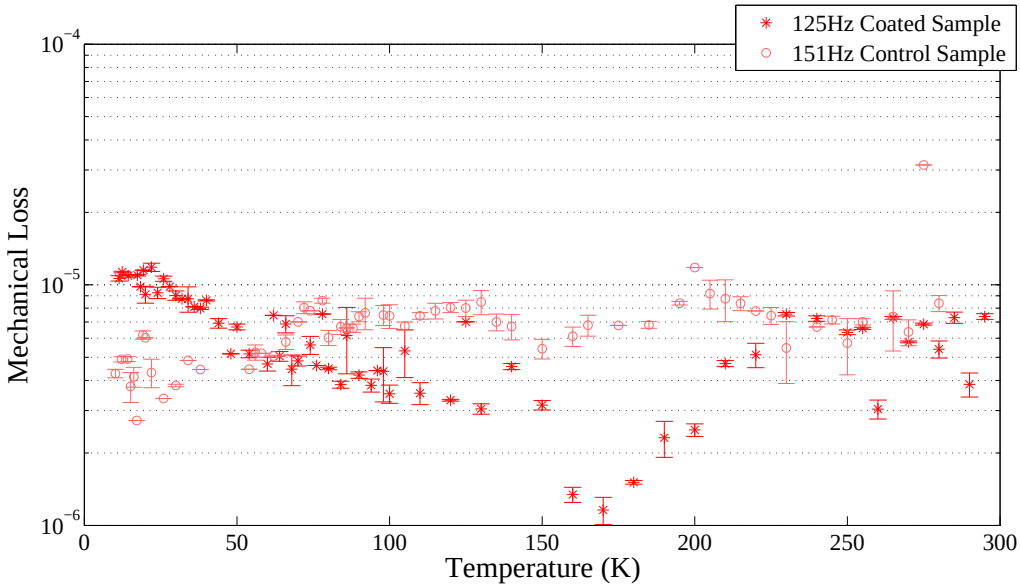

Figure 4.15: The mechanical loss of a silicon cantilever coated with 557.0 ± 3.4nm of ion-beam sputtered silica at 124Hz and heat-treated at 600^oCand an uncoated silicon cantilever at 151Hz.

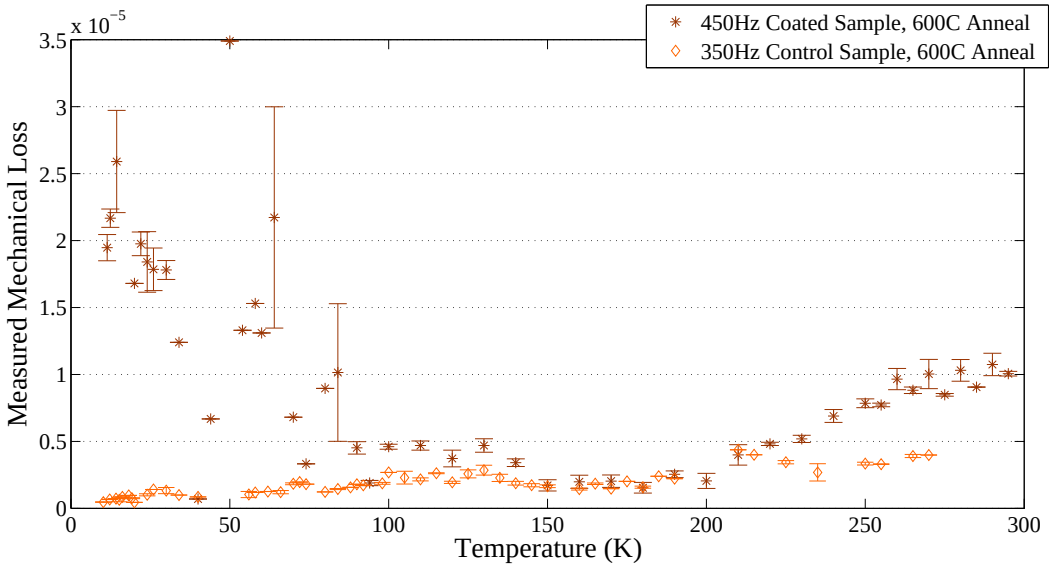

Figure 4.16: The mechanical loss of a silicon cantilever coated with 557.0 ± 3.4nm of ion-beam sputtered silica at 390Hz and heat-treated at 600^oC and an uncoated silicon cantilever at 410Hz.

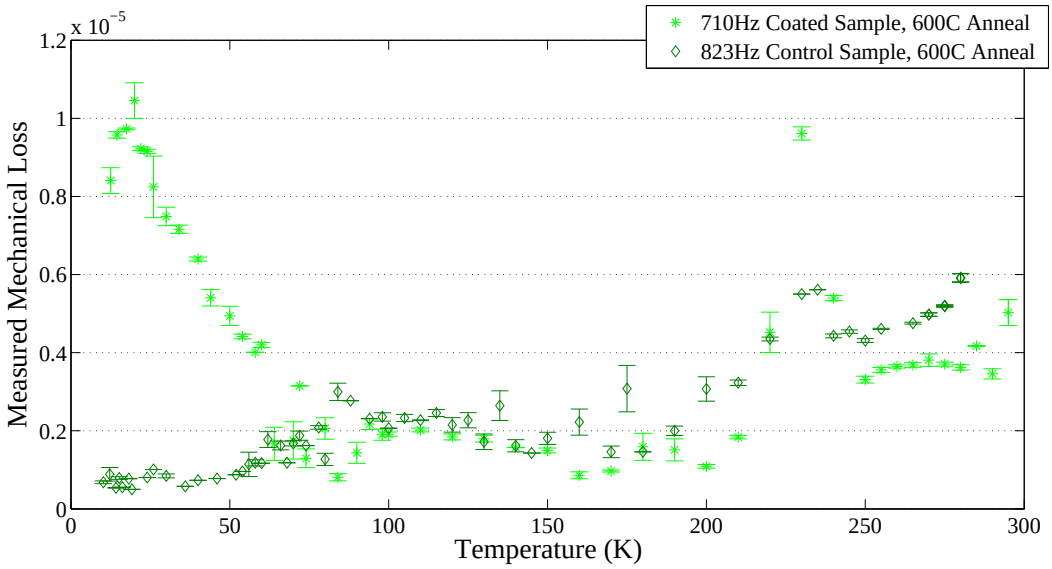

Figure 4.17: The mechanical loss of a silicon cantilever coated with 557.0 ± 3.4nm of ion-beam sputtered silica at 750Hz and heat-treated at 600^{o}C and an uncoated silicon cantilever at 823Hz.

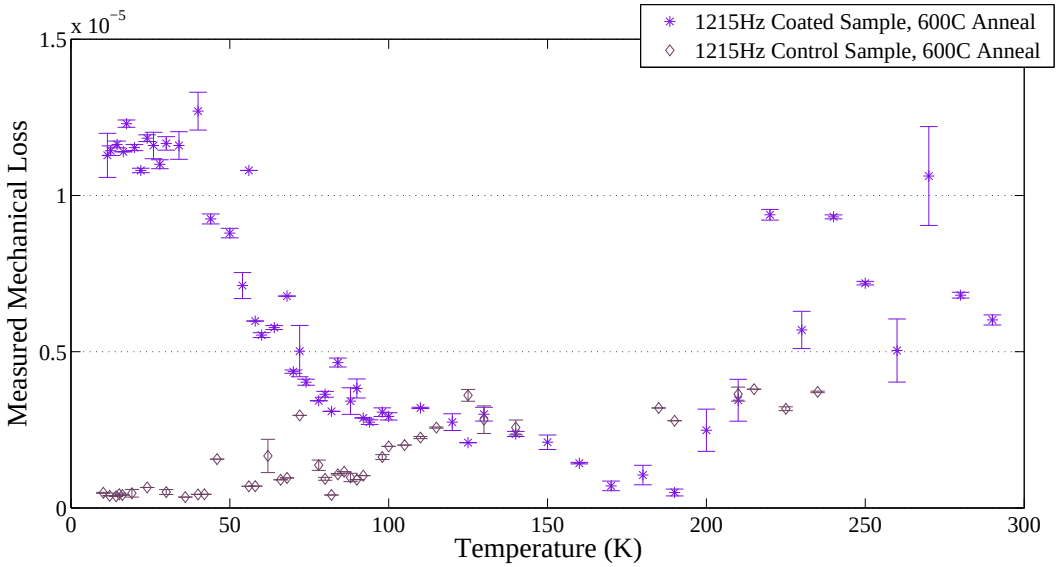

Figure 4.18: The mechanical loss of a silicon cantilever coated with 557.0 ± 3.4nm of ion-beam sputtered silica at 1205Hz and heat-treated at 600^{o}C and an uncoated silicon cantilever at 1215Hz.

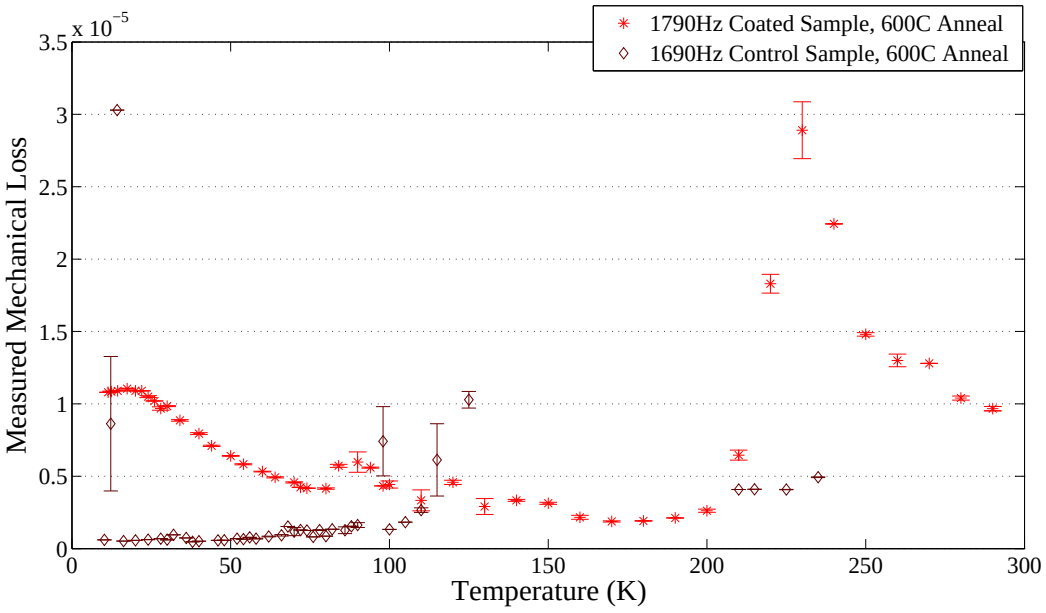

Figure 4.19: The mechanical loss of a silicon cantilever coated with 557.0 ± 3.4nm of ion-beam sputtered silica at 1750Hz and heat-treated at 600^{o}C and an uncoated silicon cantilever at 1750Hz.

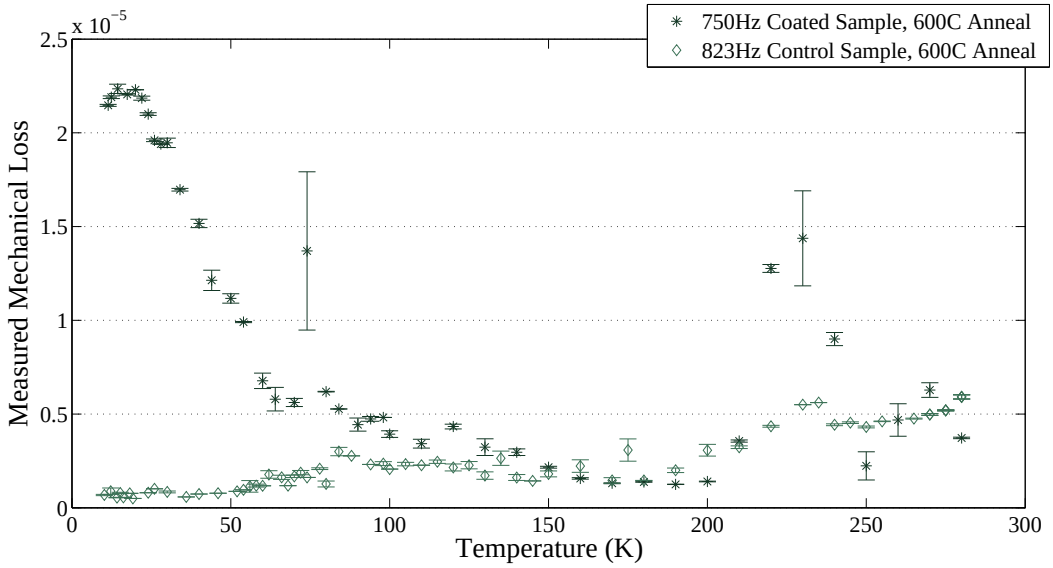

Figure 4.20: The mechanical loss of a silicon cantilever coated with 557.0 ± 3.4nm of ion-beam sputtered silica at 750Hz and heat-treated at 600^{o}C and an uncoated silicon cantilever at 823Hz. This mode is believed to be a torsional mode.

Due to the poor quality of the control data for the 21Hz fundamental mode, the coating loss was calculated using the control data from the equivalent mode of the 300C control sample. For all other modes, the averaged control data shown in Figures 4.14 to 4.20 was spline interpolated to provide estimates of the substrate loss at the temperatures required.

As can be seen from Figures 4.14 to 4.20, the measured loss of the control substrate for each mode was not always lower than the measured loss of the coated sample, leading to unphysical negative coating loss values. These have been omitted from the calculated coating losses in Figures 4.21 to 4.26. The values in Table 4.4 were used to calculate the coating energy ratio. The small temperature dependence of Young's Modulus was not taken into account.

	Silicon	Silica
Property	Value	Value
Young's Modulus	164 ± 3GPa	72GPa
Thickness	$50 \pm 5\mu$m	557.0 ± 3.4nm

Table 4.4: The parameters used to calculate the coating losses for the silica coating heat-treated at 600°C.

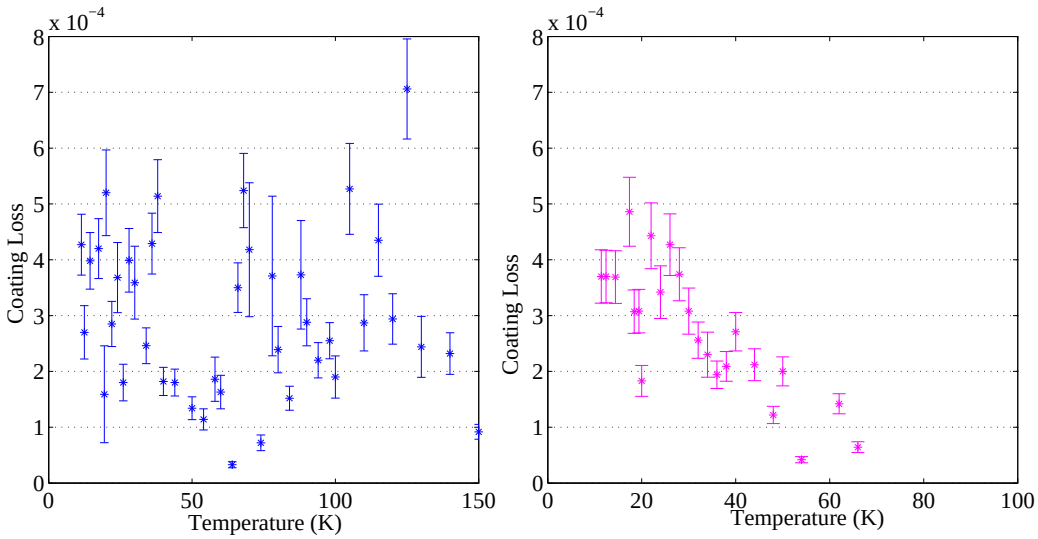

Figure 4.21: The calculated coating loss at 21Hz and 125Hz for the ion-beam sputtered silica coating heat-treated at 600^{o}C .

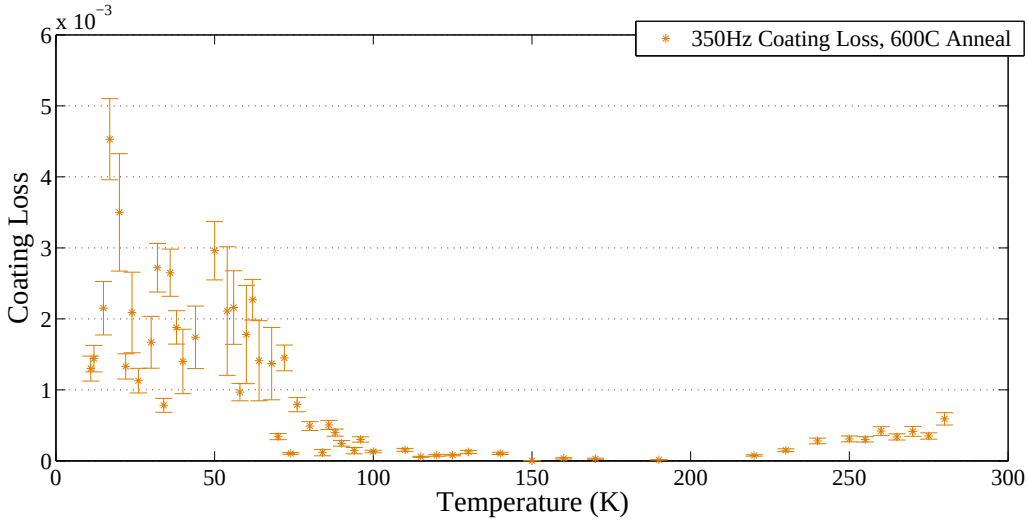

Figure 4.22: The calculated coating loss at 410Hz for the ion-beam sputtered silica coating heat-treated at 600^{o}C .

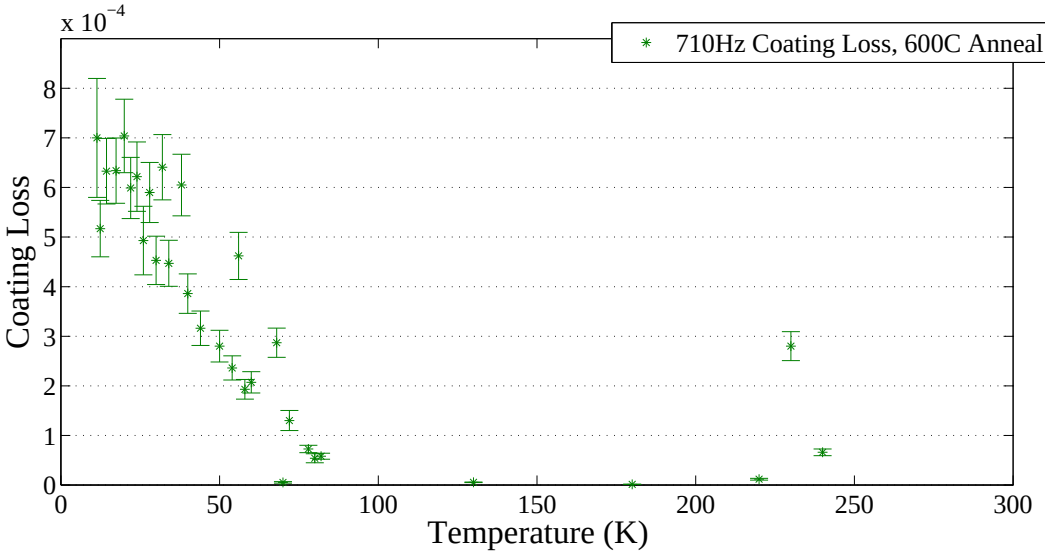

Figure 4.23: The calculated coating loss at 710Hz for the ion-beam sputtered silica coating heat-treated at 600^{o}C .

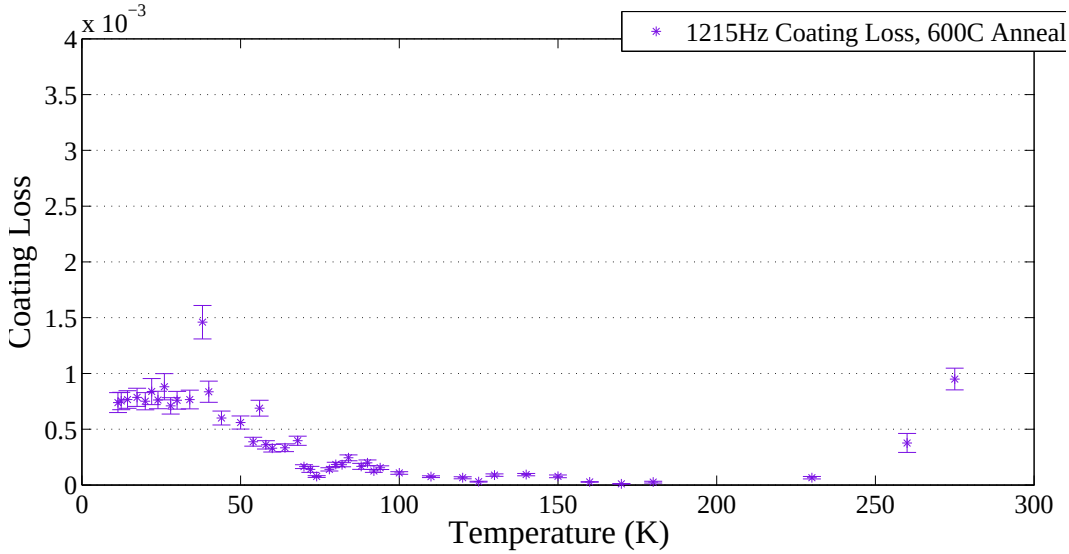

Figure 4.24: The calculated coating loss at 1215Hz for the ion-beam sputtered silica coating heat-treated at 600^{o}C .

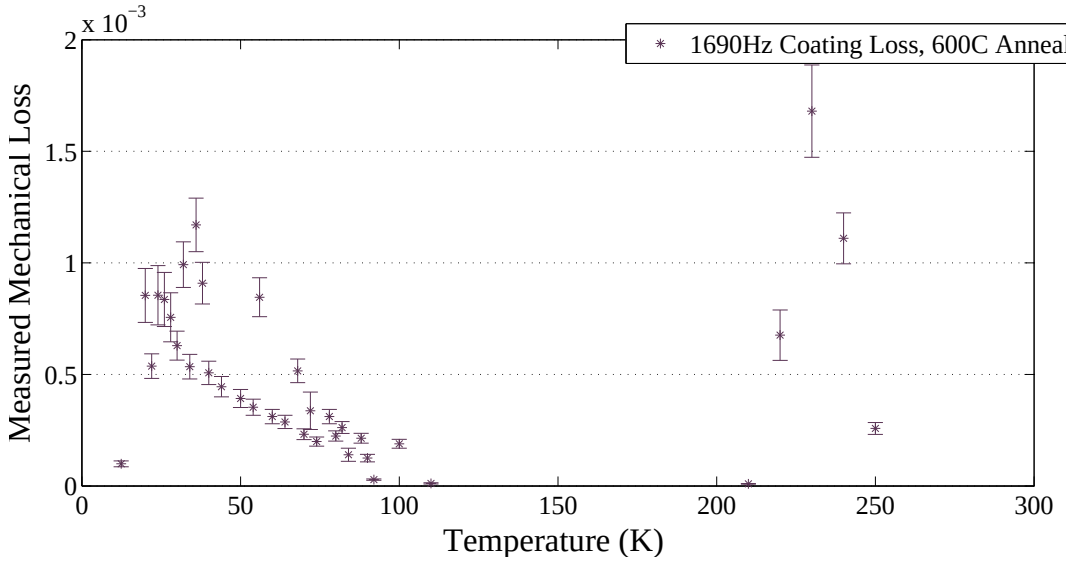

Figure 4.25: The calculated coating loss at 1690Hz for the ion-beam sputtered silica coating heat-treated at 600^{o}C .

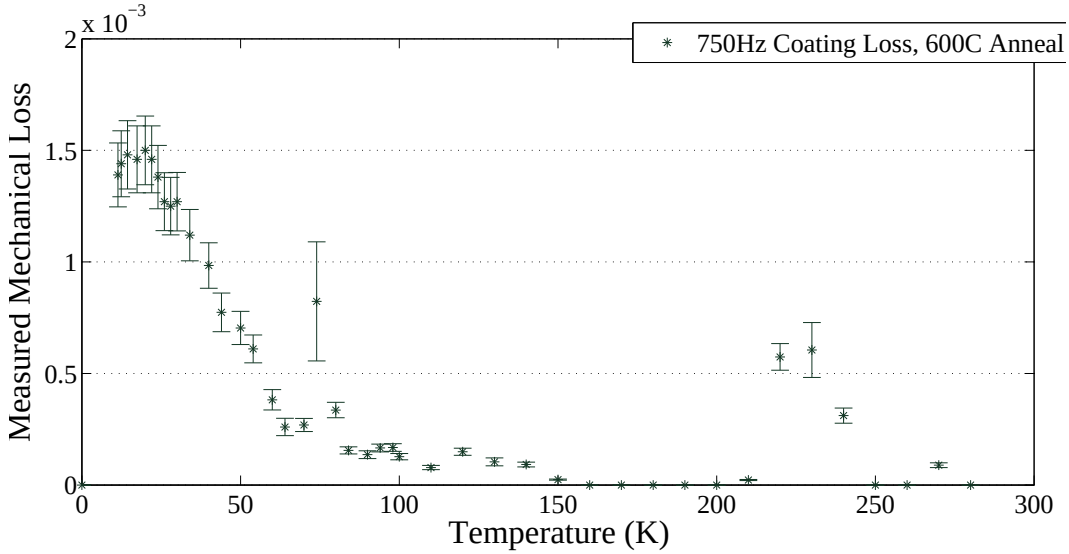

Figure 4.26: The calculated coating loss at 750Hz for the ion-beam sputtered silica coating heat-treated at 600^{o}C .

As the values were calculated from measurements with a high degree of scatter, the coating losses of the first and second modes do not show any structure. The third mode has coating losses between 1×10^{-3} and 3×10^{-3} below 100K but does not show a low temperature peak. The coating losses of the fourth, fifth and sixth modes and also the torsional mode at 750Hz increase below 100K and exhibit low temperature peak features with maximum coating losses of around 1×10^{-3}. These modes also show a possible loss peak feature at around 250K. Polynomials were used to fit curves to the low temperature peaks in the measured loss data, using the same method described in Section 4.3. Peaks were found for four of the seven measured modes, using the curves as shown in Figure 4.27.

Mode	Frequency	Peak Loss Temperature
1	21Hz	no fit
2	125Hz	$(17.78 \pm 0.28)K$
3	410Hz	no fit
4	710Hz	$(17.76 \pm 0.06)K$
5	1215Hz	no fit
6	1690Hz	$(15.95 \pm 0.47)K$
T	750Hz	$(16.03 \pm 0.35)K$

Table 4.5: The resonant frequency and the temperatures of peak loss for the measured modes of the 600^{o}C heat-treated silica coating.

Plotting $\ln(\omega)$ against $1/T$ for the low temperature peaks of the sample heat-treated at 600^{o}C did not show any strong linear relationship, as illustrated in Figure 4.28. As no line could be fitted to the peak temperature data, no claim can be made as to whether the relaxation process causing the low temperature loss peaks is described by the Arrhenius equation can be made.

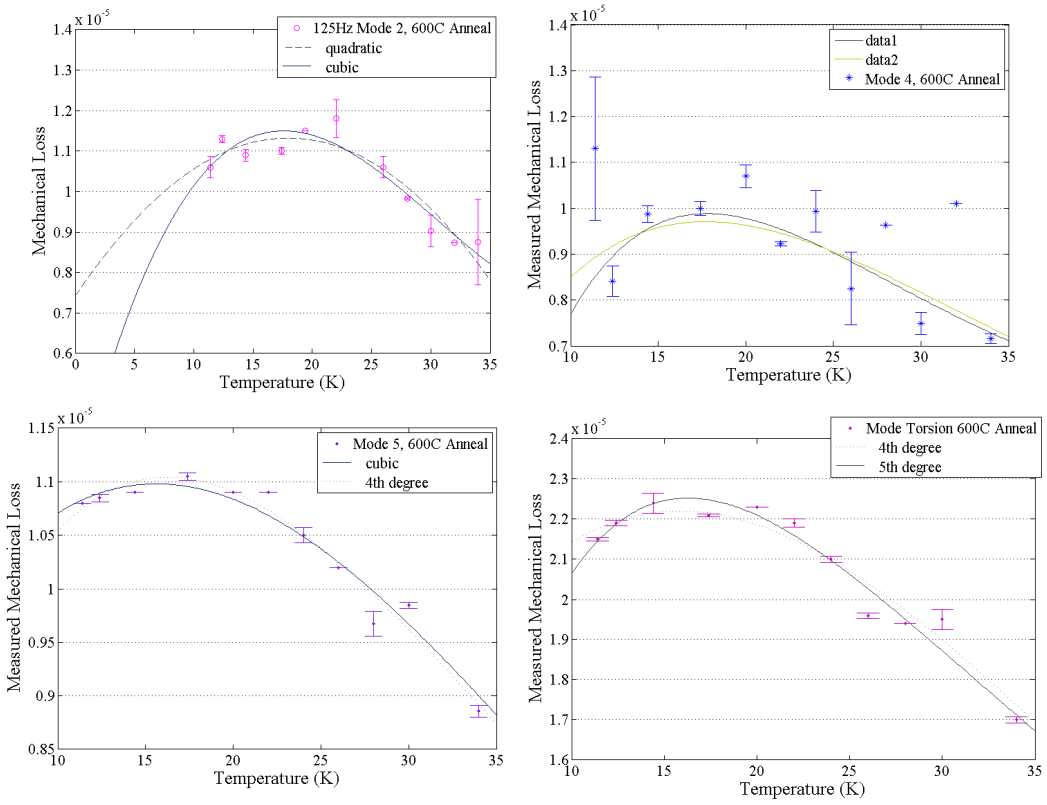

Figure 4.27: The fitting curves used to determine the temperature of peak loss for the four viable modes of the 600°C heat-treated silica coated silicon cantilever.

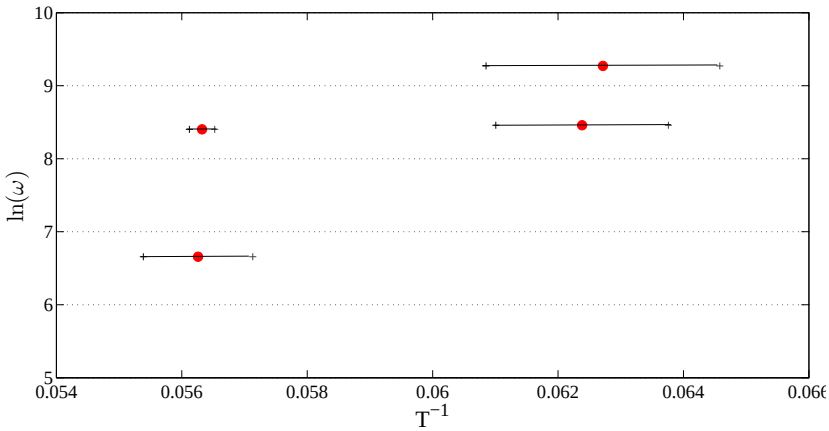

Figure 4.28: Arrhenius plot of inverse peak temperature against the logarithmic angular frequency of the mode of the silica-coated silicon cantilever annealed at 600^{o}C .

4.3 Samples heat-treated at 800C post deposition

The coated and control sample were measured together for the duration of the process. The oxide layer on both the coated and uncoated samples was around ten times thicker than that seen on the samples heat-treated at 600°C, which may have grown during the 800^{o}C heat-treated process. According to the Deal and Grove model of silicon oxidation, around 90nm of silicon dioxide may be formed during 24 hours of heat-treatment at 800^{o}C in a dry oxygen atmosphere. The oxide growth rate scales linearly with the partial pressure of oxygen so a heat-treatment at 800^{o}C in air could be expected to account for the increase in oxide thickness [90].

A large loss peak was observed in the data from the coated sample at around 250K across modes 2-5. The level of mechanical loss in the data from the uncoated control sample also increased at around 200K. These increases are thought to be instances of the thermal cycling anomaly as described in Chapter 3, Section 3.5.2.

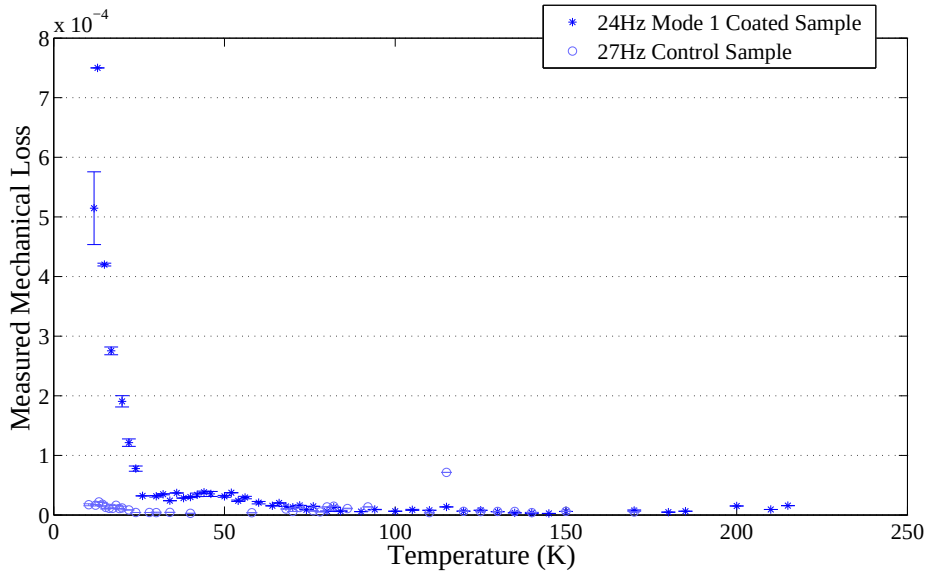

Figure 4.29: The mechanical loss of a silicon cantilever coated with 557.0 ± 3.4nm of ion-beam sputtered silica at 24Hz and heat-treated at 800^oC and an uncoated silicon cantilever at 27Hz.

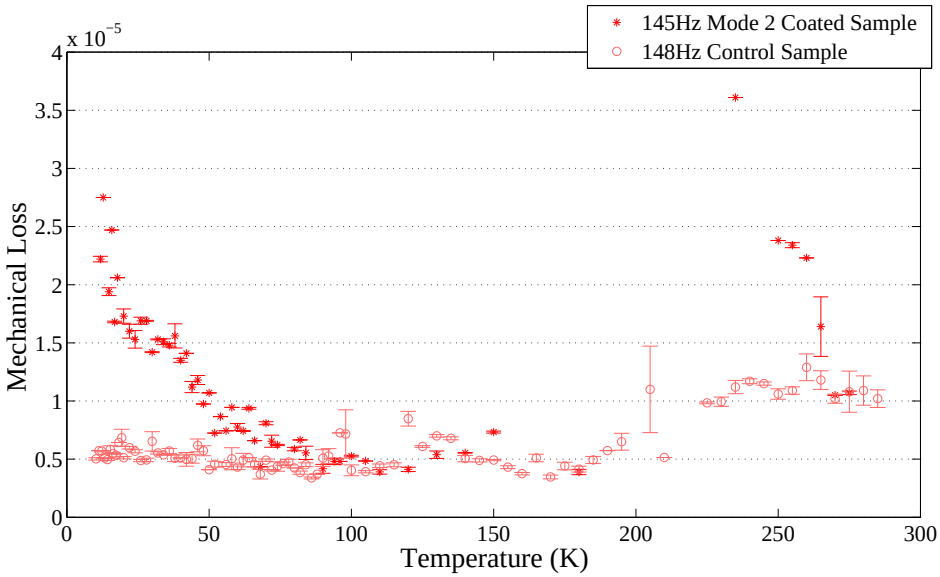

Figure 4.30: The mechanical loss of a silicon cantilever coated with 557.0 ± 3.4nm of ion-beam sputtered silica at 145Hz and heat-treated at 800^oC and an uncoated silicon cantilever at 148Hz.

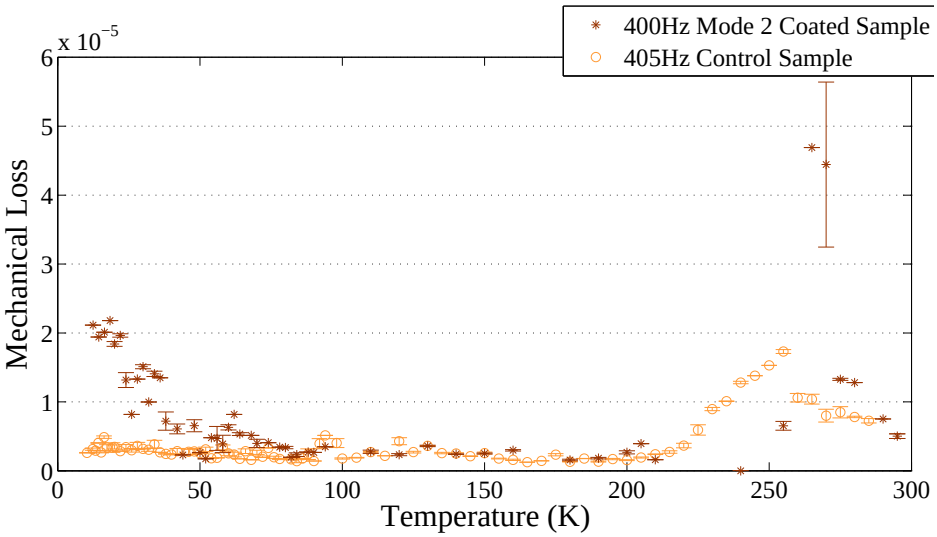

Figure 4.31: The mechanical loss of a silicon cantilever coated with 557.0 ± 3.4nm of ion-beam sputtered silica at 400Hz and heat-treated at 800^oC and an uncoated silicon cantilever at 405Hz.

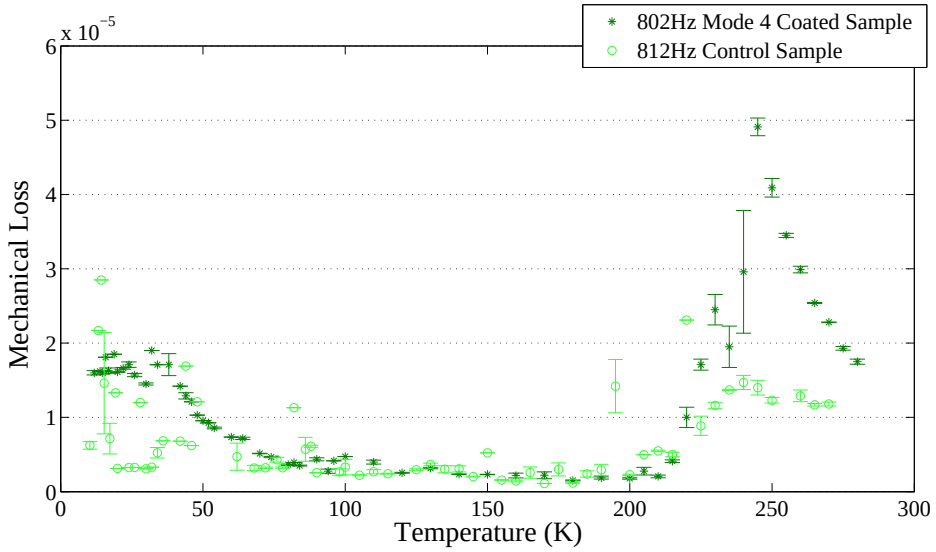

Figure 4.32: The mechanical loss of a silicon cantilever coated with 557.0 ± 3.4nm of ion-beam sputtered silica at 802Hz and heat-treated at 800^oC and an uncoated silicon cantilever at 812Hz.

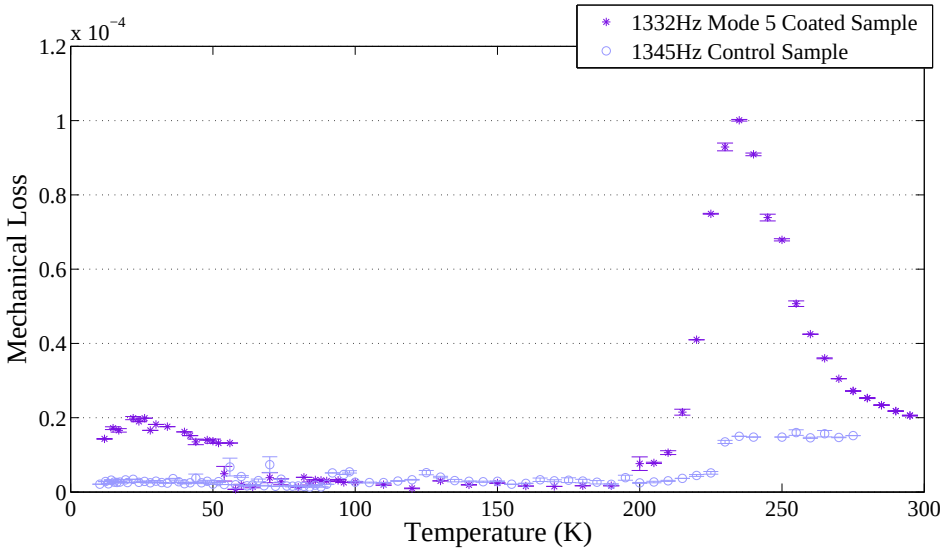

Figure 4.33: The mechanical loss of a silicon cantilever coated with 557.0 ± 3.4nm of ion-beam sputtered silica at 1332Hz and heat-treated at 800^{o}C and an uncoated silicon cantilever at 1345Hz.

	Silicon	Silica
Property	Value	Value
Young's Modulus	164 ± 3GPa	72GPa
Thickness	$50 \pm 5\mu$m	557.0 ± 3.4nm

Table 4.6: The parameters used to calculate the coating losses for the 600°C heat-treated silica coating.

To calculate the energy ratio, the values for the Young's moduli and thicknesses shown in Table 4.6 were used. The small temperature dependence of Young's Modulus was not taken into account. For the temperatures where the differences between the coated and control mechanical loss data resulted in an unphysical negative value for the coating loss, the data has been omitted.

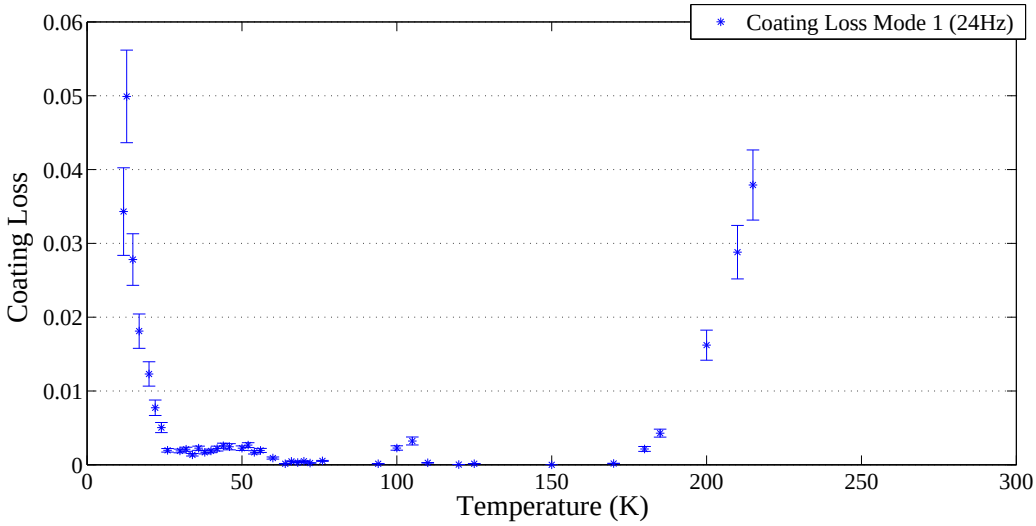

Figure 4.34: The calculated coating loss at 24Hz for the ion-beam sputtered silica coating heat-treated at 800°C .

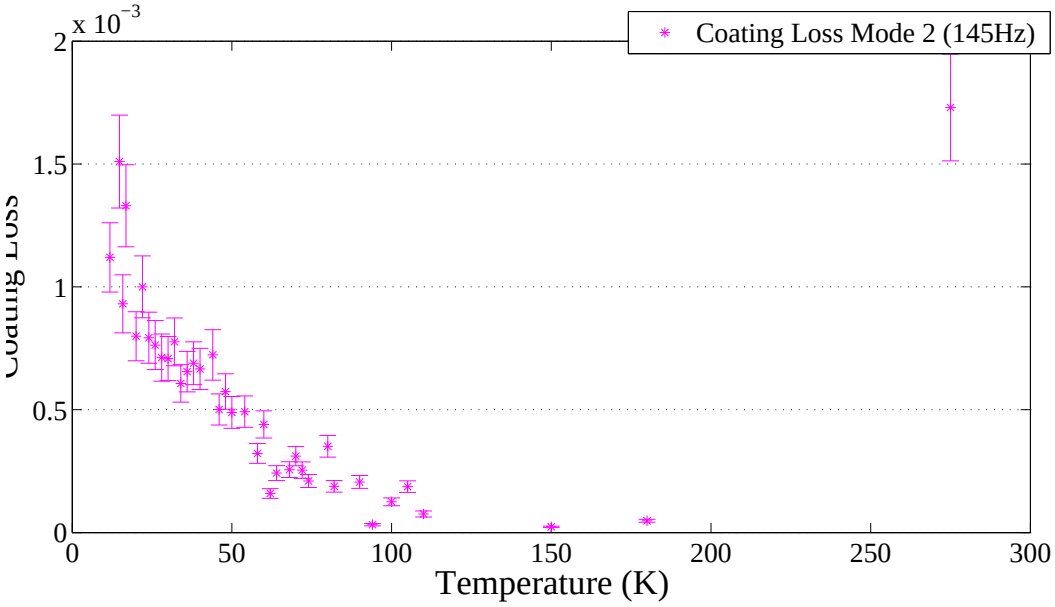

Figure 4.35: The calculated coating loss at 145Hz for the ion-beam sputtered silica coating heat-treated at 800^{o}C .

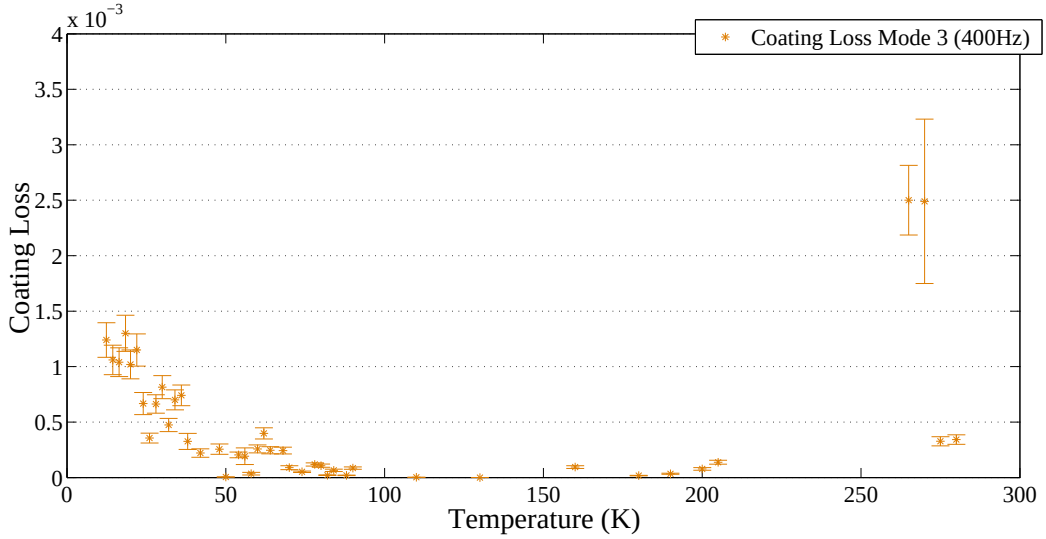

Figure 4.36: The calculated coating loss at 400Hz for the ion-beam sputtered silica coating heat-treated at 800^{o}C .

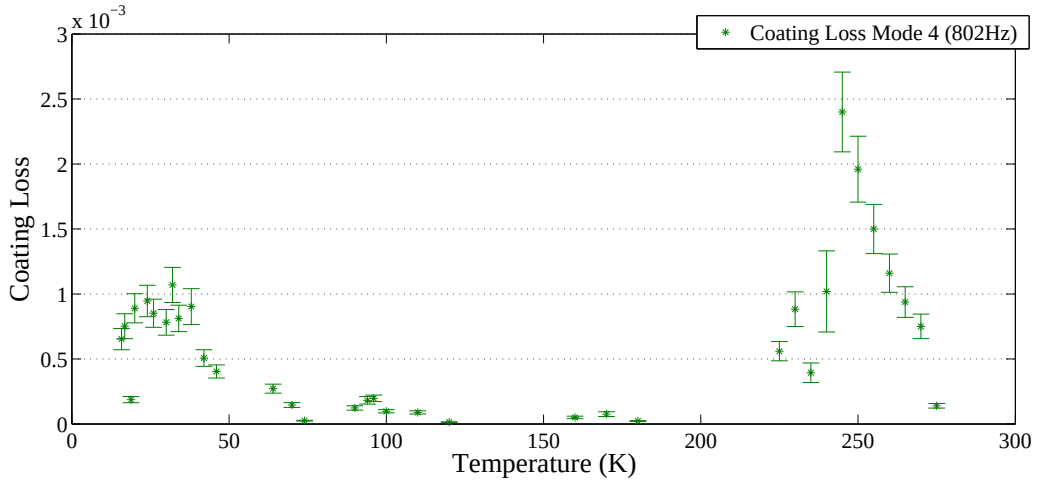

Figure 4.37: The calculated coating loss at 802Hz for the ion-beam sputtered silica coating heat-treated at 800^{o}C .

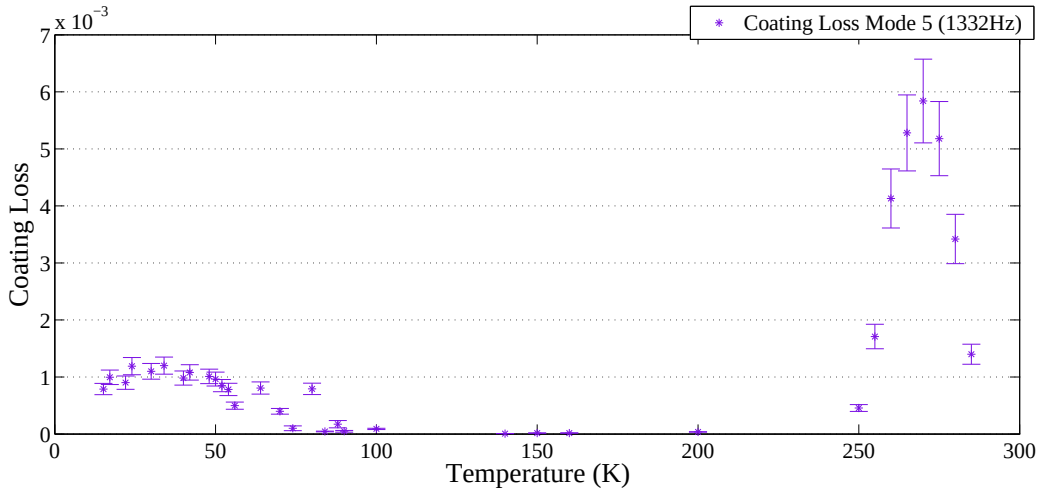

Figure 4.38: The calculated coating loss at 1332Hz for the ion-beam sputtered silica coating heat-treated at 800^{o}C .

The coating loss at the fundamental mode (24Hz) rose to $(4.99 \pm 0.63) \times 10^{-2}$ at 12K, although this is likely to be a recurrence of the low temperature anomaly. A small feature occurs at around 50K, which could be an intrinsic feature of the coating material. The rapid increase in calculated coating loss at the top of the temperature range is due to the difficulty of interpolating the substrate loss accurately from the small number of usable data points in that range.

The second and third modes showed increasing, but scattered coating loss values below 77K and no peaks could be discerned. The coating loss of the second mode at 11K was $(1.12 \pm 0.14) \times 10^{-3}$ and the loss at 12.4K for the third mode was $(1.24 \pm 0.16) \times 10^{-3}$. A low temperature peak feature was visible in the fourth and fifth modes, with a peak loss of around 1×10^{-3}. These modes also showed very strong loss peaks above 200K, with the maximum loss of $(2.40 \pm 0.31) \times 10^{-3}$ for the fourth mode occurring at 240K, and the maximum loss of $(5.83 \pm 0.74) \times 10^{-3}$ for the fifth mode occurring at 270K. These features are likely to be connected to the thermal cycling anomaly as described in Chapter 3, Section 3.5.2.

No clear low temperature peaks could be fitted for the first, second or third modes, although the loss did increase below 77K. The fourth and fifth modes contained broad, shallow low temperature loss peaks which could be fitted to polynomials. The temperatures of peak loss for these two modes were calculated as in the two previous samples, by locating the maximum of the fitted polynomial function. Two temperature points were not sufficient to perform the linear regression to obtain the parameters of the Arrhenius equation for this dataset. If the possible feature at around 43K in the fundamental mode coating data is included to give a third

Mode	Frequency	Peak Loss Temperature
1	24Hz	no fit
2	145Hz	no fit
3	400Hz	no fit
4	802Hz	$(27.08 \pm 1.37)K$
5	1332Hz	$(23.34 \pm 0.18)K$

Table 4.7: The resonant frequency and the temperatures of peak loss for the measured modes of the 800^{o}C heat-treated silica coating.

point, the line of best fit given by this data results in a negative value for the height of the potential energy barrier in the hypothetical two-level system, which would be unphysical.

4.4 Analysis, Dissipation Mechanisms and Further Investigations

Figures 4.39, 4.40 and 4.41 show the measured mechanical losses and the calculated coating losses of the fourth and fifth bending modes over the three heat-treatment temperatures. From these plots, the low temperature loss feature can be seen to develop through the levels of heat-treatment. The details of the graphs of coating loss in Figure 4.41 show that the low temperature peak is widest when the coating is heat-treated at 300^{o}C and that the coatings heat-treated at 600^{o}C and 800^{o}C had peaks with similar widths. The magnitude of the peak loss may also increase slightly with the increasing heat-treatment temperature, but the size of the coating loss error bars places limits on what can be inferred.

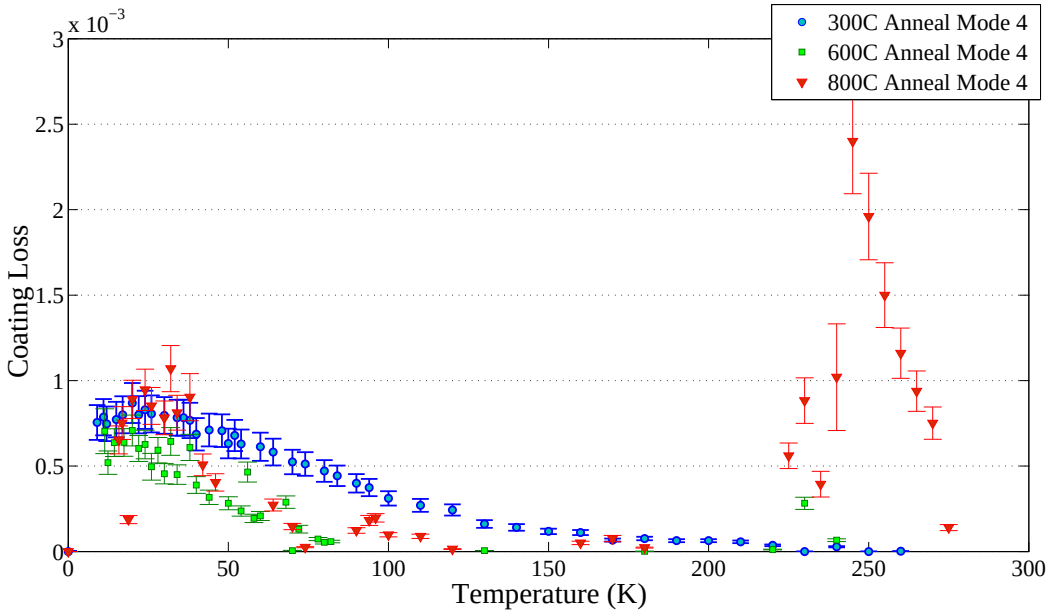

Figure 4.39: The calculated mechanical losses for the fifth bending mode of the silica coating heat-treated at 300°C, 600°C and 800°C .

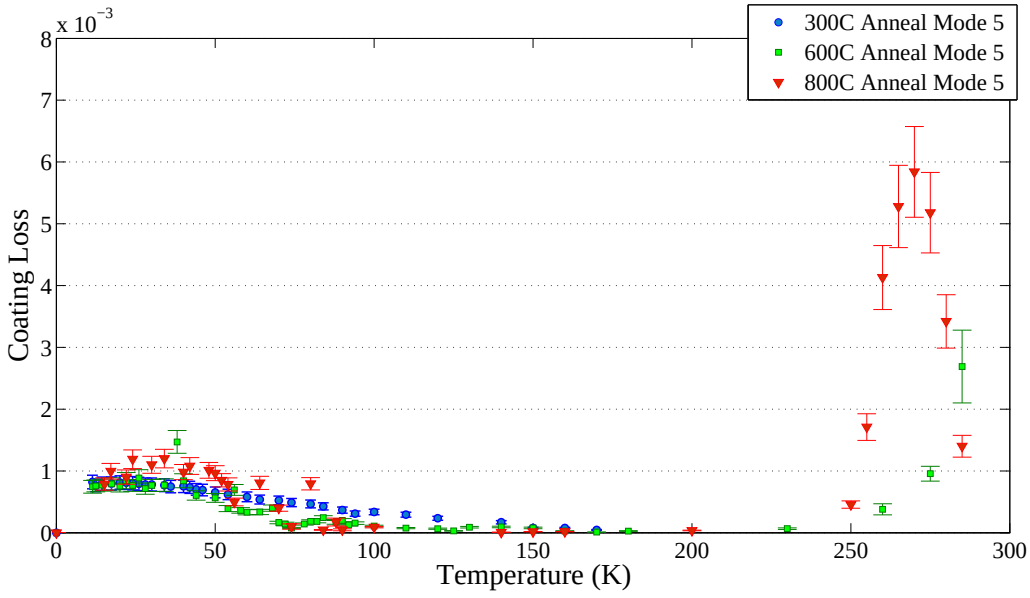

Figure 4.40: The calculated mechanical losses for the fifth bending mode of the silica coating heat-treated at 300°C, 600°C and 800°C .

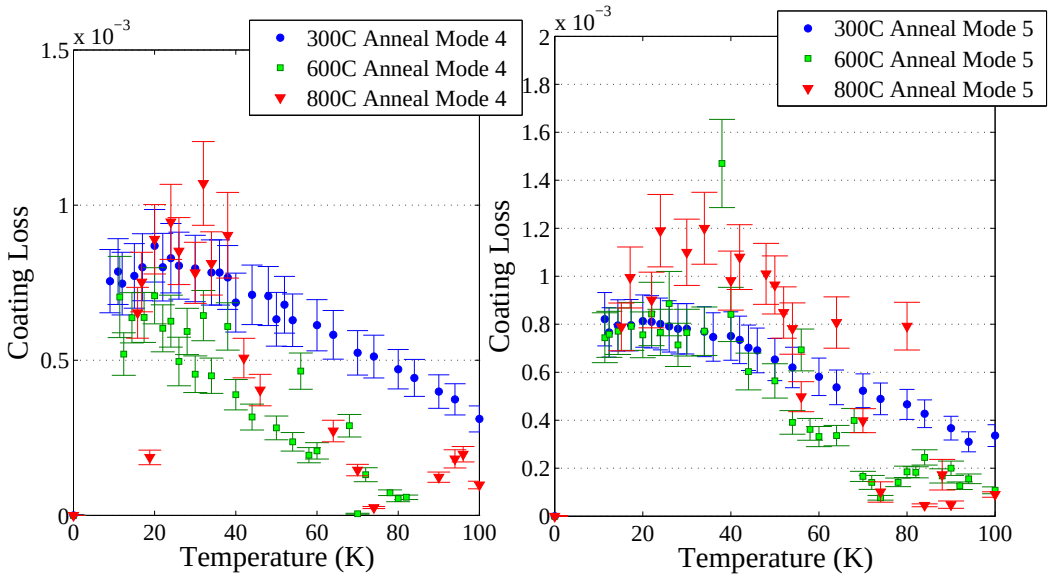

Figure 4.41: Details of Figures 4.39 and 4.40 between 0-100K.

If the model of the relaxation process causing the low temperature peak as a two-level asymmetric potential well with a distribution of barrier heights is a good representation of the real system, and the width of the relaxation peak is a good proxy measurement for the width of the distribution of barrier heights, then this data suggests that annealing an ion-beam sputtered silica coating above 300^{o}C causes a narrowing of the barrier height distribution.

In Figures 4.39 and 4.40, the high temperature thermal cycling feature can be seen most prominently in the data from the coating heat-treated at 800^{o}C . The same feature appears only as a slight bump in the data from the coating heat-treated at 600^{o}C and is not at all noticeable in the data from the coating heat-treated at 300^{o}C .

4.5 Conclusion

This work has been successful in showing the development of loss features with increasing annealing temperature and has produced Arrhenius parameters of (17.3 ± 2.3)meV for H_b, the barrier energy, and a value of $(8.86 \pm 0.43) \times 10^7 s^{-1}$ for the relaxation rate, τ for the coating annealed at 300^{o}C . This value is significantly lower than the values of (54.4±5.5)meV and 44meV from previous work by Martin [51] and Anderson and Bommell respectively [75]. This implies that there is a significant structural difference in the amorphous silica network when heat-treated at 300^{o}C and 600^{o}C or that there is some unknown error in the mechanical loss measurements which were used to locate the temperature of the maxima of the Debye peaks. The change in shape of the Debye peak between the 300^{o}C heat-treated silica and the silica treated at higher temperatures indicates that heat-treatment may narrow the distribution of bond angles in the amorphous silica network, which could be the mechanism responsible for the change in barrier energy height.

Repeat measurements of the samples, concentrating particularly on tracing Debye peaks of each mode with a finer temperature resolution would enable the Arrhenius equation parameters for the material treated at each temperature to be extracted. A repeat measurement of the Debye peaks in the fundamental mode of each sample and the location and measurement of Debye peaks in higher frequency modes will allow the Arrhenius factors to be found with higher confidence.

Chapter 5

The Effect of Post-deposition Heat Treatment On The Mechanical Loss of An Ion-Beam Sputtered Hafnia Film

As described in Chapter 3, characterisation of the temperature dependence of mechanical loss in materials which are not currently used in gravitational wave detector mirror coatings may provide information on the general model for dissipation in amorphous oxides, and could also lead to a new candidate material for multilayer coatings in advanced detectors. Hafnia (HfO_2) was selected for characterisation as it is a commonly deposited dielectric coating material with a higher refractive index than tantala. A higher refractive index means that a thinner layer is required to produce the required $\lambda/4$ effective thickness. If the amount of lossy material used in a mirror can be reduced, the overall level of thermal noise will be

reduced.

5.1 Initial Measurements of the Mechanical Loss of a Hafnia Coating Between 10-300K.

The sample used in these measurements was coated by the Materials Science and Engineering Division of CSIRO [80] using the same ion-beam-assisted sputtering process used to produce the amorphous tantala used in previous experiments and the silica coatings measured in Chapter 4. The coating was deposited upon a 40mm x 10mm x 57.2μm cantilever substrate, which was etched from a silicon wafer by colleagues at Stanford University. After the coating was deposited, the sample was placed in an oven and heat treated in air at 300^{o}C for 24 hours, then left to cool naturally to room temperature.

The mechanical losses of the first five pure bending modes of the cantilever were measured between 10K and 300K, using the cryogenic apparatus described in Chapter 3. The method remained as described in Chapter 3, but the ringdown measurements, data taking and temperature settings were performed manually. The data is shown in Figures 5.2 to 5.6.

Existing measurements of the biaxial modulus $\left(B = \frac{Y}{1-\nu}\right)$, of hafnia [91] where Y is Young's Modulus and ν is Poisson's ratio) obtained from studies of thermally induced bending of substrates to which thin films were applied show that the form and method of growth of hafnia can cause variation in the mechanical properties.

In the referenced study by Thielsch et al, the biaxial modulus of bulk monoclinic crystalline HfO_2 was quoted as 410GPa, while a 272nm thick film of amorphous ion-beam-sputtered HfO_2 was found to have a biaxial modulus of 305GPa. Under the assumption that the Poisson's ratio of the thin film HfO_2 is the same as the value of 0.298 for bulk HfO_2 , then amorphous thin film hafnia would be found to have a Young's Modulus of 220GPa. However, if the change in form from monoclinic crystalline bulk hafnia to thin film amorphous hafnia is sufficient to significantly reduce the Young's Modulus, the Poisson's ratio may also be altered. The value used in the coating loss calculations in this chapter is 220GPa, as this value was calculated using measurements of a sample similar to that used in this chapter.

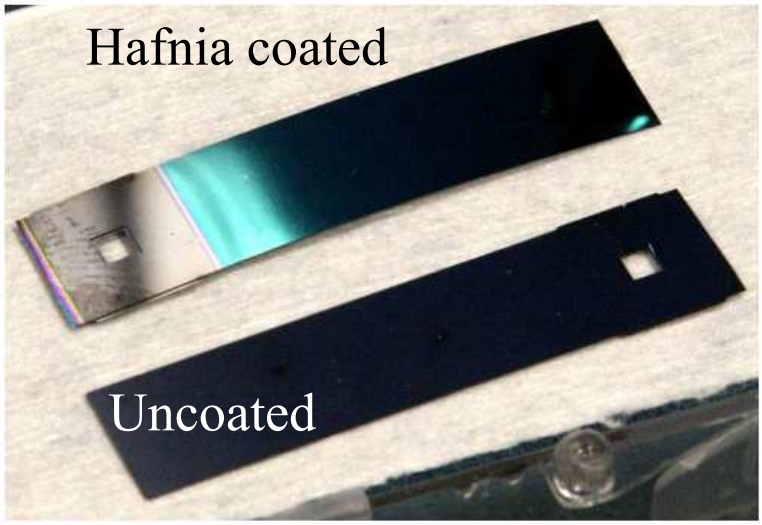

Figure 5.1: The hafnia coated and uncoated silicon cantilever samples, with a visible degree of curvature present in the coated sample.

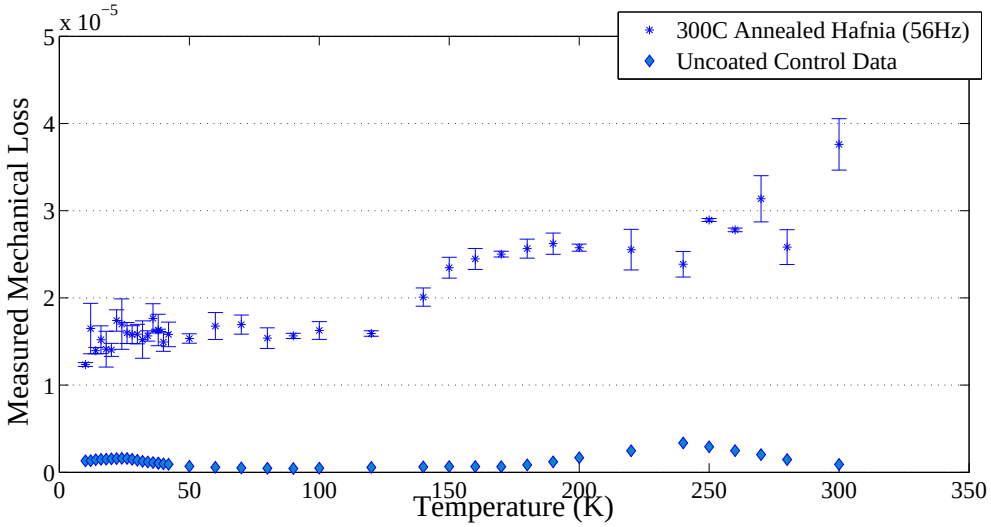

Figure 5.2: The measured mechanical loss of the 56Hz bending mode of a hafnia coated silicon cantilever and interpolated control data of an uncoated silicon cantilever.

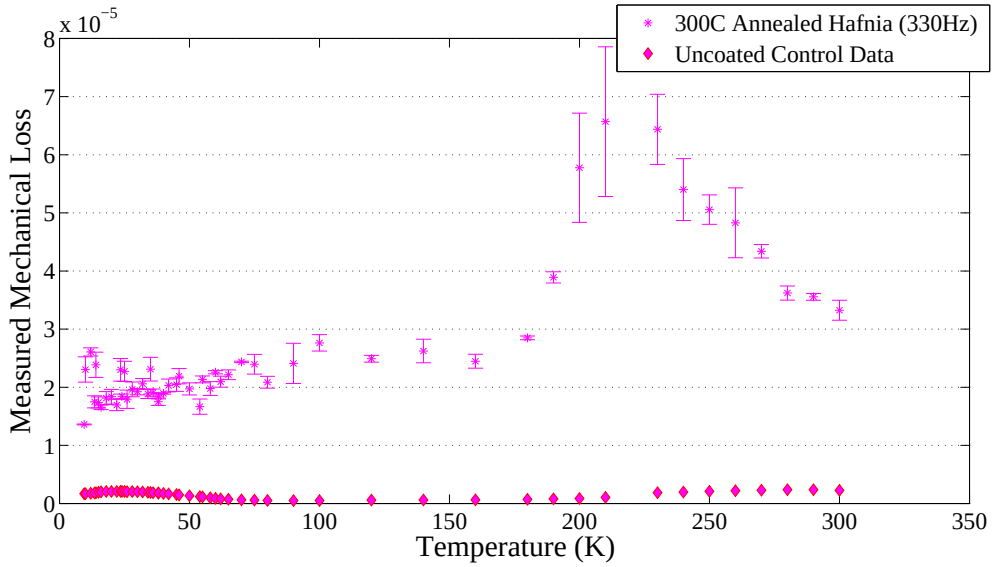

Figure 5.3: The measured mechanical loss of the 330Hz bending mode of a hafnia coated silicon cantilever and interpolated control data of an uncoated silicon cantilever.

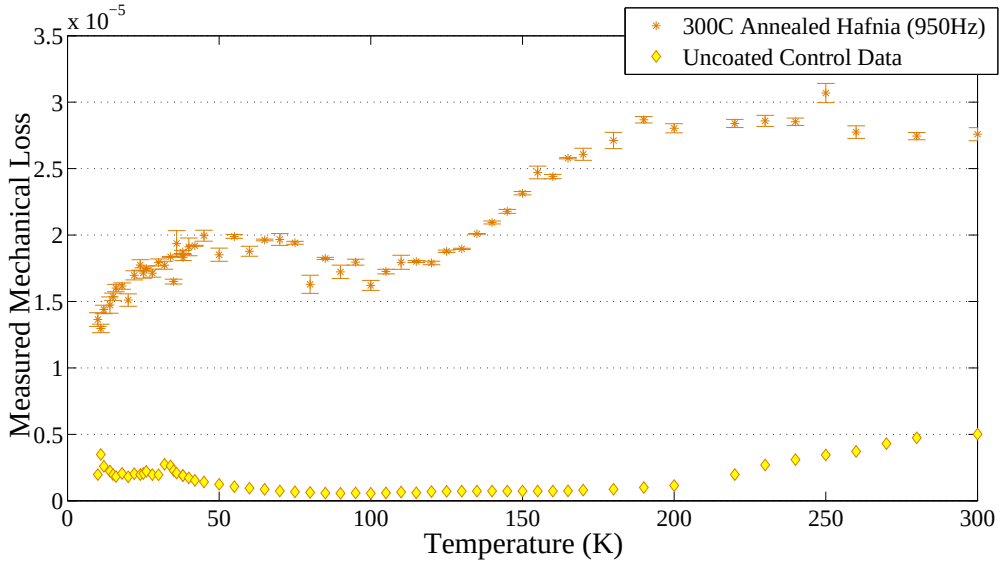

Figure 5.4: The measured mechanical loss of the 950Hz bending mode of a hafnia coated silicon cantilever and interpolated control data of an uncoated silicon cantilever.

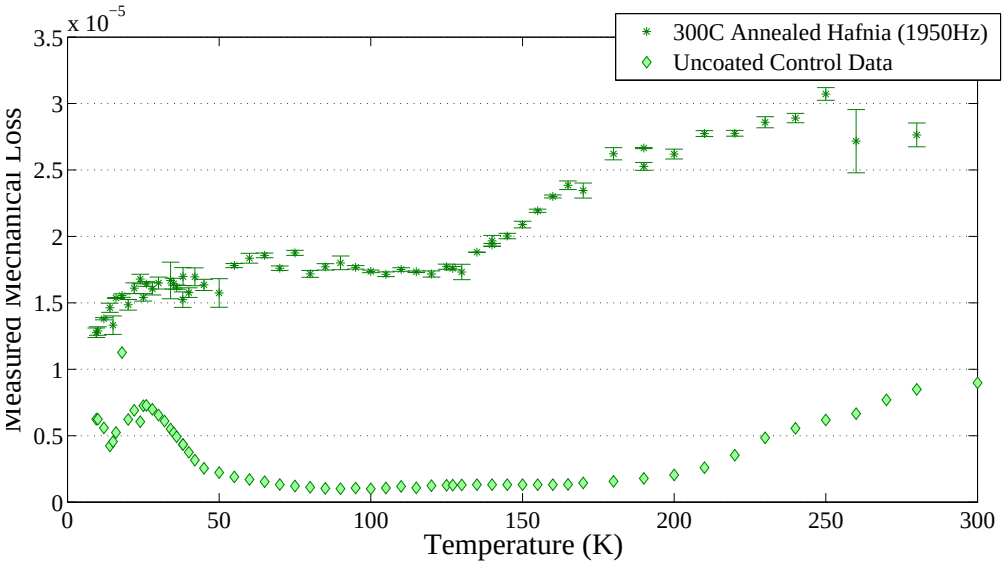

Figure 5.5: The measured mechanical loss of the 1950Hz bending mode of a hafnia coated silicon cantilever and interpolated control data of an uncoated silicon cantilever.

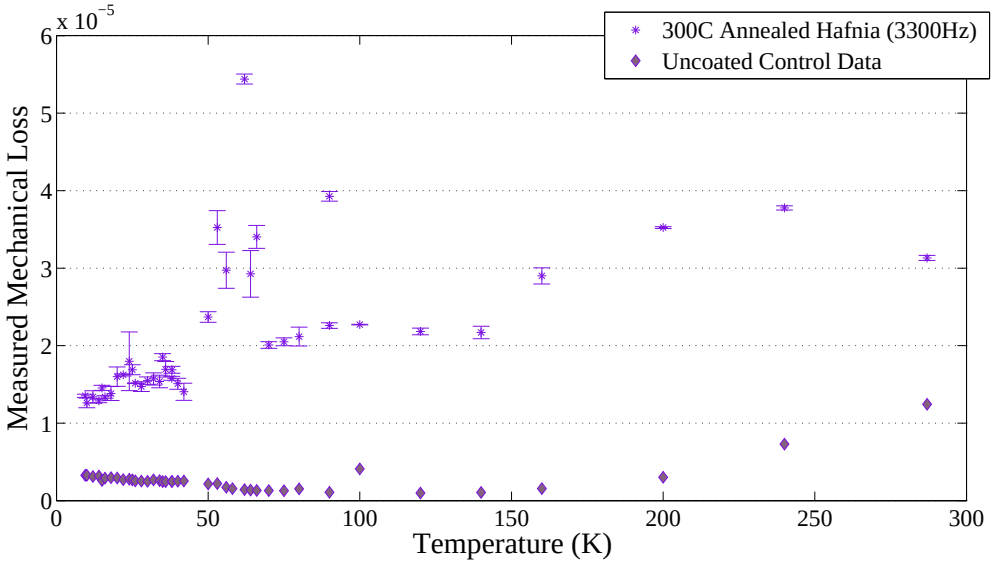

Figure 5.6: The measured mechanical loss of the 3300Hz bending mode of a hafnia coated silicon and interpolated control data of an uncoated silicon cantilever.

	Silicon	Hafnia
Property	Value	Value
Young's Modulus	164 ± 3GPa	220GPa
Thickness	$59.2 \pm 5.0\mu$m	512 ± 15nm

Table 5.1: Values used to calculate the ratio of strain energy stored in the 300^oC heat-treated hafnia coating to the total strain energy.

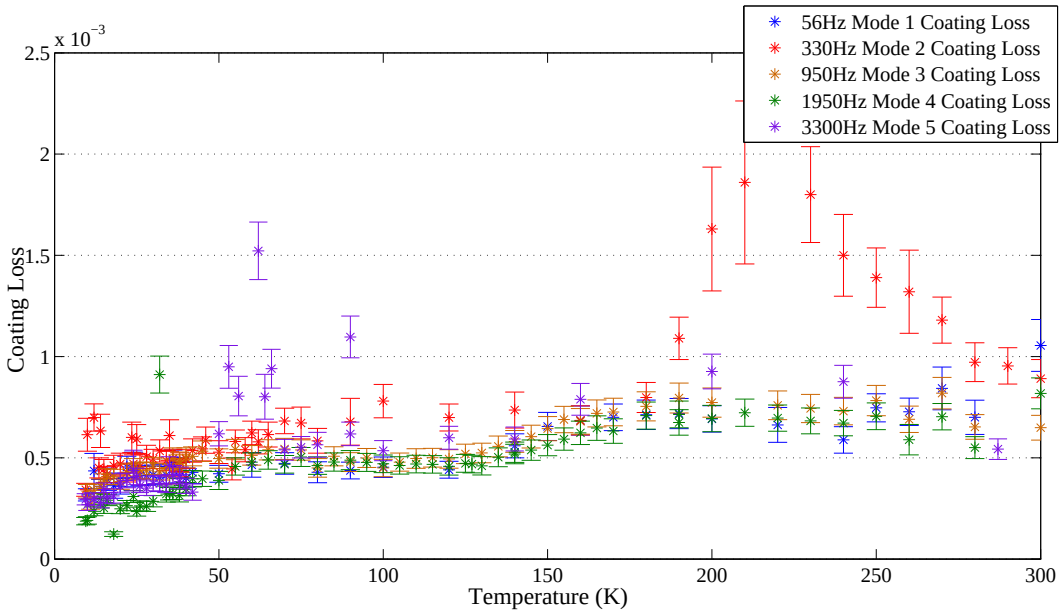

Figure 5.7: The coating loss of a 512nm thick hafnia coating as calculated from measurements of the first five bending modes, using $Y_{hafnia} = 220$GPa.

The main features of the temperature dependence of the mechanical loss of the amorphous hafnia coating material appear to be two broad, low peaks, one centered at around 60K and another at around 200K. A peak appears in the data from the 330Hz mode, and is not thought to be an intrinsic feature of the material, but an occurrence of the thermal cycling feature as described in Chapter 3. The mechanical loss measurements which make up the 330Hz series were only available from the final thermal cycling before the sample was reclamped - as the size of the thermal cycling feature increased with repeated thermal cycling and the feature was 'reset' by reclamping, it would follow that the 330Hz mode was worst affected.

If the two-level system model of mechanical loss discussed earlier is valid for all amorphous oxides, then the loss of hafnia as a function of temperature might be expected to contain similar features to those observed in studies of the loss of tantala as a function of temperature. In this case, the peak at lower temperatures could be a Debye peak, representing a thermally activated relaxation process between two states that possess different energy levels separated by a potential barrier. By fitting the data between 10-100K to polynomial curves using the method described in Chapter 4, the temperatures at which the low temperature loss peaked were found to be (63.6 ± 0.9)K for the 950Hz mode and (85.2 ± 9.0)K for the 1950Hz mode.

As the hafnia coating had been heat-treated at 300^{o}C , and it is known that amorphous hafnia films recrystallise readily at these temperatures, it was necessary to assess the structure of the coating. The characterisation of tantala coatings [51] suggested that large mechanical loss features near room temperature may be as-

sociated with developing levels of polycrystallinity.

In order to investigate levels of polycrystallinity in the studied sample, electron microscopy and electron diffraction imaging was performed by Riccardo Bassiri, a Glasgow colleague. Figure 5.9 shows a section through a multilayer hafnia/silica coating deposited by the same supplier as the hafnia cantilever sample. The multilayer coating was sliced and polished into a thin section, and an ion beam was used to mill a hole in the section to allow electron microscopy. Figure 5.9 is an image of the hafnia and silica layers closest to the milled hole. In the image, some regions in the hafnia layer appeared to show granularity indicating regions of polycrystallites, especially those close to the hole edge. If the polycrystallisation was a result of the 300^{o}C heat-treatment, then it is likely that the coating on the measured cantilever is also partially polycrystalline. It is possible that the polycrystallisation observed in the electron micrograph may have been exacerbated by the sample preparation methods.

Figure 5.10 shows that the electron diffraction pattern of the hafnia coating material is a mixture of diffuse rings, which are produced by the diffraction of electrons through an amorphous material and can be used to calculate average bond lengths in the material, and diffraction spots which are produced by the diffraction of electrons by crystalline material. These images show that the hafnia coating material heat-treated at 300^{o}C had begun the transition from an amorphous state to polycrystallinity.

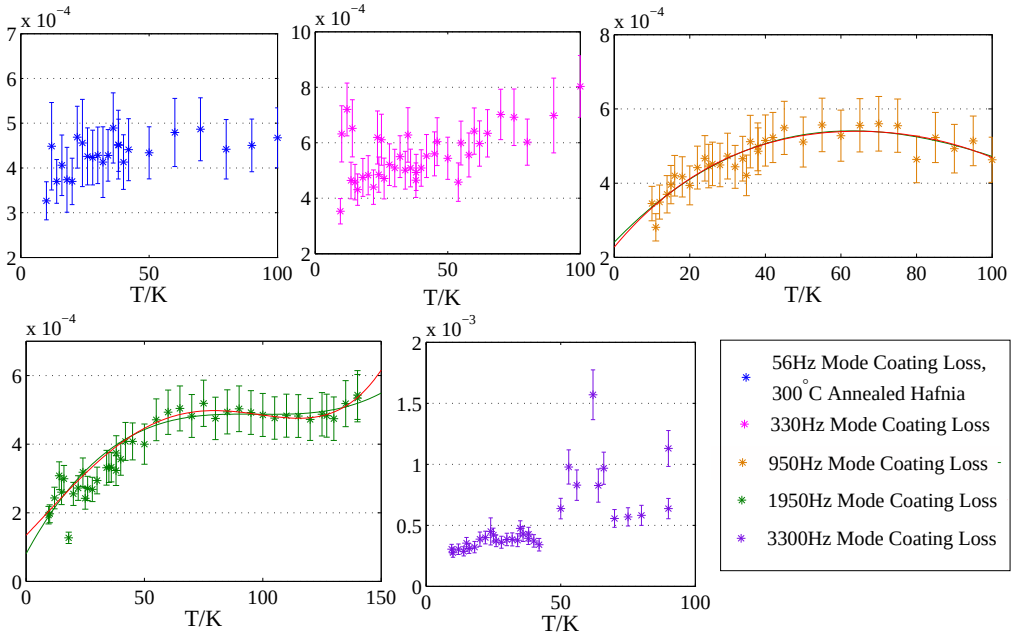

Figure 5.8: Details of the plots shown in Figure 5.7 between 10K and 100K, showing the polynomials used in curve fitting.

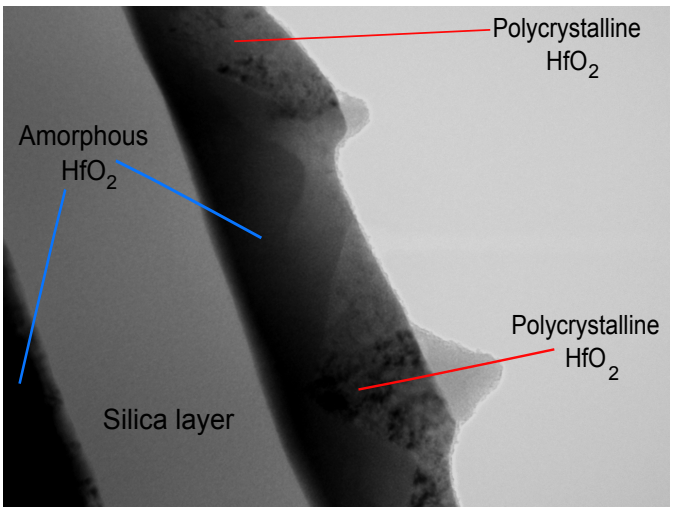

Figure 5.9: Electron micrograph showing a section through a multilayer hafnia/silica coating heat-treated at 300^{o}C . The dark bands show hafnia. Solid grey in the hafnia regions show amorphous hafnia and speckled dark and light grey regions show hafnia which has recrystallised. The light grey band is a silica layer and the lightest region is the hole at the centre of the prepared sample. Image by R. Bassiri.

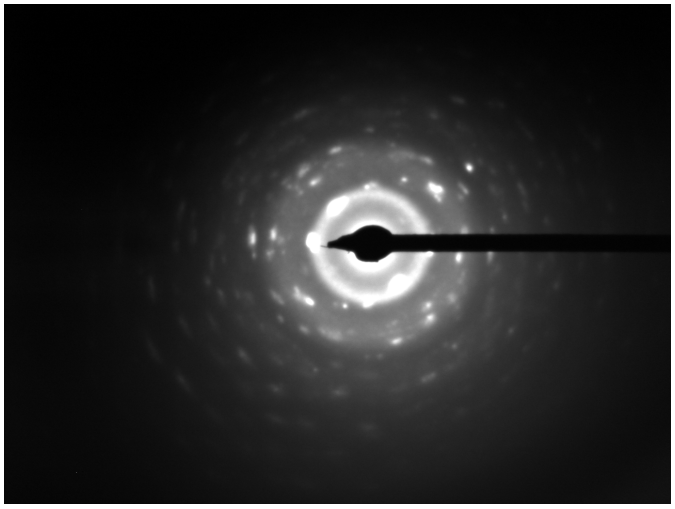

Figure 5.10: Electron diffraction pattern of a fragment of the hafnia coating heat-treated at 300^{o}C , showing diffuse rings which are the signature of amorphous material and diffraction spots which signal the presence of crystalline material. Image by R. Bassiri.

5.2 The Effect of Post-Deposition Heat Treatment on Hafnia Films Between 10-300K

Previous experiments at Glasgow on the effect of post-deposition heat-treatment on tantala and silica films have used 300°C, 600^{o}C and 800^{o}C as standard heat-treatment temperatures to compare the behaviour of the films under these conditions. As Figures 5.9 and 5.10 show, the amorphous hafnia films can begin to crystallise at 300°C, so coating samples heat-treated at temperatures below 300^{o}C were necessary to explore the amorphous form.

A batch of silicon cantilevers were manufactured by Kelvin Nanotechnology (KNT) to the dimensions shown in Figure 5.11. Cantilevers were produced in pairs and one cantilever from each pair was coated with 455±5nm of hafnia by the Materials Science and Engineering Division of CSIRO [80]. The coating thickness was measured ellipsometrically by Mark Gross of CSIRO [81].

The pair of samples used in this study were not heat-treated after deposition, although the temperature experienced during the deposition process is equivalent to heat-treatment at around 100^{o}C [92].

The first four modes of the as-deposited hafnia coated cantilever were measured using the apparatus and method described in Chapter 3. The measured mechanical loss values are shown as a function of temperature in Figure 5.17. The control values in Figures 5.13 to 5.16 are mechanical loss measurements for an uncoated, untreated silicon cantilever of the same dimensions as the coated cantilever.

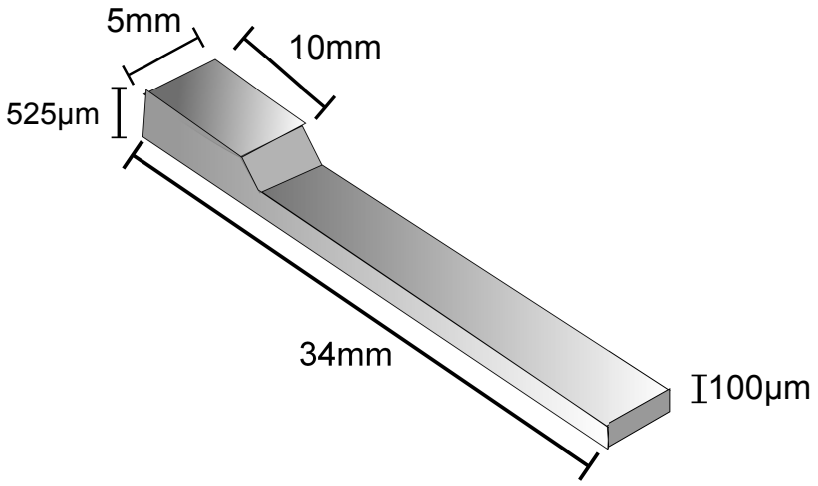

Figure 5.11: The dimensions of the silicon cantilevers manufactured by KNT and used in the measurements of an as-deposited hafnia coating without heat treatment.

The measured mechanical losses for the hafnia-coated untreated cantilever showed a significant decrease from room temperature to 10K. The measurements are summarised in Table 5.2. The fundamental mode (127Hz) was affected by the low temperature anomaly below 30K, so the lowest measured $\phi(\omega)$ at low temperature is quoted. The third measured mode at 1557Hz was a torsional mode and contains serious scatter in the 50-100K region. No large peak like that found in silica or tantala is evident at low temperatures.

Figures 5.13 to 5.16 show that the high losses close to room temperature are largely due to the thermoelastic loss of the silicon substrate. The thermoelastic

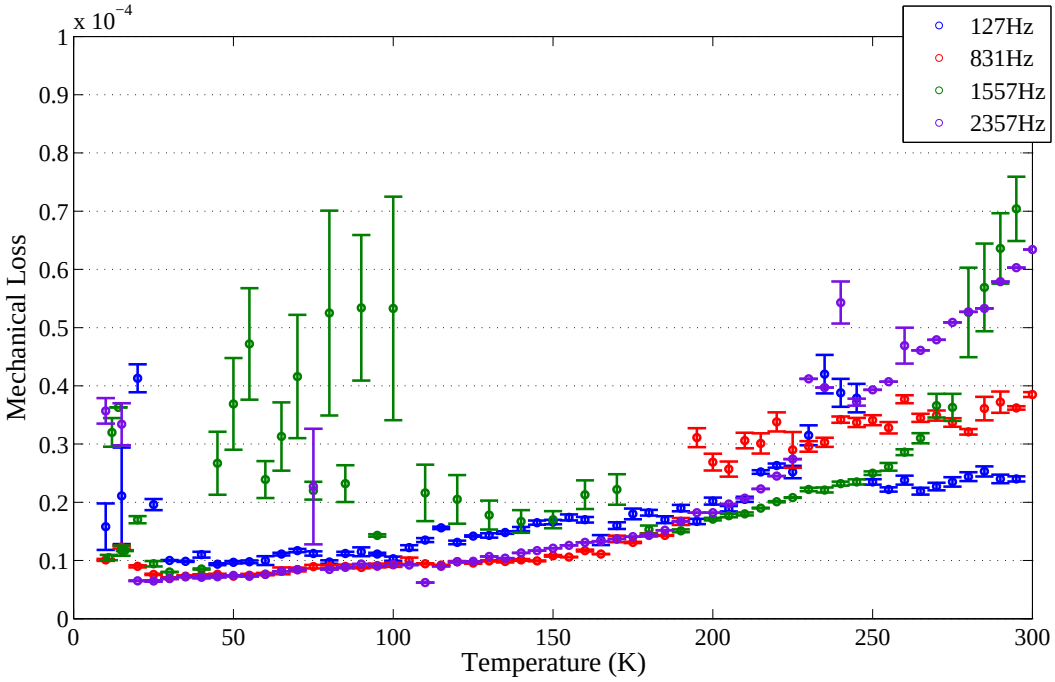

Figure 5.12: The mechanical loss of a silicon cantilever coated with 455±5nm of as-deposited hafnia between 10K and 300K for the first four resonant modes.

Mode	Frequency	$\phi(\omega)$ at 300K	$\phi(\omega)$ at low temperature
1	127Hz	2.4×10^{-5} at 295K	1.0×10^{-5} at 30K
2	831Hz	3.85×10^{-5}	1.01×10^{-5} at 11K
3	1557Hz	7.04×10^{-5} at 295K	1.05×10^{-5} at 11K
4	2357Hz	6.34×10^{-5}	6.51×10^{-6} at 20K

Table 5.2: Summary of measured mechanical losses for the cantilever with an as-deposited hafnia coating.

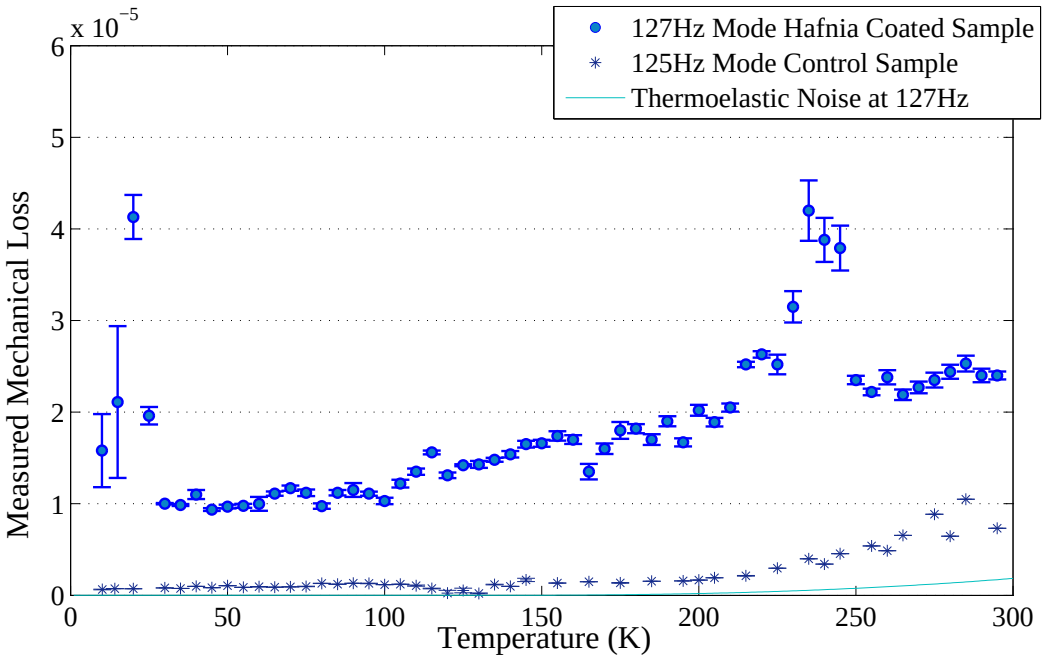

Figure 5.13: The mechanical loss of the 831Hz mode of a silicon cantilever coated with 455±5nm of as-deposited hafnia between 10K and 300K.

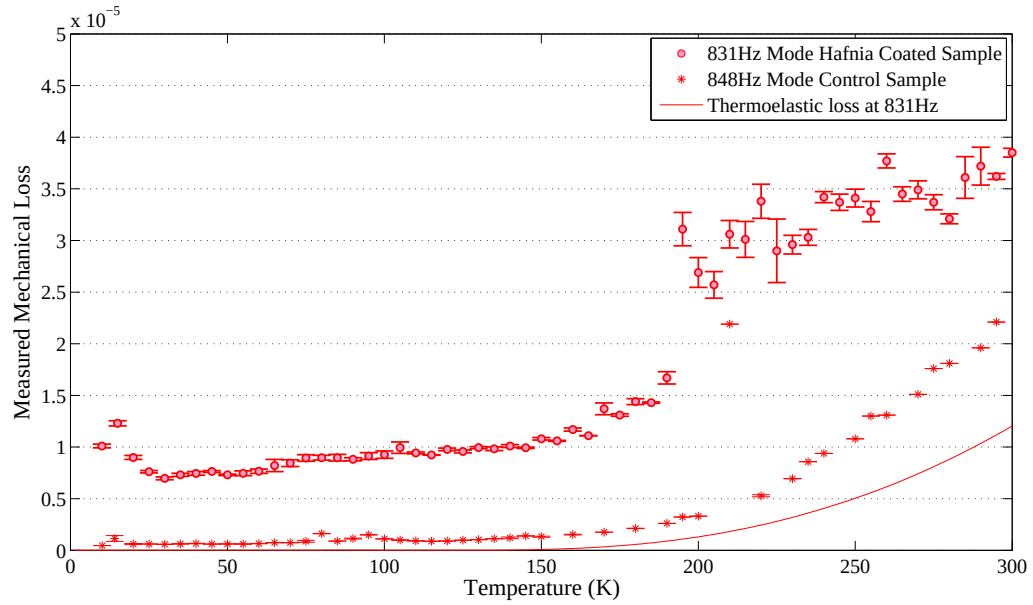

Figure 5.14: The mechanical loss of the 831Hz mode of a silicon cantilever coated with 455±5nm of as-deposited hafnia between 10K and 300K.

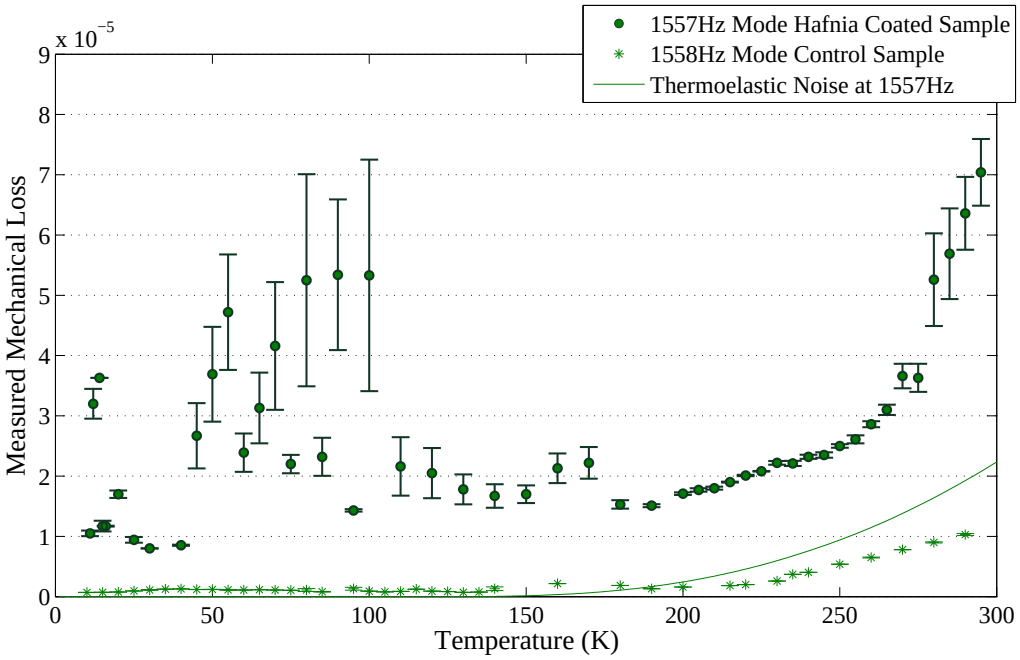

Figure 5.15: The mechanical loss of the 1557Hz mode of a silicon cantilever coated with 455±5nm of as-deposited hafnia between 10K and 300K.

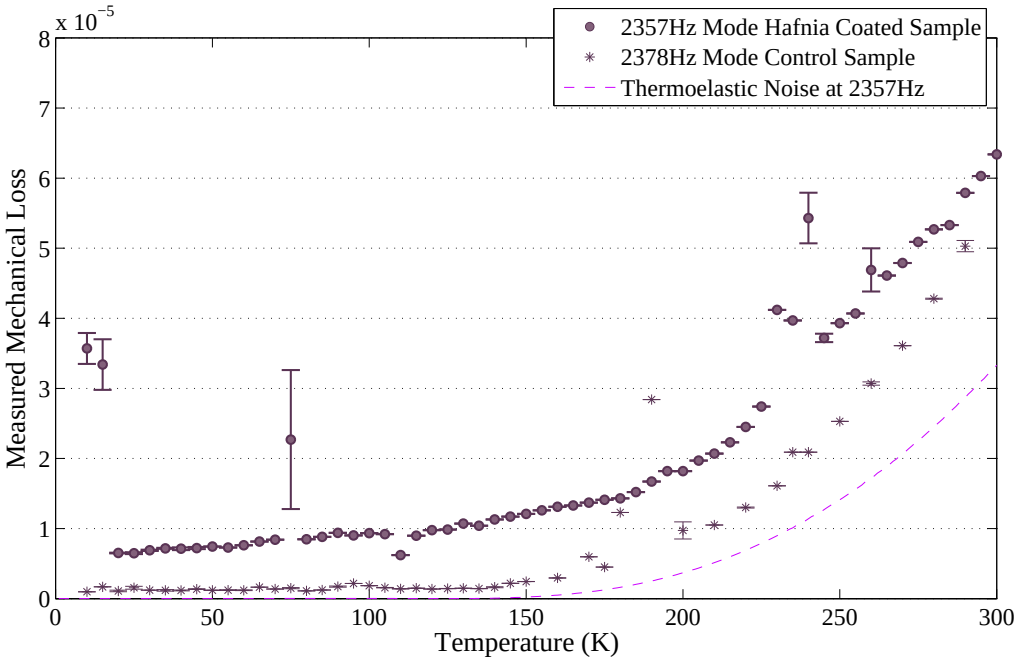

Figure 5.16: The mechanical loss of the 2357Hz mode of a silicon cantilever coated with 455±5nm of as-deposited hafnia between 10K and 300K.

	Silicon	Hafnia	
Property	Value	Value	
Young's Modulus	164 ± 3GPa	288 ± 5GPa(bulk)	220 ± 5GPa (film)
Thickness	$100 \pm 5\mu$m	455 ± 5nm	

Table 5.3: Values used to calculate the ratio of strain energy stored in the as-deposited hafnia coating to the total strain energy.

loss curve in Figure 5.15 exceeds the loss of the control sample as 1557Hz is a torsional mode and the formula quoted in Section 2.3 assumes a pure bending mode. A correction called the 'participation factor' which is based on the level of motion in the modeshape may be numerically calculated to give the true level of thermoelastic loss [93].

The mechanical losses of the as-deposited coating calculated from the measurements are shown in Figure 5.17. The coating loss of the fundamental mode at 127Hz decreases from 5.76×10^{-4} at 295K to 3.18×10^{-4} at 30K and the 831Hz mode decreases from 4.86×10^{-4} at 295K to 3.86×10^{-4} at 15K with a minimum loss of 2.20×10^{-4} at 30K. The calculated mechanical loss of the coating at the 1557Hz torsional mode at high temperatures is affected by the different level of thermoelastic loss and decreases from 1.84×10^{-3} at 295K and decreases to 3.38×10^{-4} at 11K. The calculated coating loss at 2357Hz decreases from 2.62×10^{-4} at 300K to 1.87×10^{-5} at 20K. There is no evidence for a low temperature Debye peak between 300K and 10K, although these measurements do not rule out the existence of a Debye peak below 10K. It is also possible that there is a slight increase in

coating loss at around 240K, but the existence of the intermittent thermal cycling anomaly described in Chapter 3 makes it difficult to be certain.

Figure 5.18 shows a comparison between the coating losses of the hafnia heat-treated at 300°C and the as-deposited hafnia. The coatings have roughly the same mechanical loss at room temperature, but below 200K the un-heat-treated hafnia is less lossy. The lack of a low temperature Debye peak in the as-deposited hafnia is also highlighted in this comparison.

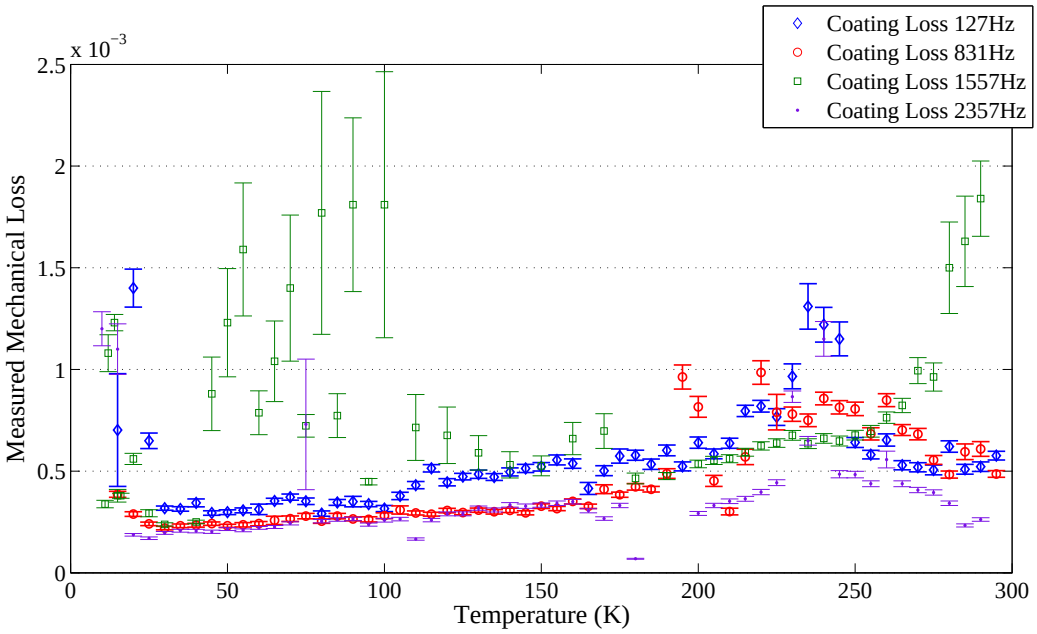

Figure 5.17: The calculated coating loss of a silicon cantilever coated with (455 ± 5)nm of as-deposited hafnia between 10K and 300K for the first four resonant modes.

5.2.1 Comparison of Hafnia, Silica and Tantala

Figure 5.19 shows the coating loss of the silica, tantala and hafnia coatings treated at 300^{o}C alongside data from the as-deposited hafnia coating. The temperature variance of mechanical loss in hafnia coatings at both annealing temperatures is at first glance quite different to that displayed in silica, but closer examination reveals similar underlying structures.

The silica and tantala coatings display low temperature loss peaks approaching magnitudes of 1×10^{-3}, but the 300^{o}C hafnia low temperature loss peak has a significantly lower peak loss at around 4×10^{-4}. The peaks for hafnia, tantala and silica also differ significantly in shape. It is currently thought that the width

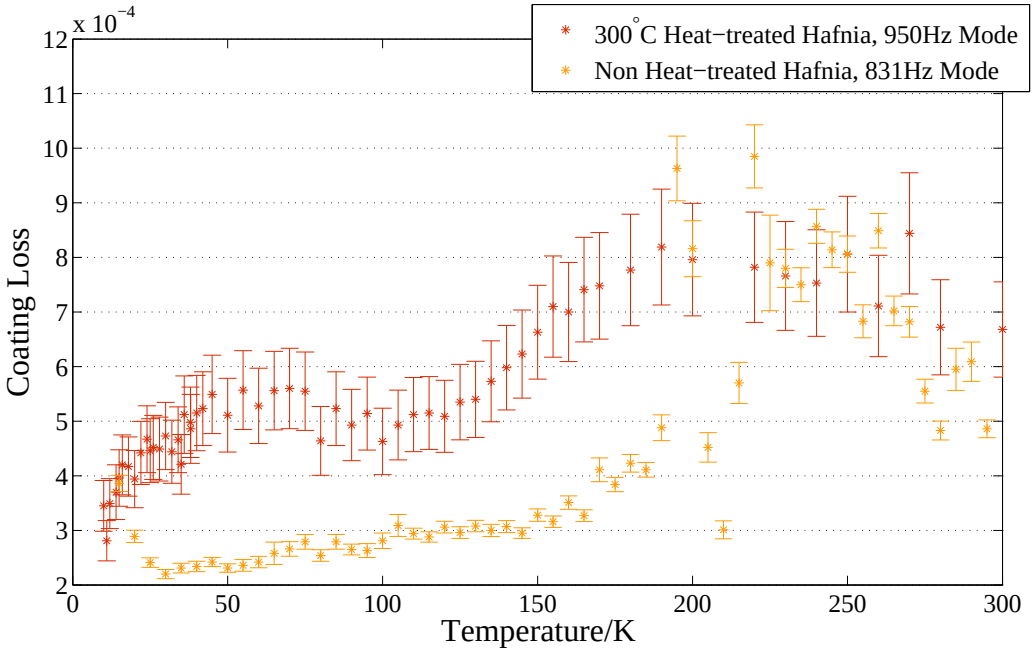

Figure 5.18: The coating loss of the 950Hz mode of the initial hafnia coating, heat-treated at 300^{o}C and the 831Hz mode of the as-deposited hafnia coating.

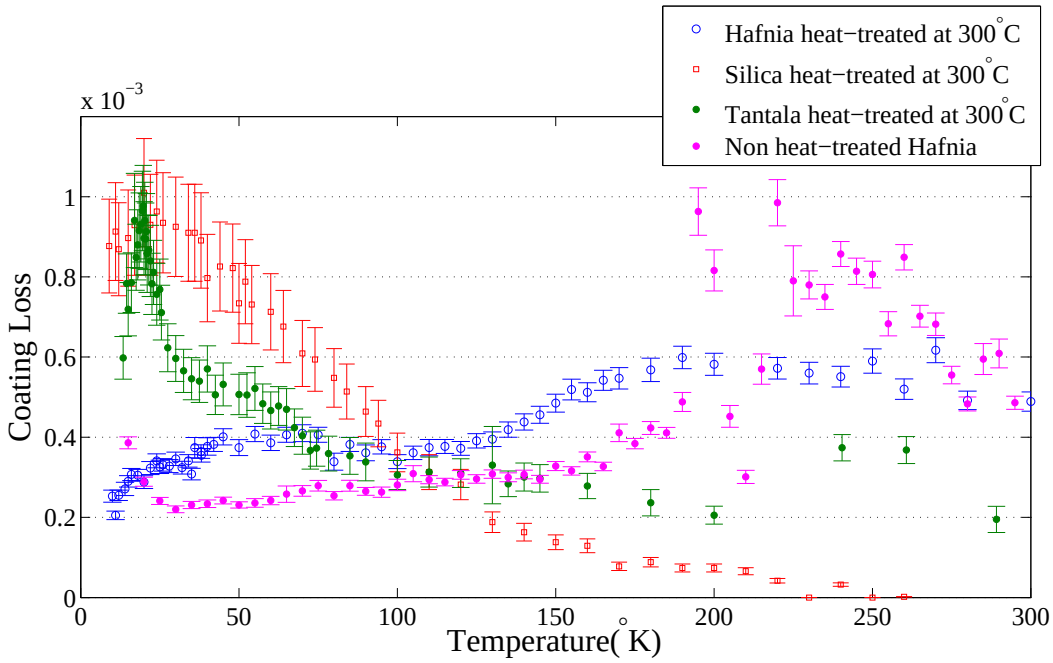

Figure 5.19: Comparison of coating losses for modes near 1kHz in tantala, hafnia and silica coatings.

and shape of the low temperature mechanical loss peak can be used as a form of proxy measurement of the distribution of potential barrier heights in an amorphous system, where narrower peaks represent a tighter distribution of potential barrier heights in the hypothetical two-level systems in the material and wider peaks represent wider barrier height distributions.

If the two-level system represented by the loss peak is the flipping of molecules between two quasi-stable bond angle configurations, then it would be expected that systems which are closer in form to a crystal would exhibit a narrow peak and systems which are highly amorphous would produce wider mechanical loss peaks. It is therefore surprising that the hafnia coating which has begun to recrystallise shows the very widest and shallowest mechanical loss peak, while the peak in the

mechanical loss of the tantala coating would suggest, in this model, that the variation in bond angles of the material was very small.

If the mechanical loss of the material was the sole deciding factor in the choice of a high-index dielectric coating material for a cryogenic multilayer mirror coating, then this study indicates that in the 10-15K range, hafnia has a factor of three lower loss than tantala, leading to a significant reduction in coating thermal noise.

Chapter 6

The Mechanical Loss of A Hydroxy-Catalysis Bond between 10-300K

Assessing the variation of the mechanical loss of a hydroxy-catalysis bond at low temperatures will provide information likely to be useful for the estimation of noise levels in future cryogenic gravitational wave detectors which may involve bonds between silicon optical components. The mechanical losses of bonds have been measured before at room temperature as described in Chapter 3. The earlier measurements were made using large cylindrical substrates on thread suspensions, which are difficult to repeat at low temperature. This work describes a method of measuring the mechanical loss of a bond between samples of the silicon cantilever type which are known to perform well at low temperatures.

6.1 The Mechanical Losses of Oxidised Cantilevers Before Bonding

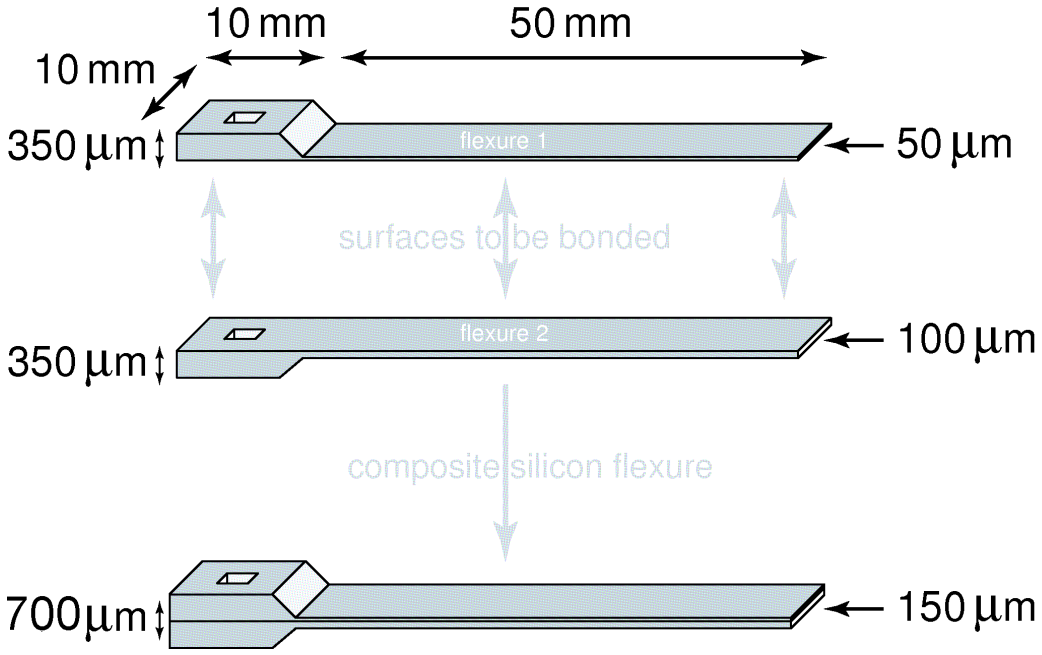

Figure 6.1: Diagrammatic view of the silicon cantilever samples showing the individual cantilever samples top and centre and the bonded combination at the bottom.

Two pairs of silicon cantilevers, with dimensions as shown in Figure 6.1 were oxidised for 8 hours to produce the layer of silica required for the hydroxy-catalysis bonding process. The mechanical losses of the first six bending modes of each oxidised cantilever were measured between 10K and 300K in the cryostat apparatus described in Chapter 3. Measurements continued until each mode had a representative curve throughout the temperature range and then the sample was reclamped in order to identify any instances of excess loss which could be connected to the manner in which sample was clamped. The values shown in Figures 6.3 to 6.15

Property	Value	Source
Young's modulus E	$164 \pm 3Gpa$	[94]
Density	2330 kg m^{-3}	[89]
Coefficient of thermal expansion	see Figure 6.2	[95]
Specific heat capacity	see Figure 6.2	[95]
Thermal conductivity	see Figure 6.2	[89]

Table 6.1: The values used to calculate the thermoelastic loss in silicon cantilevers as a function of temperature.

are the average mechanical loss calculated from the three lowest mechanical loss measurements at each temperature across all measurement runs, with the size of the error bars being the standard error in this average.

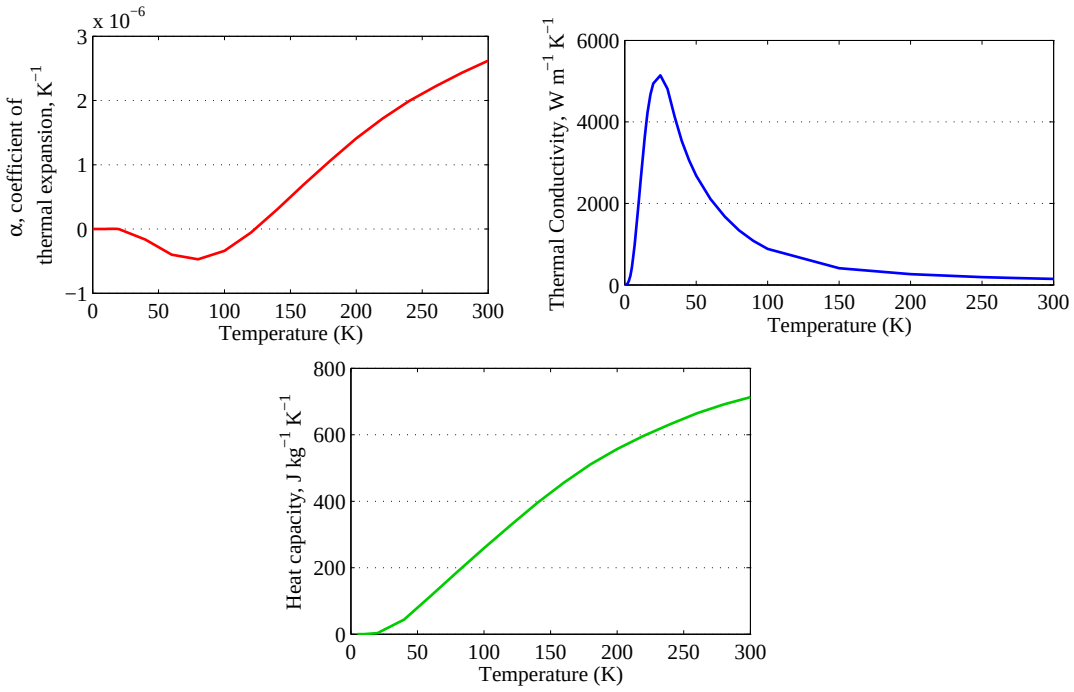

Figure 6.2: The thermal expansion coefficient, thermal conductivity and heat capacity of silicon as a function of temperature.

The level of thermoelastic loss was calculated for the silicon cantilevers at each mode frequency using Equation 2.40 and the values in Table 6.1. The calculated thermoelastic loss is shown on same axes as the measured mechanical losses in Figures 6.4 to 6.8 and 6.10 to 6.15. At low temperatures, the loss due to thermoelastic effects in the substrate is many orders of magnitude below the measured loss across all modes on both cantilevers, and can therefore be declared negligible. In the highest third of the temperature range, however, the loss due to thermoelastic effects in the substrate approaches the measured loss and for several modes of the 50μm cantilever, the calculated level of thermoelastic loss close to room temperature is approximately equal to the measured loss of the oxidised cantilever.

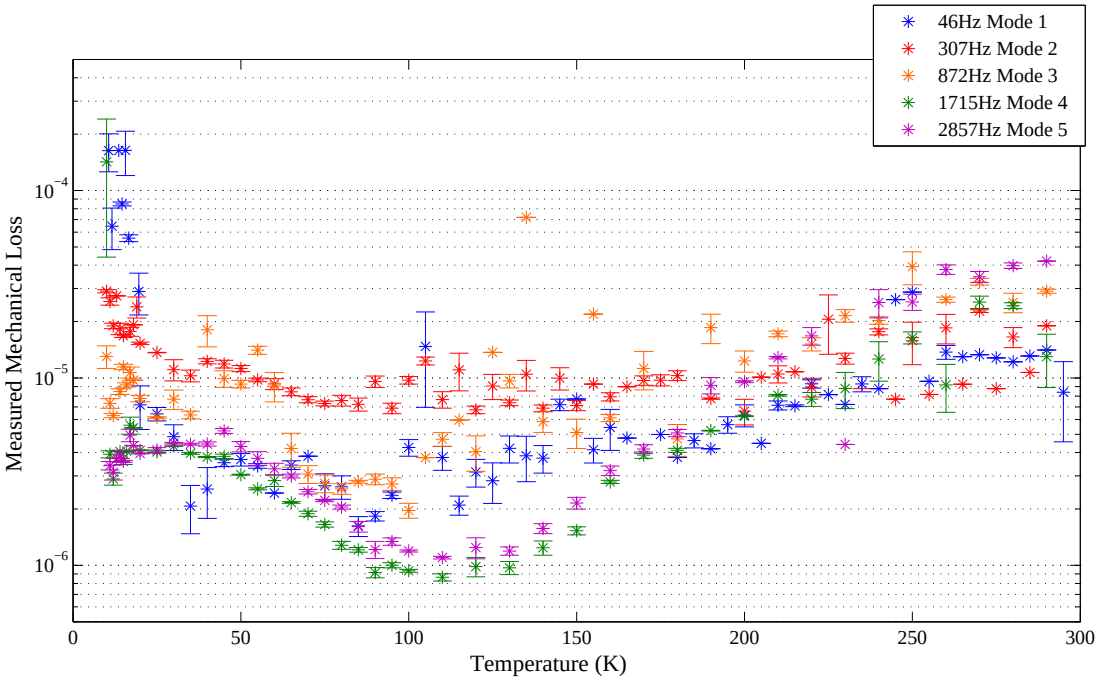

Figure 6.3: The mechanical loss as a function of temperature for the first five bending modes of a 100μm thick silicon cantilever sample.

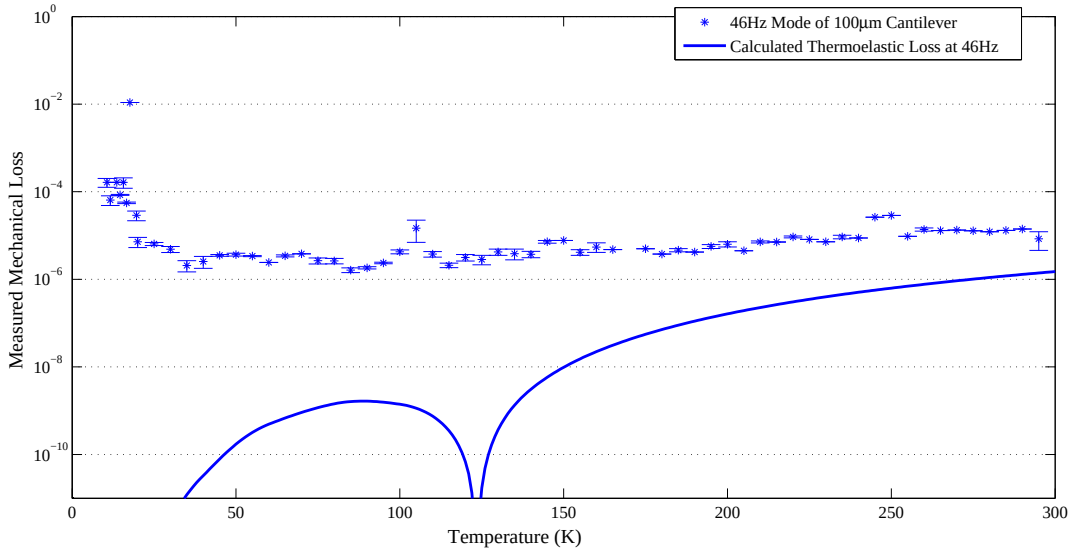

Figure 6.4: The mechanical loss as a function of temperature for the 46Hz fundamental bending modes of a 100μm thick silicon cantilever sample showing calculated levels of thermoelastic loss.

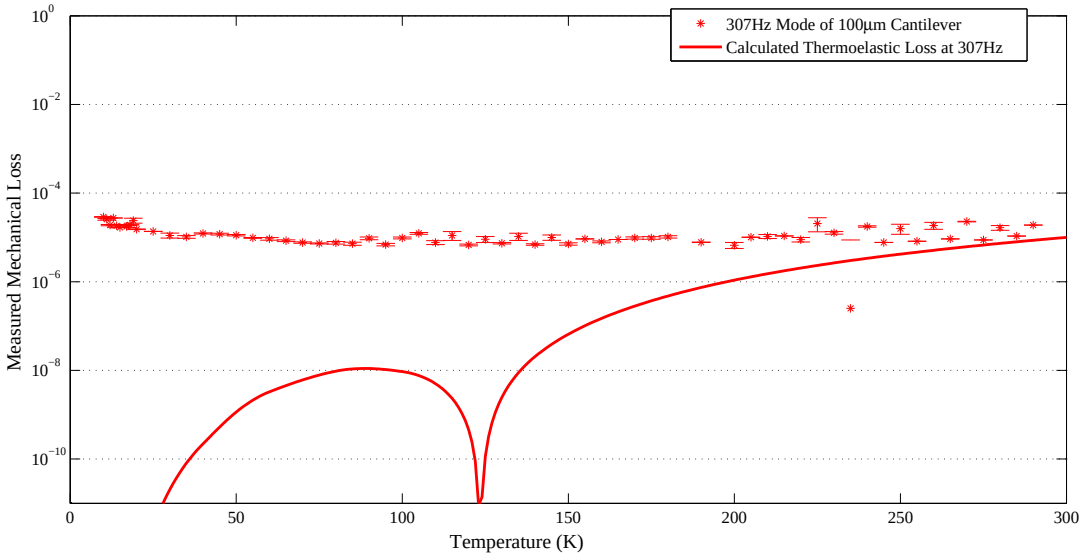

Figure 6.5: The mechanical loss as a function of temperature for the 307Hz pure bending mode of a 100μm thick silicon cantilever sample showing calculated levels of thermoelastic loss.

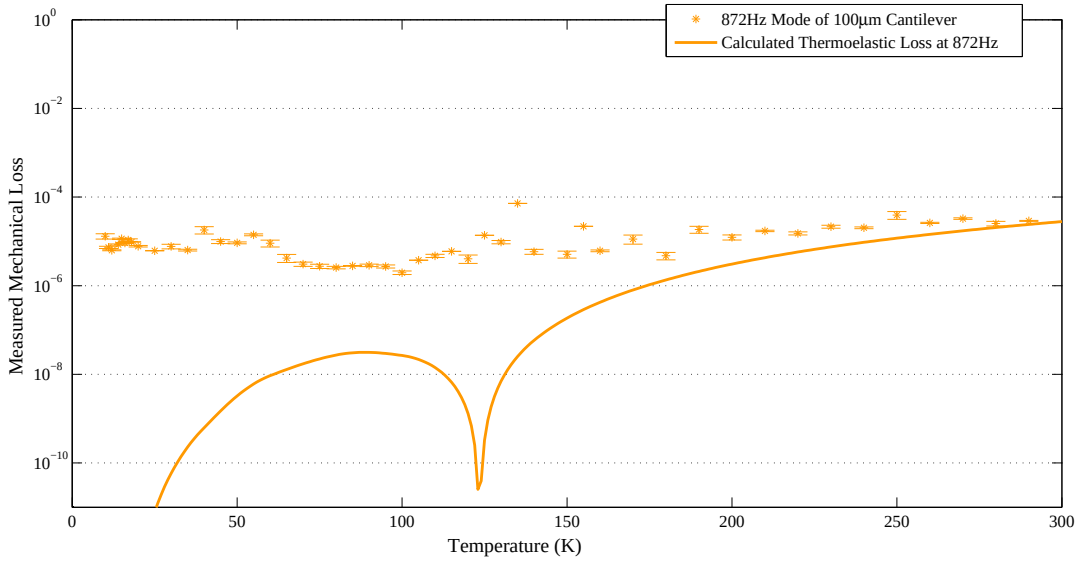

Figure 6.6: The mechanical loss as a function of temperature for the 872Hz pure bending mode of a 100μm thick silicon cantilever sample showing calculated levels of thermoelastic loss.

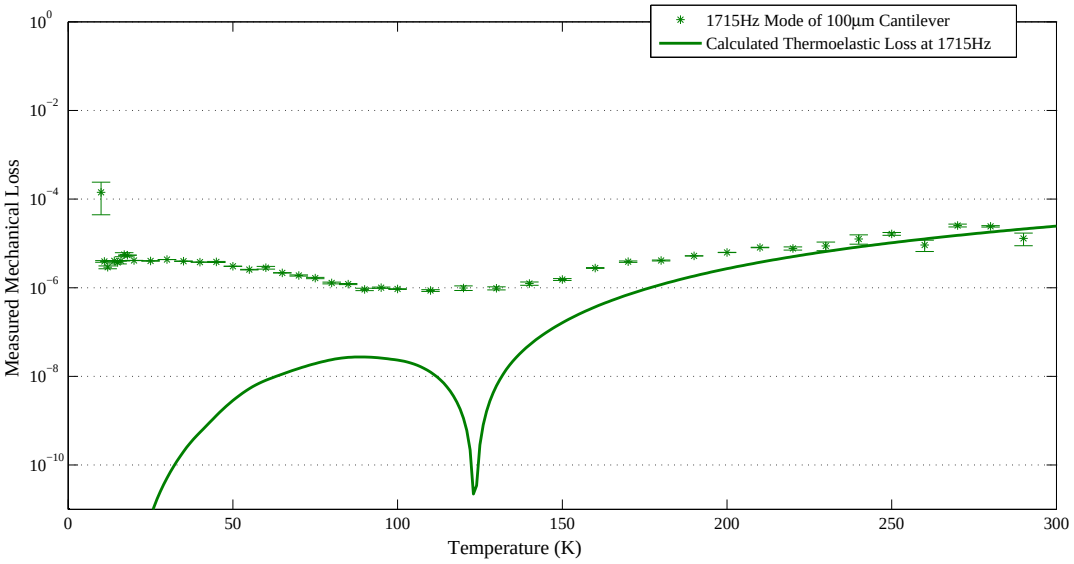

Figure 6.7: The mechanical loss as a function of temperature for the 1715Hz pure bending mode of a 100μm thick silicon cantilever sample showing calculated levels of thermoelastic loss.

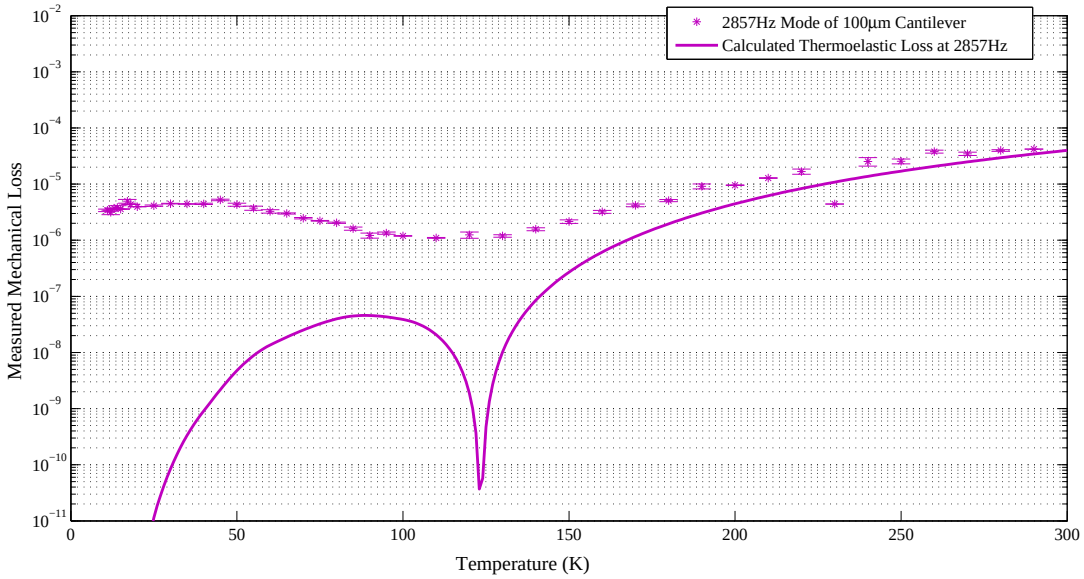

Figure 6.8: The mechanical loss as a function of temperature for the 2857Hz pure bending mode of a 100μm thick silicon cantilever sample showing calculated levels of thermoelastic loss.

The first five pure bending modes of the 100μm thick cantilever were observable using the automated mode locating and ringdown measurement program, and are shown together in Figure 6.3. The measured mechanical loss values for each mode are plotted on the same axes as the calculated thermoelastic loss at that frequency in Figures 6.4 to 6.8. The second (307Hz) and third (872Hz) modes showed higher levels of mechanical loss over the whole temperature range from 10K to 300K. The low temperature anomaly discussed in Section 3.5.1 is present in the fundamental mode (46Hz) below 20K, but the data above 20K is likely to be the intrinsic loss of the cantilever.

The fourth (1715Hz) and fifth (2857Hz) modes showed shallow, broad peaks with a maximum loss of 4.4×10^{-6} centered around 20K and 28K respectively which are

likely to be the Debye peaks of the oxide layer. Above 100K, the mechanical loss at all frequencies steadily increases with increasing temperature to a few $\times 10^{-5}$, reaching losses limited by thermoelastic loss close to room temperature.

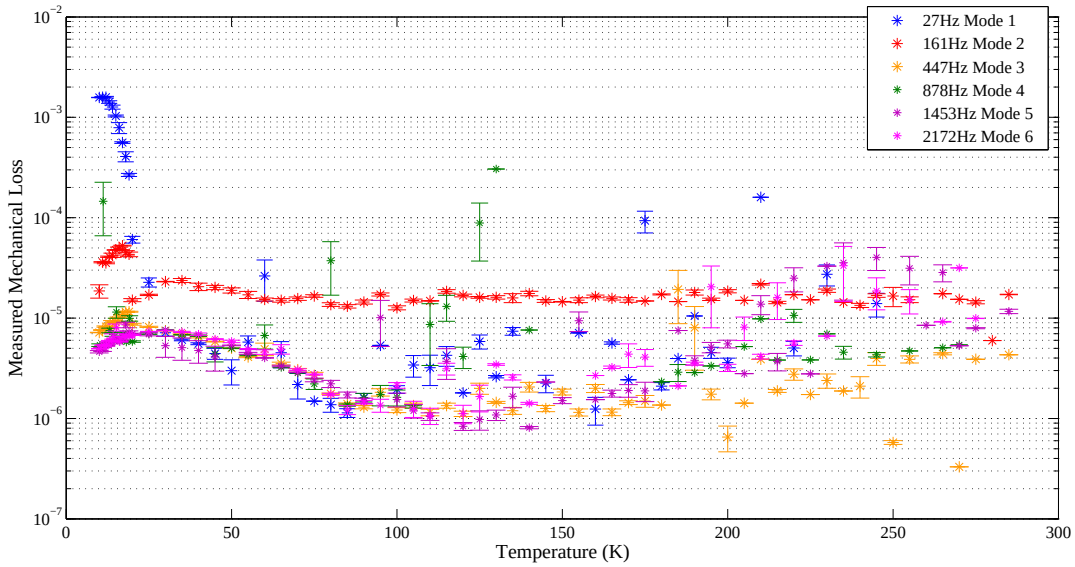

Figure 6.9: The mechanical loss as a function of temperature for the first five bending modes of a 50μm thick silicon cantilever sample.

The first six pure bending modes of the 50μm sample were observable and are shown in summary in Figure 6.9. The mechanical loss measurements for each mode are plotted on the same axes as the calculated thermoelastic loss in Figures 6.10 to 6.15. Once again, the fundamental mode (27Hz) displayed the low temperature anomaly, peaking at more than 1×10^{-3} at 11K. It was more difficult to obtain smooth and clear ringdown signals for the 50μm sample as the temperature increased, and this can be seen in the high degree of scatter above 100K in the fundamental mode measurements. Again, the second mode (161Hz) showed an almost

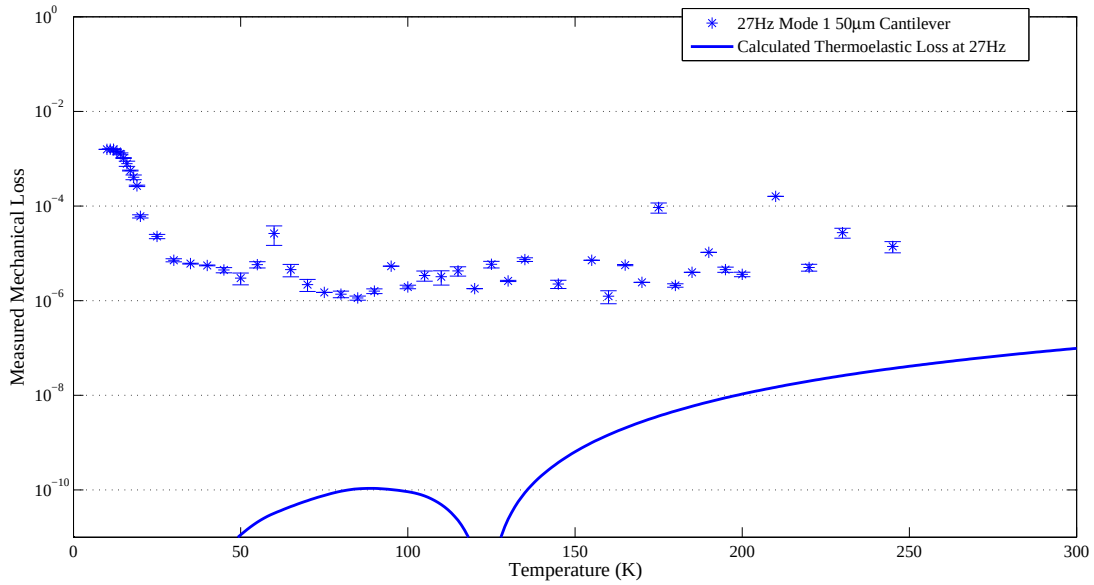

Figure 6.10: The mechanical loss as a function of temperature for the 27Hz fundamental bending mode of a 50μm thick silicon cantilever sample showing calculated levels of thermoelastic loss.

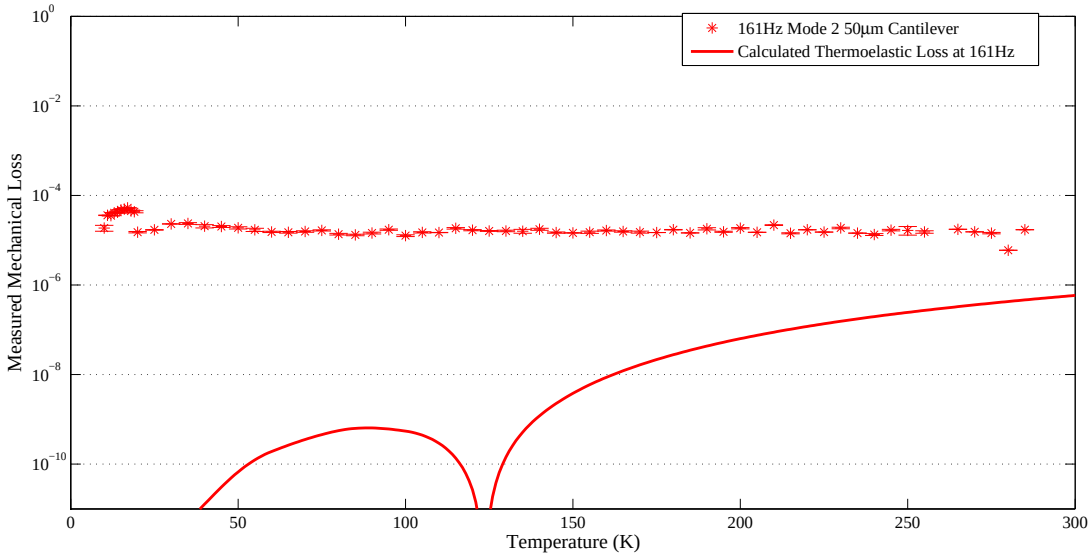

Figure 6.11: The mechanical loss as a function of temperature for the 161Hz pure bending mode of a 50μm thick silicon cantilever sample showing calculated levels of thermoelastic loss.

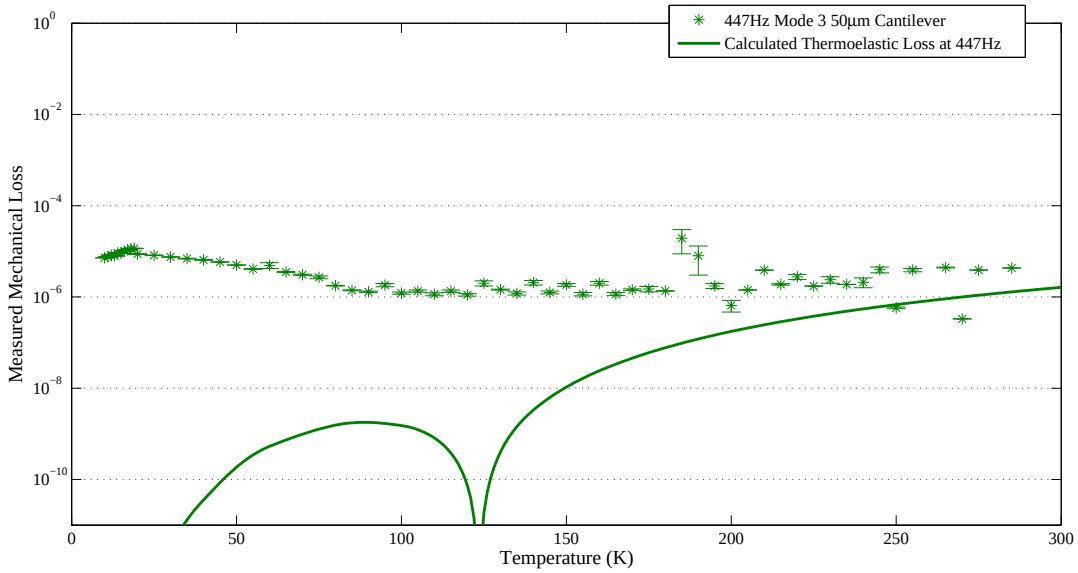

Figure 6.12: The mechanical loss as a function of temperature for the 447Hz pure bending mode of a 50μm thick silicon cantilever sample showing calculated levels of thermoelastic loss.

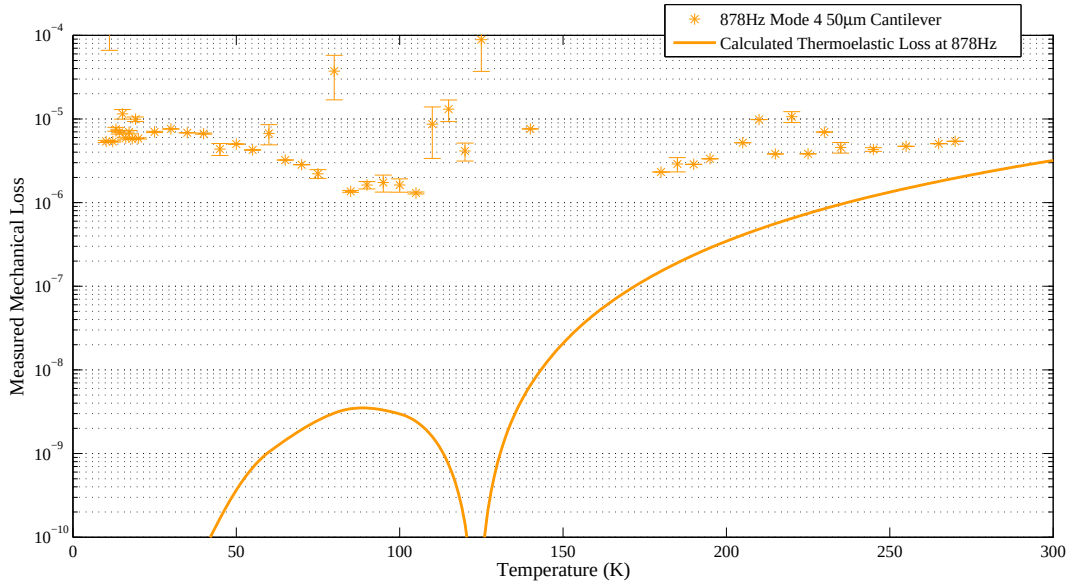

Figure 6.13: The mechanical loss as a function of temperature for the 878Hz pure bending mode of a 50μm thick silicon cantilever sample showing calculated levels of thermoelastic loss.

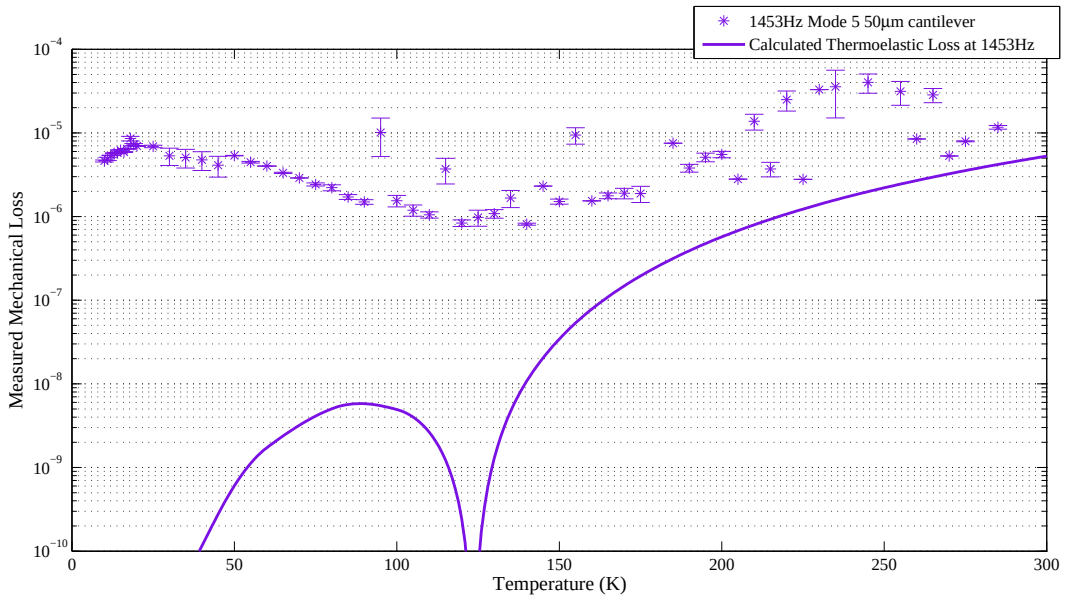

Figure 6.14: The mechanical loss as a function of temperature for the 1453Hz pure bending mode of a 50μm thick silicon cantilever sample showing calculated levels of thermoelastic loss.

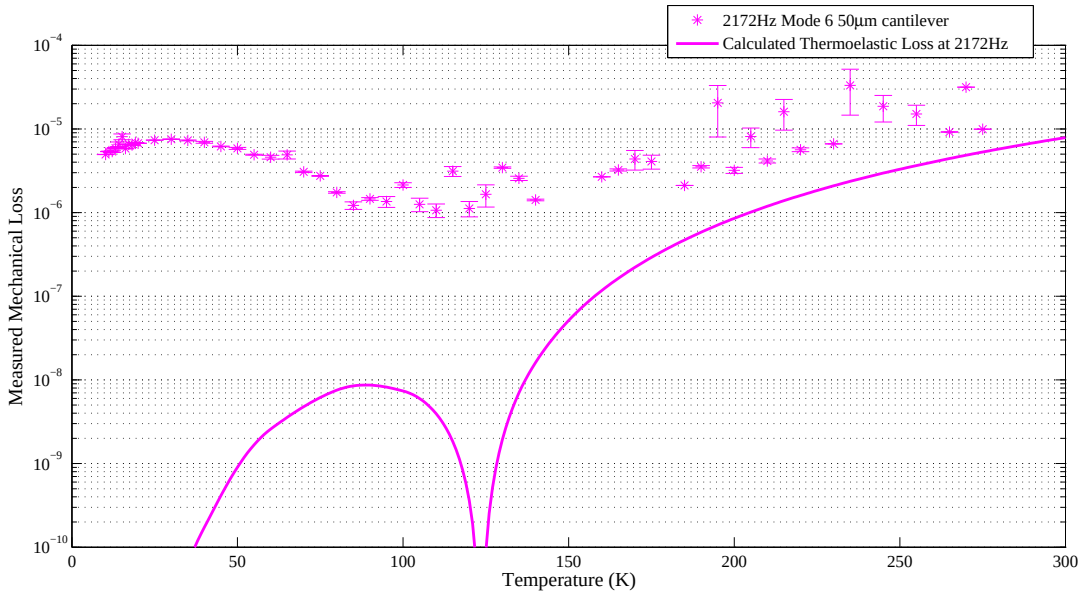

Figure 6.15: The mechanical loss as a function of temperature for the 2172Hz pure bending mode of a 50μm thick silicon cantilever sample showing calculated levels of thermoelastic loss.

featureless profile of excess loss, remaining above 2×10^{-5} through the whole temperature range. The other measured modes (447Hz, 878Hz, 1453Hz and 2172Hz) all show a similar shallow, broad peak centered around 25K with a peak loss of 7×10^{-6}. Above 100K, these modes show a steady increase in mechanical loss as the temperature approaches 300K, although the scatter in these measurements makes this feature less visible than in the measurements on the 100μm cantilever.

As both samples have been oxidised, these mechanical losses represent the sum of the mechanical loss from the silicon substrate and the mechanical loss from the thermally grown silicon dioxide layer. A good estimate of the mechanical loss of the thermally grown silicon dioxide layer may be extracted by comparing the measured losses above with the mechanical loss of a sample of the same type without an oxide layer and scaling the difference by the ratio of stored elastic energy between the oxide and substrate. If mechanical loss data is not available for comparison, as is the case here, an estimate of the upper limit on the mechanical loss of the thermally grown oxide layer can be calculated by subtracting the calculated level of thermoelastic loss at each temperature and scaling by the ratio of stored elastic energy between the oxide and substrate, assuming that the mechanical loss of the silicon substrate is negligible, which is reasonable in this case.

6.1.1 The Bonding Process and The Mechanical Loss of the Bonded Structures

The oxidised silicon cantilever pair was bonded by Stuart Reid using the method described in Chapter 3 of [96]. The cleaning process was altered slightly to avoid

use of abrasives on the fragile cantilevers. In order to remove contaminants, the cantilevers were dipped in a warm piranha solution consisting of four parts sulphuric acid to one part hydrogen peroxide. This was followed by a rinse in de-ionised water to remove any traces of piranha solution, and then rinses in acetone and isopropanol to remove the remnants of the water rinse.

The bonding solution used was one part commercial sodium silicate solution to six parts de-ionised water, with $0.4\mu l$ of bonding fluid used per cm^2 of bond area. The cantilever pairs were bonded and allowed then to cure for four weeks [97]. As thermally grown silicon dioxide layers can contain fluctuations in thickness and density, the chemical etching that occurs as part of the bonding process may penetrate the underlying silicon substrate, causing the dissociation of hydrogen which forms bubbles between the bond layer and the silicon.

The infrared image of the bonded structure in Figure 6.17 shows a number of darker regions along the length of the cantilever, which are likely to be voids in the bond layer. Analysis of the infrared image showed that around 5% by area of the bond region had formed void regions. As these void regions represent discontinuities and rough areas, it is likely that they will be responsible for some of the internal friction present in the bond region and it is possible that temperature cycling of the cantilever may cause a hydroxy-catalysis bond with gas-filled voids to degrade.

Ellipsometric measurements by R. Nawrodt and S. Reid found that the average

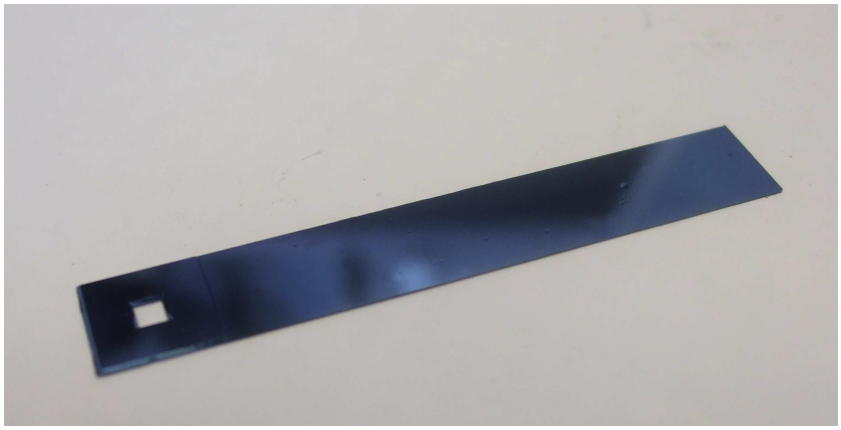

Figure 6.16: A pair of 100μm and 50 μm cantilevers bonded together to form a single structure of thickness 150μm.

thickness of the oxide layer on the outer surfaces of the bonded structure was 140 $\pm$ 3nm, with the thickness increasing from 133nm (100μm cantilever) and 134nm (50μm cantilever) at the end of clamping block to 149nm (100μm cantilever) and 150nm (50μm cantilever) at the free end.

The mechanical loss of the fully bonded sample was measured as previously described in Chapter 3, in the same measurement apparatus. Figure 6.18 shows a summary of the three measured modes, with the low temperature anomaly visible in the fundamental mode (75Hz). Figures 6.19 to 6.21 show the mechanical losses of each mode alongside the estimated thermoelastic loss present. An estimate of the thermoelastic loss of the bonded structure was calculated using the assumption that the body could be modelled as a single silicon cantilever with a thickness of 150μm, using the thermomechanical properties set out in Table 6.1.

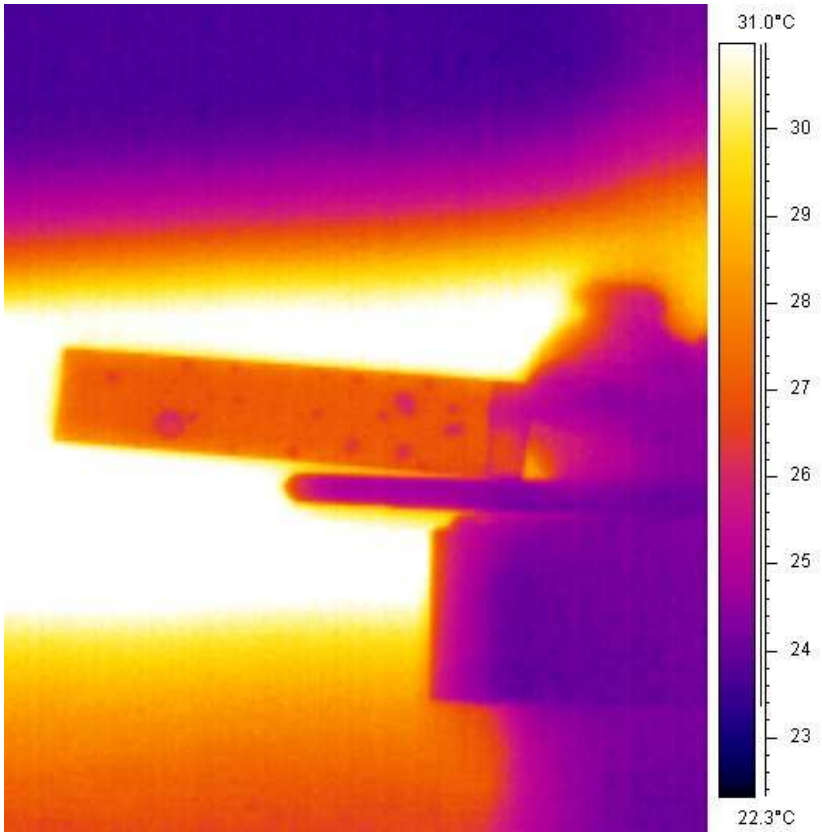

Figure 6.17: An infrared image of a pair of 100μm and 50μm cantilevers bonded together to form a single structure of thickness 150μm showing darker void regions within the structure. (Image by S. Reid)

6.2 Stored Energy In The Bonded Structure

For the bonded cantilever structure, the total mechanical loss may be broken down into the intrinsic losses of the silicon substrate, the loss of the thermally grown silicon dioxide layers and the intrinsic loss of the bond. As discussed in Chapter 2, the thermoelastic loss in the substrate is a calculable component of the overall loss of such a structure.

In order to examine the relative mechanical losses associated with the different

parts of the bonded structure, the way in which different losses add must be considered. The product of the total mechanical loss of the bonded structure and the total strain energy stored in the system is equal to the sum of the products of the mechanical losses and stored strain energies for each mechanical loss component. This may be written as [98],

$$\phi_{total} E_{total} = E_{substrate} \left(\phi_{substrate} + \phi_{sub.TE}\right) + E_{bond}\phi_{bond} + E_{oxide}\phi_{oxide}. \qquad (6.1)$$

As the bond has a much smaller volume than the whole structure, it can be assumed that almost all the elastic strain energy in the structure is stored in the silicon substrate, so $E_{substrate} \approx E_{total}$. Rearranging Equation 6.1 for ϕ_{total} gives,

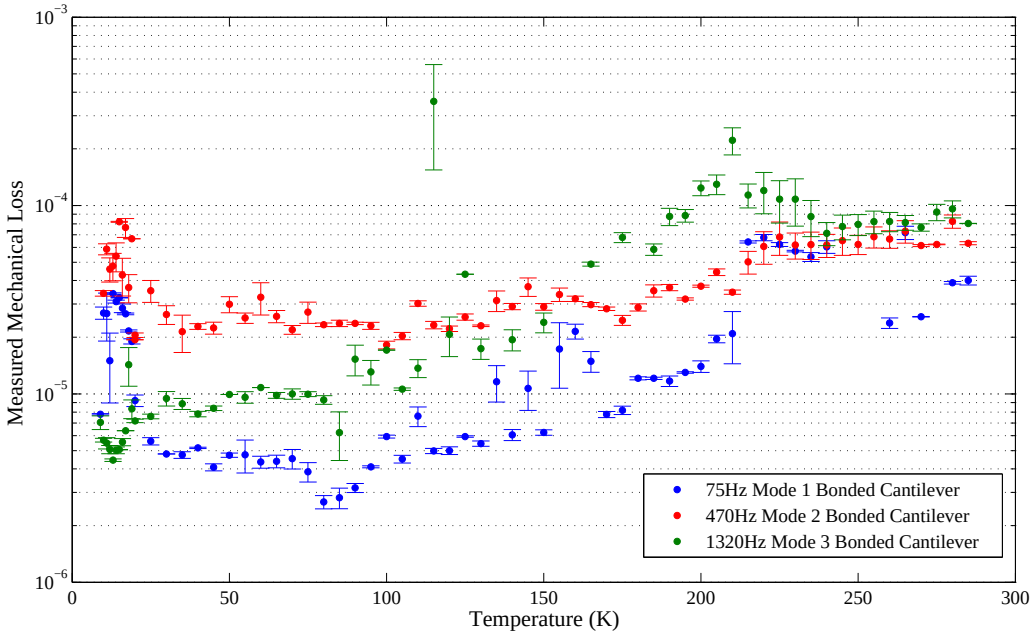

Figure 6.18: The mechanical loss as a function of temperature for a 150μm thick bonded silicon cantilever sample

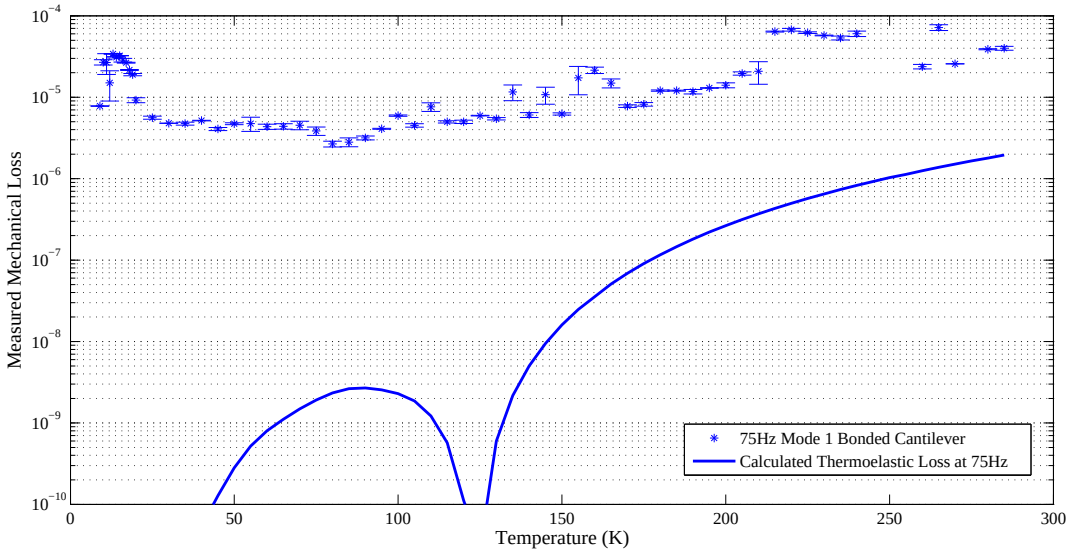

Figure 6.19: The mechanical loss as a function of temperature for the 75Hz fundamental bending mode of a 150μm thick bonded silicon cantilever sample, showing calculated levels of thermoelastic loss.

$$\phi_{total} = \phi_{substrate} + \phi_{sub.TE} + \frac{E_{bond}}{E_{total}}\phi_{bond} + \frac{E_{oxide}}{E_{total}}\phi_{oxide}. \tag{6.2}$$

Therefore, to separate out the component losses of a structure with multiple materials, it is necessary to obtain expressions for the ratios of strain energy stored in the parts of the system to the total strain energy stored in the whole system. These energy ratios are the scaling factor by which the intrinsic component loss are multiplied.

The value of $\phi_{substrate}$ is usually found by measuring an untreated substrate and the values of $\phi_{sub.TE}$ may be calculated from the known dimensions and material properties of the sample. Finding the intrinsic mechanical loss of the material

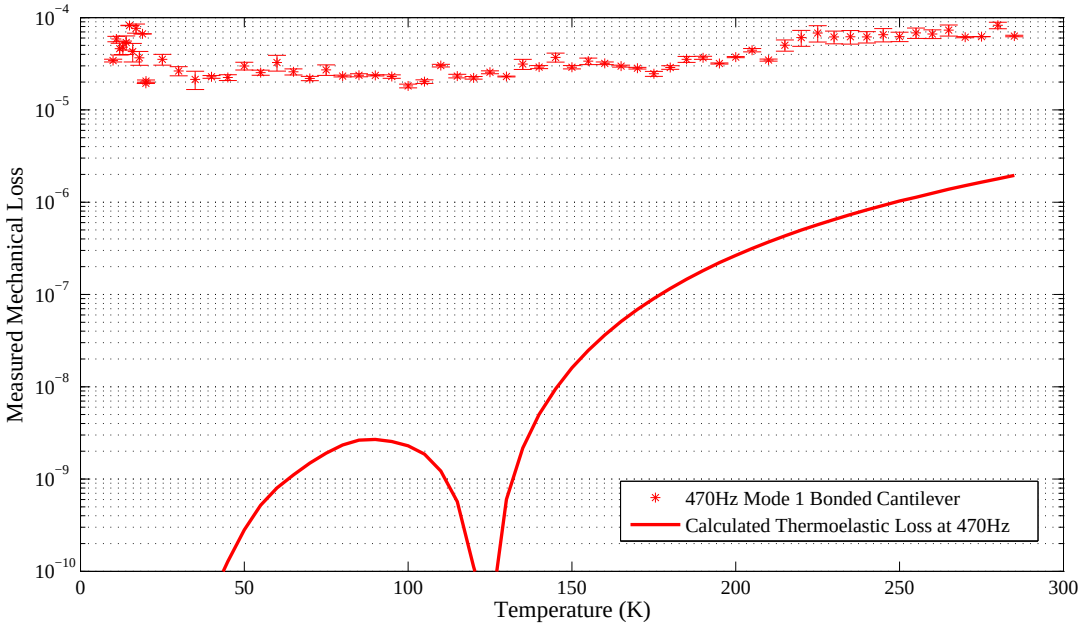

Figure 6.20: The mechanical loss as a function of temperature for the 470Hz pure bending mode of a 150μm thick bonded silicon cantilever sample, showing calculated levels of thermoelastic loss.

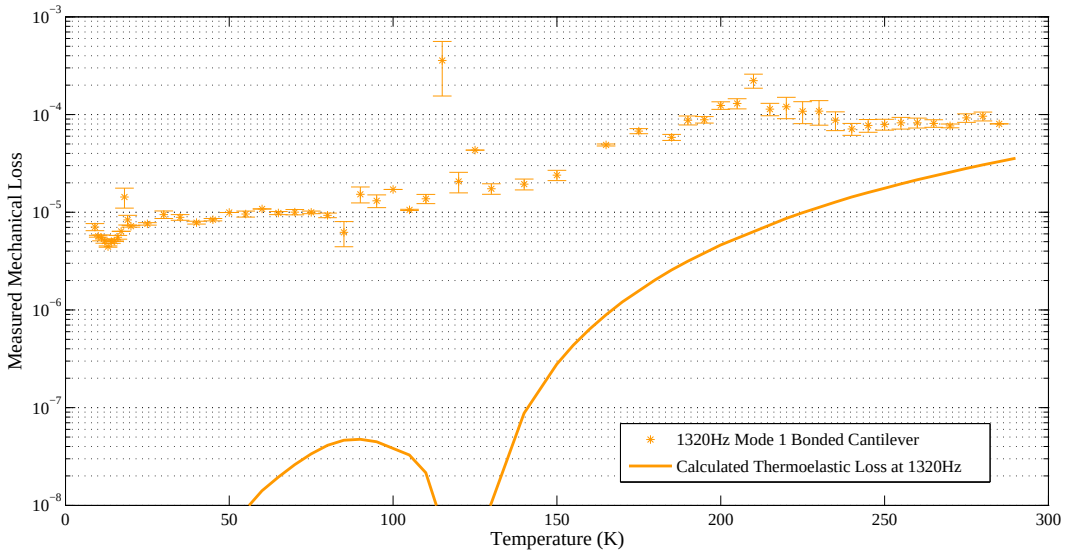

Figure 6.21: The mechanical loss as a function of temperature for the 1320Hz pure bending mode of a 150μm thick bonded silicon cantilever sample (Bonded Structure 1) showing calculated levels of thermoelastic loss.

which comprises a thin lossy layer on the surface of a substrate is often the object of calculations using this form. The method for the calculation of the energy ratio for a a single thin lossy layer of thickness t upon the surface of a rectangular substrate of thickness a is well known [98][88].

The simplest model of the bonded structure studied in this chapter has similarities to the case of a lossy layer on a substrate. In this case, the lossy bond layer can be thought of as being a distance a beneath the surface of a thin rectangular beam with total thickness $a + b$, where a and b are the thicknesses of the component cantilevers as shown in Figure 6.23. As the energy ratio is calculated analytically using the geometry of the structure, the expression for the stored energy in the bond layer can be based upon geometric corrections to the known expression for

the elastic strain energy stored in a coating applied to one surface of a cantilever [88],

$$E_{coating} = \frac{Ytw}{2L}\Delta L^2, \tag{6.3}$$

where Y is the Young's modulus of the lossy material, t and w are the thickness and width of the lossy layer, L is the unstrained length of the structure and ΔL is the change in the length of the lossy material caused by the applied strain.

Even before beginning to calculate the energy ratios $\frac{E_{bond}}{E_{total}}$ and $\frac{E_{oxide}}{E_{total}}$, some constraints can be placed upon the outcome. The energy ratio for a lossy layer located at the neutral bending axis (the case where the thicknesses of the component cantilevers are equal, so $a = b$) should be 0, and the cases where either a or b are zero, placing the lossy layer at the effective surface, should be equivalent to the energy ratio for a coating upon the surface of a substrate,

$$\frac{E_{coating}}{E_{total}} = \frac{3Y_{coating}t_{coating}}{Y_{substrate}t_{substrate}}. \tag{6.4}$$

6.3 The Analytical Stored Energy Calculation

The calculation is based upon quantification of the relative amounts of energy stored in the parts of a system composed of multiple layers undergoing curvature. Generally, the stored elastic energy in a volume is equal to the integral of the force exerted on the volume with respect to the resultant extension. The force exerted on the volume is given by,

$$F = \frac{Ywt}{L}\Delta L. \tag{6.5}$$

Where Y is the Young's modulus of the material, w is the width and t the thickness of the bent component, L is the natural, unstressed length of the component and ΔL is the amount by which the bending has stretched the component. These quantities can all be seen in diagram 6.22. Integrating Equation 6.5 with respect to ΔL gives the equation for the elastic energy stored in a layer extended by curvature [88],

$$E = \frac{Ywt}{2L}\Delta L^2. \tag{6.6}$$

In the model of the curved multilayer beam the natural length, L, occurs at the point where the tensile and compressive stresses in the bent system cancel. This point is known as the neutral axis, and the distance from the central point to the neutral axis will be given the symbol, R.

6.4 The Elastic Strain Energy Stored In The Bond Layer

For the bond section of the system, Equation 6.6 can be applied as follows. Using the small angle approximation, from observation of Figure 6.24 the length of the unstressed bond, L, is equal to the angle θ multiplied by the distance from the central point to the position of the neutral axis: $L = \theta R$.

As the cantilevers are both made from the same material, it can be assumed that

the neutral axis occurs halfway through the sample, along the blue dotted line in Figures 6.23 and 6.24, which gives $L = \theta(p + 1/2(a + b))$. The position of the bond at $r = p + a$ allows us to say that $L - \Delta L$ for the bond is given by $\theta(p + a)$ and so it follows that,

$$L - (L - \Delta L) = \theta(p + \frac{a+b}{2}) - \theta(p + a) \tag{6.7}$$

$$\Delta L = \theta\left(\frac{b-a}{2}\right) \tag{6.8}$$

As the thickness of the bond, $h \ll a, b$ it can be assumed that ΔL does not change by any significant amount between the top and bottom surfaces. This means that the total energy stored in the bond layer can be written as,

$$E_{bond} = \frac{Y_{bond} h w}{2L} \theta^2 \left(\frac{b-a}{2}\right)^2 \tag{6.9}$$

6.5 The Elastic Strain Energy Stored In The Oxide Layers

The bonded structure is composed of two cantilevers with oxide layers on both sides. If the oxide layer is not destroyed during the etching stage of the hydroxy-catalysis bonding process, then the final bonded structure will contain four oxide layers which will contribute towards ϕ_{total}.

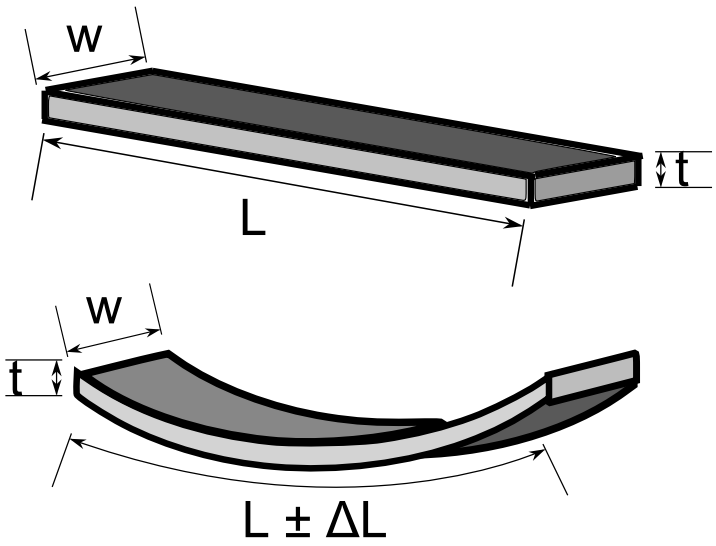

Figure 6.22: The layer dimensions used in Equations 6.5 and 6.6.

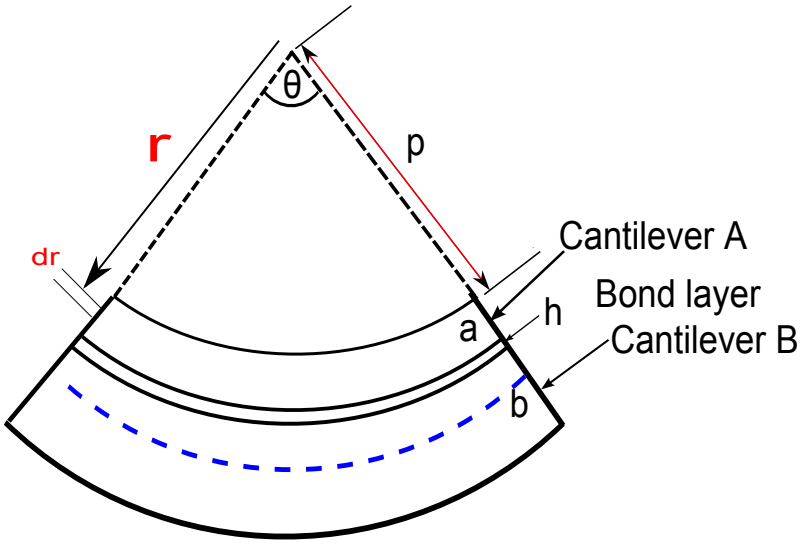

Figure 6.23: The geometry of the bending multilayer beam showing definitions of symbols used in calculations.

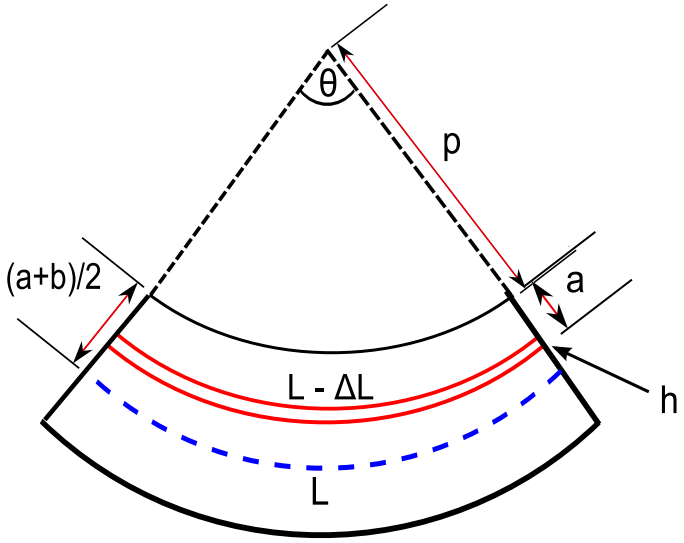

Figure 6.24: Important variables for bond energy stage, bond highlighted in red

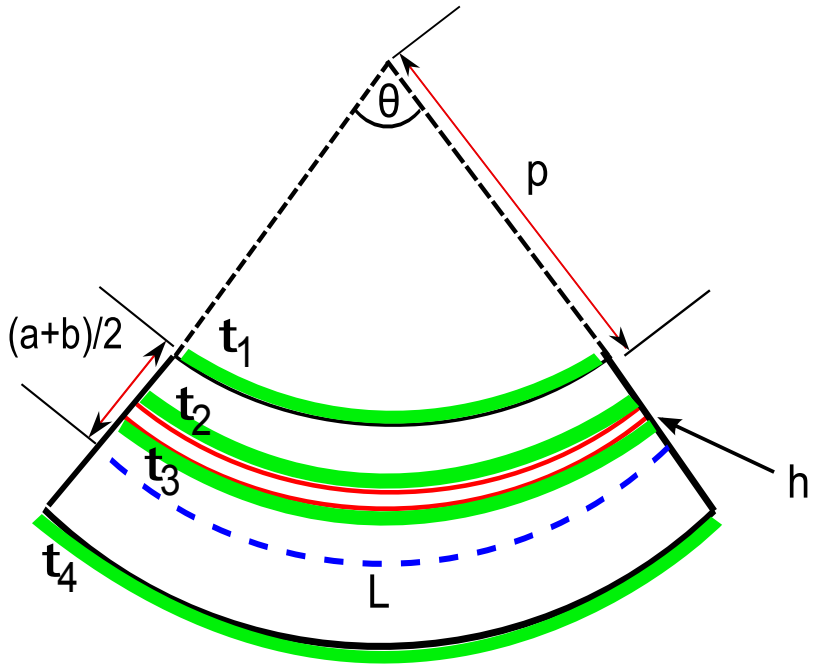

Figure 6.25: The positions of the four oxide layers in the bonded structure are shown in green, with numbering as used in the calculations.

The two oxide layers on the outside of the bonded structure, with thicknesses t_1 and t_4, can be treated as the simple case for a coating on a substrate. Therefore,

$$\frac{E_{oxide.1}}{E_{total}} = \frac{3Y_{oxide}t_1}{Y_{substrate}t_{substrate}}, \tag{6.10}$$

$$\frac{E_{oxide.4}}{E_{total}} = \frac{3Y_{oxide}t_4}{Y_{substrate}t_{substrate}}. \tag{6.11}$$

The two oxide layers immediately adjacent to the bond layer with thicknesses t_2 and t_3 can be treated in the same way as the bond layer itself. This leads to the following expressions for the energy in each of the inner oxide layers,

$$E_{oxide.2} = \frac{Y_{oxide}t_2w}{2L}\theta^2\left(\frac{b-a}{2}\right)^2 \tag{6.12}$$

$$E_{oxide.3} = \frac{Y_{oxide}t_3w}{2L}\theta^2\left(\frac{b-a}{2}\right)^2 \tag{6.13}$$

The term representing the change in length experienced by the oxide layer in Equations 6.11 and 6.12 is $\theta^2\left(\frac{b-a}{2}\right)$, which is the same as that calculated for Equation 6.9. It is possible to derive more expressions for the change in length experienced by the oxide layer that take into account the effect of the thicknesses of all four oxide layers and the bond layer upon the level of bending experienced by each oxide layer. For oxide layer 2, the length-change term (given the symbol ΔL) becomes,

$$\Delta L_{oxide.2} = \theta\left(\frac{1}{2}(h + t_2 + t_3 + t_4 - t_1) + \frac{1}{2}(b-a)\right) \tag{6.14}$$

When the bond layer and all the oxide layers have thicknesses close to 100nm, the difference between the energy ratios calculated by using Equation 6.14 or Equation 6.8 as the length-change term ΔL is around 2%. In the calculation of the contribution of the mechanical loss of the oxide layers to the total mechanical loss of the bonded structure, the simplified versions of the expressions to find the energy ratios were used.

6.6 Energy Stored In Cantilevers

Assuming that the presence of the bond and the oxide layers does not alter the overall elastic behaviour, the bonded structure can be considered as a single cantilever of thickness $T = (a+b)$. As shown in Appendix A of [88], the energy stored in a bending cantilever of thickness T, width, w, length, L and Young's Modulus, $Y_{substrate}$ is given by,

$$\frac{E_{substrate}}{2} = \frac{1}{48}\frac{Y_{substrate} w \theta^2 T^3}{L}, \tag{6.15}$$

where θ is the angle subtended by the radii of curvature. Substituting in $a+b$ for the thickness of the structure results in,

$$E_{substrate} = \frac{1}{24}\frac{Y_{substrate} w \theta^2 (a+b)^3}{L}. \tag{6.16}$$

All that remains is to find the ratio $E_{bond}/E_{substrate}$:

$$\frac{E_{bond}}{E_{substrate}} = \frac{Y_{bond}hw}{2L}\theta^2 \left(\frac{b-a}{2}\right)^2 \frac{24L}{Y_{substrate}w\theta^2(a+b)^3}. \tag{6.17}$$

This cancels to,

$$\frac{E_{bond}}{E_{substrate}} = \frac{3Y_{bond}}{Y_{substrate}} \frac{h(a-b)^2}{(a+b)^3} \tag{6.18}$$

A measurement of the value of $Y_{bond} = 7.9$GPa using nanoindentation was made using nanointentation by S. Bull of School of Chemical Engineering and Advanced Materials, University of Newcastle, and was previously used in calculations of the loss of a bond between two silica cylinders [82].

6.7 Bond Thickness and Metrology Details

The cross-section of a broken fragment of a bonded structure was examined by J. Scott and S.Reid using scanning electron microscopy (SEM). Figure 6.26 confirms the presence of voids in the bond layer. The void regions and clumps of bond material around them are likely to contribute to a higher level of mechanical loss in the measurement of the bonded structures. As the process of growing an oxide layer and making of a hydroxy-catalysis bond in any future gravitational wave detector will be performed under exacting tolerances, these regions may not occur in 'production' bonds.

The SEM images were also used to measure the thickness of the bond region and

survey the state of the oxide layer on the inner surfaces of the bonded structure. The full set of SEM images from which Figure 6.27 was taken showed that the thickness of the bond varied across the cantilever. For regions which were not void, the thickness of the bond layer was around (150 ± 50)nm. It was also clear that the inner oxide layers remained largely intact despite the etching process. The average values of t_2 and t_3 from the full set of SEM measurements were (100 ± 6)nm and (112 ± 11)nm respectively.

The irregular thickness of the bond region and variation in the degree of etching away of the oxide layer may have been caused by an intrinsic curvature of the silicon cantilevers. Surface quality measurements using a Talysurf profiler were performed on the wafer from which the 100μm cantilevers were etched. These measurements, summarised in Figure 6.29, showed a fluctuation in surface flatness

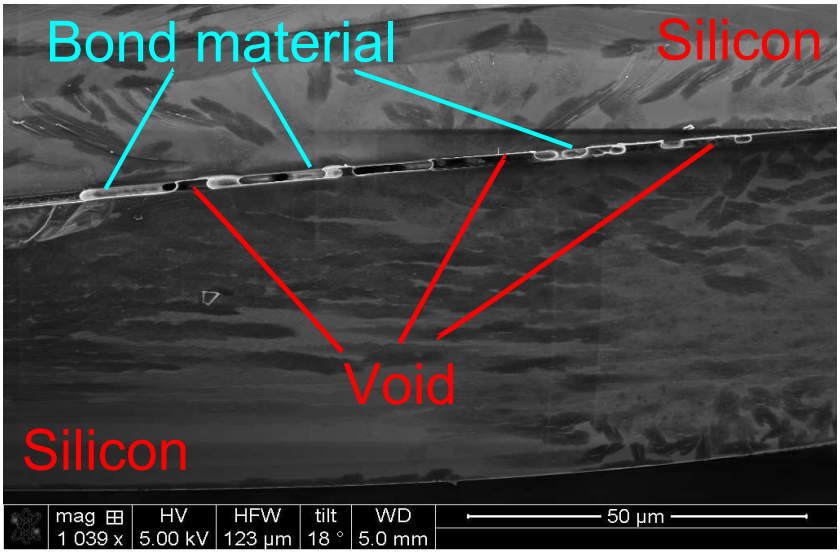

Figure 6.26: An SEM image showing irregular clumps of bond material and voids in the bond layer between the 50μm and 100μm silicon cantilevers (Image J. Scott and S. Reid)

of several microns over the length scale of the cantilever. If the cantilever exhibits a similar degree of curvature to the wafer, then the imperfections in the hydroxy-catalysis bond are likely to be related. To produce a hydroxy-catalysis bond of the quality used in a gravitational wave detector, flatness levels of $\lambda/10$ are required. While the thin silicon cantilevers are likely to have been able to flex to conform to each others shape, the irregular thickness and presence of voids in the bond region suggest that the adaptations to the bonding process for flexible cantilevers did not produce the highest quality bond.

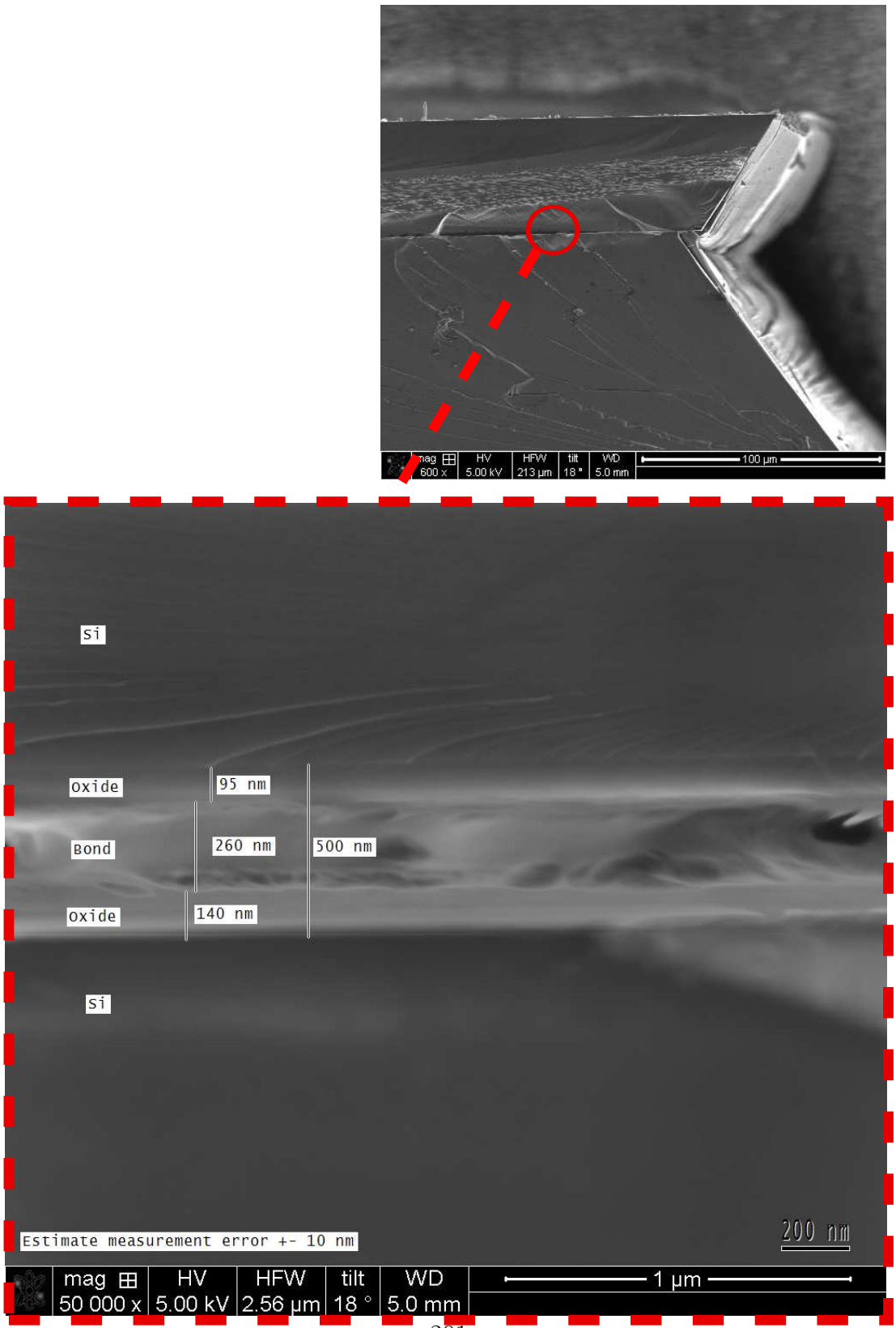

Figure 6.27: SEM images showing a fragment of the bonded cantilever structure and the bond region in a bonded cantilever structure.(Image J. Scott and S. Reid)

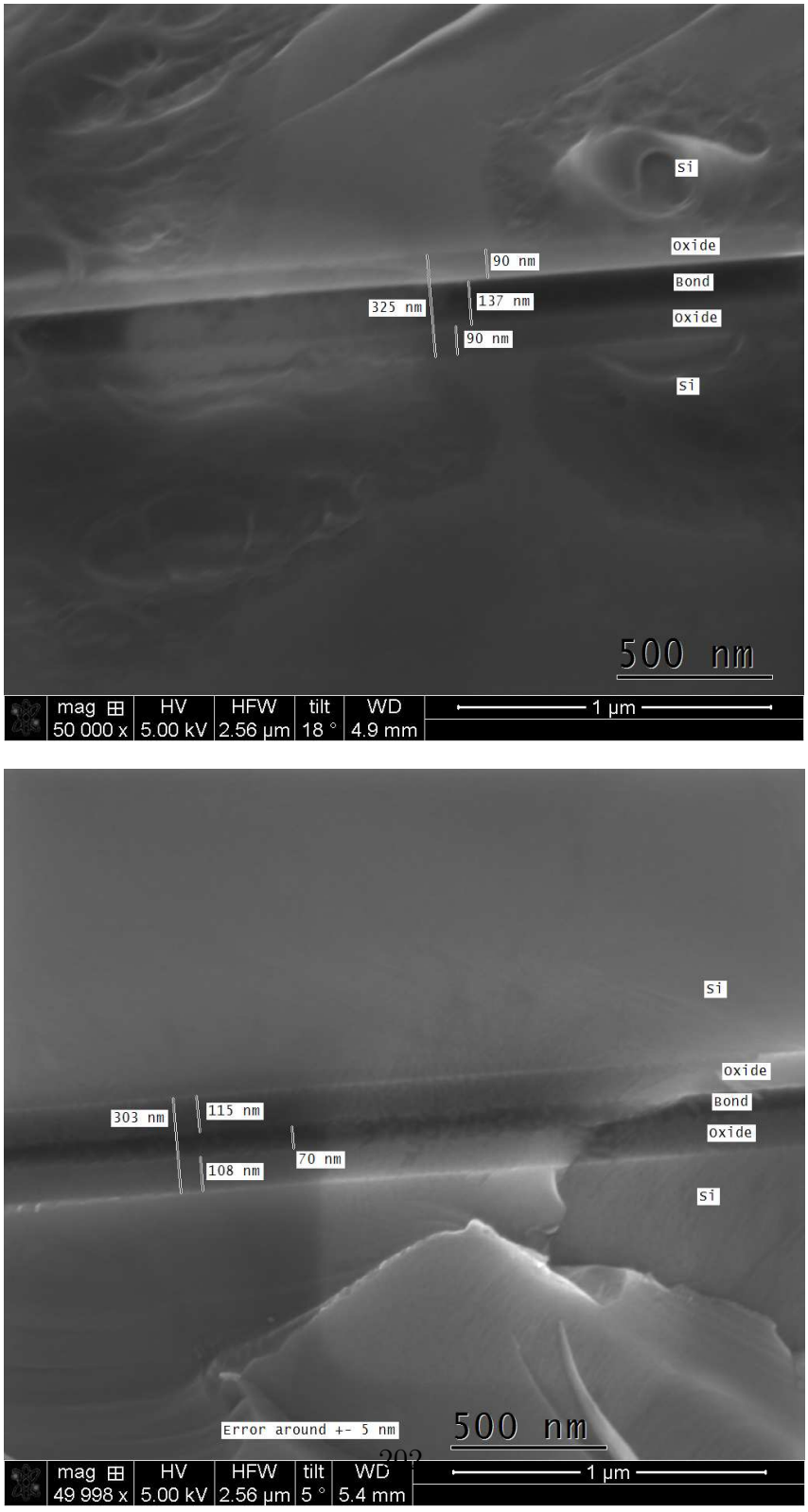

Figure 6.28: SEM images showing the variations in the thicknesses of the oxide layers and bond region in fragments of the bonded cantilever structure.(Image J. Scott and S. Reid)

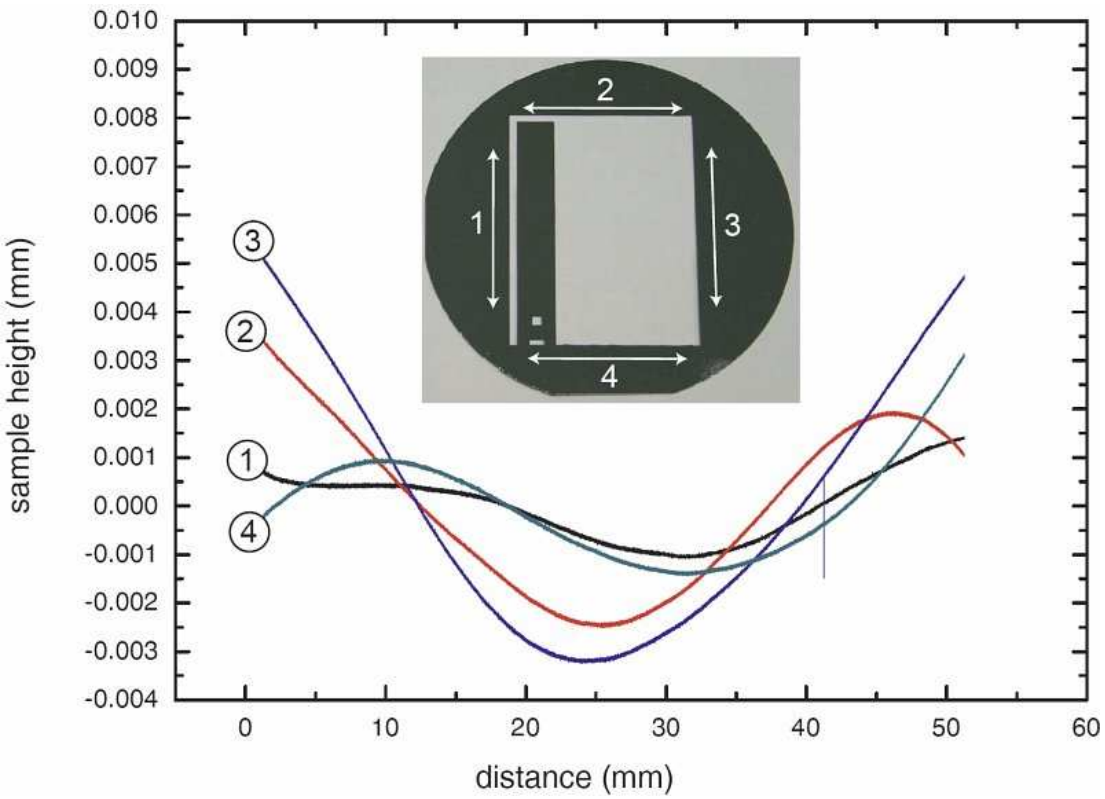

Figure 6.29: The surface quality data obtained using a Talysurf profiler on the 100μm thick silicon wafer from which the 100μm thick silicon cantilever was etched.(Image S. Reid)

6.8 Calculation of the Component Mechanical Losses Of the Bonded Structure

If it is assumed that the vast majority of the loss measured in the bonded structure results from the thermoelastic loss in the substrate, the loss of the bond region and the losses of the thermal oxide layers, then an upper limit on the loss of the bond material may be calculated. The sum of the products of mechanical loss and energy for this case is,

$$E_{total}\phi_{measured} = E_{sub}\phi_{sub} + E_{bond}\phi_{bond} + E_{sub.TE}\phi_{sub.TE} + E_{oxide.1}\phi_{oxide.1} + \ldots$$

$$\ldots E_{oxide.2}\phi_{oxide.2} + E_{oxide.3}\phi_{oxide.3} + E_{oxide.4}\phi_{oxide.4}. \qquad (6.19)$$

Dividing Equation 6.19 through by E_{tot}, and rearranging for ϕ_{bond} gives,

$$\frac{E_{bond}}{E_{total}}\phi_{bond} = \phi_{measured} - \frac{E_{sub}}{E_{total}}(\phi_{sub} + \phi_{sub.TE}) - \frac{E_{oxide.1}}{E_{total}}\phi_{oxide.1} - \ldots$$

$$\ldots \frac{E_{oxide.2}}{E_{total}}\phi_{oxide.2} - \frac{E_{oxide.3}}{E_{total}}\phi_{oxide.3} - \frac{E_{oxide.4}}{E_{total}}\phi_{oxide.4} \qquad (6.20)$$

As the material of all the oxide layers is the same, they are assumed to have the same mechanical loss. This allows $\phi_{oxide.1-4}$ to be set to ϕ_{oxide}. The energy ratios for the oxide layers were calculated in Section 6.5. The energy ratios and measured thicknesses for the outer oxide layers are the same, so $\frac{E_{oxide.1}}{E_{total}} = \frac{E_{oxide.4}}{E_{total}}$. As before,

E_{sub} is assumed to be equal to E_{total}. Substituting this into Equation 6.20 gives,

$$\frac{E_{bond}}{E_{total}}\phi_{bond} = \phi_{measured} - \phi_{sub} - \phi_{sub.TE} - \frac{2E_{oxide.1}}{E_{total}}\phi_{oxide} - \ \ldots$$

$$\ldots \frac{E_{oxide.2}}{E_{total}}\phi_{oxide} - \frac{E_{oxide.3}}{E_{total}}\phi_{oxide}. \tag{6.21}$$

To use Equation 6.21, the amount of mechanical loss contributed by the thermally grown amorphous silicon dioxide must be extracted. The bonding process required an oxide layer to be grown on the bonding surfaces of the cantilevers and due to the method of oxidisation used, oxide also grew upon the outside surfaces. For the purposes of calculating an energy ratio, the individual cantilevers are considered as having lossy layers of equal thickness on both sides.

The mechanical losses of the individual cantilevers were not measured before oxidisation, so an experimental value for $(\phi_{sub}+\phi_{sub.TE})$ is unavailable. It is known that mechanical loss measurements of silicon cantilevers are dominated by thermoelastic loss at the upper end of the temperature range studied here. Measurements of uncoated silicon cantilevers also show that the mechanical loss at low temperatures can be as low as 4.4×10^{-7} and that at high temperatures the measured mechanical loss is extremely close to the thermoelastic noise [94]. The intrinsic mechanical loss of silicon is several orders of magnitude lower than the mechanical loss of the bonded cantilever structure between 10K and 300K. As $\phi_{sub.TE}$ is the only substrate component which approaches the measured mechanical loss of the

substrate, ϕ_{sub}, can be declared negligible.

In the absence of a set of mechanical loss measurements of the cantilevers pre-oxidisation to use as control measurements, an estimate of the loss due to the oxide layer on the component cantilevers may be calculated by subtracting the contribution of thermoelastic loss from the measurements of the oxidised cantilevers and scaling the result by the energy ratio for a lossy coating on both sides of a cantilever,

$$\frac{E_{oxide.1}}{E_{cantilever}} = \frac{6Y_{oxide}t_{oxide.1}}{Y_{silicon}t_{substrate}}, \tag{6.22}$$

which uses the assumption that $t_1 = t_4$. For the thick cantilever, $t_{substrate} = b = 100\mu m$ and for the thin cantilever, $t_{substrate} = a = 50\mu m$. The results of the application of this technique to the mechanical loss data from Section 6.1 are summarised in Figures 6.30 and 6.31. These values are used in the next stage of the calculation, and represent an upper limit upon the level of mechanical loss present in the material that makes up the oxide layers.

6.8.1 Calculation of the Bond Loss

The upper limit values for the mechanical loss of the oxide layer calculated above were used to calculate an average curve for the mechanical loss of the oxide layer at each mode frequency on each of the cantilevers, which was then interpolated to give loss values for the temperature values required. The average oxide layers consisted of the oxide loss estimates calculated from all measured modes except

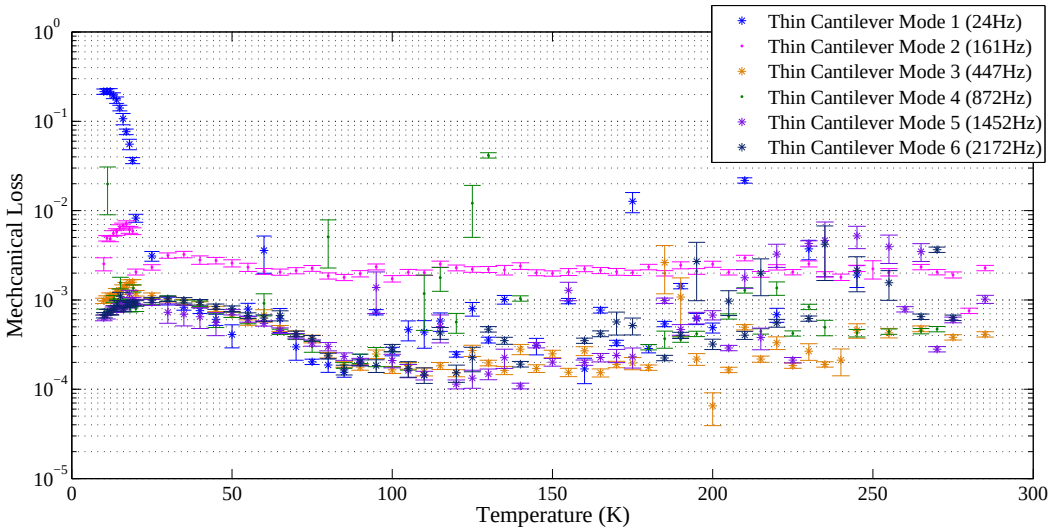

Figure 6.30: The upper limits on the mechanical loss of the oxide layers deposited on the 50μm cantilever sample.

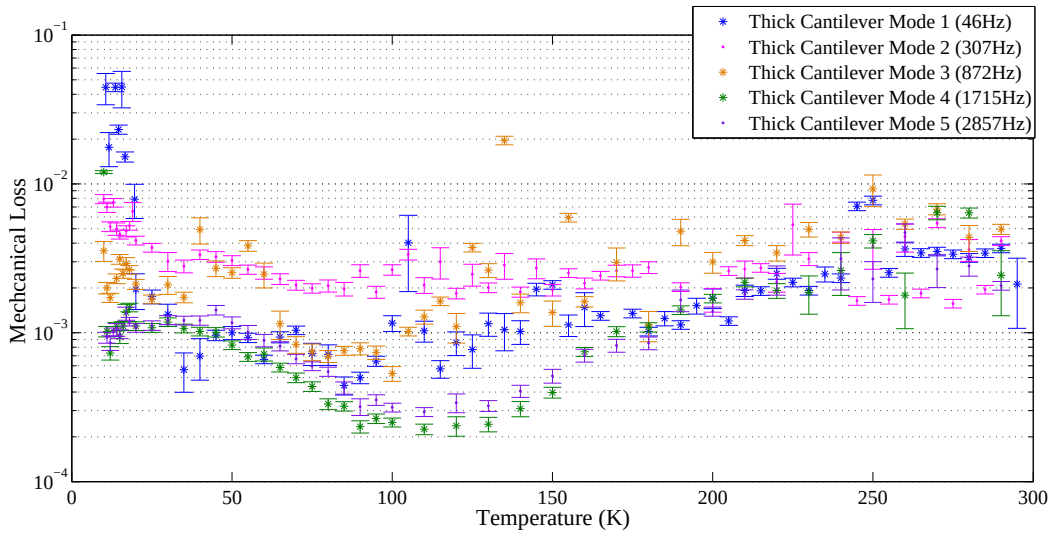

Figure 6.31: The upper limits on the mechanical loss of the oxide layers deposited on the 100μm cantilever sample.

the excessively lossy second mode (161Hz for the 50μm sample and 307Hz for the 100μm sample).

The upper limits for ϕ_{oxide} were averaged and interpolated to find a value for each temperature point in the bonded cantilever mechanical loss dataset. The values for ϕ_{oxide} were scaled by the ratios of the stored energy expressions derived in Sections 6.5 and 6.6 to provide the quantities $\frac{2E_{oxide,1}}{E_{total}}\phi_{oxide}$, $\frac{E_{oxide,2}}{E_{total}}\phi_{oxide}$ and $\frac{E_{oxide,3}}{E_{total}}\phi_{oxide}$.

The scaled oxide quantities and $\phi_{sub.TE}$ were subtracted from the mechanical loss of the bonded cantilever structure, and the remainder was scaled by the ratio $\frac{E_{bond}}{E_{total}}$ to give an upper limit upon the mechanical loss of the bond material. Usually, $\phi << 1$ and the small angle approximations apply to calculations using the me-

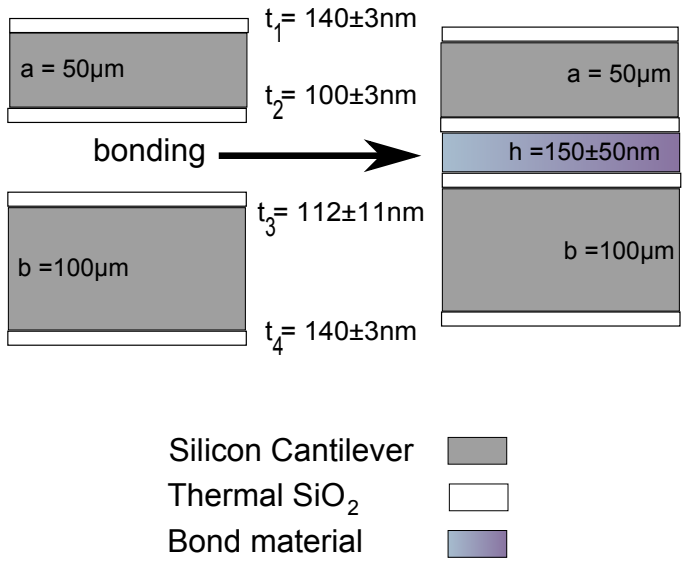

Figure 6.32: The layers of the cantilevers and structure before and after the bonding process and the dimensions used in the calculation of the energy ratio.

Property, Symbol	Value	Source
Cantilever thickness, a	$(50 \pm 1)\mu$m	Cantilever etch specifications
Oxide Thickness, t_1	(140 ± 3)nm	Ellipsometric data [99]
Oxide Thickness, t_2	(100 ± 6)nm	SEM imaging [100]
Bond Thickness, h	(150 ± 50)nm	SEM imaging [100]
Oxide Thickness, t_3	$(112 \pm 11)nm$	SEM imaging [100]
Oxide Thickness, t_4	$(140 \pm 3)\mu$m	Ellipsometric data [99]
Cantilever thickness, b	$(100 \pm 1)\mu$m	Cantilever etch specifications
Silicon Young's Modulus, Y_{sil}	164 ± 3GPa [94]	
Oxide Layer Young's Modulus, Y_{oxide}	72GPa [101]	
Bond Region Young's Modulus, Y_{bond}	7.9GPa [82]	

Table 6.2: The quantities used in the calculation of the energy ratios used in the calculation of the mechanical loss of the bond material showing the value, symbol and source of the measurement.

chanical loss angle. Some of the bond loss values resulting from this calculation are larger than 1, which means that the small angle approximations in the definition of mechanical loss cease to apply. The value calculated by the method of subtracting components and scaling by the stored energy is $tan(\phi_{bond})$, so ϕ_{bond} is recovered by taking the inverse tangent of the calculated results. A critically damped system at resonance has a mechanical loss of 2. If this is taken to be the largest meaningful loss angle, then ϕ_{max} is $tan^{-1}(2) = 1.107$.

The lowest upper limits found using this method were derived from the data for the 75Hz mode of the bonded structure. At 285K the upper limit is (1.39 ± 0.94), which is much higher than the value of $(2.8 \pm 0.4) \times 10^{-1}$ measured in [82], the values measured in [83] and exceeds the maximum meaningful mechanical loss of 1.107. The lowest value for the upper limit occurred at 80K and was (0.13 ± 0.03) and the bond loss at 10K was (0.91 ± 0.58). The bond losses calculated using the

470Hz data were close to 1 throughout the temperature range and showed little variation. The bond losses calculated using the 1320Hz data were above 1.107 and therefore unphysical near room temperature, but decreased with temperature to as low as (0.19 ± 0.04) at 16K.

6.9 Discussion and Conclusions

Bonds between oxidised silicon substrates have already been shown to have comparable strength to those between fused silica components, and this work shows that at low temperatures the mechanical loss of silicon-silicon bonds is at least as good as the loss of previously measured silica-silica bonds at room temperature. The extension of this work to low temperatures shows a minimum mechanical loss

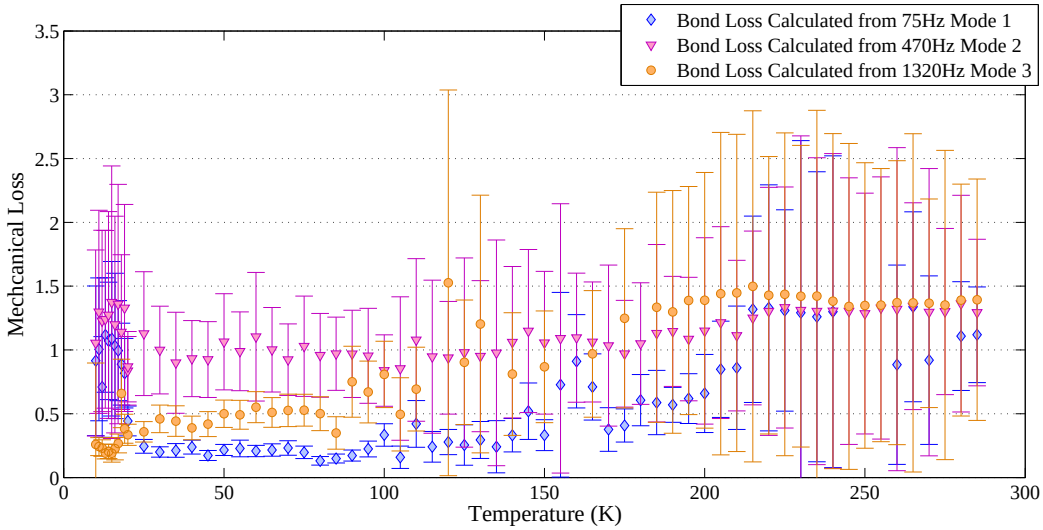

Figure 6.33: The upper limit of the mechanical loss of the bond material calculated using measurements of the first three modes, after the subtraction of the thermoelastic loss in the substrate and the mechanical loss due to the layer of thermally grown oxide.

for the bond material at around 80K and now upper limit values exist from 300K to 10K for the mechanical loss of the material in a hydroxy-catalysis bond between silicon. If it is possible to strip the outer oxide layers from the bonded structures without compromising the bond material and the values of the mechanical loss of comparable silicon cantilevers pre-oxidisation become available, then it will be possible to adjust this upper limit closer to the real value of the mechanical loss of the bond material.

At (1.39 ± 0.94) the upper limit set for the room temperature mechanical loss of the silica-gel network that forms the bond material is several orders of magnitude higher than the loss of more usual forms of silica at room temperature: amorphous ion beam sputtered silica has a room temperature mechanical loss of $(1.0 \pm 0.2) \times 10^{-4}$[79], thermally grown silica has a room temperature mechanical loss of 1×10^{-4} [51] and fused silica has a mechanical loss of 4.3×10^{-7} [102]. This wide range of mechanical losses over eight orders of magnitude shows how strongly mechanical loss may vary with changes in microscopic structure, even in materials which are chemically very similar.

This previously untested method for obtaining the temperature dependence of the mechanical loss of the material in a hydroxy-catalysis bond was successful in producing credible upper limit values for temperatures below 200K. In other measurements using this apparatus, the data above 200K often exhibited large levels of scatter and excess loss, which has been attributed to the effects of temperature cycling upon the clamp, so it is not unexpected that the data taken at higher temperatures in this experiment produced a much lossier than expected result. These

measurements show that for the fundamental mode between 20K and 200K, the upper limit on the loss of the material in an hydroxy-catalysis bond is around 0.2, with the lowest bond loss of (0.13 ± 0.03) occurring in the fundamental mode at 80K and a bond loss of (0.19 ± 0.07) occurring in the third mode at 15K. As these values are upper limits, the mechanical loss of a hydroxy-catalysis bond in a gravitational wave detector is likely to be lower across the full temperature range. Factors such as the surface quality of the silicon wafers from which the component cantilevers were etched and the surface features and stresses caused by the oxidisation process may have contributed to the irregularity of quality of the bonds measured in this work.

Chapter 7

Mechanical Loss Measurements With A Nodal Support

As stated in Chapter 2, the Brownian thermal noise from the mirror substrates is a contributing factor to the thermal noise in a gravitational wave detector and must be quantified so that an accurate noise budget may be calculated. As described in Chapter 2 a prediction of the thermal noise spectrum resulting from the use of a particular material in the optics may be calculated from the mechanical loss, $\phi(\omega_0)$, of the material if other parameters such as the Young's Modulus are known.

Fused silica substrates have been used in the optics of the current LIGO, VIRGO and GEO600 detectors. The plans for future detectors include the use of lasers of much higher power than in current detectors, and with the use of Fabry-Perot interferometer arm cavities, very high laser powers will be incident upon the optics. While the absorption of the fused silica used in the mirrors is only a few parts per million, with higher laser powers the laser energy absorbed by the substrate leads

to thermal distortions of the substrate. Thermal distortions cause fluctuations in the interferometer beam alignment and so must be counteracted or minimised.

To minimise these thermo-optic distortions in future gravitational wave detectors it may be necessary to use a different substrate material in the interferometer optics. Two candidate materials are silicon and sapphire. Sapphire substrates can be used in the same optical configurations as fused silica, but a switch to silicon optics would require more far-reaching changes: either using all-reflective interferometry schemes or moving to a laser wavelength where silicon is transparent. As future gravitational wave detectors could operate cryogenically, the properties of the potential substrate materials require investigation at low temperatures.

7.1 Loss Measurements on Bulk Substrates

As for the cantilever samples measured in earlier chapters, the mechanical loss of low loss bulk materials is easiest to measure by observation of the resonant modes of the sample. The principles of mechanical loss measurement in bulk substrates remain the same as in cantilever samples: the resonant modes must be located and excited, and then the decay of the oscillation amplitude must be measured.

Many measurements of the bulk mechanical loss of a variety of fused silica samples have been carried out, stemming from work on ultra-low loss resonators [72]. In the context of gravitational wave detectors, a mechanical loss of $\phi = 4.9 \times 10^{-9}$ has been measured at room temperature [103]. The mechanical loss of fused silica appears to vary between manufacturers [104] and sufficient data has been gathered on

the variation of mechanical loss with various parameters to allow a semi-empirical model to be developed that describes the mechanical loss of a piece of silica as a function of frequency and surface/volume ratio [105]. In this model, the loss of bulk fused silica is given by,

$$\phi(f, \frac{V}{S}) = C_1 \left(\frac{V}{S}\right)^{-1} + C_2 \left(\frac{f}{1Hz}\right)^{C_3} + C_4 \phi_{TE}, \tag{7.1}$$

where $\frac{V}{S}$ is the volume/surface area ratio of the piece of silica, f is the frequency and ϕ_{TE} is the thermoelastic loss calculated using Equation 2.40. The constants C_1, C_2, C_3, and C_4 vary with each variety of fused silica.

Sapphire is a crystalline form of aluminium oxide with a rhombohedral crystal structure that leads to anisotropies in its material properties. Synthetically grown single sapphire crystals can be sliced and polished to a similar quality to fused silica optics. The lowest known loss in sapphire at room temperature is 2×10^{-9} for a resonator measured by Braginsky [106]. Sapphire was chosen as the substrate material for LCGT [37][38] after a study showed that a sapphire cylinder of 100mm diameter and 60mm length suspended on sapphire fibres had a mechanical loss of 4.0×10^{-9} at 4.2K and 2.2×10^{-7} at 300K [107].

Crystalline silicon is of particular interest for potential cryogenic detectors as the linear coefficient of thermal expansion drops to zero at around 125K and 18K. As described in Chapter 2, the magnitude of thermoelastic loss is described by,

$$\phi_{TE} \sim \frac{E\alpha^2 T}{C} \tag{7.2}$$

where E represents Young's Modulus, α is the linear coefficient of thermal expansion, T is the temperature and C is the heat capacity of the material, the contribution of thermoelastic dissipation to thermal noise could be negligible at these temperatures [66]. Investigations of the mechanical loss of silicon over the temperature range 4K-273K are therefore of interest as part of the investigation of candidate optical substrate materials for future gravitational wave detectors.

At room temperature, the lowest published mechanical loss for crystalline silicon is 1×10^{-8} [104], although unpublished results from Glasgow show that it is possible to reach lower losses at room temperature - a mechanical loss of 8.51×10^{-9} was measured for one mode of a silicon cylinder oriented along the (111) crystal axis [83]. At low temperatures, a Q factor corresponding to a mechanical loss of 5×10^{-10} was measured by at 3.5K on a silicon cylinder oriented along the (111) crystal axis whose room temperature mechanical loss was 5×10^{-8} [108]. The very low mechanical loss of silicon at low temperatures may be approaching the level of dissipation introduced by the method used to support the sample. A method of suspending bulk samples for mechanical loss measurements which effectively eliminates support losses may improve the quality of low temperature mechanical loss measurements so that recent measurements of extremely low mechanical losses at room temperature may lead to measurements of even lower mechanical loss at low temperatures.

7.2 Motivation for an Improved Suspension Method

Mechanical loss measurements made at Glasgow and elsewhere suggest that the method of supporting a bulk sample on a silk thread or tungsten wire can introduce additional mechanical loss, termed 'support loss' [106][58]. By rotating a silicon sample in a silk thread suspension and performing a series of mechanical loss measurements on resonant modes with four-fold symmetry, it was observed that the mechanical loss oscillated between higher and lower values with a period of 90°, suggesting that some vibrational coupling exists between the motion in certain resonant modes and the 'break-off points' where the thread suspension loses contact with the barrel of the sample [83].

Kenji Numata, working at the University of Tokyo, developed the nodal support as a method of securing bulk samples that eliminated the presence of a 'break-off point' and could potentially eliminate support losses for certain resonant modes [109]. Using the nodal support, Numata made a series of mechanical loss measurements on a single crystal silicon cylinder; the lowest measured mechanical loss was 1×10^{-8}. Numata also compared the losses of 21 measured modes with the r.m.s. mean displacement at the nodal contact point for that mode, and found that the mechanical loss decreases linearly with decreasing displacement at the contact point [104].

7.2.1 Finite Element Calculations of Strain Energy Ratios

If the effectiveness of a nodal support for a particular resonant mode depends on the amount of motion present at the nodal contact point, then it may be possible

to determine for which modes of a bulk sample a nodal support may outperform a thread suspension.

By modelling a silica sample of the typical size used in the mechanical loss measurements of bulk substrates using the finite element analysis package, ANSYS, the deformed shapes and strain energy distribution of the various resonant modes can be calculated. Figure 7.1 shows the total displacement of the surface of the substrate, which is $\bar{d} = \sqrt{dx^2 + dy^2 + dz^2}$ for each element in the simulated substrate. The value for $\bar{d}$ is normalised to give the value as a dimensionless number between 0 and 1. In Figure 7.1 dark blue is the lowest level of displacement and dark red is the highest.

By selecting only the elements where the silk suspension loop contacts the mass - those around the centre of the barrel of the sample - the ratio of the elastic strain energy in the contact region to the total elastic strain energy of each modeshape can be calculated. Assuming that the additional dissipation in suspended mechanical loss measurements can be correlated with friction between the most highly deformed and energetic regions of the mass and the suspension loop, it can be seen that certain modes ought to experience more support loss than others.

McMahon developed a classification system for the description of mode shapes in isotropic, elastic cylinders [110]. The degree of rotational symmetry of the displacement of the modeshape corresponds to the order, n, of the mode. The modes can further be divided into the categories *symmetric* and *antisymmetric*, which de-

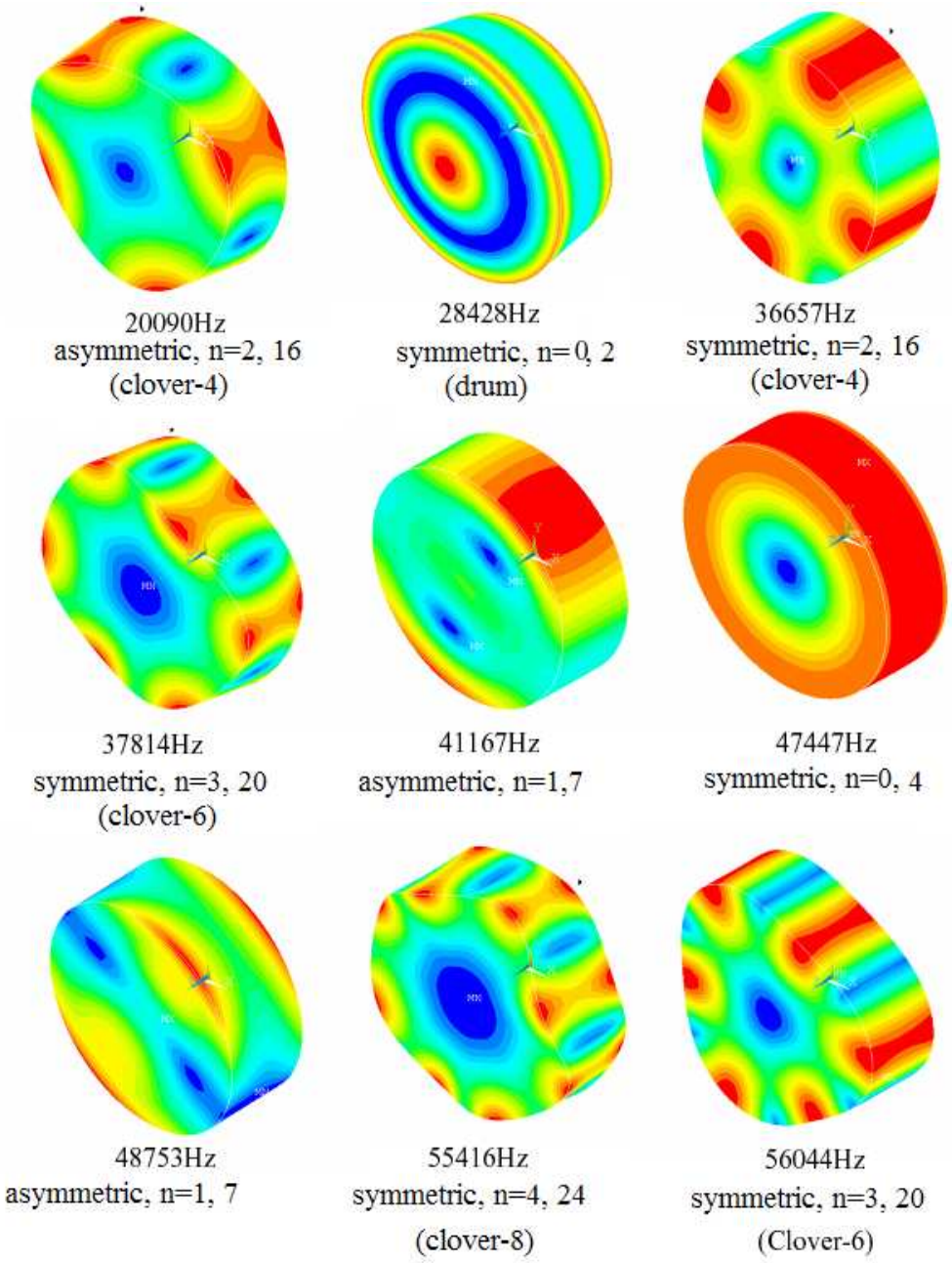

Figure 7.1: A summary of the normalised total displacement in the deformed mode shapes of resonant modes of a silica sample of 25mm diameter and 75mm length.

scribes whether the motion of the cylinder is symmetric about a plane across the diameter, halfway along its length. McMahon also gave numbers to modeshapes within these categories. In the results of the finite element analysis calculations, the McMahon method of modeshape classification is used to identify particular modeshapes.

By examining the deformed modeshapes, a broad category of modes which experience a high degree of deformation around the barrel, and experience little or no motion at the centre of the face can be identified. These are the modes which are described by the McMahon system as having a mode order where $n > 1$. The common laboratory term that developed for this class was *clover-m* modes, where m is the number of areas of high motion around the circumference of the mass (see Figure 7.1 for pictoral examples). Assuming that some of the excess loss is support loss caused by friction between the break off point of the suspension material and the vibrating mass, then reducing or removing contact with the regions which vibrate most vigorously could diminish the excess loss. By replacing the silk suspension loop with a point contact at the points of minimum motion on the centres of the test mass faces, it may be possible to obtain a loss measurement which approaches the true intrinsic loss of the material.

In order to illustrate this, the ratio of strain energy present in the region around the centre of the test mass face to the total strain energy was calculated using the ANSYS model referred to above. This allows a comparison between the potential for dissipation in loop suspended loss measurements and nodally supported loss measurements. The two sets of calculated strain energy ratios can be seen in Fig-

ure 7.2. A larger strain energy ratio means that larger displacement occurs in that contact region, and therefore a higher level of excess loss.

Using the model used to produce Figure 7.2 to examine individual modes, it can be seen that the stored energy ratio for the thread suspension region of the fundamental mode at 28.4kHz is significantly larger than the stored energy ratio

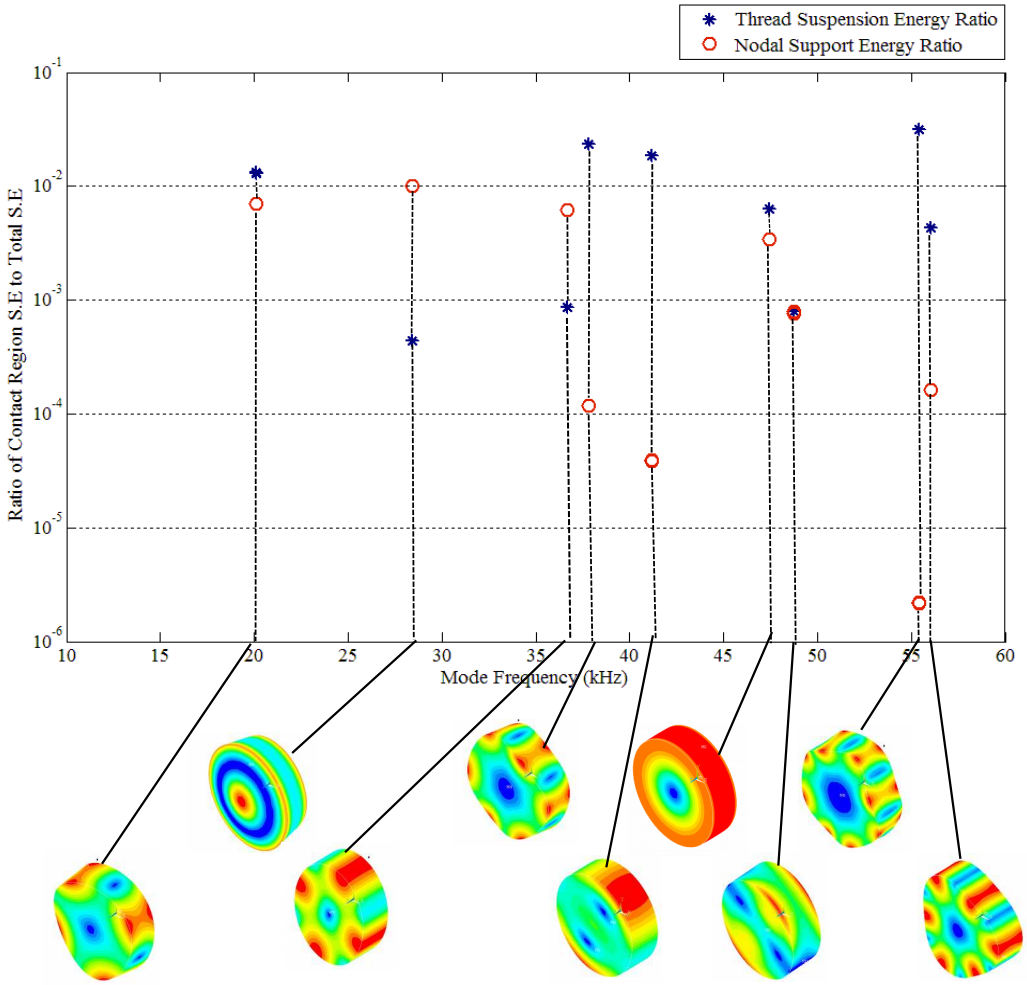

Figure 7.2: The ratio of elastic strain energy in the contact region to total elastic strain energy, with the modeshapes at each frequency for comparison.

for the nodal support region. This would imply that you would expect that the nodal support would experience a larger amount of excess support loss than the thread suspension for this mode. In the cases of the three simple *clover-m* modes at 20.1kHz, 37.8kHz and 55.4kHz, the thread suspension energy ratio is always higher than the nodal support energy ratio, and as m increases, the 'advantage' of the nodal support over the thread suspension increases.

These models indicate the lowest excess support losses will be experienced when using a nodal support to measure high m value *clover-m* modes.

7.3 Nodal Support Tests with Sapphire

Mechanical loss measurements on bulk substrates differ in the readout method used to determine the amplitude of the resonant oscillations. The sample is isolated from external vibrations and disturbances using the chosen support method, placed in an evacuated vessel and then its resonant modes are excited independently using a high frequency oscillating electric field generated by an excitation plate. The motion of the front face of the bulk sample in any mode is much smaller in magnitude than that seen in the bending modes of the silicon cantilevers measured in earlier chapters and so a simple Michelson interferometer is used to monitor the amplitude and frequency of the oscillations.

Initial tests of the nodal support were conducted in a high vacuum tank which had been used previously for thread suspension loss measurements. The prototype nodal support was constructed from adapted mirror mounts bolted into an aluminium baseplate, with support rods tipped with ruby spheres. The nodal support was constructed for the measurement of cylindrical samples measuring 75mm in diameter with a thickness of 25mm, and the support rods were positioned in order to contact the centre of the face of the sample. The baseplate was bolted, upside down, into the existing suspension frame, and an electrostatic exciter plate was positioned close to the back face of the sample.

This prototype was used in the measurement of a single crystal sapphire sample that had previously been thoroughly characterised using a thread suspension [83].

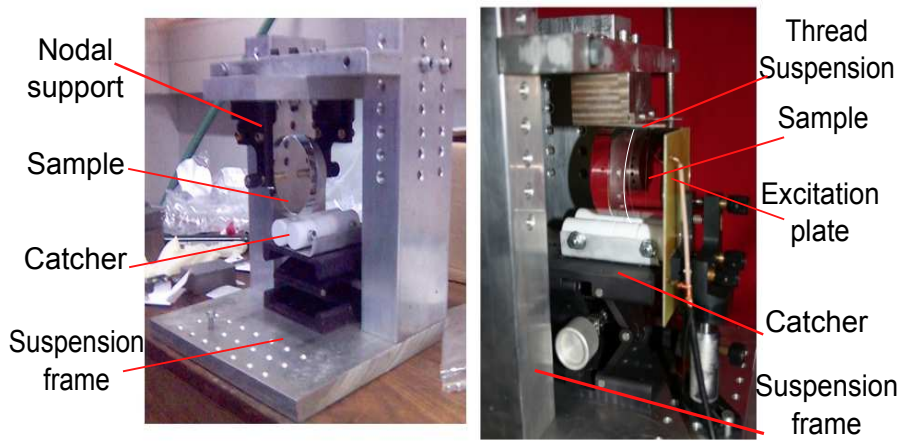

Figure 7.3: The suspension cradle with a 76mm diameter silica cylinder sample in a prototype nodal support fitted (left) and a thread suspension (right).

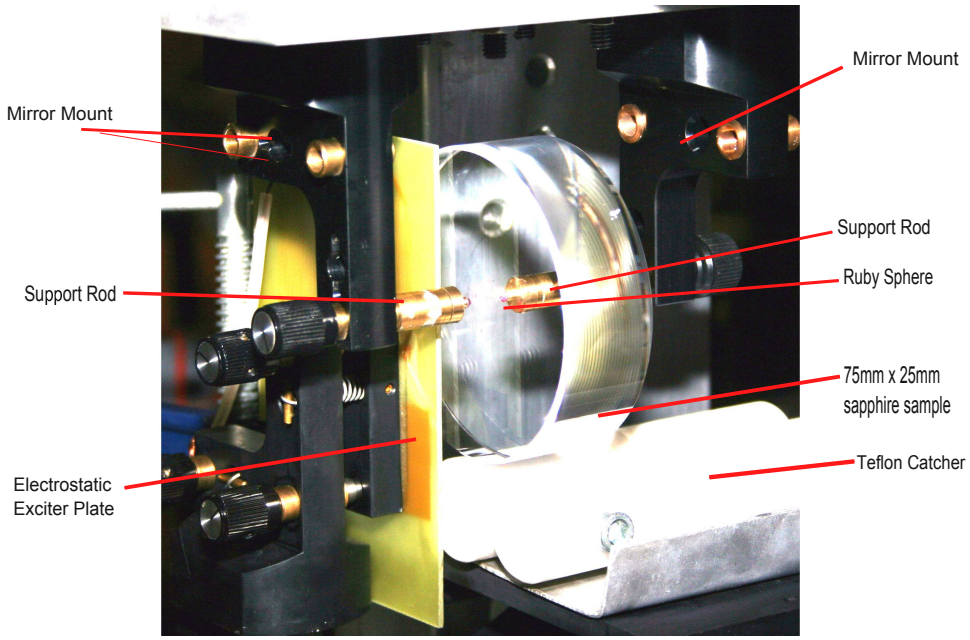

Figure 7.4: The prototype nodal support showing major features, with a 76mm diameter silica cylinder sample in position.

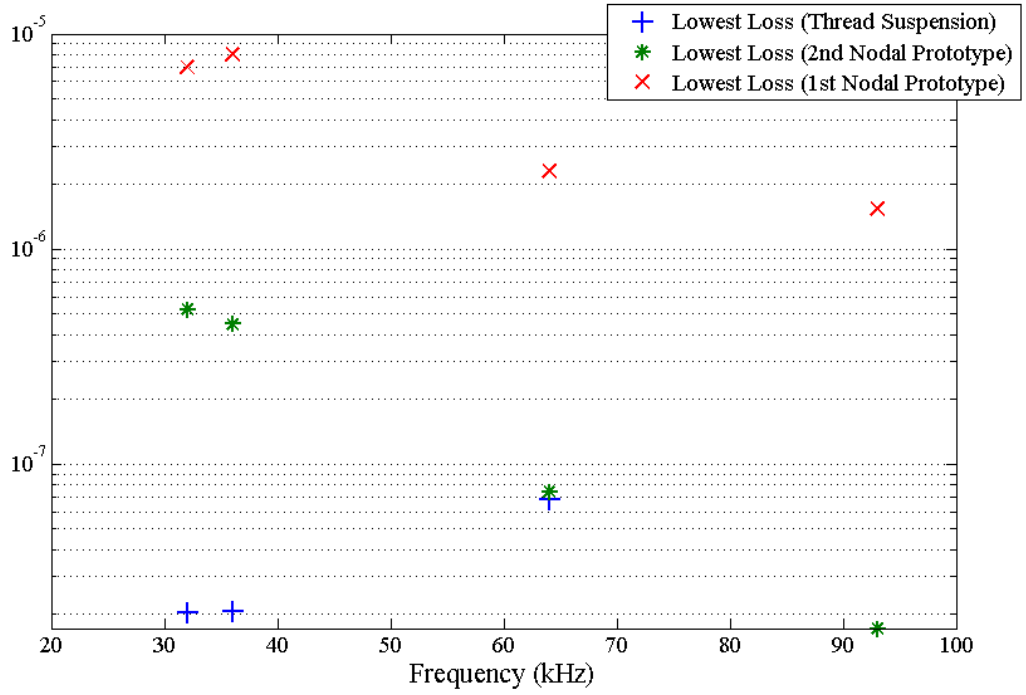

Figure 7.5: Mechanical losses measured on a cylindrical sapphire sample using two iterations of the prototype nodal support, compared with the best mechanical losses measured with a thread suspension.

7.3.1 Improvements to the Prototype Nodal Support - Designing NS2

These initial tests indicated that the nodal support itself was responsible for some of the measured dissipation, and that a lossy contact at a node can still be worse in terms of dissipation than a low loss contact at a region of large displacement. The nodal support was redesigned to produce NS2, which featured increased rigidity. The threaded support rods were replaced with heavier, sliding support rods that were bolted through into the structure of the nodal support. The ruby spheres were held in press-fit cavities in order to reduce the potential for dissipation caused

by motion of the ruby ball against the holder.

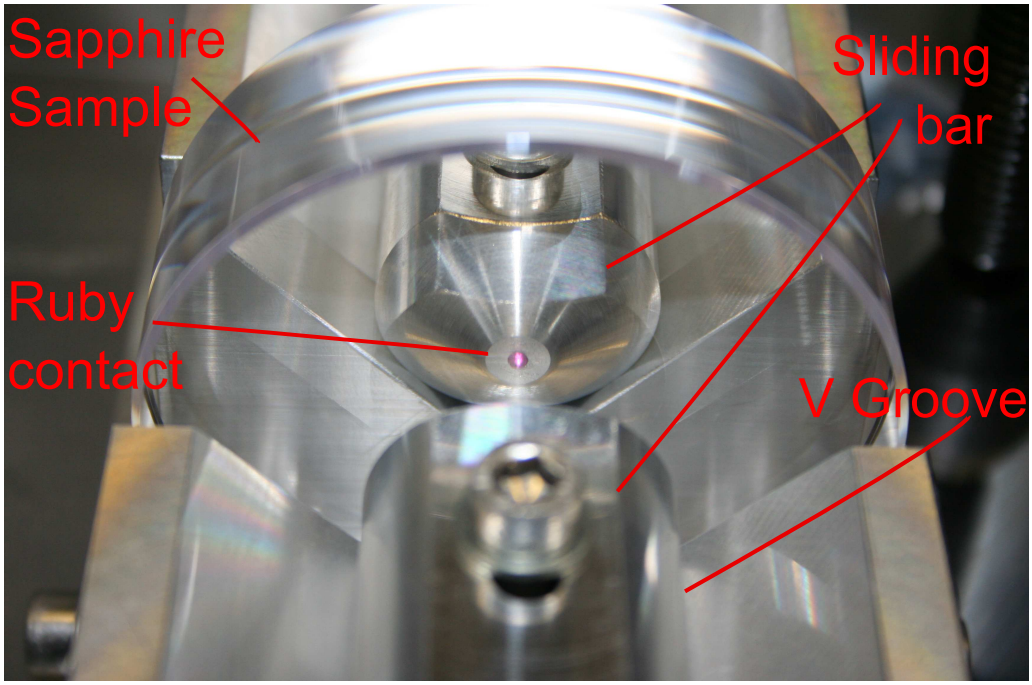

Figure 7.6: The improved nodal support (NS2), showing one of two ruby spheres contacting a sapphire sample.

It was also apparent from the small scratches present on the surface of the measured test masses that the prototype had not always been positioned over the same point at centre of the face. The improved nodal support was machined to position the centre of the mass to a higher tolerance and a V-block structure also worked to keep the support rods in the correct position. In theory, this positioned the centre of the mass to an accuracy of 0.1mm, by manoeuvreing the sample into the correct position by the use of two removable catchers that were designed to be of the correct size to allow the desired contact point to meet the ruby sphere.

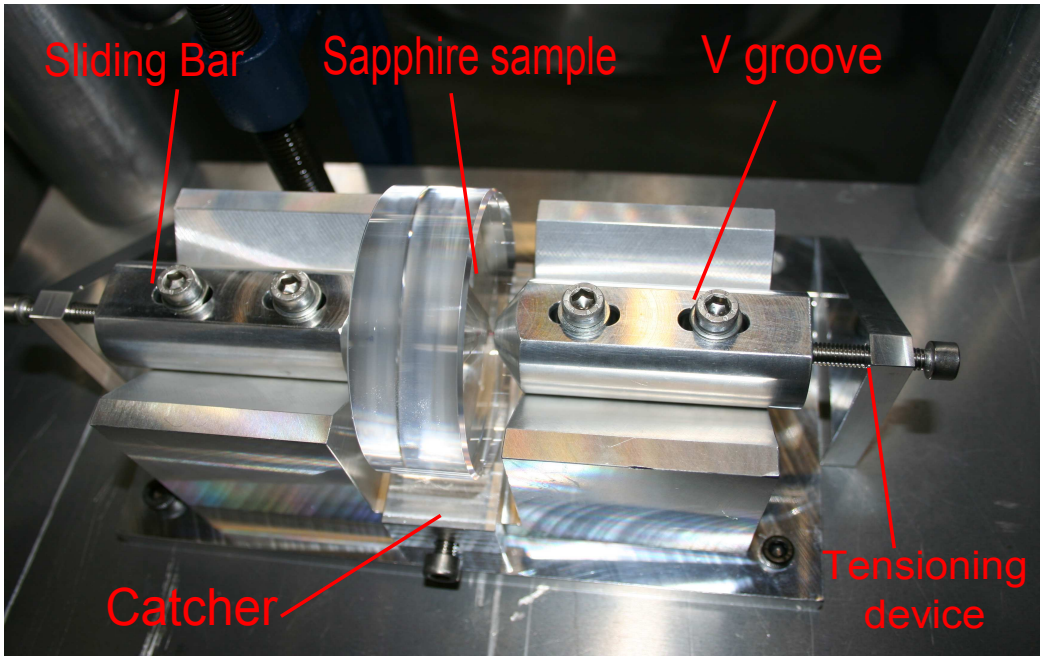

Figure 7.7: The improved nodal support (NS2) showing major features.

7.4 Room Temperature Measurements of Silicon Using NS2

One aim for the nodal support is to provide a safe, low-loss support method to aid in the measurements of bulk samples at low temperatures that will provide information leading towards a substrate material choice for the optics in future gravitational wave detectors. With a view to repeating these measurements at lower temperatures, the improved nodal support was used to measure a silicon cylinder sample that had previously been measured using a thread suspension.

The silicon sample studied was 75.4mm in diameter, with a thickness of 25.4mm and the crystal axes aligned so that the [1,1,1] direction is perpendicular to the front face of the mass. ANSYS modelling of this mass using finite element analysis found the total normalised surface displacement resonant modes as summarized in Figure 7.8, where dark blue is minimum displacement and dark red as maximum displacement [110].

The sample was suspended in the nodal support by placing the sample on two aluminium catchers that held the sample in a position where the centre of the face of the mass was at the correct location to be contacted by the ruby tips of the nodal support rods. The sample was then suspended by compressing the rods using a specially constructed vice-like device tightened with measured torques applied with a torque wrench.

Once the sample was held securely, the catchers were then removed, leaving the

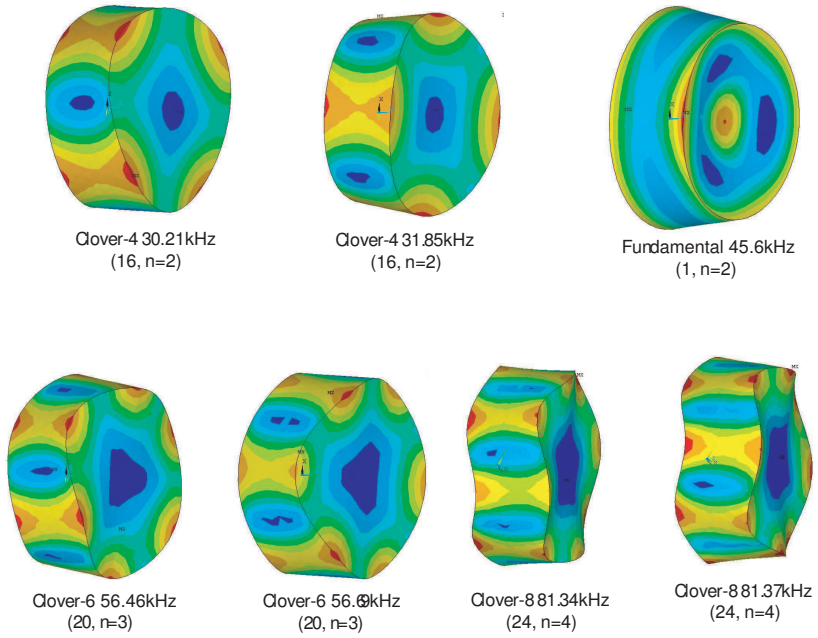

Figure 7.8: Summary of total surface displacements for the resonant modes for a silicon sample (75mm diameter x 25mm thick).

sample supported only at the centre of each face. The nodal support assembly was then placed on a bench inside a vacuum tank, with an electrostatic drive plate positioned ∼2mm away from the back face of the sample. The oscillations of the front face of the sample were sensed using an interferometric laser readout. The mechanical loss measured using the NS2 nodal support shows the same frequency dependence as that measured using the NS1 nodal support. For the lowest frequency modes satisfying the symmetry criterion (16, n=2) [110], the best nodal support measurements are over an order of magnitude worse than the best measurements made using a silk thread suspension.

The apparent frequency dependence could be due to coupling between the resonant modes of the sample and the modes of the nodal support. The contact

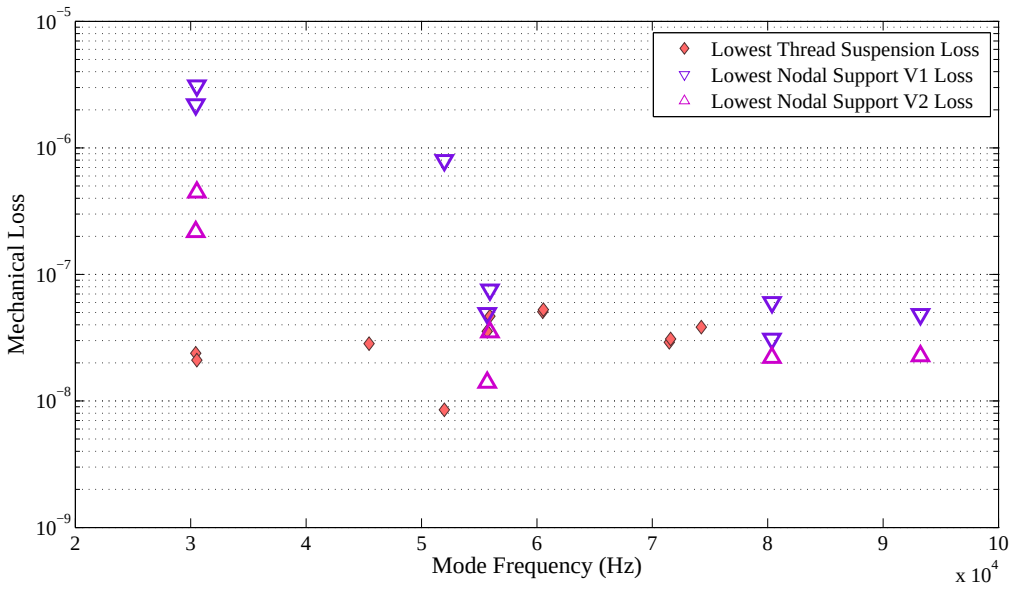

Figure 7.9: Summary of mechanical loss measurements for nine resonant modes of a silicon sample (75mm diameter x 25mm thick).

region over the centre of the disc encompasses not just the nodal point of zero motion but also points which are experience displacement in the resonance. The ANSYS modelling in Section 7.2 suggests that for the lower frequency modes there is a larger magnitude of motion in the contact region for nodal supports, resulting in more coupling between the substrate and support. This implies that excess loss caused by this coupling may be present when measuring the lowest modes with a nodal support. The highest frequency modes measured in this experiment produced mechanical losses as low as or lower than the best thread suspensions, as predicted in Section 7.2.

The main achievement of this series of measurements is that for the pair of resonant modes at 55.6kHz and 55.9KHz, the mechanical loss measured with NS2 was

lower than that measured with a silk thread suspension. As with the measurements of a sapphire coin using the prototype nodal support in Section 7.3, it was possible to measure high frequency modes which had been previously inaccessible using a silk thread suspension. The mechanical loss measured for these modes was in broad agreement with the loss levels measured for other modes using a silk thread suspension.

7.4.1 Sample Surface Damage

After repeated use of the nodal support on the silicon sample described above, damage to the sample was noted. Silicon lies at 6.5 on the Mohs hardness scale and could therefore be expected to be scratched by a ruby at 9.0, especially when held in compression. All samples used with the nodal support display some signs of damage. A Veeco interferometric profiler was used to investigate the damage to the surface of the silicon sample.

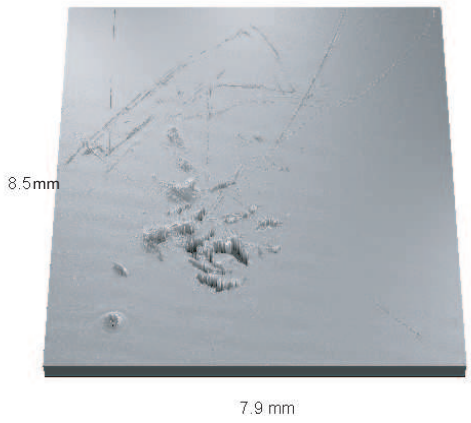

Figure 7.10: Profile of a 8.5mm x 7.9mm region of the surface of cylindrical silicon sample, 75mm diameter x 25mm thick, showing surface damage caused by the nodal support.

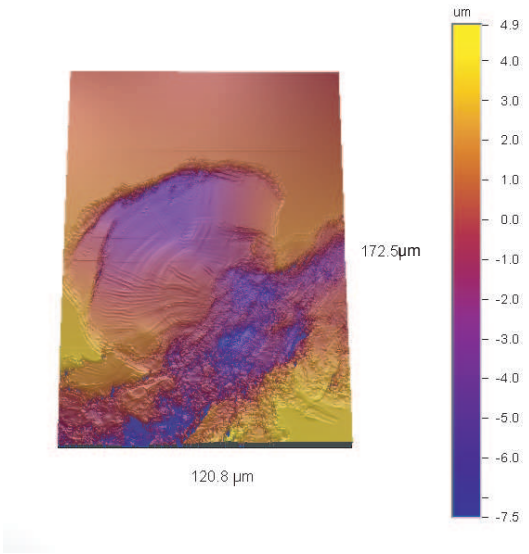

Figure 7.11: Detail of Figure 7.10, showing the profile of a scratch 7μm deep next to a chip 3μm deep.

This damage, while worrying in appearance, may not necessarily have had a detrimental effect on the mechanical loss values measured. Over several sets of measurements, between which the suspension was changed and the repeated repositionings presumably increased the level of damage, the measured mechanical loss remained roughly constant. However, the surface damage makes this nodal support unsuitable for use with coated samples or samples with delicate surface features such as diffraction gratings.

7.5 Cryogenic Measurements With A Nodal Support

The overall aim of these measurements of mechanical loss is to work towards a description of the thermal noise in silicon between 273K and 4K. The method for

measuring mechanical loss at room temperature can be extended to low temperatures, but special consideration must be given to the behaviour of the mass and the nodal support itself during cooling.

7.5.1 Experimental Design

Initial attempts had been made to measure the mechanical losses of bulk samples supported by thread suspensions cryogenically, but the processes of sealing the cryostat and cooling the setup caused levels of mechanical vibrations which caused the extremely delicate suspensions to fail. If the nodal support could be relied upon not to drop, damage or add excess loss to the sample, then it could be used for low temperature mechanical loss measurements.

Initial calculations showed that thermal contraction of the nodal support could have possibly unwanted effects. Between 300K and 77K, 25mm of silicon contracts by 6μ m and a 25mm gap in a body made of aluminium contracts by 97.5μ m. Effectively, the nodal support will attempt to compress the silicon resulting in a large increase in the force applied through the ruby contacts. If the nodal support is not well centred when this compressive force is applied, the sample may shift in the support or the suspension may fail.

In order to ascertain the effects of the compression from cryogenic contraction, the silicon sample was suspended in the nodal support in the usual manner, and then partially lowered into a bath of liquid nitrogen and monitored as it cooled. Three such trials took place; in the first trial (using 20Nm of torque to secure the

mass) the mass slipped from the nodal support during the warming phase, and one of the ruby contacts was found to have shattered. This could be due to a crack that had formed during manufacture and was exacerbated by cooling, or it is also possibly that the contraction of the nodal support around the mass could have caused the ruby to shatter. Two further cooling trials used 15Nm to support the mass, and were successful.

It was also observed that the mass took much longer to cool than the nodal support. This supports the idea that, just as the nodal support technique is an effective method of preventing mechanical dissipation, it is also a poor thermal transfer route. The force that the nodal support exerts upon the sample can be calibrated at room temperature using a torque wrench, but as the mass and nodal support contract during cooling, the clamping force will increase and possibly cause further surface damage.

7.5.2 NS2 Low Temperature Silicon Measurements

The improved nodal support was used in a cryogenic mechanical loss measuring setup based around the cryostat pictured in Figures 7.12 and 7.13. The nodal support sat in a tray suspended from the cold plate of the experimental chamber by threaded rods.

The temperature of the experimental chamber was monitored using DT-670 silicon diode sensors and a Lakeshore 340 temperature controller. One temperature sensor was attached to the top plate of the chamber and one attached to a support

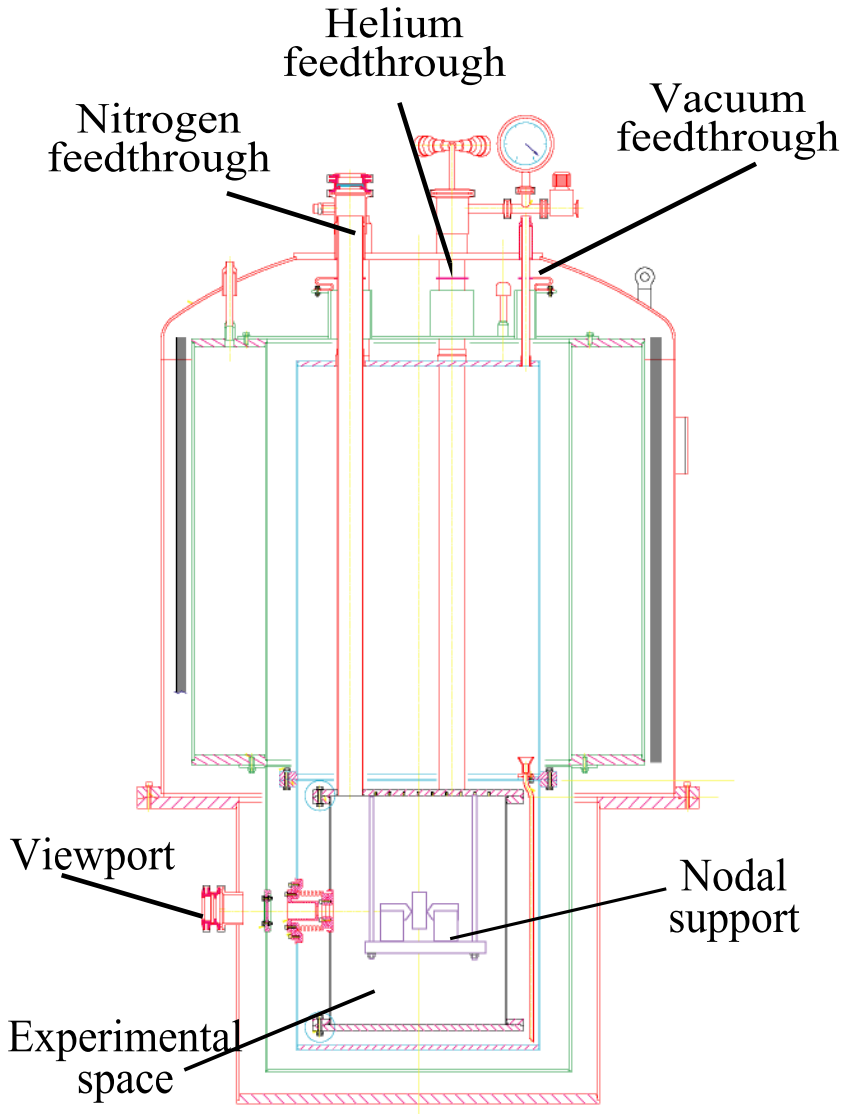

Figure 7.12: Schematic of large cryostat showing optical, electrical, vacuum and cryogen feedthroughs, plus detail showing placement of NS2 in experimental chamber

rod of the nodal support.

The cryostat has two spaces for cryogens, an inner space which is intended for liquid helium, and an outer space for liquid nitrogen. In these measurements, liq-

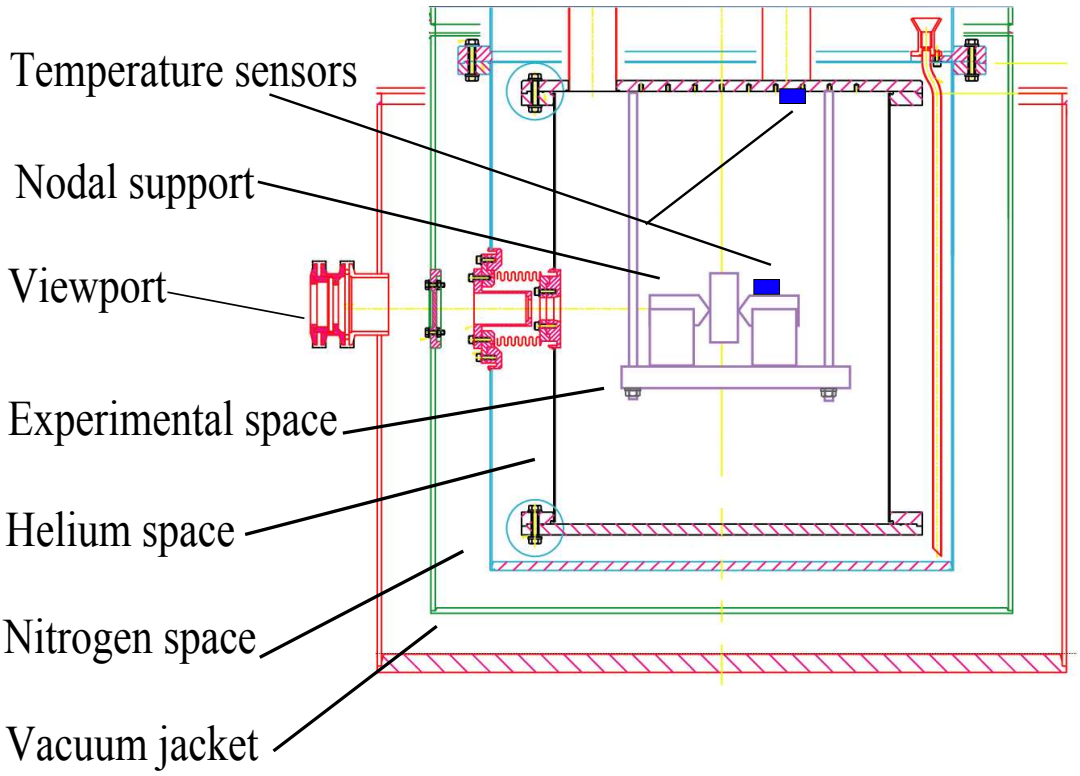

Figure 7.13: Detail of schematic of large cryostat showing optical, electrical, vacuum and cryogen feedthroughs, plus detail showing placement of NS2 in experimental chamber

uid nitrogen only is used. The most efficient initial cooling was achieved by filling the helium space with liquid nitrogen and allowing the chamber to cool for six hours.

Cooling of the experimental chamber proceeded more quickly if the chamber was at a pressure of 10^{-4}bar, rather than the high vacuum of 10^{-6}bar. Conductive cooling of the nodal support was fairly slow, due to the poor thermal transfer route provided by the threaded rods, but operating the tank at a slightly higher vacuum pressure allowed for a faster cooling rate without risking water vapour freezing onto the nodal support and mass. After six hours, the nodal support

was at around 200K and the top plate at around 130K - after this, the nitrogen and helium spaces were filled alternately with 25L of liquid nitrogen. Filled in this manner, the experimental chamber cooled at a rate of 5K/h and reached 77K in just over two days. The setup returned to room temperature naturally at an average rate of around 3K/h. It can be seen in Figure 7.14 that the nodal support continues to cool for over 1000 minutes after the temperature of the cold plate began to rise, indicating that all liquid nitrogen had boiled away. This lag in cooling is likely to result from the poor thermal conduction path between the cold plate and the nodal support along the threaded rods. The poor thermal conductivity also results in a significant lag in the warming of the setup, with the temperature of the nodal support being lower than that of the cold plate from 3000 minutes to the end of the cooling run.

During the initial cooling run, water vapour froze onto the inside of the outermost viewport, so the laser beam did not contact the test mass face and so no mechanical loss values could be measured. The seals of the cryostat were remade and the vacuum system left to pump out water vapor over a weekend, so that on the second cooling run the viewport remained free of frost. Mechanical loss values were measured at room temperature and for two lower temperatures, 100K and 150K. The measurements are shown in Figure 7.15 and show that the overall trend was for mechanical loss to decrease as temperature decreased. As the temperature sensor was placed upon the clamping bar of the nodal support, rather than the test mass itself, the recorded temperatures will differ from the true temperature the test mass itself. The poor thermal transfer through the ruby ball contacts means that the cooling of the test mass will significantly lag the clamp cooling.

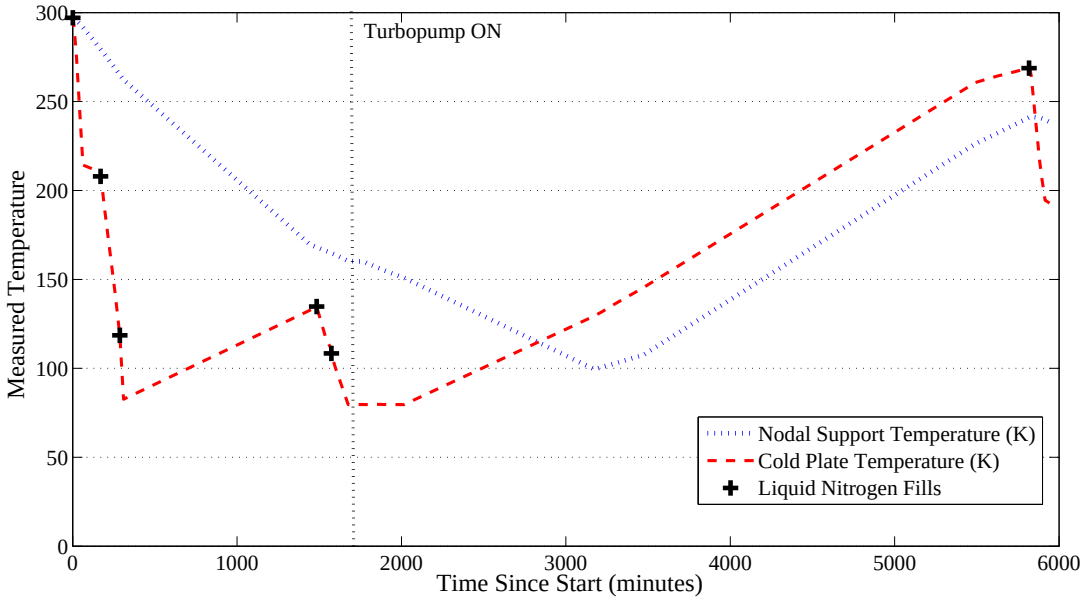

Figure 7.14: Temperature measured at the nodal support and at the top plate of the experimental chamber over 6000 hours, showing the times at which liquid nitrogen was added to the cryostat.

While the clear downward trend in mechanical loss with decreasing temperature displayed in these results was as expected, the measurements taken in the cryostat at 294K were an order of magnitude worse than the best values achieved with NS2 in the room temperature tank.

Significant alterations would be required to construct a nodal support that could produce a credible series of low temperature measurements. The contacts would be required to exert a constant force upon the sample at all temperatures between 4K and 300K, which requires very careful matching of the thermal contractions of the components of the nodal support. The central axis of the nodal support should be made vertical to allow for easier balancing of the sample and to reduce

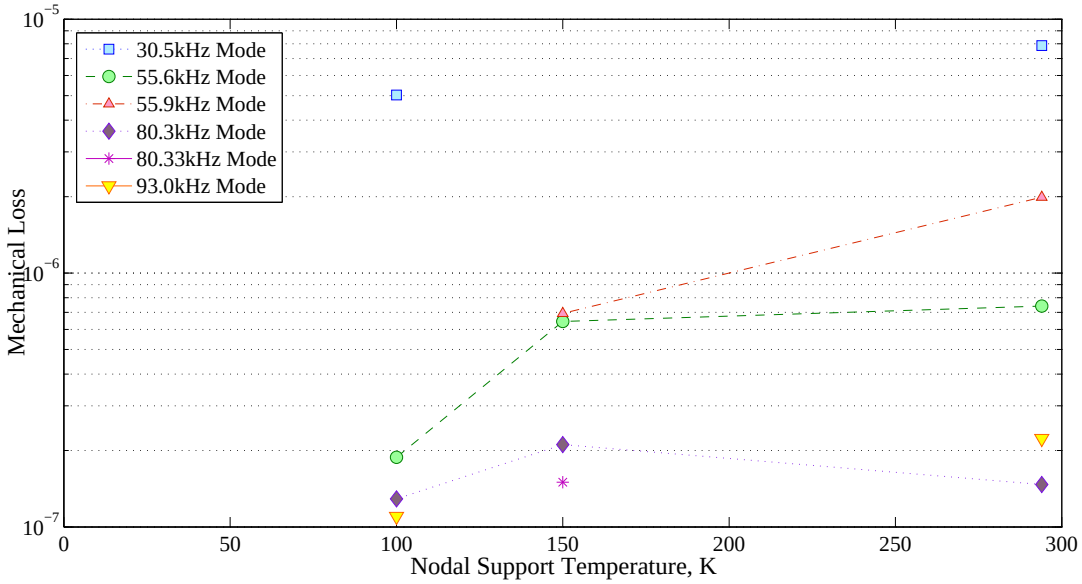

Figure 7.15: Summary of low temperature mechanical loss measurements for six resonant modes of a silicon coin sample.

the amount of force required to secure the sample.

7.6 Conclusions

A nodal-type support may be a good way of effectively removing the excess losses associated with the sample support, but the NS2 nodal support described in this work is not suitable for the intended purpose of producing non-destructive measurements of the mechanical loss of silicon at temperatures below 300K.

At room temperature, the lowest measured mechanical loss using a nodal support was 1.8×10^{-8} for a 55.6kHz mode and a mechanical loss of 2.3×10^{-8}. When measured in the cryogenic bulk mechanical loss measurement apparatus, the mechanical losses of the 55.6kHz mode ranged from 7.4×10^{-7} at 300K to 1.7×10^{-7}

at a nodal support temperature of 100K. The lowest loss measured at low temperature was 1.1×10^{-7} for the 93kHz mode.

The poor losses measured at room temperature in the cryostat are likely to be connected with the lack of rigidity in the system attaching the nodal support to the cold plate of the cryostat. In the development of the nodal support at room temperature it was found that the lowest losses were measured when the nodal support was highly isolated from external vibrations by stiff rubber pads. The threaded rods used in the cryostat system are unlikely to have provided the requisite level of vibrational isolation. The observed surface damage to the silicon sample may have caused the low losses measured at all temperatures.

Chapter 8

Conclusions

The global network of gravitational wave detectors relies on many advanced technologies to obtain the levels of sensitivity required to even have a chance of detecting a gravitational wave signal from a distant astrophysical event. To increase the chances of detection, further advances in technology are required to drive down the levels of all noise types in the interferometer system. Work is underway to reduce the levels of noise resulting from external vibrations, quantum fluctuations, and thermally-induced dissipation which is present in the interferometer signal.

A critical factor for future gravitational wave detectors is the reduction of the thermal noise in the interferometer optics, especially in the dielectric multilayer coatings used to achieve the high laser powers in the interferometer arms. The thermal noise resulting from the use of a particular material in an interferometer is proportional to the square root of the mechanical loss of the material. In this thesis, the variation of mechanical loss with temperature was measured for some of the candidate materials for future gravitational wave detectors. A table-

top cryogenic mechanical loss measurement apparatus was constructed to produce measurements of coated and uncoated silicon cantilever samples between 10K and 300K. Two anomalies in the mechanical loss measurements made using this apparatus were discovered: anomalously high mechanical losses at low temperatures in the fundamental mode caused by the excitation system and high losses at around 250K related to the thermal cycling of the sample clamping method.

Ion-beam sputtered silica coatings are currently used in the dielectric multilayer coatings in gravitational wave detectors. In this thesis, measurements of a ion-beam sputtered silica coating heat-treated at 300^{o}C found a Debye peak, Arrhenius analysis of which provided a characteristic energy of (17.3 ± 2.3)meV for the dissipation process causing the Debye peak. Measurements of silica coatings heat-treated at 600^{o}C and 800^{o}C showed that the Debye peak appeared to narrow, which was thought to be indicative of the narrowing of the distribution of bond angles in the amorphous silica network. None of the heat-treatment temperatures significantly reduced the magnitude of the mechanical loss in the Debye peak. Further research is still required to reduce the contribution of the silica component to the thermal noise resulting from multilayer coatings, but the work presented in Chapter 4 of this thesis adds to the knowledge of the dissipation processes in silica.

Hafnia was investigated as an alternative coating material in Chapter 5. The mechanical loss of hafnia heat-treated at 300^{o}C was measured and two excess loss features were discovered below 100K and above 200K, but neither had the sharp rise in mechanical loss that marked it as a Debye peak. Electron scattering measurements indicate that this sample may already have developed polycrystalline

regions which are known to be connected to high levels of mechanical loss. The mechanical loss of an un-heat-treated hafnia coating is also measured and a coating loss of 1.87×10^{-5} is found at 20K. At temperatures in the 10-20K range, un-heat-treated hafnia has a factor of three lower loss than tantala. The combination of the lower intrinsic mechanical loss and the higher refractive index means that less material is required to produce the $\lambda/4$ optical length required. These two factors mean that a hafnia/silica multilayer coating would cause less thermal noise at low temperatures than a tantala/silica multilayer. Unfortunately, the optical absorption of hafnia is not low enough to sustain the high powered laser beams used in future detectors. If the optical properties of hafnia coatings can be controlled, hafnia is a promising candidate for a high refractive index dielectric coating material.

Future gravitational wave detectors are likely to require the use of hydroxy-catalysis bonding between silicon components, possibly in the construction of suspensions or in composite masses. Chapter 6 described a new experimental technique for measuring the mechanical loss of a hydroxy-catalysis bond between silicon cantilevers at temperatures between 10K and 300K. This new technique for the measurement of the mechanical loss of bond material produced an upper limit of (0.13 ± 0.03) occurring in the fundamental mode at 80K and an upper limit bond loss of (0.19 ± 0.07) occurring in the third mode at 15K. The apparent decrease in the mechanical loss of bond material at low temperatures is a good indication that hydroxy-catalysis bonding may be a suitable technology for future cryogenic silicon-based gravitational wave detectors.

The substrates of gravitational wave detectors also contribute thermal noise, and

in Chapter 7 the development and testing of a nodal support system to enable cryogenic measurements of cylindrical bulk mirror substrates was described. The nodal support was effective at producing mechanical loss measurements of high order clover-type modes, but ineffective for low frequency modes and non-clover-type modes, as predicted by finite element analysis. The nodal support was found to cause damage to the contact region of the silicon sample, possibly reducing the mechanical loss measured from the sample. Low temperature measurements using the nodal support were partially successful, but improvements are required to the mounting of the nodal support inside the cryostat to improve the thermal conduction paths and damping of external vibrations. The nodal support itself also requires some alteration to compensate for the difference in thermal contraction between the support and the sample.

The effort to extend the technology and knowledge of thermal dissipation and mechanical loss in optical coatings is important not only to improving the sensitivity of gravitational wave detectors, but to all fields of optical precision measurement reaching thermal noise limited performance.

Appendix A

Towards A Method For Simultaneous Measurement of the Elastic Modulus and Coefficient of Thermal Expansion For A Thin Film

A.1 Introduction

The evaluation of the suitability of an optical coating for use in a gravitational wave detector does not rely solely upon the mechanical loss characteristics. Other properties of the material are required before a full thermal noise spectrum can be calculated for a particular system. The properties which are of particular interest are Young's modulus, Poisson's ratio and the coefficient of thermal expansion

for each of the materials used in the gravitational wave detector optics. These values are well known for the bulk materials used as substrates, but are less well quantified for the thin films used in multilayer coatings. Therefore, a method of measuring the elastic moduli and coefficient of thermal expansion of thin films of silica, tantala and other materials of interest is required.

The thermally induced bending technique for measuring the mechanical properties of thin films on a substrate is suitable for application to the existing set of cantilever samples, as it is a non-contact, non-destructive technique based on the simple mechanical principles illustrated by Stoney's formula, [111][112]

$$\sigma_{film} = \frac{E_s t_s^2}{6(1-\nu_s)t_f}\left(\frac{1}{R_0} - \frac{1}{R}\right). \tag{A.1}$$

This form of Stoney's formula applies to a structure consisting of a substrate and a thin film, where the thickness of the film is given by t_f and the thickness of the substrate is given by t_s. The formula describes the connection between the total amount of stress in the film, given by σ_{film} and the measured radius of curvature of the system, R, relative to an initial radius of curvature, R_0, which may be infinite if the substrate was negligibly curved before the film was applied. This formula also involves the biaxial modulus for a material, which for the case of the substrate is written as,

$$B_s = \frac{E_s}{(1-\nu_s)} \tag{A.2}$$

Where E represents the Young's Modulus for the substrate material and ν represents the Poisson's ratio. The use of the biaxial modulus in these formulae signifies

that the bending of the film/substrate system is occurring such that the stress in the film is isotropic. The properties used in the calculation of the biaxial modulus must be either entirely totally isotropic or isotropic in the plane relevant to the bending of the structure.

Using the same principles as those occurring in a bimetallic strip, by varying the temperature of the measured system it is possible to deduce the magnitude of the film stress which is due to the mismatch of thermomechanical properties between the material of the substrate and the thin film. The total internal stress in the film is the sum of the intrinsic stress due to the phase transition which occurred upon application of the film, σ_i and the stress resulting from the mismatch of thermal expansion coefficients, $\sigma_{thermal}$, can be written as,

$$\sigma = \sigma_i + \sigma_{thermal} = \sigma_i + ((\alpha_s - \alpha_f)\frac{E_f}{(1-\nu_f}))(T - T_0) \tag{A.3}$$

Where T_0 is the temperature at which the film was deposited, T is the temperature at which the stress is measured, and other symbols are as defined above with the subscript 'f' denoting the property of the film. By differentiating equation A.3 it can be shown that,

$$\frac{d\sigma}{dT} = (\alpha_s - \alpha_f)\frac{E_f}{(1-\nu_f)} \tag{A.4}$$

Therefore, the gradient of a line of best fit plotted through the stresses measured in the system for a range of temperatures can be used to calculate the biaxial modulus of the film, assuming the coefficients of thermal expansion of both the substrate and film are well known. Alternatively the coefficient of thermal expansion may

be calculated assuming the biaxial modulus is well known. If the same coating is applied to substrates of two different materials for which the biaxial modulus and coefficient of thermal expansion are known, then a pair of simultaneous equations can be formed to allow the coefficient of thermal expansion and biaxial modulus of the film to be determined [113]. If the properties of the two substrate materials are distinguished by the subscripts 1 and 2, the equation for the biaxial modulus of the film is,

$$B_f = \frac{E_f}{(1-\nu_f)} = \frac{1}{\alpha_1 - \alpha_2}\left(\frac{d\sigma_1}{dT} - \frac{d\sigma_2}{dT}\right), \tag{A.5}$$

and the thermal expansion coefficient of the film can be calculated with,

$$\alpha_f = \alpha_1 - (\alpha_1 - \alpha_2)\frac{d\sigma_1}{dT}\left(\frac{d\sigma_1}{dT} - \frac{d\sigma_2}{dT}\right)^{-1}. \tag{A.6}$$

In order to separate the values of E_f, the elastic modulus and ν_f, the Poisson's ratio, from the biaxial modulus given by the experimental result, a third different substrate material may be used and further simultaneous equations constructed [114].

A.2 Experimental Design and Preliminary Testing

In order to determine $^{d\sigma_f}/_{dT}$, from which the properties of the film can be extracted, the thermal mismatch stress in the film is calculated from the radius of curvature of the film/substrate structure. The radius of curvature of the film/substrate structure is measured as the temperature of the apparatus is varied, then substituted

into Equation A.1, along with the appropriate values for the properties of the substrate, to calculate the stress in the film at each temperature. The calculated stresses are plotted against their respective temperature measurements, and linear regression is applied to the dataset to determine the rate of change of film stress with temperature.

The sample was held in a clamp similar to those used in mechanical loss measurements and heated to thermal equilibrium using resistive heaters. The radius of curvature was measured by profiling the sample using a Zygo phase shift interferometer. The radius of curvature was extracted from the profile using the *radcrv* function of the MetroPro interferometry analysis package. The extracted radii of curvature are used to calculated stress values, which were then plotted against the measurement temperature.

The first iteration of the experimental apparatus consisted of a thermally conductive copper box, upon which was mounted a clamp of the 'bolt-through' type used in mechanical loss experiments, two 24Ω resistive heaters, and three PT100 temperature sensors, two of which were mounted on the clamp and the remaining one mounted on the surface of the box. This system was bolted to the Zygo gridded mount, resulting in the sample pointing around 40° from vertical.

The Zygo phase shift interferometer was used to image the curvature of the cantilever. The sample was imaged on the uncoated side, as the tantala layer was not reflective enough to produce fringes. Initial tests showed that environmental vibrations and motion of air from the clean room air conditioning was enough to

cause the interferometric image to be decayed or illegible. The first course of action was to make measurements with the air-conditioning turned off. This allowed the accurate measurement of the radius of curvature of the cantilever at the room ambient temperature to be made. Over 40 measurements at ambient temperature, without airconditioning and using the first iteration of the apparatus, the average radius of curvature was measured to be (-88.13 ± 4.88)m. In order to produce the

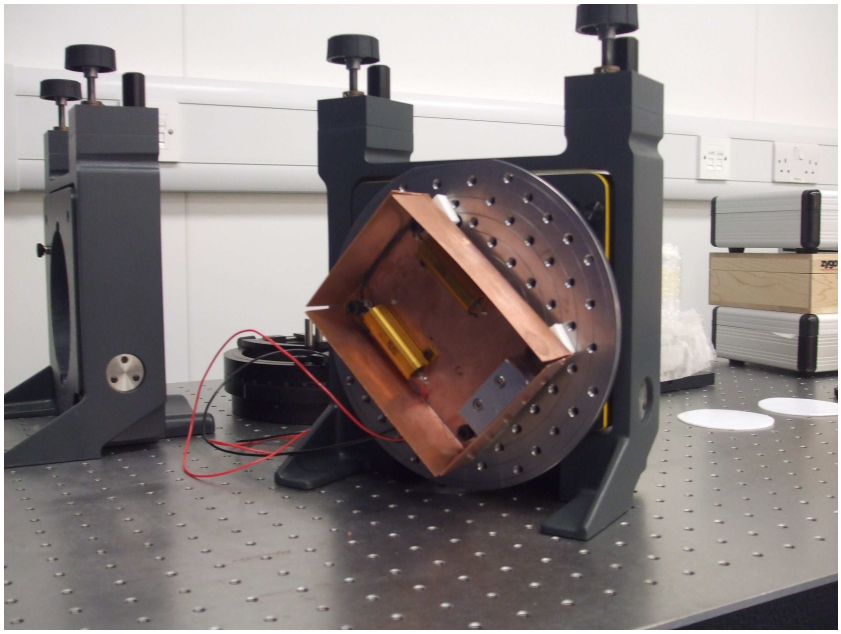

Figure A.1: Early iteration of experimental apparatus

stress/temperature gradient, we attempted to measure the radius of curvature as the sample was first heated and then cooled. It became clear that at a few degrees above ambient temperature, some effect was causing the cantilever to wave. This effect was thought to be related to one or more of the following:

- The thermal motion or thermally induced refractive index change of the air column between the sample and the interferometer

- Convection currents operating around the sample
- Vibration leaking into the isolation bench

In order to isolate the sample from the motion of external air, a copper lid for the box was constructed. Using this lid, at a temperature reading of $25°C$, the average radius of curvature over 7 legible measurements was (-88.70 ± 0.24)m - indicating good stability. Once the heating process had begun, the measurement stability was lost and the average radius of curvature was (-90.16 ± 1.30)m

AC off	Lid	Hood	Temperature	Radius of Curvature
x			25C	(-88.13 ± 4.88)m.
x	x		25C	(-88.70 ± 0.24)m.
x	x		29C	(-90.15 ± 1.30)m.
	x	x	25C	(-98.33 ± 7.68)m.
x	x	x	25C	(-85.68 ± 0.32)m.

The level of image stability obtained by containing the heated sample within an insulated copper box, under a perspex hood with the lab air conditioning turned off was found to be suitable for making measurements that could detect the expected amount of thermally induced bending in the sample.

The image obtained from the Zygo shows the curvature of the uncoated side of the cantilever. By convention, the z-axis is parallel to the direction of the impinging light, with $z = 0$ at the wavefront.

From observation of the image, which was taken at room temperature under the best measurement conditions described above, the film is under tensile stress. The

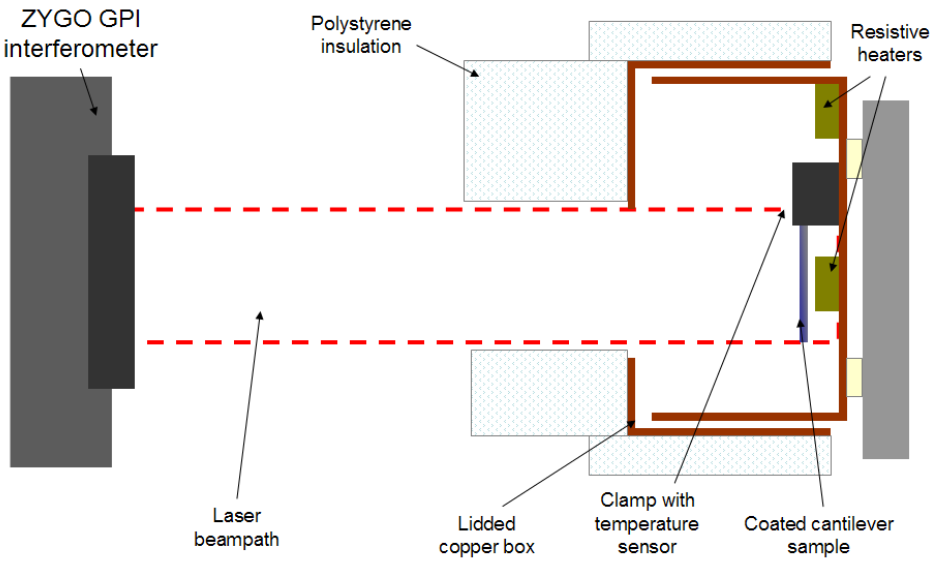

Figure A.2: Cutaway diagram showing experimental apparatus

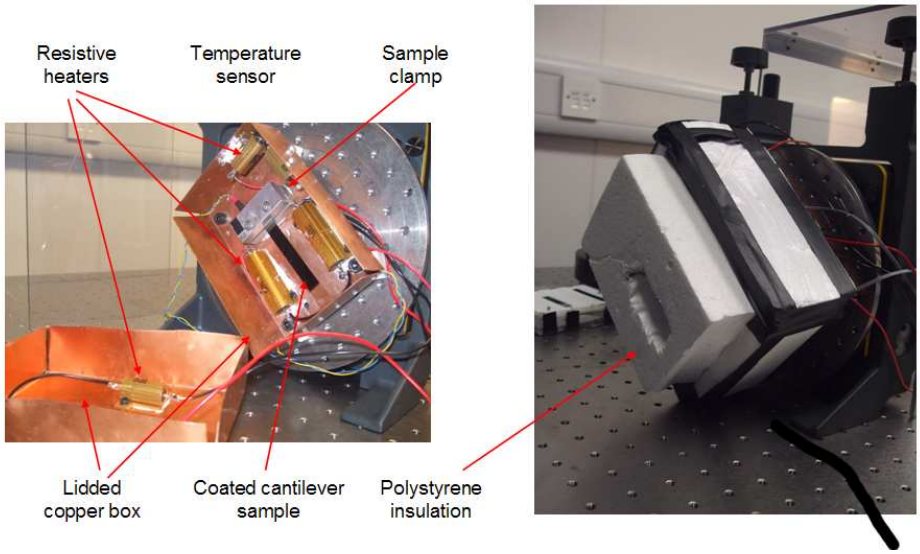

Figure A.3: Final version of experimental apparatus

concave appearance of the cantilever means that all automatic readings of the radius of curvature will be negative by convention.

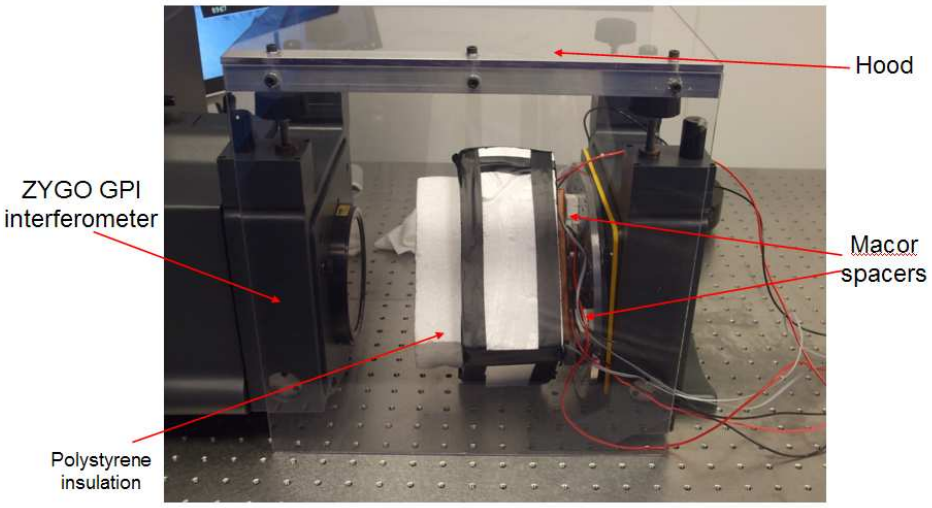

Figure A.4: Final version of experimental apparatus

A.3 Use of Appropriate Values for Known Parameters

The choice of appropriate values for the elastic modulus and coefficient of thermal expansion of the substrate are vital to the production of an accurate result of acceptable precision.

Silicon		
Quantity	Value	Source
E	$163GPa \pm 4GPa$	[94]
ν	0.2 ± 0.03	Touloukian [89]
α	$(2.54 \pm 0.1) \times 10^{-6\circ}C^{-1}$	Touloukian [89]
t	$92 \pm 5\mu$m	Cantilever specifications

Table A.1: The values for the properties of silicon used in the analysis of the data from this experiment, with the source of the measurement.

Substituting the appropriate values in to equation A.4, and assuming the proper-

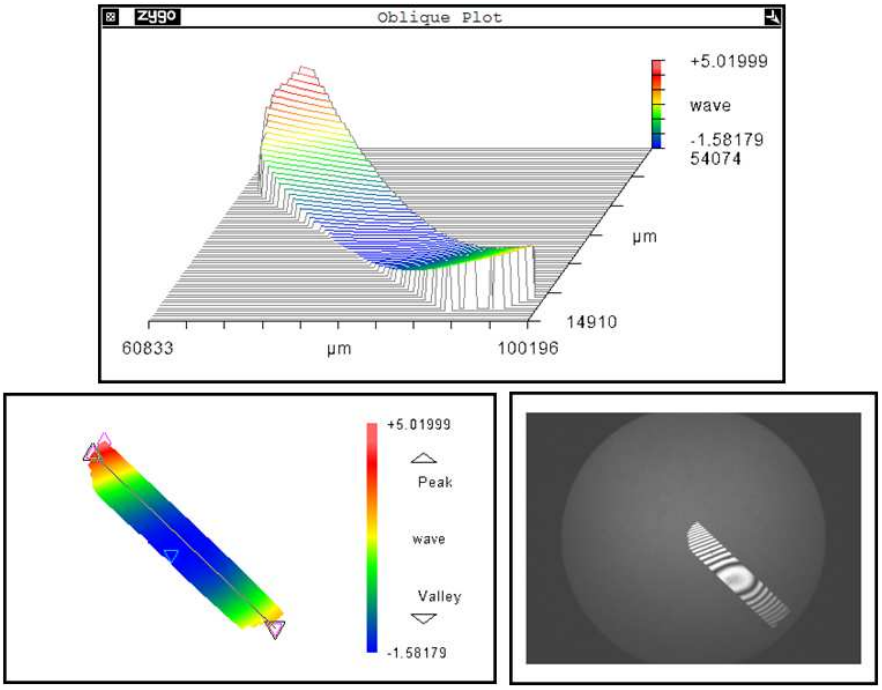

Figure A.5: Plots from MetroPro phase shift interferometry software

Tantalum Pentoxide		
Quantity	Value	Source
E	$120 \pm 20 GPa$	Martin and Bendavid, 1993 [115]
ν	0.23 ± 0.03	Touloukian [89]
α	$(3.6 \pm 0.5) \times 10^{-6\circ} K^{-1}$	Tien and Lee [116]
α	$(5 \pm 1) \times 10^{-6\circ} K^{-1}$	Braginsky and Samoilenko [117]
t	418 ± 2nm	Ellipsometric measurement

Table A.2: The values for the properties of tantala used in the analysis of the data from this experiment, with the source of the measurements. The literature values of biaxial modulus and α are compared with the results of the measurements.

ties of the tantalum pentoxide samples measured in the literature are similar to those of the amorphous ion-beam sputtered material measured in this case, the value of $d\sigma/dT$ should be $-(1.65 \pm 0.42) \times 10^5 PaT^{-1}$.

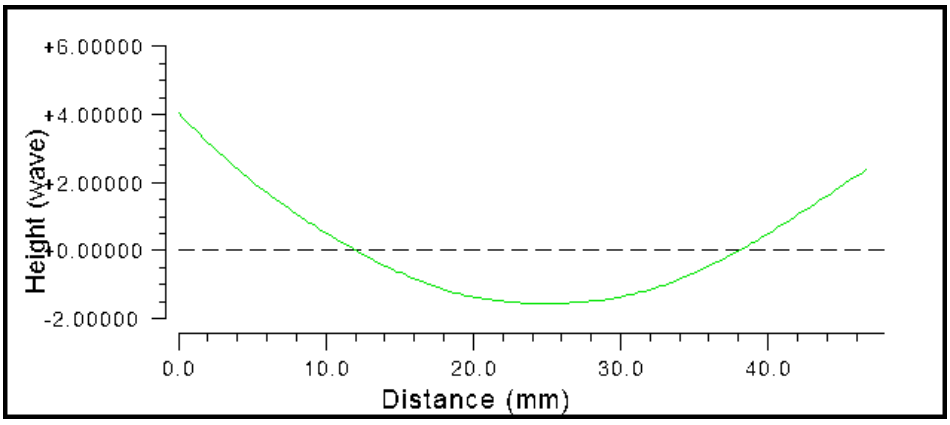

Figure A.6: Profile of curved cantilever, showing wavefront position

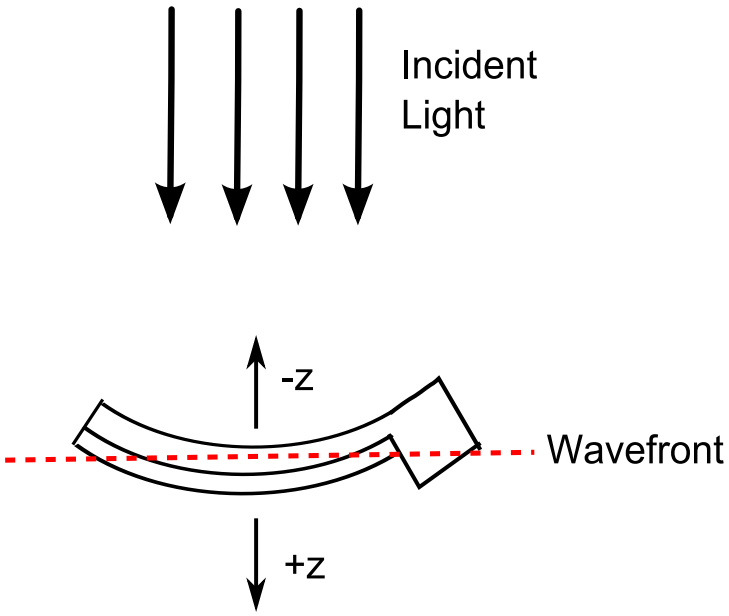

Figure A.7: Schematic of bending cantilever, showing film under tensile stress.

A.4 Measurements of a Tantala Coating

The technique described above was used to characterise a cantilever measuring $35mm \times 10mm \times 92\mu m$, coated with (418 ± 2)nm of amorphous tantalum pentoxide [118]. The radius of curvature was measured during a cooling cycle (Set A) and a heating cycle (Set B) on consecutive days using the same calibration of the lateral distance on the Zygo image. Figure A.8 shows the measured radii of curvature.

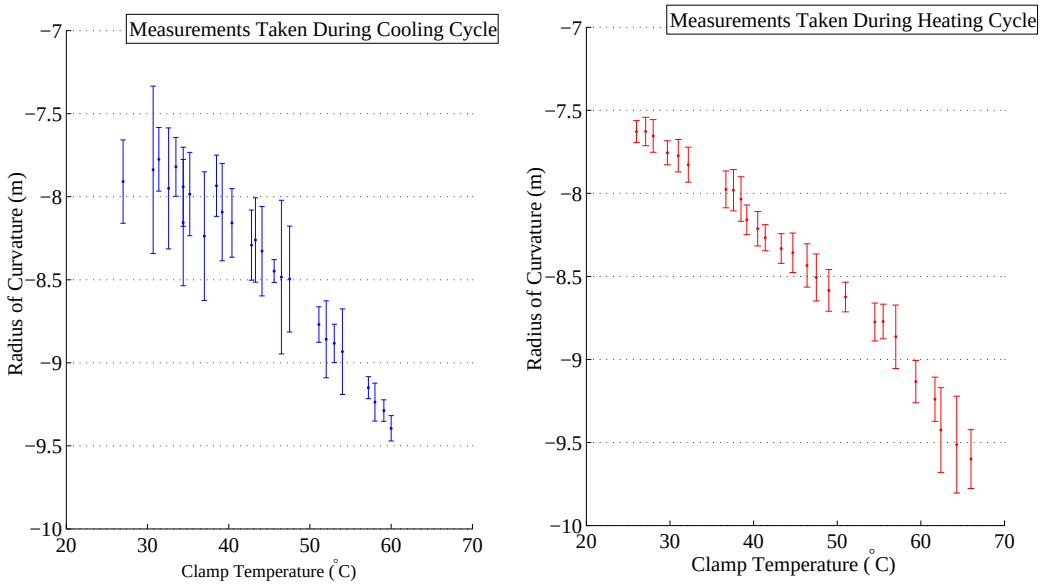

Figure A.8: The radii of curvature measurements against the clamp temperature for a cooling cycle and a heating cycle.

The gradients are obtained using a weighted least squares fit algorithm which uses the errors in the measured radius of curvature to place an importance value upon each point. As the errors in the measured radius of curvature remain roughly constant throughout, the results of the weighted least squares technique yield a so-

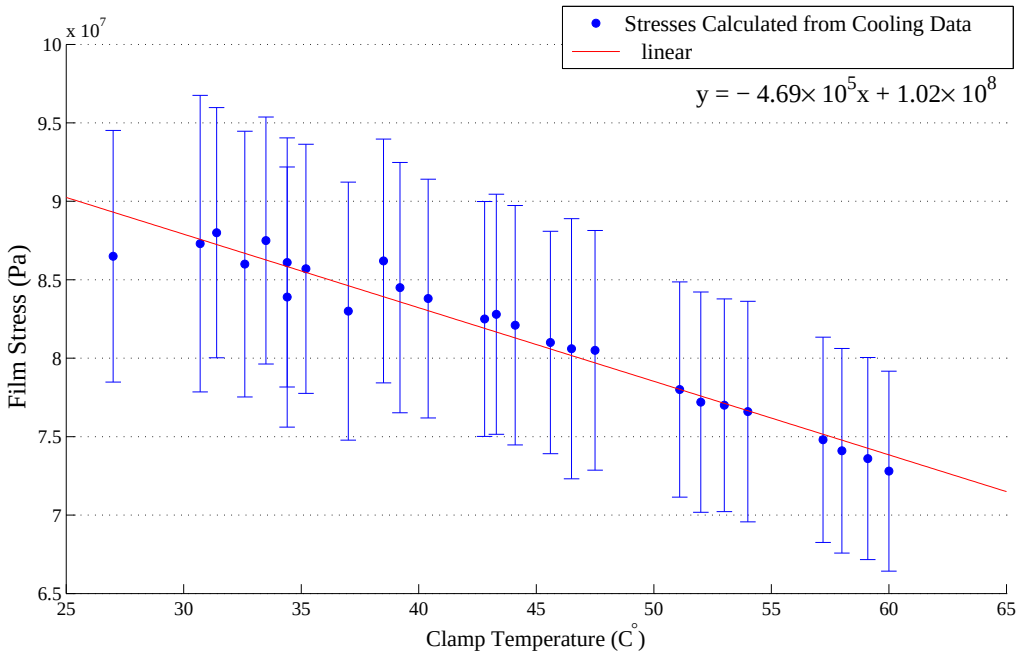

Figure A.9: The film stresses calculated from the radius of curvature measurements against the clamp temperature for the cooling data from a heating cycle, showing the gradient and intercept calculated by least squares regression.

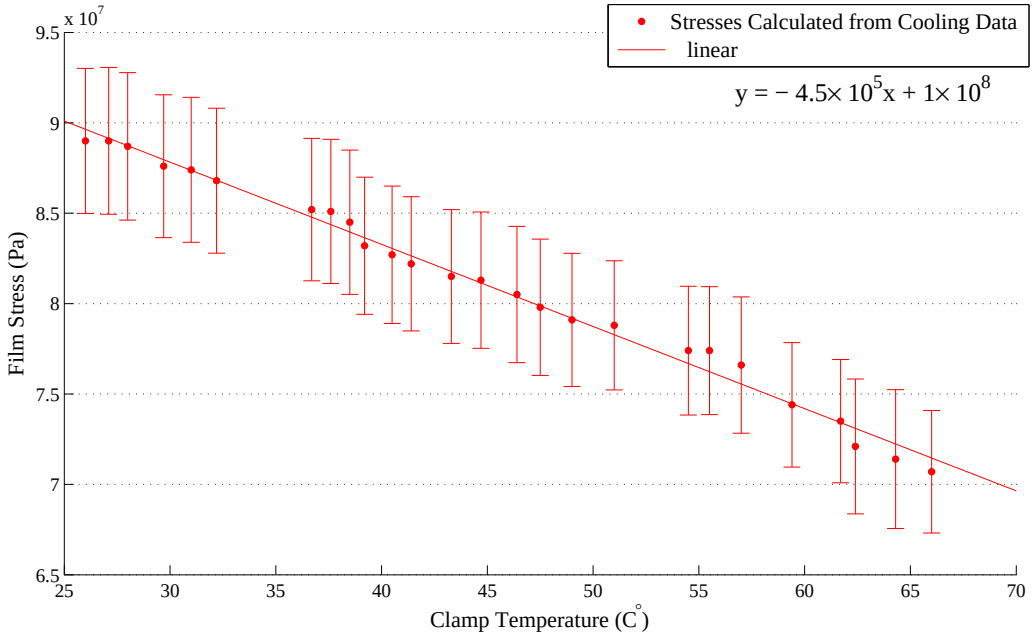

Figure A.10: Film stresses calculated from the radius of curvature measurements and the clamp temperature for the heating data from a cooling cycle, showing the gradient and intercept calculated by least squares regression.

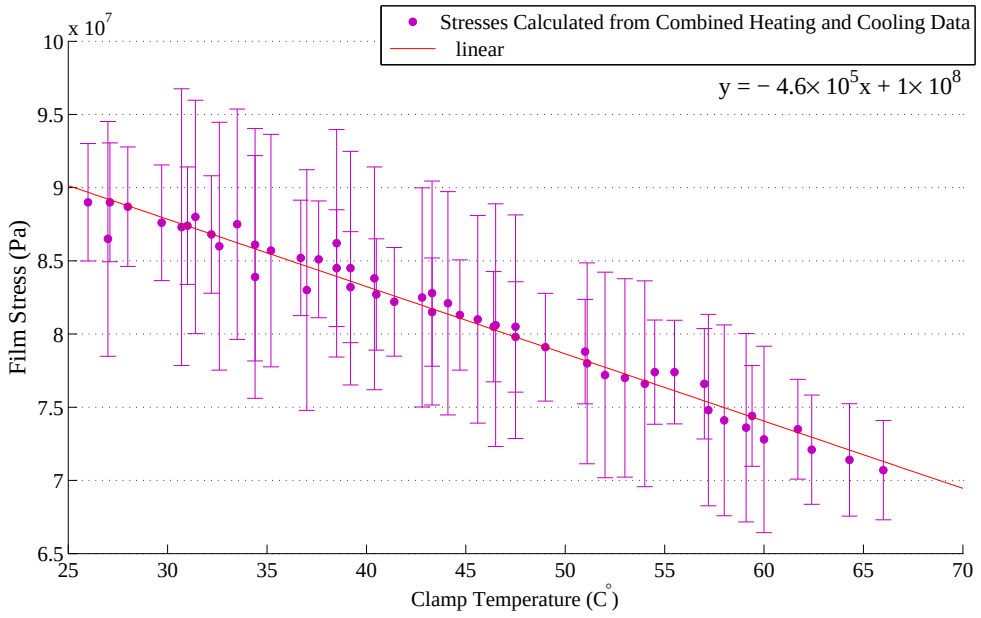

Figure A.11: Film stresses calculated from the radius of curvature measurements and the clamp temperature for the combined data from the heating and cooling cycles, showing the gradient and intercept calculated by least squares regression.

lution which only differs from the solution obtained by using a simple least squares fit which takes no account of the error in X or Y by 2%. The line parameters found from the least squares fits are in Table A.3.

Dataset	Gradient	Intercept	R^2
Cooling	-4.68×10^5	1.02×10^5	5.41×10^6
Heating	-4.55×10^5	1.01×10^5	2.78×10^6
Combined	-4.60×10^5	1.02×10^5	6.12×10^6

Table A.3: The parameters of the lines fitted to the stress/temperature plots in Figures A.9 to A.11.

The gradient values quoted in Table A.3 correspond to a set of values for the expression $(\alpha_s - \alpha_f)\frac{E_f}{(1-\nu_f)}$. The allowed values are shown as a contour across the α-B parameter space in Figure A.12, alongside the rectangles representing the literature values for $\alpha_{tantala}$ and $B_{tantala}$.

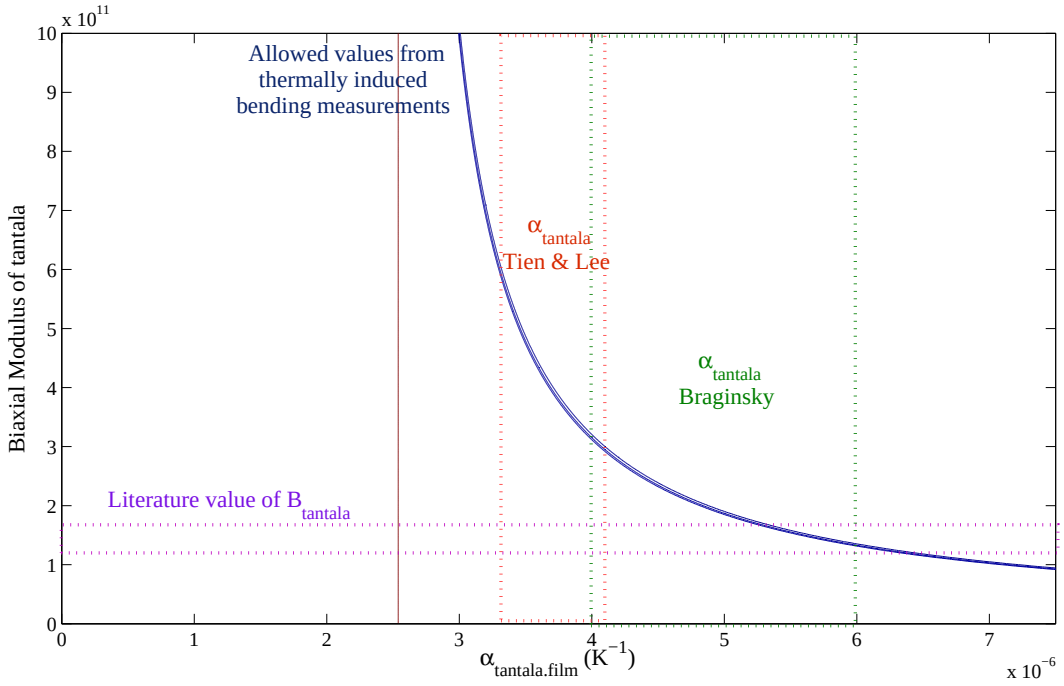

Figure A.12: The curve representing values allowed by the rate of change of film stress with temperature shown in Figures A.9 to A.11 and the literature values of biaxial modulus [115] and the two literature values of thermal expansion [117][116] for amorphous tantala.

The intersection of the curve of allowed values and the values found in the literature for $\alpha_{tantala}$ and $B_{tantala}$ suggest that the measured tantala film may have properties similar to those of the bulk. Further work is needed to improve this experimental setup so that a two-substrate experiment can be performed to separate the product of the thermal expansion coefficient and the biaxial modulus of

the film and ascertain the level of confidence in these results.

The main areas for ongoing improvement are in the measurement of the radius of curvature. The usefulness of the Zygo interferometer in this technique is limited; while the Zygo interferometer was able to correctly identify the profile of the tantala/silicon sample, the interferometer failed to resolve a profile when the method was trialled with other samples with a higher degree of curvature. 'Bulls-eye' fringes appeared over small areas of the highly curved samples, indicating that the surface was too curved to resolve correctly. Other thermally induced bending experiments use optical lever techniques to monitor the change in curvature of the sample. The experiment could be altered to use an optical lever readout to monitor the deflection of the end of the cantilever, and Equation A.1 could be recast in terms of the deflection of a cantilever of a known length.

These initial measurements proved partially successful, but did not lead to a reliable procedure for simultaneously measuring the biaxial modulus and thermal expansion coefficient for an optical thin film material.

Bibliography

[1] C. W. Misner, K. S. Thorne, and J. A. Wheeler. *Gravitation*. W. H. Freeman, San Francisco, U.S.A., 1973.

[2] P. R. Saulson. *Fundamentals of Interferometric Gravitational Wave Detectors*. World Scientific, Singapore, 1994.

[3] K. S. Thorne. Multipole expansions of gravitational radiation. *Rev. Mod. Phys.*, 52(2):299–339, 1980.

[4] B. F. Schutz. Determining the Hubble constant from gravitational wave observations. *Nature*, 323(6086):310–311, 1986.

[5] B. J. Kelly, J. G. Baker, W. D. Boggs, J. M. Centrella, J. R. van Meter, and S. T. McWilliams. Gravitational radiation characteristics of nonspinning black-hole binaries. *J. Phys.: Conf. Ser.*, 154(1):012050, 2009.

[6] C. Cutler and K. Thorne. An overview of gravitational-wave sources. In N. T. Bishop & D. M. Sunil, editor, *General Relativity and Gravitation, Proceedings of the 16th International Conference on General Relativity and Gravitation*, page 72. World Scientific, Singapore, 2002.

[7] B. F. Schutz. Gravitational wave astronomy. *Class. Quantum Grav.*, 16(12A):A131–A156, 1999.

[8] K. S. Thorne. Gravitational Waves. In E. W. Kolb and R. D. Peccei, editors, *Particle and Nuclear Astrophysics and Cosmology in the Next Millenium*, page 160, 1995.

[9] B. J. Owen. Maximum elastic deformations of compact stars with exotic equations of state. *Phys. Rev. Lett.*, 95(21):211101, 2005.

[10] C. D. Ott. TOPICAL REVIEW: The gravitational-wave signature of core-collapse supernovae. *Class. Quantum Grav.*, 26(6):063001, 2009.

[11] J. A. Lobo. General relativity: proceedings of the forty sixth scottish universities summer school in physics, 1995.

[12] M. Maggiore. Gravitational wave experiments and early universe cosmology. *Physics Reports*, 331(6):283 – 367, 2000.

[13] R. A. Hulse and J. H. Taylor. Discovery of a pulsar in a binary system. *Astrophys. J*, 195:L51–L53, 1975.

[14] P. M. McCulloch J. H. Taylor, L. A. Fowler. Measurements of general relativistic effects in the binary pulsar PSR1913 + 16. *Nature*, 277:437–440, 1979.

[15] J. M. Weisberg and J. H. Taylor. The Relativistic Binary Pulsar B1913+16: Thirty Years of Observations and Analysis. In F. A. Rasio and I. H. Stairs, editors, *Binary Radio Pulsars*, volume 328 of *Astronomical Society of the Pacific Conference Series*, page 25, July 2005.

[16] P. R. Saulson. If light waves are stretched by gravitational waves, how can we use light as a ruler to detect gravitational waves? *Am. J. Phys.*, 65:501–505, 1997.

[17] R. L. Forward. Wideband laser-interferometer graviational-radiation experiment. *Phys. Rev. D*, 17(2):379–390, Jan 1978.

[18] B. W. Barr. *Experimental Investigations into Advanced Configurations and Optical Techniques for Laser Interferometric Gravitational Wave Detectors*. PhD thesis, Department of Physics and Astronomy, University of Glasgow, 2003.

[19] W. A. Edelstein, J. Hough, J. R. Pugh, and W. Martin. Limits to the measurement of displacement in an interferometric gravitational radiation detector. *J. Phys. E*, 11(7):710–712, 1978.

[20] S. A. Hughes and K. S. Thorne. Seismic gravity-gradient noise in interferometric gravitational-wave detectors. *Phys. Rev. D*, 58(12):122002.

[21] D. Sigg *et al.* Status of the LIGO detectors. *Class. Quantum Grav.*, 25(11):114041, 2008.

[22] B. Abbott *et al.* LIGO: The laser interferometer gravitational-wave observatory. *Rep. Prog. Phys.*, 72(7):076901, 2009.

[23] J. Giaime, P. Saha, S. Shoemaker, and L. Sievers. A passive vibration isolation stack for LIGO: Design, modeling, and testing. *Rev. Sci. Instrum.*, 67(1):208–214, 1996.

[24] I. Mandel *et al.* Predictions for the rates of compact binary coalescences observable by ground-based gravitational-wave detectors. *in press.*

[25] F. Acernese *et al.* Status of Virgo. *Class. Quantum Grav.*, 25(11):114045, 2008.

[26] F. Acernese *et al.* Status of Virgo detector. *Class. Quantum Grav.*, 24(19):S381, 2007.

[27] B. Caron *et al.* The Virgo interferometer. *Class. Quantum Grav.*, 14(6):1461–1469, 1997.

[28] G. Ballardin, L. Bracci, S. Braccini, C. Bradaschia, C. Casciano, G. Calamai, R. Cavalieri, R. Cecchi, G. Cella, E. Cuoco, E. D'Ambrosio, V. Dattilo, A. Di Virgilio, L. Fabbroni, F. Fidecaro, F. Frasconi, A. Gaddi, A. Gennai, G. Gennaro, A. Giazotto, G. Losurdo, L. Holloway, P. La Penna, F. Lelli, E. Majorana, M. Mazzoni, F. Paoletti, M. Pasotti, A. Pasqualetti, R. Passaquieti, D. Passuello, R. Poggiani, P. Puppo, F. Raffaelli, P. Rapagnani, F. Ricci, P. Ruggi, R. Stanga, R. Taddei, F. Vetrano, A. Vicerè, and Z. Zhang. Measurement of the Virgo superattenuator performance for seismic noise suppression. *Rev. Sci. Instrum.*, 72(9):3643–3652, 2001.

[29] H. Grote *et al.* The status of GEO 600. *Class. Quantum Grav.*, 25(11):114043, 2008.

[30] K. A. Strain and B. J. Meers. Experimental demonstration of dual recycling for interferometric gravitational-wave detectors. *Phys. Rev. Lett.*, 66(11):1391–1394, 1991.

[31] M. V. Plissi, K. A. Strain, C. I. Torrie, N. A. Robertson, S. Killbourn, S. Rowan, S. M. Twyford, H. Ward, K. D. Skeldon, and J. Hough. Aspects of the suspension system for GEO 600. *Rev. Sci. Instrum.*, 69(8):3055–3061, 1998.

[32] D. Tatsumi, R. Takahashi, K. Arai, N. Nakagawa, K. Agatsuma, T. Yamazaki, M. Fukushima, M. Fujimoto, A. Takamori, A. Bertolini, V. Sannibale, R. DeSalvo, S. Márka, M. Ando, K. Tsubono, T. Akutsu, K. Yamamoto, H. Ishitsuka, T. Uchiyama, S. Miyoki, M. Ohashi, K. Kuroda, N. Awaya, N. Kanda, A. Araya, S. Telada, T. Tomaru, T. Haruyama, A. Yamamoto, N. Sato, T. Suzuki, and T. Shintomi. Current status of Japanese detectors. *Class. Quantum Grav.*, 24(19):S399–S403, 2007.

[33] R. Adhikari, P. Fritschel, and S. Waldman. Enhanced LIGO. Technical Report LIGO-T060156-01-I, LIGO Scientific Collaboration, July 2006.

[34] J. R. Smith *et al.* The path to the enhanced and advanced LIGO gravitational-wave detectors. *Class. Quantum Grav.*, 26(11):114013, 2009.

[35] Advanced LIGO Team. Advanced LIGO Reference Design. Technical report, LIGO Scientific Collaboration, May 2007. LIGO-060056-08-M.

[36] R. Flaminio, A. Freise, A. Gennai, P. Hello, P. La Penna, G. Losurdo, H. Lueck, N. Man, A. Masserot, B. Mours, M. Punturo, A. Spallicci, and A. Vicere. Advanced Virgo white paper. Technical Report VIR-NOT-DIR-1390-304, Virgo Collaboration, November 2005.

[37] K. Kuroda *et al.* The status of LCGT. *Class. Quantum Grav.*, 23(8):S215, 2006.

[38] M. Ohashi *et al.* Status of LCGT and CLIO. *Jour. Phys.: Conf. Ser.*, 120(3):032008, 2008.

[39] B. Willke *et al.* The GEO-HF project. *Class. Quantum Grav.*, 23(8):S207, 2006.

[40] R. Schnabel, J. Harms, K. A. Strain, and K. Danzmann. Squeezed light for the interferometric detection of high-frequency gravitational waves. *Class. Quantum Grav.*, 21(5):S1045, 2004.

[41] Einstein Telescope Design Study Collaboration. Einstein telescope project website: http://www.et-gw.eu.

[42] LISA - Laser Interferometer Space Antenna. http://lisa.nasa.gov.

[43] M. Sallusti, P. Gath, D. Weise, M. Berger, and H. R. Schulte. LISA system design highlights. *Class. Quantum Grav.*, 26(9):094015, 2009.

[44] A. Einstein. *The Collected Papers of Albert Einstein. Volume 2: The Swiss Years*, pages 206–222. Princeton University Press, U.S.A., 1989.

[45] H. B. Callen and T. A. Welton. Irreversibility and generalized noise. *Phys. Rev.*, 83(1):34–40, 1951.

[46] H. B. Callen and R. F. Greene. On a theorem of irreversible thermodynamics. *Phys. Rev.*, 86(5):702–710, 1952.

[47] R. F. Greene and H. B. Callen. On a theorem of irreversible thermodynamics II. *Phys. Rev.*, 88(6):1387–1391, 1952.

[48] P. R. Saulson. Thermal noise in mechanical experiments. *Phys. Rev. D*, 42(8):2437–2445, 1990.

[49] A. S. Nowick and B. S. Berry. *Anelastic Relaxation in Crystalline Solids*. Academic Press, New York, 1972.

[50] J. Ferrerinho. *The Detection of Gravitational Waves*, chapter 6, Internal Friction in High Q Materials, pages 116–168. Cambridge University Press, Cambridge, 1991.

[51] I. Martin. *Studies of materials for use in future interferometric gravitational wave detectors*. PhD thesis, Department of Physics and Astronomy, University of Glasgow, September 2008.

[52] A. Gillespie and F. Raab. Thermally excited vibrations of the mirrors of laser interferometer gravitational-wave detectors. *Phys. Rev. D*, 52(2):577–585, 1995.

[53] Y. Levin. Internal thermal noise in the LIGO test masses: A direct approach. *Phys. Rev. D*, 57(2):659–663, 1998.

[54] F. Bondu, P. Hello, and J. Vinet. Thermal noise in mirrors of interferometric gravitational wave antennas. *Physics Letters A*, 246(3-4):227 – 236, 1998.

[55] D. R. M. Crooks, P. Sneddon, G. Cagnoli, J. Hough, S. Rowan, M. M. Fejer, E. Gustafson, R. Route, N. Nakagawa, D. Coyne, G. M. Harry, and A. M. Gretarsson. Excess mechanical loss associated with dielectric mirror coatings on test masses in interferometric gravitational wave detectors. *Class. Quantum Grav.*, 19(5):883, 2002.

[56] S. D. Penn *et al.* Mechanical loss in tantala/silica dielectric mirror coatings. *Class. Quantum Grav.*, 20(13):2917, 2003.

[57] G. Cagnoli, L. Gammaitoni, J. Hough, J. Kovalik, S. McIntosh, M. Punturo, and S. Rowan. Very high Q measurements on a fused silica monolithic pendulum for use in enhanced gravity wave detectors. *Phys. Rev. Lett.*, 85(12):2442–2445, 2000.

[58] W. J. Startin, M. A. Beilby, and P. R. Saulson. Mechanical quality factors of fused silica resonators. *Rev. Sci. Instrum.*, 69(10):3681–3689, 1998.

[59] S. Miyoki, T. Uchiyama, K. Yamamoto, H. Hayakawa, K. Kasahara, H. Ishitsuka, M. Ohashi, K. Kuroda, D. Tatsumi, S. Telada, M. Ando, T. Tomaru, T. Suzuki, N. Sato, T. Haruyama, Y. Higashi, Y. Saito, A. Yamamoto, T. Shintomi, A. Araya, S. Takemoto, T. Higashi, H. Momose, J. Akamatsu, and W. Morii. Status of the CLIO project. *Class. Quantum Grav.*, 21(5):S1173, 2004.

[60] G. M. Harry, A. M. Gretarsson, P. R. Saulson, S. E. Kittelberger, S. D. Penn, W. J. Startin, S. Rowan, M. M. Fejer, D. R. M. Crooks, G. Cagnoli, J. Hough, and N. Nakagawa. Thermal noise in interferometric gravitational wave detectors due to dielectric optical coatings. *Class. Quantum Grav.*, 19(5):897–917, 2002.

[61] C. Zener. Internal friction in solids, I: Theory of internal friction in reeds. *Phys. Rev.*, 52(3):230–235, 1937.

[62] C. Zener. Internal friction in solids, II: General theory of thermoelastic internal friction. *Phys. Rev.*, 53(1):90–99, 1938.

[63] R. Lifshitz and M. L. Roukes. Thermoelastic damping in micro- and nanomechanical systems. *Phys. Rev. B*, 61(8):5600–5609, 2000.

[64] V. B. Braginsky, M. L. Gorodetsky, and S. P. Vyatchanin. Thermodynamical fluctuations and photo-thermal shot noise in gravitational wave antennae. *Phys. Lett. A*, 264(1):1 – 10, 1999.

[65] Y. T. Liu and K. S. Thorne. Thermoelastic noise and homogeneous thermal noise in finite sized gravitational-wave test masses. *Phys. Rev. D*, 62(12):122002, 2000.

[66] M. M. Fejer, S. Rowan, G. Cagnoli, D. R. M. Crooks, A. Gretarsson, G. M. Harry, J. Hough, S. D. Penn, P. H. Sneddon, and S. P. Vyatchanin. Thermoelastic dissipation in inhomogeneous media: loss measurements and displacement noise in coated test masses for interferometric gravitational wave detectors. *Phys. Rev. D*, 70(8):082003, 2004.

[67] Heraeus commercial website. http://optics.heraeus-quarzglas.com.

[68] C. J. Walsh, A. J. Leistner, J. Seckold, B. O. Oreb, and D. I. Farrant. Fabrication and measurement of optics for the Laser Interferometer Gravitational wave Observatory. *Appl. Opt.*, 38(13):2870–2879, 1999.

[69] H. A. Macleod. *Thin-Film Optical Filters*. Adam Hilger Ltd, London, 1986.

[70] D. R. M. Crooks, G. Cagnoli, M. M. Fejer, A. Gretarsson, G. Harry, J. Hough, N. Nakagawa, S. Penn and, Route R., S. Rowan, and P. H. Sneddon. Experimental measurements of coating mechanical loss factors. *Class. Quantum Grav.*, 21(5):S1059, 2004.

[71] P. J. Martin. Ion-based methods for optical thin film deposition. *J. Mater. Sci.*, 21:1–25, 1986.

[72] B. Lunin. *Physical and chemical bases for the development of hemispherical resonators for solid-state gyroscopes*, chapter 3, Internal Friction In Hemispherical Resonator Material, pages 38–60. Moscow Aviation Institute Publishing, Moscow.

[73] B. E. White and R. O. Pohl. Internal friction of subnanometer α-SiO_2 films. *Phys. Rev. Lett.*, 75(24):4437–4439, 1995.

[74] B. E. White and R. O. Pohl. How do two-level systems come about? *Physica B.*, 219:267–269, 1996.

[75] O. L. Anderson and H. E. Bömmel. Ultrasonic absorption in fused silica at low temperatures and high frequencies. *J. Am. Ceram. Soc.*, 38(4):125–131, 1955.

[76] R. E. Strakna. Investigation of low-temperature ultrasonic absorption in fast-neutron irradiated SiO_2 glass. *Phys. Rev.*, 123(6):2020–2026, 1961.

[77] M. R. Vukcevich. A new interpretation of the anomalous properties of vitreous silica. *J. Non-Cryst. Solids*, 11(1):25–63, 1972.

[78] K. S. Gilroy and W. A. Phillips. An asymmetric double-well potential model for structural relaxation processes in amorphous materials. *Philos. Mag. B*, 43(5):735–746, 1981.

[79] D. R. M. Crooks, G. Cagnoli, M. M. Fejer, G. Harry, J. Hough, B. T. Khuri-Yakub, S. Penn, R. Route, S. Rowan, P. H. Sneddon, I. O. Wygant, and

G. G. Yaralioglu. Experimental measurements of mechanical dissipation associated with dielectric coatings formed using SiO_2, Ta_2O_5 and Al_2O_3. *Class. Quantum Grav.*, 23:4953–4965, 2006.

[80] Materials Science and Bradfield Road West Lindfield Sydney NSW 2070 Australia Engineering Division, CSIRO. http://www.csiro.au/.

[81] R. Dannenberg. Analysis of CSIRO sample HfO_2 sample 971 on 1" fused silica. private communication, July 2009.

[82] P. H. Sneddon, S. Bull, G. Cagnoli, D. R. M. Crooks, E. J. Elliffe, J. E. Faller, M. M. Fejer, J. Hough, and S. Rowan. The intrinsic mechanical loss factor of hydroxy-catalysis bonds for use in the mirror suspensions of gravitational wave detectors. *Class. Quantum Grav.*, 20(23):5025, 2003.

[83] P. Murray. *Measurement of the Mechanical Loss of Test Mass Materials for Advanced Gravitational Wave Detectors*. PhD thesis, Department of Physics and Astronomy, University of Glasgow, 2008.

[84] A. A. van Veggel, J. Scott, D. A. Skinner, B. Bezensek, W. Cunningham, J. Hough, I. Martin, P. Murray, S. Reid, and S. Rowan. Strength testing and sem imaging of hydroxide-catalysis bonds between silicon. *Class. Quantum Grav.*, 26(17):175007, 2009.

[85] D.-H. Gwo. Ultraprecision bonding for cryogenic fused-silica optics. In J. B. Heaney & L. G. Burriesci, editor, *Society of Photo-Optical Instrumentation Engineers (SPIE) Conference Series*, volume 3435 of *Society of Photo-Optical Instrumentation Engineers (SPIE) Conference Series*, pages 136–142, 1998.

[86] Stanford Research Systems. SR560 product page. http://www.thinksrs.com/products/SR560.htm, 2009.

[87] M. Tilsch, V. Scheuer, and T. T. Tschudi. Effects of thermal annealing on ion-beam-sputtered SiO_2 and TiO_2 optical thin films. In R. L. Hall, editor, *Optical Thin Films V: New Developments*, volume 3133 of *SPIE*, pages 163–175, San Diego, CA, USA, 1997. SPIE.

[88] A. Heptonstall, G. Cagnoli, J. Hough, and S. Rowan. Characterisation of mechanical loss in synthetic fused silica ribbons. *Phys. Lett. A*, 354(5-6):353 – 359, 2006.

[89] Y. S. Touloukian and E. H. Buyco. *Thermophysical Properties of Matter, TPRC data series*. IFI/Plenum, New York, 1970.

[90] B. E. Deal and A. S. Grove. General Relationship for the Thermal Oxidation of Silicon. *J. App. Phys.*, 36:3770–3778, 1965.

[91] R. Thielsch, A. Gatto, and N. Kaiser. Mechanical stress and thermal-elastic properties of oxide coatings for use in the deep-ultraviolet spectral region. *Appl. Opt.*, 41(16):3211–3217, 2002.

[92] CSIRO Mark Gross. Private communication.

[93] B. H. Houston, D. M. Photiadis, M. H. Marcus, J. A. Bucaro, X. Liu, and J. F. Vignola. Thermoelastic loss in microscale oscillators. *App. Phys. Lett.*, 80(7):1300–1302, 2002.

[94] S. Reid, G. Cagnoli, D. R. M. Crooks, J. Hough, P. Murray, S. Rowan, M. M. Fejer, R. Route, and S. Zappe. Mechanical dissipation in silicon flexures. *Phys. Lett. A*, 351:205–211, 2006.

[95] R. Hull. *Properties of crystalline silicon*. INSPEC, London, 1999.

[96] S. Reid. *Studies of materials for future ground-based and space-based interferometric gravitational wave detectors*. PhD thesis, Department of Physics and Astronomy, University of Glasgow, 2006.

[97] S. Reid. Private communication. 2009.

[98] D. Crooks. *Mechanical Loss and its Significance in the Test Mass Mirrors of Gravitational Wave Detectors*. PhD thesis, Department of Physics and Astronomy, University of Glasgow, 2003.

[99] S. Reid and R. Nawrodt. private communication. October 2009.

[100] J. Scott and S. Reid. private communication. October 2009.

[101] R. G. Munro. Elastic moduli data for polycrystalline ceramics. *NISTIR, National Institute of Standards and Technology, Maryland*, 6853, 2002.

[102] K. Numata, K. Yamamoto, H. Ishimoto, S. Otsuka, K. Kawabe, M. Ando, and K. Tsubono. Systematic measurement of the intrinsic losses in various kinds of bulk fused silica. *Phys. Lett. A*, 327:263–271, 2004.

[103] A. Ageev, B. C. Palmer, A. De Felice, S. D. Penn, and P. R. Saulson. Very high quality factor measured in annealed fused silica. *Class. Quantum Grav.*, 21(16):3887–3892, 2004.

[104] K. Numata, G. B. Bianc, M. Tanaka, S. Otsuka, K. Kawabe, M. Ando, and K. Tsubono. Measurement of the mechanical loss of crystalline samples using a nodal support. *Phys. Lett. A*, 284(4-5):162 – 171, 2001.

[105] S. D. Penn, A. Ageev, D. Busby, G. M. Harry, A. M. Gretarsson, K. Numata, and P. Willems. Frequency and surface dependence of the mechanical loss in fused silica. *Phys. Lett. A*, 352:3–6, 2006.

[106] V. B. Braginsky, V. P. Mitrofanov, V. I. Panov, and R. Krotkov. Systems with Small Dissipation. *Am. J. Phys.*, 55:1153–1154, December 1987.

[107] T. Uchiyama, T. Tomaru, M. E. Tobar, D. Tatsumi, S. Miyoki, M. Ohashi, K. Kuroda, T. Suzuki, N. Sato, T. Haruyama, A. Yamamoto, and T. Shintomi. Mechanical quality factor of a cryogenic sapphire test mass for gravitational wave detectors. *Phys. Lett. A*, 261(1-2):5 – 11, 1999.

[108] D. F. McGuigan, C. C. Lam, R. Q. Gram, A. W. Hoffman, D. H. Douglass, and H. W. Gutche. Measurements of the mechanical Q of single-crystal silicon at low temperatures. *J. Low Temp. Phys.*, 30:621–629, 1978.

[109] K. Numata, G. B. Bianc, N. Ohishi, A. Sekiya, S. Otsuka, K. Kawabe, M. Ando, and K. Tsubono. Measurement of the intrinsic mechanical loss of low-loss samples using a nodal support. *Phys. Lett. A*, 276(1-4):37 – 46, 2000.

[110] G. W. McMahon. Experimental Study of the Vibrations of Solid, Isotropic, Elastic Cylinders. *J. Acoust. Soc. Am.*, 36:85, 1964.

[111] G. G. Stoney. The Tension of Metallic Films Deposited by Electrolysis. *Proc. R. Soc. A*, 82:172–175, 1909.

[112] P. H. Townsend, D. M. Barnett, and T. A. Brunner. Elastic relationships in layered composite media with approximation for the case of thin films on a thick substrate. *J. App. Phys.*, 62:4438–4444, 1987.

[113] M. Janda. Elasticity modulus E_f and temperature expansion coefficient αf of aluminium thin films measured by a new method. *Thin Solid Films*, 112:219–225, 1984.

[114] J.-H. Zhao, Y. Du, M. Morgen, and P. S. Ho. Simultaneous measurement of Young's modulus, Poisson ratio, and coefficient of thermal expansion of thin films on substrates. *J. App. Phys.*, 87:1575–1577, 2000.

[115] P. J. Martin, A. Bendavid, M. V. Swain, R. P. Netterfield, T. J. Kinder, W. G. Sainty, and D. Drage. Mechanical and optical properties of thin films of tantalum oxide deposited by ion-assisted deposition. *Materials Research Society Symposium Proceedings*, 308:583–588, April 1993.

[116] C.-L. Tien, C.-C. Jaing, C.-C. Lee, and K.-P. Chuang. Simultaneous determination of the thermal expansion coefficient and the elastic modulus of Ta_2O_5 thin film using phase shifting interferometry. *J. Mod Opt.*, 47:1681–1691, 2000.

[117] V. B. Braginsky and A. A. Samoilenko. Measurements of the optical mirror coating properties. *Phys. Lett. A*, 315(3-4):175 – 177, 2003.

[118] Z. Pierpoint. Private communication. 2009.